

The Dynamics and Kinematics of Coronal Mass Ejections and Shock Waves

A dissertation submitted to the University of Dublin
for the degree of *Philosophiae Doctor (PhD)*

Eoin P. Carley
Supervisor: Dr. Peter T. Gallagher
Trinity College Dublin, December 2013

SCHOOL OF PHYSICS
UNIVERSITY OF DUBLIN
TRINITY COLLEGE



Declaration

I declare that this thesis has not been submitted as an exercise for a degree at this or any other university and it is entirely my own work.

I agree to deposit this thesis in the University's open access institutional repository or allow the library to do so on my behalf, subject to Irish Copyright Legislation and Trinity College Library conditions of use and acknowledgement.

Name: Eoin Carley

Signature: **Date:**

Summary

Coronal mass ejections (CMEs) are large-scale eruptions of magnetized plasma from the low solar atmosphere into interplanetary space. With energies of up to 10^{26} J, they are the most energetic eruptive phenomena in the solar system and are also the driver of plasma shocks from the corona into the heliosphere. Despite many years of study, the nature of the forces governing their eruption, and the kinematical behavior of the resulting shock, remain poorly understood. This thesis will present the first accurate calculation of the magnitude of the total force on a CME. It will also present previously unobserved plasma shock behavior that sheds new light into the kinematical nature of CME-driven shocks in the corona.

In the past, measurement of the forces governing the propagation of CMEs have been hindered by highly uncertain estimates of the total mass of the ejection. The primary source of uncertainty is the unknown position and geometry of the CME, leading to an erroneous treatment of the Thomson scattering equations which are used to estimate the mass. Geometrical uncertainty on the CMEs position and size has primarily been due to observations of the eruption from a single vantage point. However, with the launch of the Solar Terrestrial Relations Observatory (STEREO) mission, the two viewpoints can be exploited to derive the CMEs position and size, ultimately resulting in mass uncertainty that is both reliably quantified and much reduced. Using the STEREO spacecraft, a CME on the 12 December 2008 was found to have a mass of $3.4 \pm 1.0 \times 10^{15}$ g, meaning the mass uncertainty was less than 30%. This is a substantial improvement

on previous uncertainties which were well above 50%, or entirely unquantifiable. The much better mass estimates can then be combined with kinematical results that are also more reliable and hence lead to the first reliable quantification of the total force acting on the CME. The dynamics are described by an early phase of strong acceleration, dominated by a force of peak magnitude of $3.4 \pm 2.2 \times 10^{14}$ N at $3 R_\odot$. Using the magnetohydrodynamics (MHD) equation of motion, the relative sizes of the forces at each stage in the CME propagation are estimated, revealing the Lorentz force is the largest source of CME acceleration early in its propagation. Quantification of the Lorentz force magnitude from observations has never been achieved in the past.

The second part of this thesis will involve an investigation into the behaviour of radio-bright plasma shocks occurring in the corona. CMEs often erupt at speeds in excess of the local magnetosonic wave speeds in the corona. Traveling in excess of Alfvén Mach 1, they often drive shocks which can have a variety of observational manifestations, such as type II and III radio bursts, coronal bright fronts (CBFs), white-light enhancements, and the eventual in-situ detection of solar energetic particles. Despite such a variety of shock phenomena being observed for decades, the unifying physical mechanism between these phenomena remains unknown. This thesis will provide an analysis that uses extreme ultraviolet, radio, and white-light imaging of a solar eruptive event on 22 September 2011 to determine the properties of a CME-driven shock in the corona. The results show that a plasma shock with an Alfvén Mach number of $2.4_{-0.8}^{+0.7}$ was coincident with a coronal bright front and an intense decametric radio burst generated by electrons with kinetic energies of 2-46 keV (0.1-0.4 c). This work provides new observational evidence to show that the relationship between CMEs, CBFs, and type II and III radio bursts is a coronal plasma shock.

For my parents.

Acknowledgements

Some sincere acknowledgements...

List of Publications

1. **Carley, E. P.**, Long, D. M., Byrne P. J., Zucca, P., & Gallagher, P. T.
“Quasi-periodic Acceleration of Electrons by a Plasmoid Driven Shock in the Solar Atmosphere ”,
Nature Physics, in press, (2013)
2. **Carley, E. P.**, MacAteer, R. T. J., & Gallagher, P. T.
“Coronal Mass Ejection Masses, Energies, and Force Estimates Using STEREO”,
The Astrophysical Journal, Volume 752, Issue 1, article id. 36, 8 pp. (2012).
3. Zucca, P., **Carley, E. P.**, McCauley, J., Gallagher, P. T. ,Monstein, C., & MacAteer, R. T. J.,
“Observations of Low Frequency Solar Radio Bursts from the Rosse Solar-Terrestrial Observatory”,
Solar Physics, Volume 280, Issue 2, pp.591-602. (2012).
4. Zucca, P., **Carley, E. P.**, Bloomfield, S. D., & Gallagher, P. T.
“The formation heights of coronal shocks from 2D density and Alfvén speed maps”,
Astronomy & Astrophysics, Volume X, Issue Y, article id. (2013)
5. Bloomfield, S. D., **Carley, E. P.**, et al.
“A Comprehensive Overview of the 2011 June 7 Solar Storm”,
Astronomy & Astrophysics, Volume X, Issue Y, article id. (2013)
6. Morosan, D. E., Zucca, P., Fallows, R., **Carley, E. P.**, & Gallagher, P. T.
“The Non-flaring Sun at Low Frequencies with LOFAR”,
Astronomy & Astrophysics, Volume X, Issue Y, article id. (2013)

-
7. Bisi, M. M., Hardwick, S. A., Fallows, R. A., Davies, J. A., Harrison, R. A., Jensen, E. A., Morgan, H., Wu, C. C., Asgekar, A., Xiong, M., **Carley, E. P.**
“The first coronal mass ejection observed with the Low Frequency Array (LOFAR)”,
The Astrophysical Journal Supplements, Volume X, Issue Y, article id. (2013)

Contents

List of Publications	vii
List of Figures	xiii
1 Introduction	1
1.1 The Sun	2
1.1.1 Solar Interior	3
1.1.2 Solar Magnetic Field and Dynamo	7
1.1.3 Solar Atmosphere	11
1.1.3.1 Photosphere	11
1.1.3.2 Chromosphere	13
1.1.3.3 Transition Region	15
1.1.3.4 Corona	15
1.2 Coronal Mass Ejections	20
1.2.1 A Brief History	20
1.2.2 Morphology and Kinematics	22
1.2.3 Masses and Dynamics	29
1.3 Coronal Shocks	37
1.3.1 Type II Radio Bursts	37
1.3.2 Herringbones and Type IIIIs	44
1.3.3 Coronal Bright Fronts	46
1.3.4 White-light Shocks	50
1.4 Thesis Outline	51

CONTENTS

2 Coronal Mass Ejection and Plasma Shock Theory	53
2.1 Plasma Physics and Magnetohydrodynamics	54
2.1.1 Maxwell's Equations	54
2.1.2 Plasma Kinetic Theory	55
2.1.3 Magnetohydrodynamics	58
2.1.4 Magnetic Reconnection	61
2.2 Coronal Mass Ejections	65
2.2.1 Catastrophe Model	66
2.2.2 Magnetic Breakout Model	69
2.2.3 Toroidal Instability	72
2.3 Coronal Shocks and Plasma Emission	75
2.3.1 Alfvén Speed in the Corona	75
2.3.2 MHD Shocks	77
2.3.3 Shock Particle Acceleration	81
2.3.4 Wave-Particle Interaction	86
2.3.5 Three-Wave Interaction and Plasma Emission	89
2.3.6 Frequency Drift of Radio Bursts	94
3 Observation and Instrumentation	98
3.1 White-Light Observations	99
3.1.1 Lyot Coronagraph	101
3.1.1.1 SOHO LASCO	102
3.1.1.2 STEREO COR1 and COR2	106
3.1.1.3 Whilte-light Image Data Reduction	110
3.2 Ultraviolet Observations	114
3.2.1 The Atmospheric Imaging Assembly	115
3.3 Radio Observations	117
3.3.1 Nançay Radioheliograph	118
3.3.2 Nançay Decametric Array	124
3.3.3 STEREO WAVES	125
3.3.4 Rosse Solar Terrestrial Observatory	128
3.3.4.1 Antennas and Spectrometers	128

CONTENTS

3.3.4.2	Nominal Operations	132
3.3.4.3	Dynamic spectra from RSTO	133
3.3.4.4	eCallisto Network	133
3.3.5	Dynamic Spectra Data Reduction	135
4	Coronal Mass Ejection Masses, Energetics, and Forces	139
4.1	Introduction	140
4.2	Observations	142
4.3	Data Analysis	146
4.3.1	Thomson Scattering in the Corona	147
4.3.2	Mass Measurement and Geometrical Uncertainties	152
4.3.3	Evaluation of uncertainties	158
4.4	Results	160
4.4.1	Mass vs. Time and Height	160
4.4.2	Kinematics and Dynamics	164
4.4.3	Evaluation of Forces	167
4.5	Conclusion	170
5	Coronal Mass Ejection Shocks and Particle Acceleration	172
5.1	Introduction	173
5.2	Coronal Bright Front and Radio Source	175
5.2.1	Observations	175
5.2.2	Radio Source Height and Speed	177
5.2.3	Radio Source Alfvén Mach	181
5.2.4	CBF Speeds	184
5.2.5	CBF Thermal Properties	185
5.3	Radio Dynamic Spectra	186
5.3.1	Observations	187
5.3.2	Particle speeds and in-situ detection	187
5.4	White-light CME and Shock	193
5.5	Discussion	195
5.5.1	Relationship Between CME, CBF, and Radio bursts	195
5.5.2	Bursty Particle Acceleration	196

CONTENTS

6 Conclusions and Future Work	200
6.1 CME Masses and Energies	201
6.1.1 Principle results	201
6.1.2 Future Work	203
6.1.2.1 CME Mass and Forces Catalogue	203
6.1.2.2 Mass Estimates with AIA	212
6.2 Coronal Shocks and Radio Bursts	217
6.2.1 Principle results	217
6.2.2 Future Work	219
6.2.2.1 Hough Transform and Herringbone Statistics . .	219
A Appendix	230
A.1 Radio Burst Emissivity	231
A.2 EUV and pB Density Measurements	232
References	235

List of Figures

1.1	The solar interior and atmosphere	7
1.2	Differential rotation rate as a function of latitude and depth	8
1.3	The solar butterfly diagram	10
1.4	The Babcock model of magnetic field evolution in the Sun	11
1.5	The temperature and density as a function of height above the photosphere	14
1.6	AIA image of the corona	16
1.7	Comparison of soft X-ray and low frequency radio observations of the corona	18
1.8	LASCO C3 image of a CME	23
1.9	Distribution of CME speeds	25
1.10	CME height, speed, and acceleration as function of time	26
1.11	CME acceleration as a function of acceleration duration	27
1.12	CME speed profile along side flare X-ray light curve	28
1.13	CME energies and masses as a function of height	31
1.14	Distribution of CME masses, kinetic and total mechanical energies	32
1.15	Acceleration due to all forces acting on CME	35
1.16	The average energies of the different components of an eruptive event for six events. The CME is the biggest consumer of energy (Emslie <i>et al.</i> , 2012).	36
1.17	Type II radio burst	38
1.18	Low frequency image of a radio shock	40
1.19	Comparison of CME and type II height-time kinematics	41
1.20	Statistical comparison of CME and type II height-time kinematics	42

LIST OF FIGURES

1.21	CME flank shock observed by the UVCS spectrometer	43
1.22	Herringbone radio bursts	45
1.23	First observation of an ‘EIT wave’	47
1.24	Comparison of EUV wave and type II height-time	48
1.25	Model of EUV wave and coronal shock	49
1.26	White-light image of shocks	50
2.1	Sweet-Parker and Petscheck reconnection models	63
2.2	The catastrophe CME model	67
2.3	The breakout CME model	71
2.4	The toroidal instability CME model	73
2.5	The toroidal instability forces	75
2.6	Model of the Aflvén speed as a function of height in the corona .	76
2.7	MHD shock framework	78
2.8	Normal incidence and de Hoffman-Teller reference frames	82
2.9	Shock drift acceleration	84
2.10	Shock drift acceleration	89
2.11	Theoretically predicted radio burst fluxes	93
2.12	Model of radio burst driven by expanding CME flanks	94
2.13	Solar radio burst morphologies	95
2.14	Various models for electron number density in the corona	96
3.1	White-light corona during an eclipse	99
3.2	Radial variation of the K and F corona	100
3.3	The Lyot coronagraph	102
3.4	The LASCO C2 coronagraph optics	103
3.5	The LASCO C2 coronagraph detail	104
3.6	LASCO C2 Observations	106
3.7	STEREO spacecraft positions	108
3.8	The COR1 coronagraph	109
3.9	The COR2 coronagraph	110
3.10	COR1 and COR2 observations	111
3.11	The AIA telescope design	115
3.12	The four telescopes of AIA	117

LIST OF FIGURES

3.13	AIA temperature response	118
3.14	The Nançay Radioheliograph layout	119
3.15	Sky brightness, visibility, beam, and sampling function	123
3.16	NRH observations	124
3.17	Nançay Decametric Array observations	126
3.18	The SWAVES antennas	127
3.19	STEREO WAVES observations	129
3.20	RSTO Instrumental Setup	131
3.21	Callisto observations type II and herringbones	134
3.22	Callisto observations type II and herringbones	135
3.23	Callisto observations type II and herringbones	136
3.24	Callisto Worldwide	137
3.25	RSTO RFI Survey	138
4.1	2008-December-12 CME observed by COR1	144
4.2	2008-December-12 CMe observed by COR2	145
4.3	Thomson scattering schematic.	148
4.4	Thomson scattering geometry in the solar corona	150
4.5	Line-of-sight and plane-of-sky orientations	152
4.6	Electron brightness as function of angle	154
4.7	Uncertainty due to CME angular width	155
4.8	Uncertainty due to unknown POS angle and angular width	157
4.9	CME mass as a function of height and time	162
4.10	CME kinematics and energetics as a function of height	165
5.1	Propagation of CBF and radio burst	176
5.2	Radio source and CBF position angle versus time	178
5.3	2D density map of the corona	180
5.4	A potential field source surface extrapolation of the corona magnetic field	182
5.5	Alfvén speed map of the solar corona.	183
5.6	Tri-color running ratio images of a CBF.	185
5.7	Radio dynamic spectra of 22-September-2011 event	189
5.8	Type III speeds	191

LIST OF FIGURES

5.9	Herringbone wavelet analysis	192
5.10	3D reconstruction of CME and white-light shock	194
5.11	CBF and shock orientation	197
6.1	CORIMP masks	204
6.2	CME Mass automatic detection	205
6.3	Inverse masks	207
6.4	Inverse mass time series	208
6.5	Mass time series error check	210
6.6	EUVI dimming region	212
6.7	Mass-temperature distribution	213
6.8	Mass evacuation with time	215
6.9	Line in polar coordinates	220
6.10	Relationship between image space and Hough space	221
6.11	Example Hough Transform	222
6.12	Herringbone observations	223
6.13	Hough transform	224
6.14	Hough transform herringbones	225
6.15	Herringbone statistics	226
6.16	Herringbone statistics 2	227
6.17	Herringbone intensity vs drift	228

1

Introduction

The Sun has long been the focus of humanity's curiosity. Throughout history it has been the harbinger of new religions, philosophies, and sciences. It has changed our understanding of our place in the Universe and allowed us to push forward the frontiers of stellar astronomy. Although our understanding of the Sun is nowadays more advanced, the curiosity we hold for it has not changed since the very early humans. Now, we understand the Sun is a star similar to any other in its class, currently going through a relatively unchanging 11 year cycle of activity that is extremely rich in physical complexity. The study of such complex phenomena has yielded immeasurable advances in many areas of physics such as spectroscopy, plasma physics, magnetohydrodynamics (MHD), particle physics, to name but a few. Although some of these sciences have grown over decades (or even centuries) they are still incomplete. I hope this theses will contribute to the continuing growth of these sciences and to the understanding of our nearest star.

This chapter will begin with a short introduction to the basic physical concepts governing the behaviour of the Sun, including the layers of solar interior and atmosphere. This will be followed by an overview of both the historical and state-of-the-art observational results of coronal mass ejections and coronal shock research. I will finish by highlighting open questions in the field and give a thesis outline for addressing these questions.

1.1 The Sun

The Sun is our nearest star, located 1.49×10^6 km from Earth at the centre of our solar system. Located on the main sequence of the Hertzsprung-Russell (HR) diagram, it has a spectral class of G2V, with a luminosity of $L_\odot = (3.84 \pm 0.04) \times 10^{26}$ W, mass of $M_\odot = (1.9889 \pm 0.0003) \times 10^{30}$ kg and radius of $R_\odot = (6.959 \pm 0.007) \times 10^8$ m (Foukal, 2004). It was born approximately 4.6×10^9 years ago when a giant molecular cloud underwent gravitational collapse and began hydrogen nuclear fusion at its core (Bouvier & Wadhwa, 2010; Montmerle *et al.*, 2006). The energy produced from this fusion resulted in enough pressure to counteract gravitational contraction and bring about a hydrostatic equilibrium, allowing the young star to reach a stability that is sustained today. It is estimated the Sun will maintain this stability for another 4.8 billion years from present time, at which point, it will move off the main sequence and into a red giant phase (Sackmann *et al.*, 1993). During this later part of its life, begin nuclear burning of heavier elements such as helium, carbon and oxygen and it will grow in size to 200 times its current radius. Once carbon burning in the core has ceased it can no longer sustain nuclear fusion of heavier elements, resulting in a gravitational instability that will eventually lead to a stellar nova. This nova will result in the loss of the outer envelopes and ultimately the Sun's death, leaving behind a

compact and dense white-dwarf.

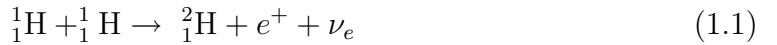
Until such time, the Sun will remain on the main sequence in a regular state of hydrogen fusion in its core. The energy released during this process is the ultimate source of light and all energetic activity that we observe from Earth and beyond. Before we can understand how this energy manifests in the solar atmosphere as a variety of energetic phenomena, it is important to understand how the energy is generated and transported through its interior and finally released into its atmosphere and interplanetary space.

1.1.1 Solar Interior

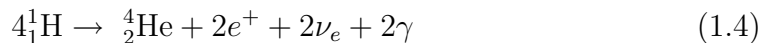
The theoretical treatment of how the solar interior is structured and how it behaves it through the ‘standard solar model’ or SSM. The SSM is a grouping of theories that described how the Sun was formed, how it maintains its stability, how it generates energy, and how this energy is transported through its interior and released at the surface. Much of the major developments of this theory have been in the 20th century, due mainly to the pioneering experiments in solar neutrino physics and helioseismology. Hence, the development of the SSM has mainly been through a refinement of the theory based on these observational fields. Although the SSM has increased in sophistication, its four main aspects remain the most general framework for describing the behavior of the solar interior.

The SSM firstly states that the Sun was born from the gravitational collapse of a primordial gas of hydrogen, helium, and traces of other heavy elements (Sackmann *et al.*, 1993). Secondly, it maintains its structural stability via a hydrostatic equilibrium such that the gravitational force is balanced by a pressure gradient ($\nabla P = -\rho g$) at each radial distance inside the star. The third main

aspect of the SSM involves the source of the Sun’s energy. The pioneering neutrino physics experiments of the 1970s confirmed that the energy source is a hydrogen fusion process, namely the proton-proton or ‘pp’ chain, in the solar core (Davis *et al.*, 1968). In this process, four protons are fused to form a helium nucleus. This can occur in a variety of ways, but at the Sun’s core temperature of 15 MK, the dominant reaction is the ppI chain given by



where ${}^1_1\text{H}$ is a hydrogen nucleus, ${}^2_1\text{H}$ is deuterium, ${}^3_2\text{He}$ is tritium, ${}^4_2\text{He}$ is helium, e^+ is a positron, ν_e is an electron neutrino, and γ is a gamma ray photon. Reactions (1.1) and (1.2) must happen twice for (1.3) to occur. Taking this into account, the entire process may be summarised as



liberating $4.2 \times 10^{-12}\text{J}$ of energy per reaction, with $\sim 2.4\%$ of the energy carried away by the neutrinos. This particular form of the pp-chain (ppI) occurs in 86% of the cases in solar core nuclear fusion (Turck-Chièze & Couvidat, 2011). However, there are other reactions capable of producing He from H categorized into ppII, ppIII etc, which each involve production of ${}^7_4\text{Be}$ and ${}^8_5\text{B}$, which were actually the first to be confirmed despite these reactions being less common than ppI (Davis *et al.*, 1968).

The neutrino experiments together with the SSM provide much of what we know about the solar energy generation and the solar core. They imply a temper-

ature of 15.6×10^6 K and density of 1.48×10^5 kg m $^{-3}$ at solar centre, where energy generation is via fusion which occurs $0.0 - 0.25 R_\odot$ (Figure 1.1). This range in heights defines the solar core and outside this range the temperature drops to a value low enough for the cessation of fusion. While thermonuclear fusion and the generation of solar energy is the third aspect of the SSM, the fourth aspect involves exactly what happens to this energy once it is generated i.e., it describes an energy transport mechanism.

Beyond $0.25 R_\odot$ the temperature drops to 8 MK, such that fusion stops but only free protons and electrons exist. In this environment, the photons continuously scatter off free particles, undergoing a random walk toward the surface over a distance of $0.25 - 0.7 R_\odot$. This region is known as the radiative zone and has densities of $2 \times 10^4 - 2 \times 10^2$ kg m $^{-3}$, resulting in a small photon mean free path (mfp) of 9.0×10^{-4} m. The photons proceed towards the solar surface over a very long time scale, taking on the order of 10^5 years to traverse this region (Mitalas & Sills, 1992). The occurrence of such a radiative energy transport results in a temperature gradient given by

$$\frac{dT}{dr} = -\frac{3}{16\sigma} \frac{\kappa\rho}{T^3} F_{rad} \quad (1.5)$$

where σ is the Stefan-Boltzman constant, κ is the mass extinction coefficient (opacity per unit mass), ρ is mass density, T is temperature, and F_{rad} is the outward radiative flux (Foukal, 2004). This implies that for a particular outward flux, if the opacity increases, a steeper temperature gradient is required to maintain such a flux. At $0.7 R_\odot$ the temperature drops to 1 MK allowing protons to capture electrons into a bound orbit. The existence of electrons in atomic orbit results in a dramatic increase in opacity of the plasma (Turck-Chièze & Couvidat, 2011) and hence the temperature gradient increases. The increased temperature

gradient required to sustain the energy flow may lead to the onset of a convective instability beyond $0.7 R_{\odot}$ toward the solar surface. This instability will occur if the temperature gradient in the star is steeper than the adiabatic temperature gradient

$$\left| \frac{dT}{dr} \right|_{star} > \left| \frac{dT}{dr} \right|_{adiabatic} \quad (1.6)$$

This is known as the Schwarzschild criterion, and it is fulfilled from $0.7 - 1 R_{\odot}$ – a region known as the convection zone. The temperature and density drop as height increases and finally reaches $T \sim 6000$ K and mass densities of $\rho \sim 1 \times 10^{-5}$ kg m⁻³ at $1 R_{\odot}$. Much of what we know about the depth, temperature, and density of the convection zone comes from a fine-tuning of the standard solar model, such that the model reproduces observational properties of neutrino experiments and the field of helioseismology. Helioseismology makes use of the fact that the Sun acts as a resonator for acoustic waves which manifest as detectable oscillations in the doppler shift of photospheric Fraunhofer lines. These acoustic waves are referred to as pressure or p-modes, and a variety of wavelengths exist, generally with a period of approximately 5 minutes (Turck-Chièze & Couvidat, 2011).

The shorter wavelengths in the mode propagate into the solar convection zone and experience a total internal reflection at a shallow depth, while longer wavelengths can penetrate into much deeper layers. Hence depending on the period observed, the oscillations provide a probe of the dynamical properties at a particular depth inside the sun. Analysis of these oscillatory modes has revealed that the differential rotation that is observed at the solar surface continues down into the convection zone, however the deeper radiative zone rotates as a solid body (Figure 1.2). In going from the convection zone to the radiative zone there is a sudden dramatic transition in the rotational dynamics of the solar interior (Thompson *et al.*, 2003). This sudden change occurs in a region sandwiched in

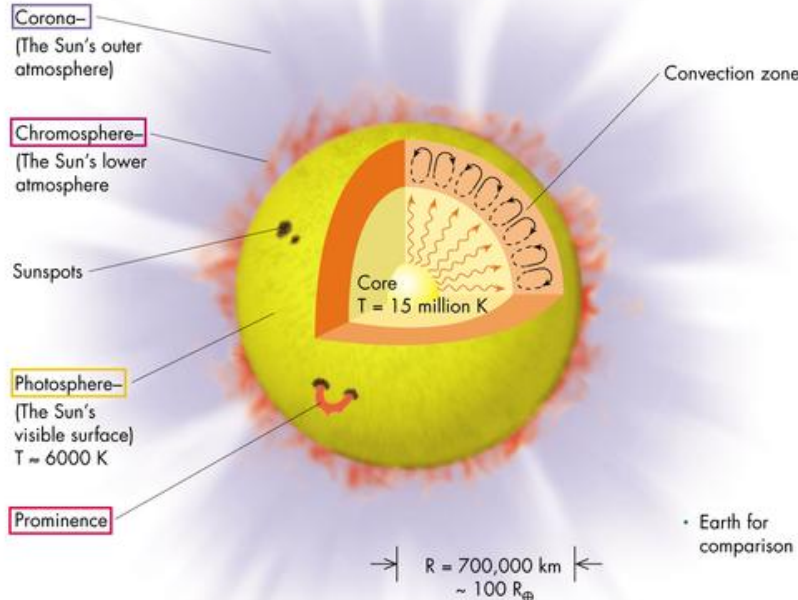


Figure 1.1: The structure of the solar interior and atmosphere, including the core, radiative zone, convective zone, photosphere, chromosphere, and corona. While the various interior zones are demarcated in terms of the dominant energy transport mechanism, the layers of the solar atmosphere are usually demarcated by temperature changes as height above the solar surface increases. The temperature ranges from ~ 6000 K in the photosphere to above 1 MK in the corona.

between the radiative and convective zones, known as the tachocline. The study of this layer is extremely active as it is believed to play an important role in the generation and evolution of the solar magnetic field.

1.1.2 Solar Magnetic Field and Dynamo

The solar magnetic field plays a dominant role in the energetic activity occurring in the solar atmosphere. At solar activity minimum the solar magnetic field has a poloidal dipolar structure, with the polar axes generally being coincident with the rotational axes. However as the activity cycle progresses towards a maximum, the field gains a strong toroidal component, making it far more dynamic and complex.

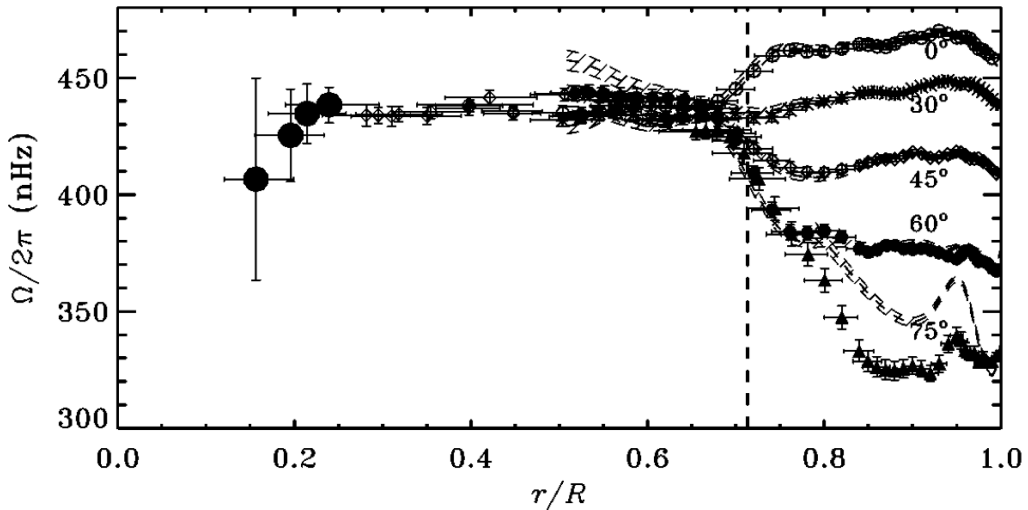


Figure 1.2: Helioseismological determination of interior rotation rate in nanoHertz (nHz) as a function solar radius, starting from solar centre ($r = 0.0$) to surface ($r = 1.0$). The separate symbols show different latitudes, from 0° to 75° . The data show that the interior rotates differentially down to $\sim 0.7 R_\odot$. The dashed line demarcates the boundary between solid body rotation and differential rotation. The transition from solid body to differential rotation occurs in a highly sheared layer known as the tachocline, a very important layer for solar magnetic field generation (Thompson *et al.*, 2003).

This complex toroidal component manifests at the surface as sunspots, hence the number of sunspots on disk has been used as a proxy for the activity cycle for over 100 years, often showing an approximate 11 year periodicity (Figure 1.3, bottom panel). At the beginning of the cycle sunspots tend to appear on disk with a latitudinal distribution of $\pm 30^\circ$ of the equator. As the cycle progresses, sunspots appear at lower and lower latitude (known as Spörer's law), until they eventually disappear at the end of a cycle. Sunspot latitude with respect to time is shown in Figure 1.3, top panel, and is known as the 'butterfly diagram'.

Sunspots in there simplest case emerge as a dipolar structure, with the leading spot being closer to the equator, such that the dipole is titled relative to the solar equator (Joy's law). In a given hemisphere, the leading sunspot and trailing spot

have opposite polarities, with the polarities reversed in the other hemisphere (Hayle's law). The trailing polarity can often be more fragmented and dispersed than the leading polarity. Despite sunspots generally having a dipolar structure, spot groups can be far more complex, having a complex multipolar structure – these spots are usually the more active.

Over the course of a solar cycle, the sun changes polarity (at the time of sunspot maximum). For example, an overall dipolar configuration of North-South will become South-North, another cycle will bring it back to North-South once more. While the activity cycle usually last 11 years, one full magnetic cycle has a period of 22 years. The complex behavior of the solar magnetic field over an 11 year activity cycle, during which the dipole reverses sign, is generally explained by solar dynamo theory. The theory employs magnetohydrodynamic (MHD) models that involve large-scale flow patterns of the solar interior that act to both induct and diffuse the magnetic field such that it produces the familiar 11 year magnetic activity cycle (Charbonneau, 2010).

Although solar dynamo theory is an active area of research and a number of questions still remain, the generally accepted paradigm for the activity cycle was first proposed by Babcock (1961). The mechanism involves differential rotation of the solar convection zone tends (Figure 1.2) that tends to drag the field from a poloidal position into a toroidal one (known as the Ω -effect), eventually winding the field around the solar axis into a stressed state, see Figure 1.4. The main storage of this wound field is in the region below the convection zone known as the tachocline. This region has an ‘overshoot’ layer, in which descending convective flows are trapped due the subadiabicity of the region (convectively stable). This stability allows field to be built up and stored into complex magnetic structures that may form twisted ‘flux-ropes’ due to the continuous wrapping of

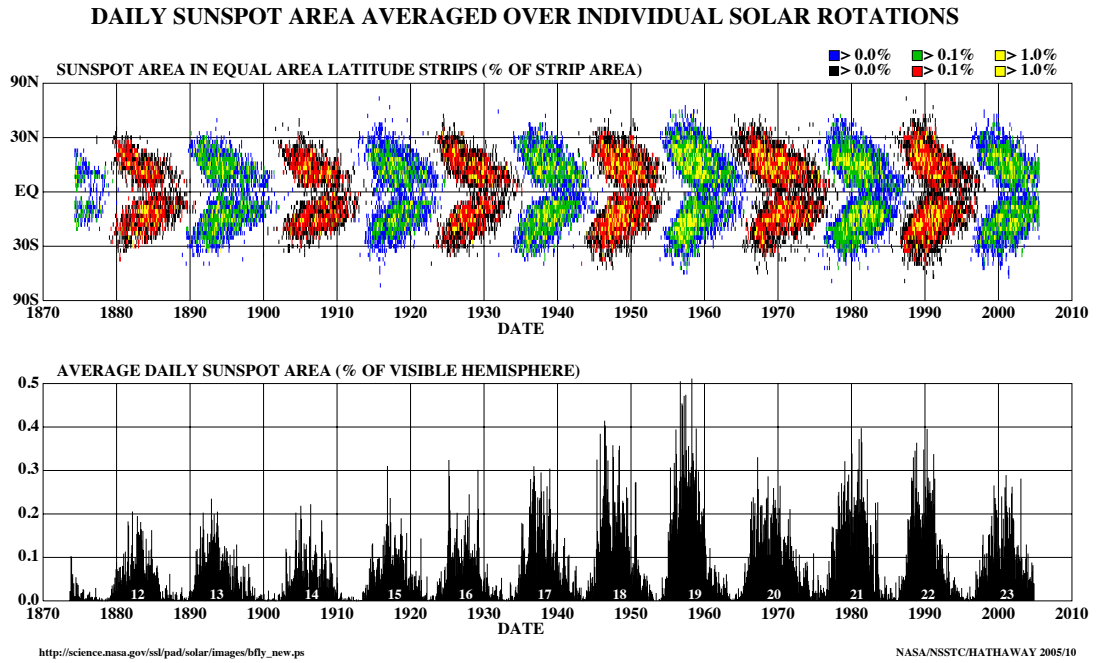
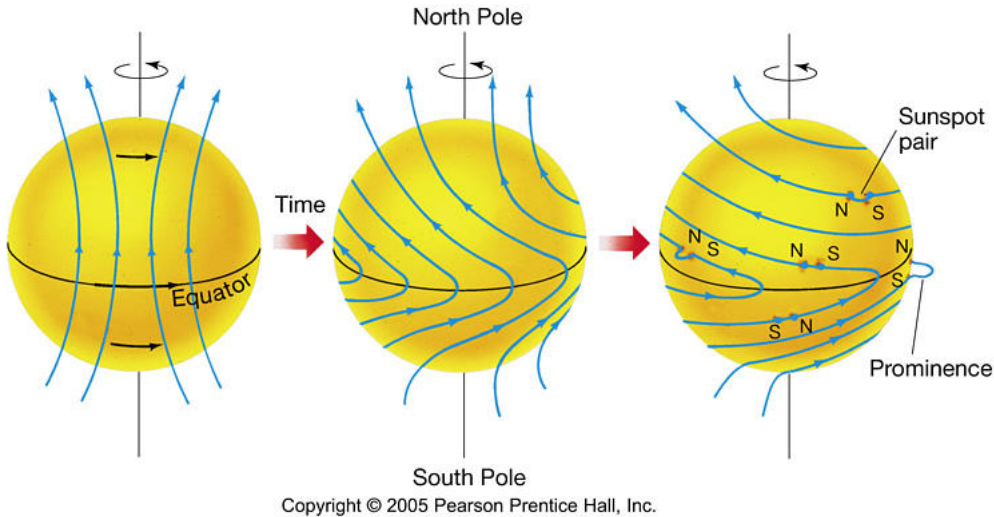


Figure 1.3: Top: The latitude of sunspots as a function of time. During the rise phase of each cycle the sunspots have a latitudinal distribution of $\pm 30^\circ$ from the equator. As the solar cycle progresses, sunspots emergence takes place at an increasingly lower latitude. Bottom: Sunspot area as a function of time. The spot area, or number of spots, is a proxy for solar magnetic activity which approximate follows and 11 year periodicity.

the field during the Ω -effect. Due to the rope's excess magnetic pressure, it becomes convectively unstable and begins to rise and experience a Coriolis force that induces a tilt of the rope with respect to the equatorial plane (this is known as the α -effect and is an explanation of Joy's law). The field eventually surfaces creating sunspots in the photosphere and a complex magnetic structure in the solar atmosphere known as an active region (Fan, 2009). The active regions themselves may be sheared, twisted and generally evolves to build huge amounts of potential energy. The release of this potential energy plays a big role in the dynamics of the solar atmosphere.



Copyright © 2005 Pearson Prentice Hall, Inc.

Figure 1.4: Differential rotation and flux freezing result in the poloidal dipolar magnetic field, generated by dynamo action, to be dragged around in a toroidal direction, an action known as the omega effect. Buoyancy of the field lines results in them rising and twisting, known as the alpha effect, eventually surfacing to become bipolar fields that extend far into the corona.

1.1.3 Solar Atmosphere

The solar atmosphere begins above the visible surface of the sun, known as the photosphere. At this point, the Sun becomes optically thin to visible radiation and light escapes from this surface. Beyond this visible surface is the solar chromosphere, and the corona, which eventually becomes the solar wind. Each of these layers is home to a complex variety of phenomena, and each layer, with its accompanying attributes, is described here.

1.1.3.1 Photosphere

As mentioned, the photosphere begins where the atmosphere becomes optically thin to visible radiation. ‘Visible light’ in this instance is usually taken to mean light with a wavelength of 5000 Å, hence the emergent light from the photosphere is taken to come from the surface at which $\tau_{5000} = 2/3$, where τ is the opti-

cal depth. The optical depth of $2/3$ is a consequence of the Eddington-Barbier approximation, and says that emergent flux F_ν from the photosphere is given by

$$F_\nu = \pi B_\nu(\tau = 2/3) \quad (1.7)$$

e.g., the emergent flux is given by π times blackbody intensity at an optical depth of $2/3$, where blackbody intensity B_ν is given by Planck's law

$$B_\nu = \frac{2h\pi\nu^3}{c^2} \frac{1}{\exp(h\nu/k_B T) - 1} \quad (1.8)$$

where h is Planck's constant, ν is frequency, c is the speed of light, k_B is Boltzmann's constant, and T is temperature. Integrating equation 1.8 over frequency this results in $F = \sigma T^4(\tau = 2/3)$, showing the frequency integrated flux is proportional to the temperature at $\tau = 2/3$, hence the effective temperature of solar blackbody radiation is $T_{eff} = T(\tau = 2/3) = 5800$ K. Solar radiation at visible wavelengths is most closely characterised by a blackbody of temperature 5800 K, although the brightness temperature T_B of the photosphere can deviate from this value, since not all frequencies emerge from the same optical depth.

The visible appearance of the photosphere reveals a small scale granular structure, with granules of typical size scale of 1000 km and a lifetime of 5–10 minutes. The granules typically show bright centers (regions of upflow) surrounded by darker intergranular lanes (regions of downflow). Such upward and downward flow indicates that granulation at the photosphere is the surface manifestation of convective activity in the deeper layers of the interior (Schrijver & Zwaan, 2008). As well as the conspicuous granulation there is also ‘super-granulation’ which has much the same mechanism as the granules, but of a much larger size of 10,000 – 30,000 km. Apart from granules and supergranules, the most conspic-

uous features of the photosphere are sunspots, regions of concentrated magnetic flux that has penetrated from the solar convective zone into the solar atmosphere. The spots have a temperature of ~ 4000 K, which is cooler than the typical solar blackbody temperature of 5800 K. Typical magnetic field strengths in sunspots are on the order of kilo-Gauss, while quiet regions are permeated by fields with tens of Gauss.

Temperature and density diagnostics of the photosphere and above are usually determined through an analysis and modeling of Fraunhofer lines e.g., such as the H α and CaII H and K lines (Fontenla *et al.*, 1988; Gabriel, 1976; Vernazza *et al.*, 1981). The temperature and density diagnostics as a function of height above the photosphere is shown in Figure 1.5. After the $\tau_{5000} = 1$ level the temperature drops to a minimum of ~ 4400 K at ~ 400 km above the photopshere before rising again, eventually undergoing a rapid increase at ~ 2000 km. The region between the temperature minimum up the height at which temperature begins to rise rapidly is the next layer of the atmosphere beyond the photosphere, known as the chromosphere

1.1.3.2 Chromosphere

As predicted by the models of (Fontenla *et al.*, 1988; Gabriel, 1976; Vernazza *et al.*, 1981), at ~ 400 km above the $\tau_{5000} = 1$ surface the temperature drops to a minimum of ~ 4400 K. Beyond this minimum the temperature begins to rise again, demarcating the beginning of the chromosphere. This layer of the atmosphere is generally accepted to extend to a height at which temperatures reach 20,000 K, however temperatures as high as $\sim 1 \times 10^5$ K are sometimes attributed to chromospheric heights, hence it is observable at ultraviolet (UV) wavelengths as well as visible.

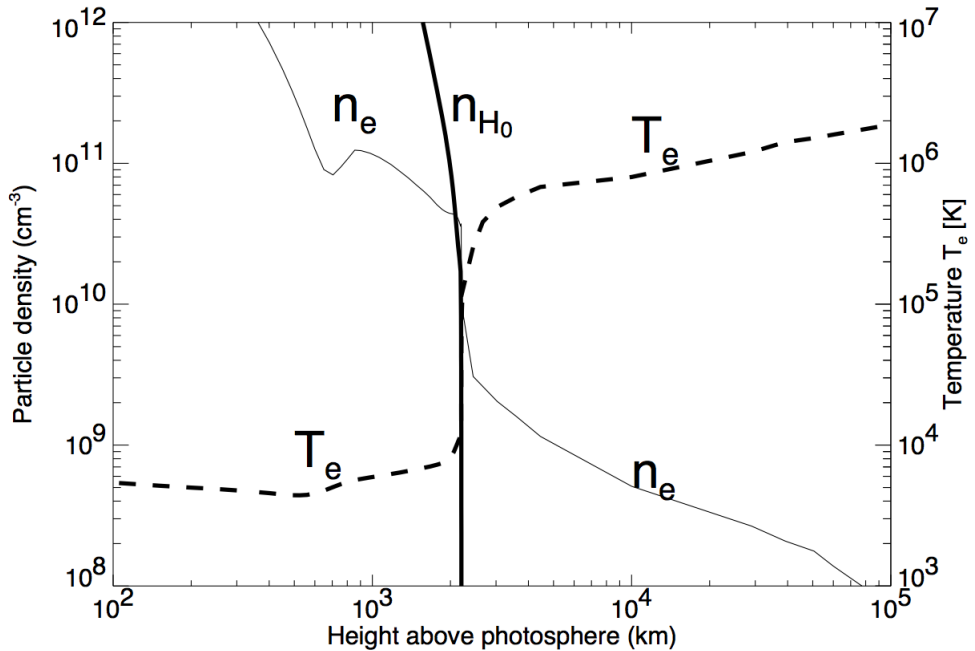


Figure 1.5: Temperature and density variation in the solar atmosphere constructed from the models of (Fontenla *et al.*, 1988; Gabriel, 1976; Vernazza *et al.*, 1981), adopted from (Phillips *et al.*, 2008).

Beyond the temperature minimum there is a broad temperature plateau between $\sim 1000 - 2000$ km, after which the temperature starts to increase dramatically. Similar to the photosphere, supergranulation is present in the chromosphere, indicating that this layer of the atmosphere is magnetically structured with concentrations or bundles of magnetic fields confined to isolated regions in the intergranular lanes. These concentrations of magnetic field are believed to play a role in chromospheric heating (Carlsson & Stein, 1997). When the temperature reaches 20,000 K the extremely prominent Ly- α emission line is formed, with a wavelength of 191.5 nm, and this is accompanied by other prominent ultraviolet lines such as those of C IV, formed at temperatures of $\sim 110,000$ K. Such high temperatures are generally considered to be outside the range of the chromosphere and are indicative of a thin layer of the atmosphere known as the

transition region.

1.1.3.3 Transition Region

The layer sandwiched in between the chromosphere and the corona is the transition region. It is characterised by temperatures of $\sim 10^5$ K and has the steepest temperature gradient in the solar atmosphere and extremely narrow at just 200 km in width. The SDO/AIA 304 Å image shows the chromosphere and transition region, in which the supergranular network can still be seen. The 171 Å image shows the upper transition region and corona. The network has just about disappeared at this height. As described, the network outlines the magnetic structure of the atmosphere, hence magnetic field goes from ordered and concentrated in the chromosphere to more ubiquitous and complex in the corona, sometimes termed the magnetic ‘canopy’.

1.1.3.4 Corona

The outermost layer of the solar atmosphere is known as the solar corona, beginning at ~ 2500 km above the photosphere. It has an electron number density of 10^9 cm^{-3} at its base in quiet regions, decreasing to 10^6 cm^{-3} at distance of $1 R_\odot$ from the solar surface. The models of (Fontenla *et al.*, 1988; Gabriel, 1976; Vernazza *et al.*, 1981) reveal that beyond the transition region (~ 2500 km) the temperature in the corona reaches well over 1×10^6 K. Such high temperatures allow the formation of emission features that belong to highly ionized heavy elements, for example Fe IX, up to as high as Fe XXIV. The presence of these highly ionized species (and many others) show that the corona has temperatures in the 1 – 2 MK range in quiet regions, active regions may exhibit temperatures in the range of 2 – 6 MK, while coronal holes may be lower than 1 MK. The temper-

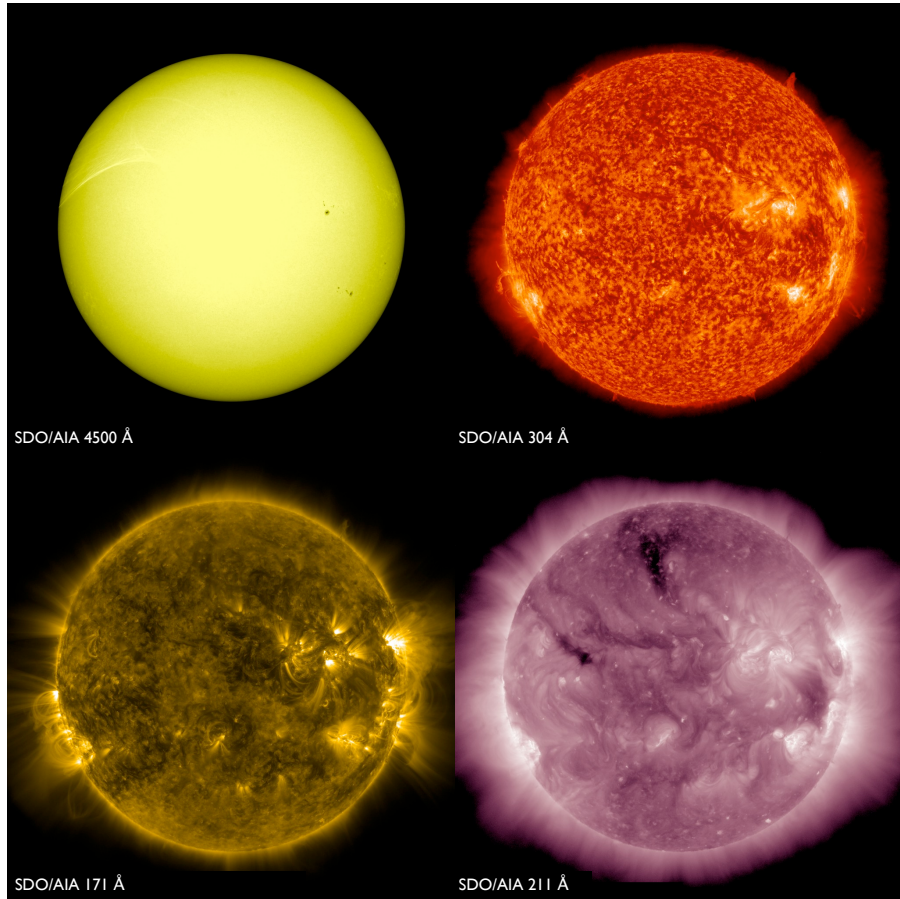


Figure 1.6: Atmospheric Imaging Assembly (AIA) observations of the photosphere (4500 Å), chromosphere (304 Å), transition region (304 Å, 171 Å), and corona (171 Å, 211 Å). Images taken on 04 September 2013.

atures of a flaring active region can be even higher than this, reaching tens of mega-Kelvin. The high temperatures and presence of highly ionized species of heavy elements means the corona may be primarily observed in the ultraviolet and X-ray. When viewed at these wavelengths, the corona appears highly structured, showing concentrations of bright loops known as active regions (Fig. 1.6).

Ultraviolet wavelengths allow observations of the very low corona, perhaps to only a few scale heights. However, the most extensive observations of the corona are in the visible, generally known as the ‘white-light’ corona (Figure 3.14). The

corona's white-light radiation is primarily due to scattering of photospheric light by particles and dust grains. The component which is due to Thomson scattering by free electrons is known as the *Kontinuierlich* or K-corona. The spectrum of this light is the same as the photospheric continuum except for the absence of Fraunhofer lines. These lines are ‘washed-out’ of the spectrum due to thermal Doppler broadening of the high-velocity free electrons that scatter the light. The emission is optically thin, so the intensity is due to the number of scattering agents along the line of site (this is explained in detail in Chapter 3, Section 3.1). The K-corona dominates white-light emission from low atmosphere to $\sim 4R_\odot$. After this height, there is an increasing contribution from Rayleigh or Mie scattering from interplanetary dust grains, known as the the Fraunhofer or F-corona. Since these dust grains move at a much slower velocities than the electrons, they do not wash out the Fraunhofer lines of the photospheric spectrum. The F-corona extends far beyond Earth and a can be viewed in the night sky as *Zodiacal light*.

Ultraviolet and white-light observations remain the primary method of imaging the low and extended corona, respectively. However, the corona is also a strong emitter across the entire radio wavelength range, from microwave to kilometric wavelengths. Indeed, metric wavelengths provide a method of imaging the quiet and thermal corona in an optically thick regime beyond $1 R_\odot$, an ability that does not exist in white-light and UV observations. These radio observations can reveal much of the same features as other wavelengths (albeit at lower spatial resolution) such as the bright emission of active regions and an emission deficiency of coronal holes (Fig. 1.7).

The quiet corona at metric wavelengths is primarily an emitter of thermal Bremsstrahlung i.e., thermal electrons accelerating in the Coulomb electric fields of protons. The height at which metric radiation escapes from the corona depends

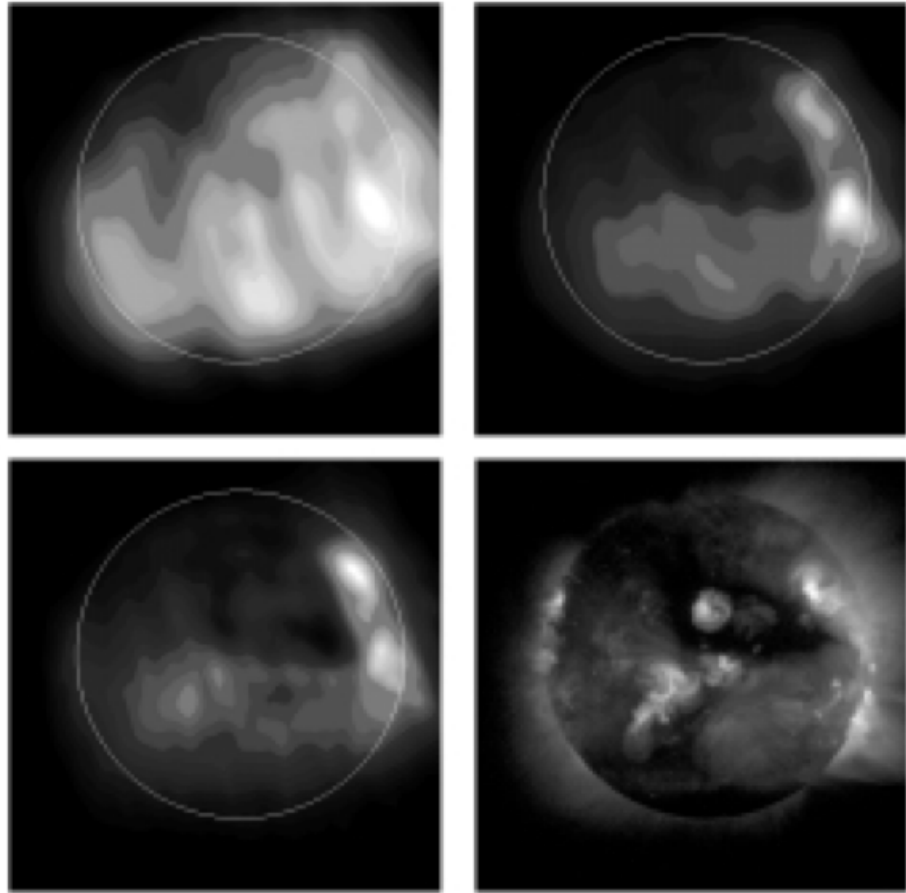


Figure 1.7: Low frequency observations of the solar atmosphere. Nan cay Radio-heliograph (NRH) 164MHz (top left), 327 MHz (upper right), and 410 MHz bottom left. Yohkoh Soft X-ray Telescope (SXT) image for comparison. Note the coronal holes in the SXT image is also in the 164 MHz image of NRH. The active regions are also bright at 327 MHz and 410 MHz (Lantos, 1999)

on the Bremsstrahlung absorption process, known as free-free opacity and given by

$$\kappa_{ff} \sim \frac{n^2}{\nu^2 T^{3/2}} \quad (1.9)$$

where n is the electron number density, ν is the frequency of electromagnetic radiation, and T is the temperature. Qualitatively, for a given frequency the density must drop below a certain value for the radiation to become optically thin and escape the solar atmosphere. In the radio band, even the highest frequency

(microwaves) do not escape until densities drop to chromospheric values. Hence a microwave image of the sun will provide a direct observation of light escaping from the chromosphere. Reducing the frequency further still to the 10^8 Hz (metric wavelengths), the density must drop to coronal values before the free-free opacity is low enough for radiation to be optically thin. Hence, metric wavelength radiation escapes the solar atmosphere only in the outer corona. For example 150 MHz imaging of the solar atmosphere may image an optically thick atmosphere out to a height of $\sim 0.5 R_\odot$ above the photosphere. The existence of an optically thick atmosphere at these wavelengths allows a direct probing of coronal temperatures at these heights. Using the solution to the radiative transfer equation

$$T_B = T_0 e^{-\tau_\nu} + T_e (1 - e^{-\tau_\nu}) \quad (1.10)$$

where T_B is the observed brightness temperature, T_0 is the background source brightness temperature, and T_e is the electron temperature of a cloud of plasma between observer and source¹, we can separate this equation into two regimes. Firstly, in the optically thick regime $\tau_\nu \gg 1$ equation 1.10 reduces to $T_B = T_e$, indicating that the brightness temperature is a direct measure of the electron temperature in solar atmospheric plasma. Secondly, in the optically thin regime $\tau_\nu \ll 1$, equation 1.10 reduces to

$$T_B = T_0 (1 - \tau_\nu) + T_e \tau_\nu \quad (1.11)$$

Considering the case of no background source we see that for the optically thin regime $T_B = T_e \tau_\nu$ i.e., the brightness temperature is not a direct measure of the

¹Note that radio observations often use brightness and electron temperatures in place of specific intensity and the source function because radio observations are often calibrated via a load of known temperature

electron temperature, but is reduced by a factor of τ_ν . Hence, radiation from an optically thick plasma provides a direct probe of the electron temperature in the corona, while radiation from an optically thin plasma provides a measure of the same temperature but diminished by the optical depth.

1.2 Coronal Mass Ejections

The solar corona is home to a variety of dynamic and highly energetic activity, the cause of which is the build-up and release of magnetic energy. Of all the activity taking place in the corona, the most spectacular manifestation of energy release is the coronal mass ejection (CME). A modern understanding of corona mass ejectionss tells us that they are large-scale eruptions of plasma and magnetic field that propagate from the low solar corona into interplanetary space. They have speeds in the range $10 - 2500 \text{ km}\cdot\text{s}^{-1}$ (Gopalswamy & Thompson, 2000), masses of $10^{13} - 10^{16} \text{ g}$, and kinetic energies of $10^{22} - 10^{25} \text{ J}$ (Vourlidas *et al.*, 2010), making them the most energetic explosive events in the solar system and a major cause of adverse space weather in the near-Earth environment. The following provides an observational overview and open questions concerning the general properties of CMEs, including their morphology, kinematics, and dynamics, as well as their ability to drive shocks, accelerate particles, and produce a variety of radio bursts.

1.2.1 A Brief History

The largest flare ever to have been recorded occurred on September 1st 1859, observed by the astronomer Richard Carrington (Carrington, 1859). Approximately 17 hours after Carrington recorded the event, a powerful geomagnetic storm began at Earth, producing brilliant aurora and damaging telegraph sys-

1.2 Coronal Mass Ejections

tems on both sides of the Atlantic ocean. The event aroused much speculation on a causal link between the phenomena Carrington observed on the Sun and the magnetic activity recorded throughout the Earth (Balfour, 1861). It was not until 1919 that a theory was put forward to suggest plasma transients emitted from the Sun may impact the Earth and cause geomagnetic activity and the aurora Lindenmann (1919), a process later elaborated upon by Chapman & Ferraro (1930). Up until 1940s, the only evidence confirming the plasma transient hypothesis was the correlation between solar and geomagnetic activity. However, following the development of radio receiver technology during World War Two, much interest was given to solar radio bursts and their indication that disturbances travel away from the Sun at speeds of up to 500 km s^{-1} (Wild *et al.*, 1959). Further evidence came from the fields of cosmic rays studies, when it was suggested the ground level detections of particles at Earth such as those reported by (Forbush, 1946) may be related to a acceleration of particles by a shock moving through the solar atmosphere (Wild *et al.*, 1963). Eventually this activity was summarised by Gold (1962), who hypothesised the expulsion of magnetized plasma from the solar atmosphere and the driving of a shock by this expulsion tha accelerates particles into interplanetary space.

Gold's paper marked over 100 years of indirect evidence for the expulsion of plasma transients from the surface of the Sun toward Earth. However, it was not until December 14th, 1971 (112 years after the Carrington event) that the first direct images of one of these plasma expulsions was made with the coronagraph on board the 7th Orbiting Solar Observatory (OSO-7) satellite (Tousey, 1973). This marked the beginning of white-light CME studies as we know them today, and it was followed by a number of other instruments, including Skylab (MacQueen *et al.*, 1980), P78-1 (Sheeley *et al.*, 1980), and the Solar Maximum

Mission (SMM) (Hundhausen, 1999), which provided coronagraph observations up until 1989. The modern era of CME observations began 1995 with the launch of the Solar and Heliospheric Observatory (*SOHO*; Domingo *et al.*, 1995) and its more sophisticated suite of instruments, including the Large Angle Spectrometric Coronagraphs (LASCO). In 2006 LASCO was joined by the COR coronagraphs onboard the Solar Terrestrial Relations Observatory (*STEREO*; Kaiser *et al.*, 2008) and together they provide observations of CMEs from the low solar atmosphere into interplanetary distances. The past 40 years of coronagraph operations in space have yielded observations of tens of thousands of CMEs, allowing a direct determination of their physical properties and a confirmation of what was first postulated by Carrington and others over 150 years ago.

1.2.2 Morphology and Kinematics

CMEs are most often observed using a coronagraph, an instrument that creates an artificial eclipse of the bright solar disk so the much fainter corona can be imaged (this instrument is described in detail in Chapter 3). Figure 1.8 shows the typical appearance of a CME in white light coronagraph images, having a three-part structure of bright front, followed by a darker cavity, and a bright core (Illing & Hundhausen, 1985). Although this CME is regarded as ‘typical’ in appearance, many CMEs do not have all of these features and some appear to have more complex morphological structures (Pick *et al.*, 2006), with only around 30% of all CMEs exhibiting the three part structure (Webb & Hundhausen, 1987). The varied nature of their appearance and morphology can usually be attributed to projection effects (Burkepile *et al.*, 2004) i.e., the CME is a 3-D object projected onto a 2-D image, hence its appearance depends on its orientation in the corona. With this in mind, a ‘plane-of-sky’ or limb CME (one that erupts on the solar limb

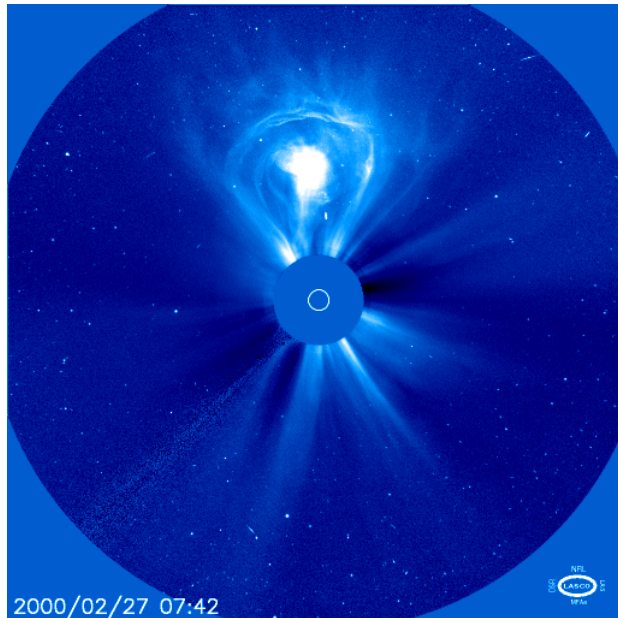


Figure 1.8: Large Angle Spectrometric Coronagraph (LASCO) C3 coronagraph image of a ‘typical’ CME, showing a bright front surrounding a dark cavity, with a bright core at the centre. The central disk is the occulter of the coronagraph, blocking out the bright light of the solar disk, so the much fainter corona may be imaged. The white circle represents the solar disk.

and propagates at right angles to the observer-sun line), offer the best measure of their properties i.e., the measured widths, appearance, speeds etc. do not suffer projection effects. Limb CMEs have a typical angular extent of approximately 50° (Burkepile *et al.*, 2004), and any CME that has width much greater than this ($> 120^\circ$) is generally regarded as a ‘partial halo’ CME (Yashiro *et al.*, 2004). Halos or partial halos are CMEs that propagate toward the observer and hence appear to have a very wide angular extent (full halos can appear to have a 360° width), due to projection effects.

The majority of CME observations rely on a 2-D projection onto the plane of sky, thereby disguising their true three-dimensional shape and geometry. Despite the majority of CME studies being constrained to 2-D measurements, there have been various studies whereby the full 3D extent of the CME bubble has been

1.2 Coronal Mass Ejections

reconstructed. The methods are varied, including polarimetry measurements (Moran & Davila, 2004), geometric localization using the stereoscopy techniques afforded by STEREO (Byrne *et al.*, 2010; de Koning *et al.*, 2009), and forward modelling (Thernisien *et al.*, 2006). Other techniques employ a combination of these simultaneously or for comparison of which preforms best (Mierla *et al.*, 2009). Although each are successful in reconstructing the CME in 3D and producing more accurate kinematics, the techniques have only been performed for a handful of cases. Unfortunately, typical CME statistics must suffer the unavoidable uncertainties of 2-D coronagraph observations.

The amount of CMEs observed during the SOHO era (which continues today) has allowed many statistical studies of CME speeds and accelerations. CME speeds can range from 20 to 2500 km s^{-1} (Gopalswamy & Thompson, 2000), however average CME speed tends to be on the order of 480 km s^{-1} (Webb & Howard, 2012; Yurchyshyn *et al.*, 2005)¹. The yearly average of CME speeds tends to change with the solar cycle, with an average of 280 km s^{-1} at solar minimum (1996), followed by a year on year increase in speed until an average of 520 km s^{-1} is reached even after solar maximum (2002) i.e., for solar cycle 23 the CME speed continued to rise even during the declining phase of the solar activity cycle (Yashiro *et al.*, 2004). The latitudinal distribution of CME launches depends on the solar cycle, with the majority of CMEs erupting close the equator at solar minimum, and generally at all latitudes occurring during solar maximum (Yashiro *et al.*, 2004). There has been some debate surrounding the possibility of a bimodal distribution of CME speeds, generally considered a distinction between fast and slow CMEs. Slow CMEs with a speed of $400 - 600\text{ km s}^{-1}$ and gradual acceleration are usually associated with prominence lift-off, while fast CMEs with

¹Statistical studies from the era of Solar Maximum Mission and Solwind have found similar average speeds (Burkepile *et al.*, 2004)

1.2 Coronal Mass Ejections

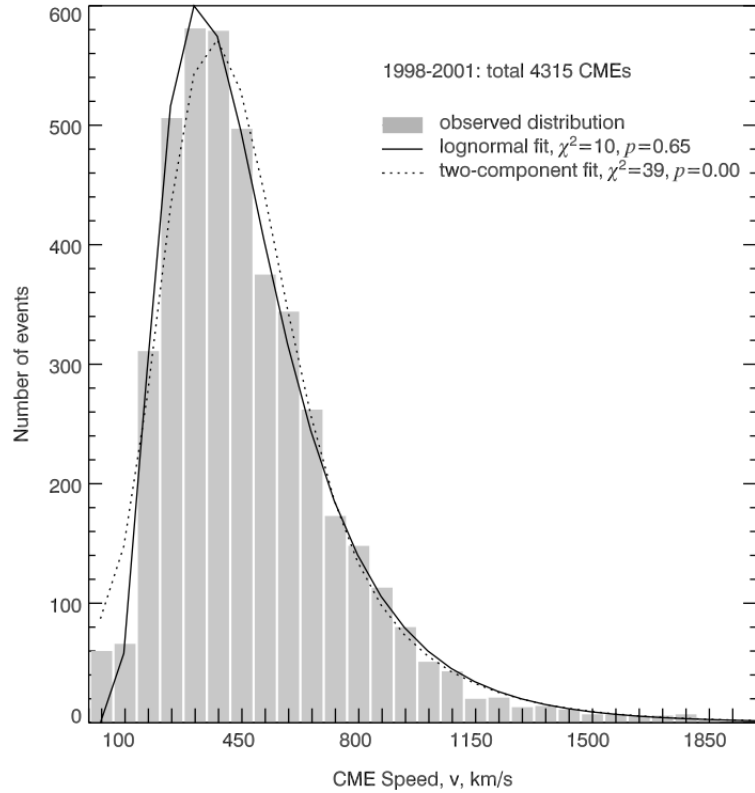


Figure 1.9: Distribution of speeds of 4315 CMEs observed by SOHO LASCO. The bin widths are 70 km s^{-1} . The solid line represents a single lognormal fit to the observed data, while the dashed line is the sum of a Gaussian and a lognormal fit. (Yurchyshyn *et al.*, 2005)

speeds in excess of 700 km s^{-1} , no acceleration (or small deceleration), and are usually associated with flaring active regions (Gopalswamy & Thompson, 2000; Moon *et al.*, 2002; Sheeley *et al.*, 1999). Other statistical studies have suggested that there is no such distinction between the speeds of filament-associated and flare-associated CMEs (Vršnak *et al.*, 2005b; Yurchyshyn *et al.*, 2005), with all CME having a more continuous distribution in speeds rather than a bimodal one (Figure 1.9). This more continuous distribution is also reflected in statistical studies of low coronal CME acceleration magnitudes and timescales. Although typical CME accelerations in the later phases of propagation tend to be centered around zero with a narrow variation of $\pm 30 \text{ m s}^{-2}$, CME accelerations in the very

1.2 Coronal Mass Ejections

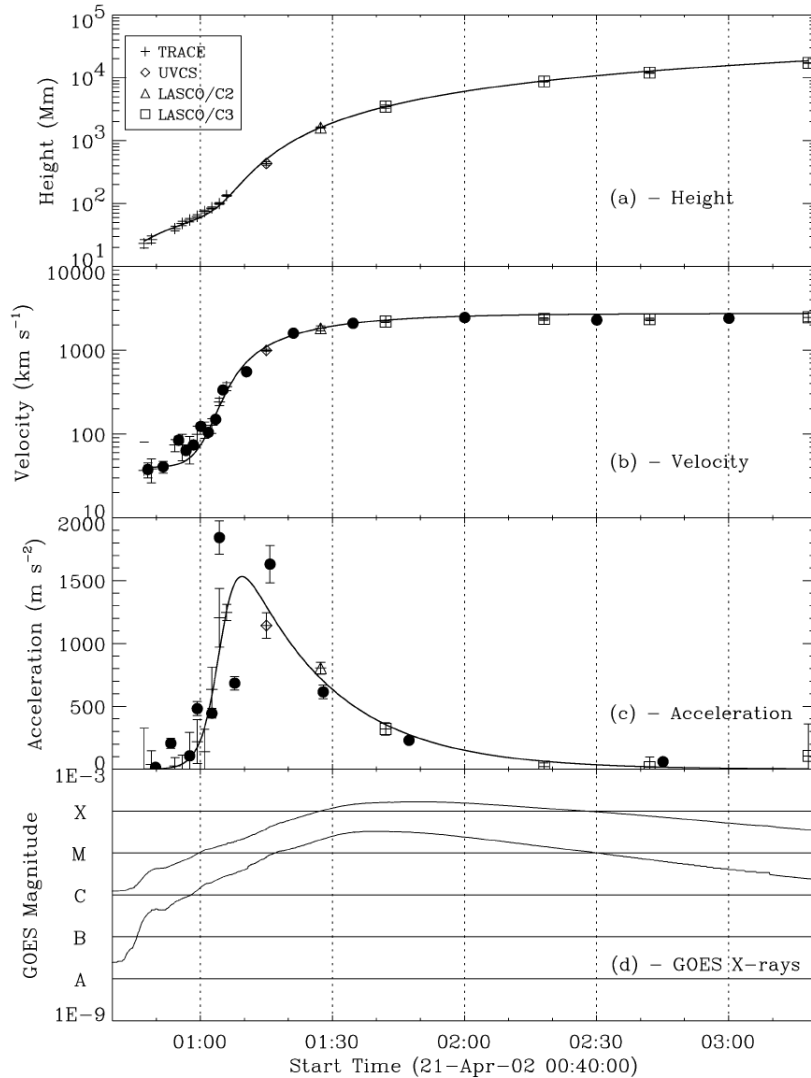


Figure 1.10: CME kinematics derived from TRACE, UVCS and the SOHO LASCO coronagraphs. The height time data is used to derive velocity and acceleration. The CME shows a peak in acceleration early in its propagation, this peak is coincident with the flare impulsive phase (indicated by the GOES) light curves in the bottom plot Gallagher *et al.* (2003)

early phases of eruption can be considerably larger. Gallagher *et al.* (2003) used TRACE and LASCO data to study the development of the kinematics of a CME from its very early impulsive phase with peak acceleration of 1500 m s^{-2} to a more gradual phase of zero acceleration (Fig. 1.10).

A larger statistical study by (Zhang & Dere, 2006) using all three LASCO

1.2 Coronal Mass Ejections

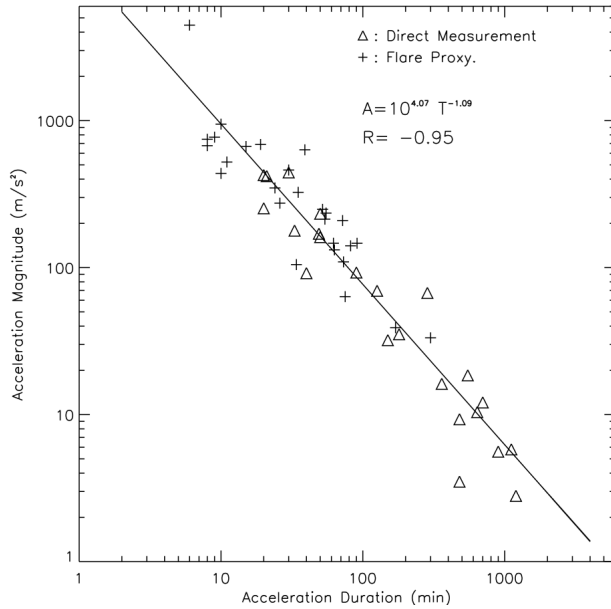


Figure 1.11: Acceleration of CMEs vs the duration of the acceleration. The data show an inverse proportionality i.e., shorter acceleration durations leads to larger magnitudes of acceleration (Zhang & Dere, 2006)

coronagraphs covering $1.1 - 30 R_{\odot}$ found accelerations in the range of $2.8 - 4464 \text{ m s}^{-2}$ with an average of 330 m s^{-2} , with the acceleration timescales ranging $6 - 1200$ minutes (average of 180 minutes). An interesting outcome of this study was the discovery that the magnitude of acceleration appears to be inversely proportional to the duration of acceleration (Fig. 1.11), following the relationship $a = 1 \times 10^4 t^{-1}$.

Unfortunately the innermost coronagraph of LASCO (C1) failed in 1998, making early phase studies of CMEs difficult. Due to the failure of C1, the only observational method to determine the early phase eruption kinematics has been with EUV imaging. Such statistical studies also show similar results of initial impulsive phase accelerations of $\sim 10 - 4000 \text{ m s}^{-2}$, followed by a residual phase of near zero acceleration (Temmer *et al.*, 2010; Vršnak *et al.*, 2007). A large acceleration during the impulsive phase followed by a smaller (or zero) acceleration is recog-

1.2 Coronal Mass Ejections

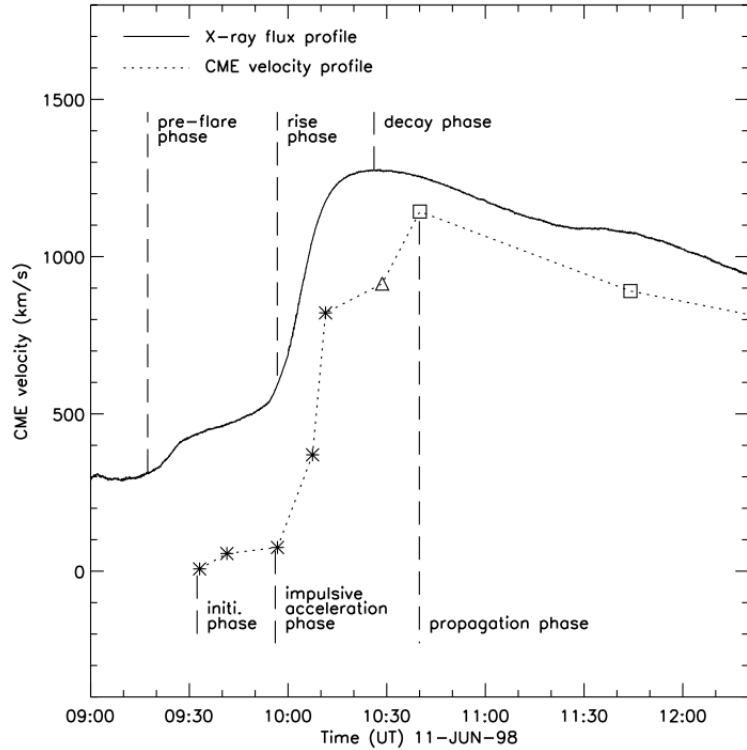


Figure 1.12: Correspondence between CME velocity profile and soft x-ray light curve from GOES. The two profiles follow each other closely showing that CME acceleration occurs during the flare rise phase. This is taken to be an effect of the CME and the flare both being manifestations of the same reconnection process Zhang *et al.* (2001).

nized as being part of three distinct phases of eruption that closely tie the CME process to the flaring process, Fig. 1.12. Zhang *et al.* (2001, 2004) reported that CMEs show a very slow rise phase of coronal loops with a speed of $10 - 100 \text{ km s}^{-1}$ over tens of minutes. This is followed by a phase of rapid acceleration which is accompanied by a simultaneous rise in soft x-ray (SXR) emission, as seen in a GOES light curve. After the flare, and during the decline of SXRs, the CME shows a near constant velocity with very little acceleration. The simultaneous rise of SXR emission at the time of maximum CME acceleration is taken to be an effect of the CME and the flare both being manifestations of the same energy release in the corona.

1.2.3 Masses and Dynamics

As mentioned above, many properties of CMEs derived from two-dimensional coronagraph images suffer large uncertainties due to lack of knowledge about the true three-dimensional shape of the object. Despite this, much work has been done on CME kinematics and the general velocity and acceleration evolution is now well known. However, much less work has been done on the observational properties of CME dynamics e.g., calculating their mass, mechanical energies and forces.

Some of the first measurement of CME mass using scattering theory were carried out by Munro *et al.* (1979) and Poland *et al.* (1981) using space-based white light coronagraphs on board *SkyLab* and U.S. military satellite *P78-1*. Both the early studies and later statistical investigations determined that the majority of CMEs have masses in the range of 10^{13} – 10^{16} g, (Vourlidas *et al.*, 2002, 2010). However, due to only a single viewpoint of observation, the longitudinal angle at which the CME propagates outwards was largely unknown in these studies and it is generally assumed that the CME propagates perpendicular to the observers line-of-sight (LOS). There is also the added assumption that all CME mass lies in the two-dimensional plane-of-sky (POS). Such assumptions can lead to a mass underestimation of up to 50% or more (Vourlidas *et al.*, 2000). More recent studies have employed the two viewpoint capabilities of the *STEREO* mission to determine the mass of numerous CMEs with much less uncertainty (Colaninno & Vourlidas, 2009). These few studies remain the only investigation into CME masses and the field has been largely overlooked due to the huge uncertainties involved in mass calculations (described in Chapter 4).

While the majority of mass estimates have come from white-light observations of CMEs, other wavelengths offer an independent measure of CME mass

1.2 Coronal Mass Ejections

estimates, usually via a different technique which pertains to the wavelength being observed. The eruption of a CME as seen by EUV imaging of the corona often shows a region of diminished intensity around the active region from which the eruption took place. This is known as an EUV dimming, and is indicative of a mass evacuation i.e., the CME carries mass away when it erupts leaving behind a deficiency in emitting material. Aschwanden *et al.* (2009) calculated the mass from EUV dimming m_{EUV} and compared it to the mass measured in white-light m_{wl} and found a close match of $m_{EUV}/m_{WL} = 1.1 - 1.3$. Although this technique provides a rare measure of the CME mass in the very early stages of eruption, few studies have used this in conjunction with the white-light measurements.

Perhaps the only measurement of CME mass via direct low frequency radio imaging was performed by Gopalswamy & Kundu (1992). An event observed on 6 February 1986 by Clarke Lake multifrequency radioheliograph showed an erupting structure at 73 MHz. On the assumption that the emission mechanism was thermal bremsstrahlung in an optically thin environment, an estimate of the emitting mass was calculated and shown to be 2.7×10^{15} g, similar to what is generally reported in white-light studies. Despite the interesting techniques afforded by radio observations, they are still not as popular as the white-light measurements of mass, due to the rarity of actually observing a CME at long wavelengths.

Given the relative ease with which CME positions and velocities may be determined, there are only a small number of studies which combine these kinematic properties with the mass estimates in an effort to derive CME mechanical energy budgets. The first study to address the issue in the SOHO era attempted to quantified the magnitude of the kinetic and gravitational potential energy and compared this to a proxy for the magnetic energy from in-situ measurements of

1.2 Coronal Mass Ejections

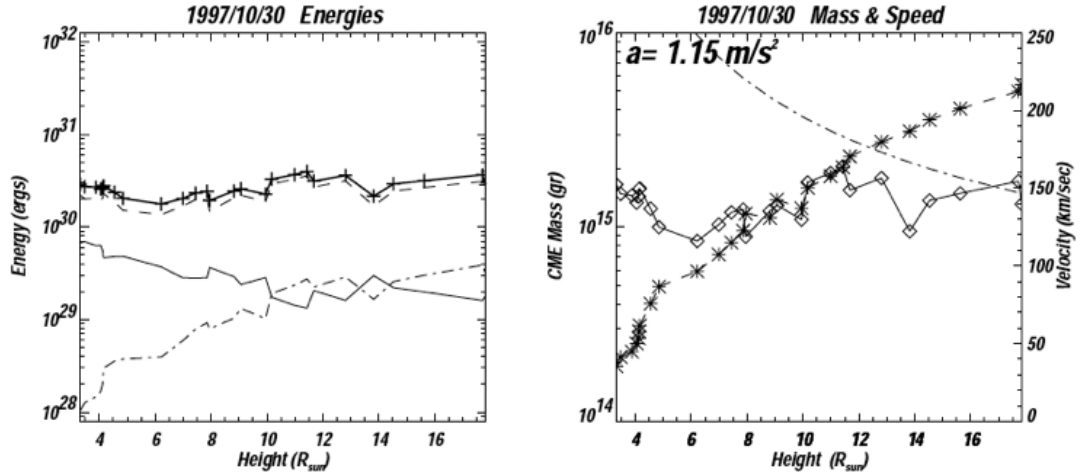


Figure 1.13: Coronal mass ejection energies and masses as a function of height for three different events. Left column shows the CME kinetic (solid), potential (dashed), magnetic (dot-dashed), and total energy as a function height. In each of the plots, kinetic and potential energy increases at the expense of decreasing magnetic energy. The total energy remains quite constant, showing that there is no external driver of the system. Right column, CME mass (solid), center of mass speed (dashed), and escape velocity (dot-dash) as a function of height. Adapted from (Vourlidas *et al.*, 2000)

magnetic clouds (Vourlidas *et al.*, 2000). Out of the 11 CMEs that were studies, it was found that the CMEs mechanical energy increases at the expense of magnetic energy, Figure 1.13. The forms of these energies are given by

$$E_{kinetic} = \frac{1}{2} \sum m_i v_{cm}^2 \quad (1.12)$$

$$E_{potential} = \sum \int_{R_\odot}^R \frac{GM_\odot m_i}{r_i^2} \quad (1.13)$$

$$E_{magnetic} = \frac{1}{8\pi} \int B^2 dV \quad (1.14)$$

where m_i and r_i are the CME mass element and distance from Sun center, respectively, v_{cm} is the center of mass velocity, M_\odot and R_\odot are solar mass and radius, respectively, B is the CME magnetic field, and V is its volume. The summation

1.2 Coronal Mass Ejections

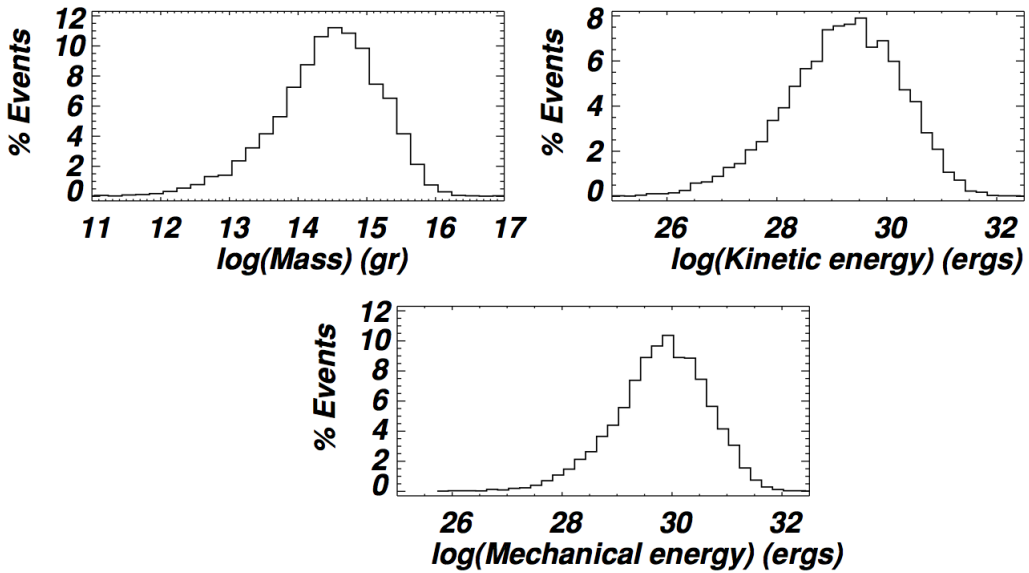


Figure 1.14: Distribution of CME masses, kinetic and total mechanical energies for 7668 CMEs observed by the LASCO coronagraphs between 1996 January 22 to 2009 July 31. The peak in kinetic energy is 2.3×10^{29} erg, while total mechanical energy is 9.0×10^{29} erg (Vourlidas *et al.*, 2010)

is carried out of each CME mass elements i.e., each image pixel that includes the CME. The total energy of the CME (kinetic + potential + magnetic, usually on the order of 10^{30} erg) remains constant, indicating that there is no external driver of the CME between $3 - 30 R_{\odot}$. Hence, CMEs much achieve escape velocity to exit the Sun's gravitational potential well, which they do so between $8 - 10 R_{\odot}$. For slow to average speed events, the potential energy dominates the kinetic energy by an order of magnitude, the opposite is found for faster events.

A much larger statistical estimate of CME mechanical energy distribution was performed by (Vourlidas *et al.*, 2010) for 7668 CMEs observed by LASCO from 22 January 1996 to 31 July 2009 (Figure 1.14). This is the most comprehensive CME mechanical energy statistics study to date and shows that both kinetic energy and total mechanical energy are normally distributed about 2.3×10^{29} erg and 9.0×10^{29} erg, again showing that potential energy (mechanical - kinetic) is dominant over kinetic energy on average.

1.2 Coronal Mass Ejections

(Subramanian & Vourlidas, 2007) investigated the energetic properties of 39 CMEs in an effort to determine if CMEs in the outer corona ($2 - 20 R_{\odot}$) are driven by momentum coupling to the solar wind or if internal magnetic energy is a viable source of driving power. They found that in 69% of the cases the mechanical energy of the CME increased linearly with time, an effect that suggests CMEs are driven by the gradual release of some form of energy. The estimated total power delivered to the CME to increase its mechanical energy was 1.6 erg hr^{-1} , which is far below the upper limit to the total power dissipated by the magnetic field in the CME (14.4 erg hr^{-1}). This is taken to be a suggestion that the CMEs magnetic field is the ultimate source of energy that drives its propagation, even out to large heliocentric distances distances. However the magnetic field estimates in this study are tenuous at best, and any magnetic power estimated derived from them should be treated with caution. Lewis & Simnett (2002) found that the solar wind may be a significant contributor to CME driving power, accounting for some proportion of an average $2.2 \times 10^6 \text{ W kg}^{-1}$ required to drive the CME, however the authors do not mention quantitatively the possible driving power of the wind, merely calling the wind an ‘infinite energy reservoir’. Hence it is difficult to affirm the possibility of their assertions.

Perhaps one of the only studies to make an observational estimate of the forces acting on CMEs is Vršnak (2006), although this study made use of kinematics to infer the dominant forces at play during CME propagation (acceleration is treated ‘force-density’ or Newtons per kilogram, a pseudo-measurement of force). The early phase eruption characteristics of a H- α spray ejection were analysed to derived the ejection’s total acceleration a (Figure 1.15). This is recognized as being due to a combination of accelerations due to the Lorentz force a_L , gravity g , and aerodynamic drag a_d , such that $a = a_L - g + a_d$, which results directly

1.2 Coronal Mass Ejections

form the MHD equation of motion (see Chapter 2, equation 2.12). Estimates of acceleration due to gravity can be made simply. Expression for drag generally take into account the interaction of the CME with the solar wind whereby drag is given by the difference between the ejecta and wind velocity $|v_{cme} - v_{sw}|$, the area of the ejecta exposed to drag by the wind A and a drag coefficient C_d which usually accounts for the shape of object. The expression may be expressed in quadratic form, $a_d = -\gamma(v_{cme} - v_{sw})|v_{cme} - v_{sw}|$, where $\gamma = C_d A \rho_{sw} / M_{cme}$ (Cargill, 2004)¹. v_{sw} may be given from a model of the solar wind, for example Sheeley *et al.* (1997). As for the γ term, Vršnak (2006) uses empirical scaling laws whereby $\gamma = 23R^{-2.2}\text{ km}^{-1}$, where R is the heliocentric distance of the ejecta. When gravity and drag are estimated in this way, a peak Lorentz acceleration is derived to be to be 1400 m s^{-2} . Taking the particle density of the ejection to be $10^{16} - 10^{17}\text{ m}^{-3}$ the volume force can then be evaluated as $f_L = 10^{-8} - 10^{-7}\text{ N m}^{-3}$. This is one of the only studies (perhaps the only) in the literature that attempted to derive a size for the Lorentz force, albeit by using an indirect proxy, and also by only looking at a H- α spray.

Recently Maloney & Gallagher (2010) determined the nature of the drag force acting on CMEs from 3D observations using the STEREO COR1 and COR2 the heliospheric imagers (HIs). It was found that drag on fast CMEs has a quadratic dependence on the velocity difference between the CME and solar wind, while slow CMEs show a linear dependence. This difference may be due to the different nature of the drag force at different at different CME speeds.

A statistical kinematical study was considered by (Bein *et al.*, 2011), where a number of parameters were compared, such as max acceleration experienced by the CME, duration of acceleration, and height of maximum acceleration. They

¹Solar wind drag on the CME is discussed further in Chapter 4

1.2 Coronal Mass Ejections

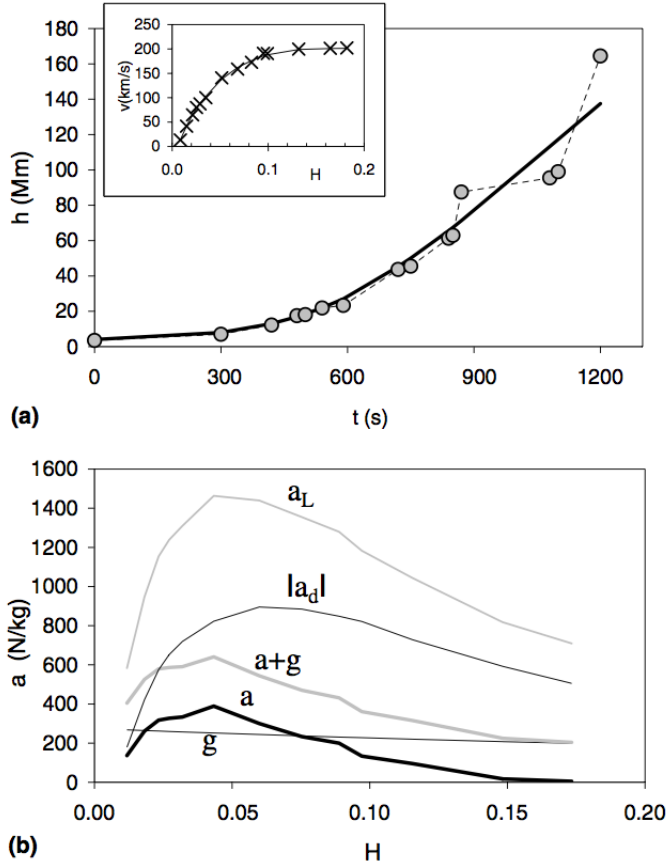


Figure 1.15: Top: the height-time velocity of a h-alpha spray, with velocity as a function of height inset. Bottom: the acceleration of the spray a as a function of height (derivative of inset in top panel), as well as the acceleration experienced from gravity a_g (also $a + a_g$), drag $|a_d|$, and acceleration due to the Lorentz force a_L (Vršnak, 2006)

find that, as in the Zhang & Dere (2006) (Fig. 1.11), the acceleration experienced is inversely proportional to the duration of acceleration, and further, the acceleration experienced and the height of peak acceleration are inversely related. This is taken to be indicative of a compact source size having a more impulsive acceleration, an effect that is consistent with the Lorentz force. Again, the nature of forces acting on CMEs in this case is only inferred from kinematics studies, and not measured directly.

The CME energy budget as compared to the total eruptive energy, including

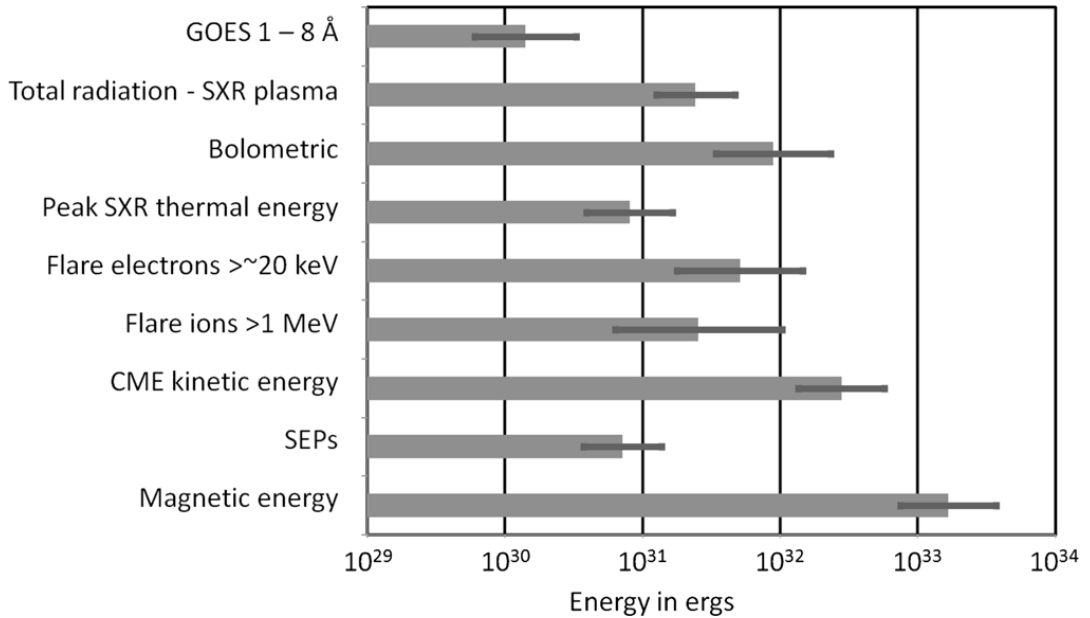


Figure 1.16: The average energies of the different components of an eruptive event for six events. The CME is the biggest consumer of energy (Emslie *et al.*, 2012).

the flare and all by-products. Emslie *et al.* (2004) studied two eruptive energy budgets, taking into account (i) the CME, (ii) the flaring thermal plasma, (iii), the electrons responsible for hard X-rays, (iv) gamma-ray producing ions, and (v) solar energetic particles detected in-situ. Accumulating all of this into an energy budget for the two events found that the CME mechanical energy of $\sim 10^{32}$ erg is the dominant single component of energy consumption, with the flare thermal plasma, non-thermal electrons and ions, and in-situ detected particles, each consuming $\sim 10^{31}$ erg. A similar study was then carried out where the same analysis was applied to 38 eruptive events, which again found that the CME is the dominant consumer of total energy released (Emslie *et al.*, 2012)

1.3 Coronal Shocks

The corona is home to a very of highly dynamic and energetic explosive events such as flares and CMEs. The velocities of the mass motions during these eruptive events can often travel with speeds in excess of the local magnetosonic wave speeds in the corona. This results in the formation of plasma shocks. Plasma shocks are an extremely complex phenomena observable at almost every part of the electromagnetic spectrum. The following will describe the typical plasma shock observables in the corona, including radio, white-light, and extreme ultraviolet observations. Particular attention will be given to the relationship between the shock observations and the observations of CMEs.

1.3.1 Type II Radio Bursts

Perhaps the first evidence of shocks transits in the corona came in the form of solar radio bursts, most notably a class known as type II. These bursts are characterized by bands of emission observed to drift slowly toward lower frequency over time in dynamic spectra (Figure 1.17). They typically start below 150 MHz, have a drift rate between ~ 0.1 to -0.4 MHz s^{-1} and last on the order of 10 minutes. They usually show two emission bands with a 2:1 ratio, with each band having a bandwidth of $\Delta f/f = 0.3$ (Mann *et al.*, 1995). Although they are now recognized as one of the chief signatures of the transit of a coronal shock (Mann *et al.*, 1996; Nelson & Melrose, 1985), the driver of this shock has remained a topic of contention since their discovery in the first half of the 20th century.

The development of radio instrumentation during and after the second world war presented scientists with the opportunity of (sometimes inadvertently) observing radio activity on the sun. Whilst performing radar tests using British mil-

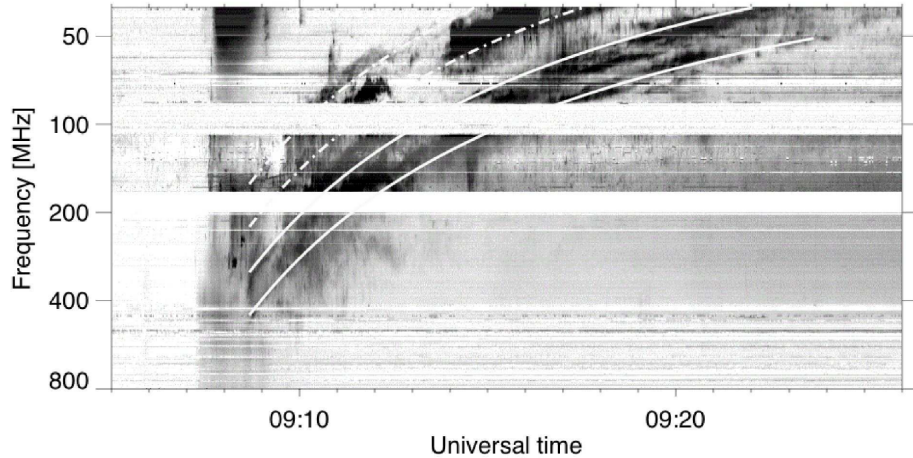


Figure 1.17: Type II radio burst observed at the Observatory Solar RadioAstronomy (OSRA) at Tremsdorf on 1997 November 3rd. Both the fundamental (dot-dash lines), and harmonic (solid lines) bands of emission are evident (Khan & Aurass, 2002).

itary equipment, (Hey, 1946) reported a very high intensity radio source (10^7 Jy) at 4-6 meters wavelength coming from the Sun. The relationship of these solar radio bursts with solar flaring activity was then reported by (Allen, 1947). In the same year, Payne-Scott *et al.* (1947) observed time series of single frequencies at 60 MHz, 100 MHz, 200 MHz and noted that a delay in onset time of the burst from high to low frequency may suggest '*the excitation of radiation at successive levels by an agency traveling at finite velocity*'. The analysis of single frequency intensity time series was then superseded by the employment radiospectrographs to produce dynamic spectra of solar radio bursts. This allowed the identification of slowly drifting type IIs that are well characterized by modern radio-spectral observations. The hypothesis for the origin of these bursts was the same as that of Payne-Scott *et al.* (1947) (a disturbance traveling into the corona at speeds of $10^2 - 10^3 \text{ km s}^{-1}$), except Wild *et al.* (1954) correctly identified the emission to be generated at the frequency of plasma oscillation at the source height in the corona. (Uchida, 1960) and others eventually attributed these radio bursts to the

1.3 Coronal Shocks

activity that they are associated with today: type IIs are generated by magnetohydrodynamic shocks transiting the corona. As the shocks propagate they excite radio emission at the local plasma frequency

$$\omega_p = \left(\frac{n_e e^2}{m_e \epsilon_0} \right)^{\frac{1}{2}} \quad (1.15)$$

Since the plasma frequency is only dependent on electron number density, as the shock propagates to larger heights in the corona the frequency of emission drops owing to the dropping density. Hence the shock excites emission at decreasing frequency over time. This effect is further described in section 2.X

At the time Uchida and others made the assertion that type IIs were generated by MHD shocks, CMEs were as yet an undiscovered phenomena. Hence, the hypothesis that the origin of the shock was a flare-induced blast wave was a common one. The close onset times of flare maximum and type II onset supported this idea (Maxwell & Thompson, 1962). The association of type II radio bursts with a Moreton wave (a disturbance propagating away from flare site, observe in H-alpha), and the modeling of the two phenomena as a flare-induced explosive MHD disturbance gave credence to the idea that type IIs were indeed signatures of blast waves (Uchida, 1974), a hypothesis later applied to type II observations (Kosugi, 1976).

Following the discovery of CMEs, the idea that mass motions (and not blast-waves) could produce type IIs came under consideration. Part of this idea came from the confirmation of the detection of in-situ shocks ahead of interplanetary CMEs, which were then called ‘plasma clouds’ or ‘magnetic clouds’ (Hundhausen, 1972). Later, (Stewart *et al.*, 1974) showed good correspondence of the height-time kinematics of a CME as observed by the coronagraph on OSO-7 and a type II burst source in images from the Culgoora Radioheliograph. This was taken

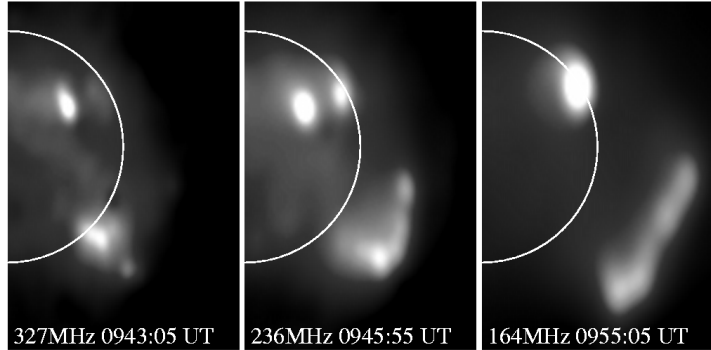


Figure 1.18: Propagating radio emission source imaged at 327, 236, 164 MHz using the Nancay Radioheliograph. The position of the emitting source is coincident with the CME leading edge (Maia *et al.*, 2000)

as evidence that a piston-driven shock (CME-driven) was responsible for the type II. Following this was a statistical study that showed type II bursts to be highly associated with fast coronal mass ejections observed by the coronagraph on board Skylab (Gosling *et al.*, 1976). However, some doubts on the relationship were raised when (Robinson & Stewart, 1985) showed that while 42% of type IIs could be placed near the leading edge of a CME, some were located well behind the leading edge, this was considered to be evidence against the CME-driven shock idea. The CME hypothesis suffered another blow when it was shown that of an observed 116 metric type II bursts, 45 had a clear association with CMEs and soft x-ray flares, but up to 19 were observed to occur without any associated CME. (Claßen & Aurass, 2002) later showed that type II burst onset times have been shown to occur up to more than one hour before CME onset time in some cases. The contradicting accounts of the association of CMEs with type IIs fueled a debate on which was the more reasonable explanation: are CMEs or flares more likely to drive a shock that causes type IIs? Direct evidence of radio bright shocks have at least shown that CMEs are capable of driving the shocks (Maia *et al.*, 2000) (Figure 1.18). In more recent times the debate continues, but the more sophisticated instrumentations, such as the Atmospheric

1.3 Coronal Shocks

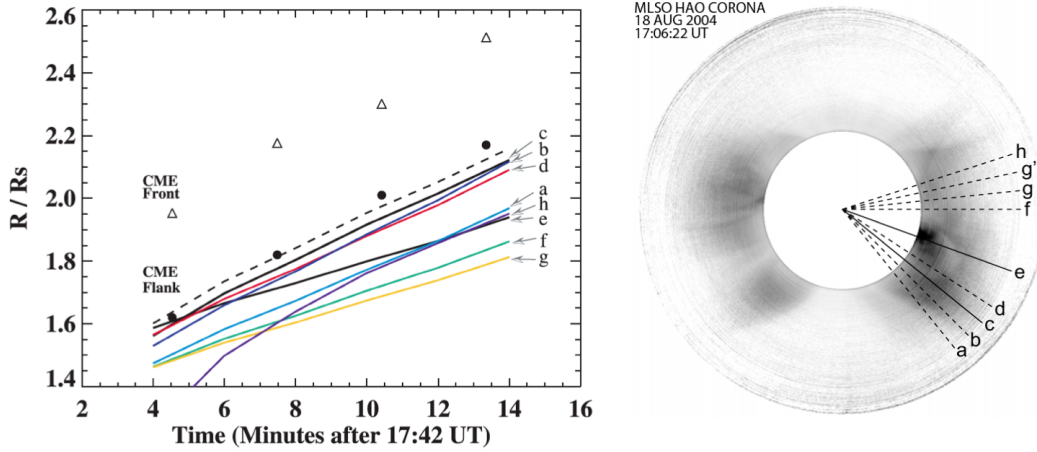


Figure 1.19: Comparison of height-time kinematics of a type II radio burst, observed using the Green Bank Solar Radio Burst Spectrometer (GBRBS), and CME as observed by the Mauna Loa coronagraph. Kinematics of CME at front and flank are shown, triangles and circles respectively. Lines *a*–*h* show the kinematics of the radio burst derived from density measurements performed along the trajectories (right panel). The CME and type II show the best match at the CME flank along trajectory *c*. Figure adopted (Cho *et al.*, 2007)

Imaging Assembly, and multi-wavelength studies have offered a clearer picture. Bain *et al.* (2012) has shown clear evidence of an erupting plasmoid with a type II radio source that sits at its nose, very direct evidence for CME driven type II. Material motions imaged at soft X-rays also suggest a driven shock (Klein *et al.*, 1999). Kinematics of the shock derived from the type II drift and position often show a good correspondence with CME kinematics (Mancuso, 2011), however a statistical study by Reiner *et al.* (2001), shown in Figure 1.20, showed there to be little correlation between CME and type II speeds. This has been described as a discrepancy attributed to the shock possibly being located on the CME flank, the kinematics match better under this assertion (Mancuso & Raymond, 2004) (Figure ??). (Cho *et al.*, 2007, 2011) has also shown that type II and CME kinematics match well when the shock is assumed to be along the CME flank (Figure 1.19). Later UV spectroscopic evidence that the flank-driven shock is

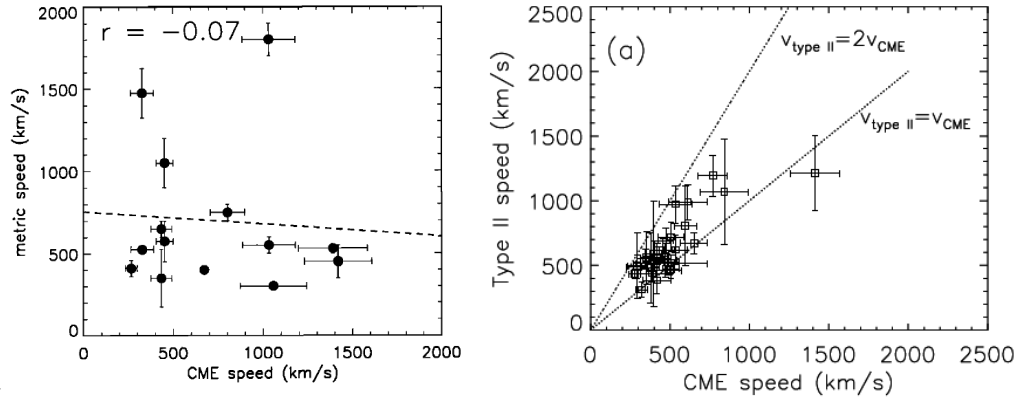


Figure 1.20: (left) A statistical comparison of metric type II speeds and CME speed Reiner *et al.* (2001). The two show no obvious relationship, taken to be evidence that a CME may not be the driver of the metric type IIs i.e., a CME was not responsible for the low coronal shock that caused these type IIs. (Right) Comparison of type II and CME kinematics taking into account that the type II may be along the CME flank, showing a much better correlation (Mancuso & Raymond, 2004).

indeed possible (Fig. 1.21).

Despite the fact that there is a large body of evidence for CME-driven shocks (at either the nose or flank) being associated with type IIs, there still remains convincing studies on the blast-wave possibility. Vršnak & Lulić (2000a,b) has formulated an analytical model to describe the blast-wave generation of type IIs. The analytical treatment shows the fast onset times (> 10 min) of type IIs after flare start cannot be accounted for by CME eruption (Vršnak *et al.*, 2001). The most recent direct evidence was given by (Magdalenić *et al.*, 2012), when they showed a compact flare with no sign of any eruption in $\text{H}\alpha$, EUV or white-light imaging. The debate rages on, and there is no consensus on either CME-driven shocks or flare-ignited blast waves (Vršnak & Cliver, 2008)¹.

¹It should be noted there is no ambiguity on the nature type IIs in the hecto-kilometric range. The accepted paradigm for these type IIs is a shock driven by a CME at interplanetary distances which may then be detected in situ as a shock. However, another controversy stemming from the flare-driven/CME-driven argument for type IIs is whether interplanetary type IIs and low coronal type IIs belong to the same driver (Cane & Erickson, 2005).

1.3 Coronal Shocks

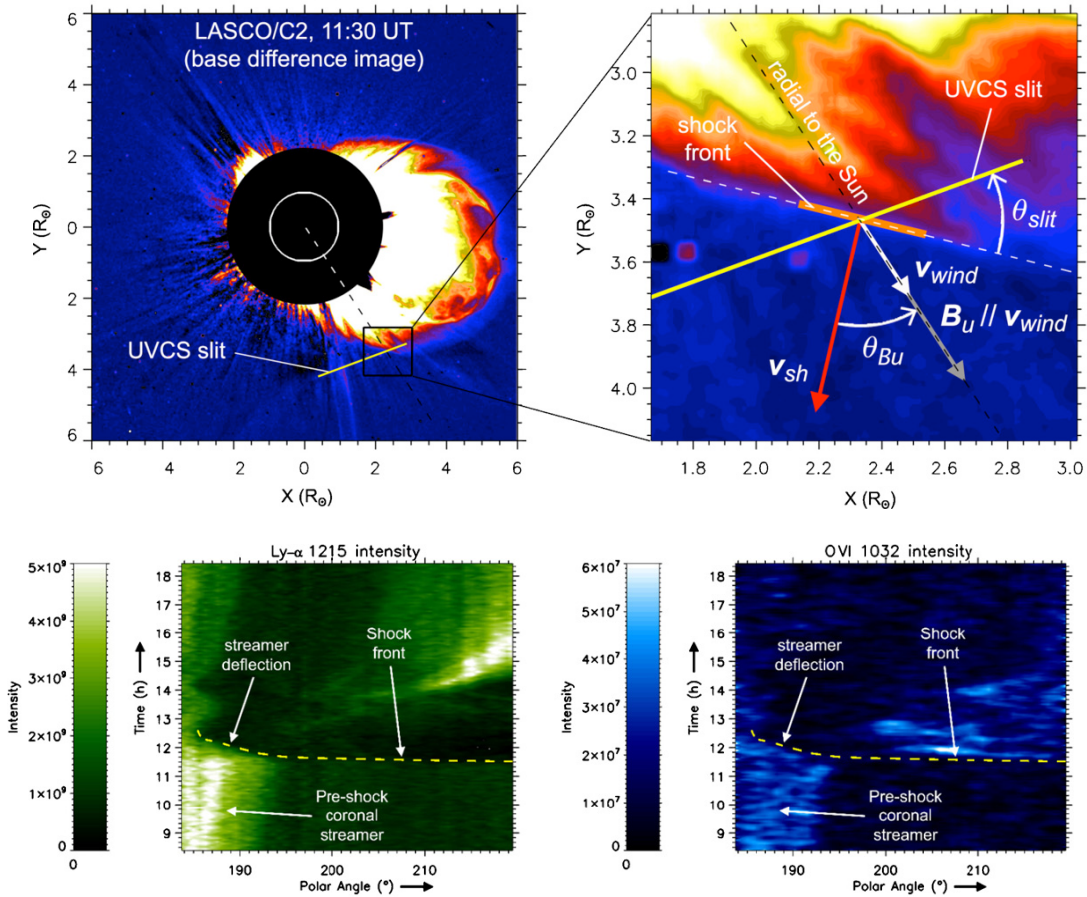


Figure 1.21: (Top) A LASCO C2 base-difference image of a CME on 2002 March 22, the yellow line marks the Ultraviolet Coronagraph Spectrometer (UVCS) slit located at CME flank. The event was associated with a type II radio burst. (Bottom) Space-time dependence of the HI Ly- α (left) and O VI 1032 Å (right) lines. The dashed yellow line shows the passage of the shock front. It results in a dimming of Ly- α , caused by a deficiency in the resonant scattering of the line. This is due the scattering agent experiencing a bulk flow velocity that doppler shifts its absorption profile with respect to the incoming radiation, hence reducing its ability to scatter Ly- α efficiently—known as the Doppler dimming effect. The oxygen line, on the other hand, is collisionally controlled and depends on the ambient free electron density. As the shock transits it heats the plasma, resulting in more further free electrons and more efficient excitation of the O VI 1032 Å, leading to brightening. The overall result is a dimming in the hydrogen line and a brightening of the oxygen line. This indication of bulk flow velocity as well as high levels of heating in the flow is evidence for a shock.

Finally, a part of the controversy with determining the source of all radio bursts (not just type II) is to do with the method by which radio burst

kinematics are deduced from density models of the solar atmosphere. The models can often lead to questionable kinematics and heights of the radio sources, as discussed in Section 2.3.6

1.3.2 Herringbones and Type IIIs

As will be shown in Chapter 2, radio burst such as type IIIs are believed to be the result of a plasma instability in the presence of high velocity electron beams. There is a subset of type II radio bursts which directly observe the electron beam nature of these radio bursts, known as ‘herringbone’ radio bursts as shown in Figure 3.22 (Cairns & Robinson, 1987; Cane & White, 1989). These are the signature of bursty electron acceleration occurring at a coronal shock front (Mann & Klassen, 2005). The herringbone spike is an individual beam of electrons traveling away from the shock.

The fact that they drift towards both low and high frequencies simultaneously means they are bi-directional in space e.g., drifting toward and away from the sun simultaneously. The ‘bursty’ or quasi-periodic nature of the herringbones occurs over timescales of seconds (Mann & Classen, 1995; Mann & Klassen, 2005) and they are believed to be a result of the shock drift acceleration (SDA) process (Miteva & Mann, 2007). The burstiness has been suggested to be due to inhomogeneity on the shock front, and may be signature of a so-called ‘wavy’ or ‘rippled’ shock front (Guo & Giacalone, 2010; Vandas & Karlický, 2011; Zlobec *et al.*, 1993). This means they provide a measure of shock structure and a timing of the particle acceleration process itself. The bursts are rare, with only 20% of type II bursts exhibiting these structures (Cairns & Robinson, 1987). Thus a complete theory on their formation does not exist. They have been attributed to shocks propagating parallel to the solar surface (tangentially across radial field

1.3 Coronal Shocks

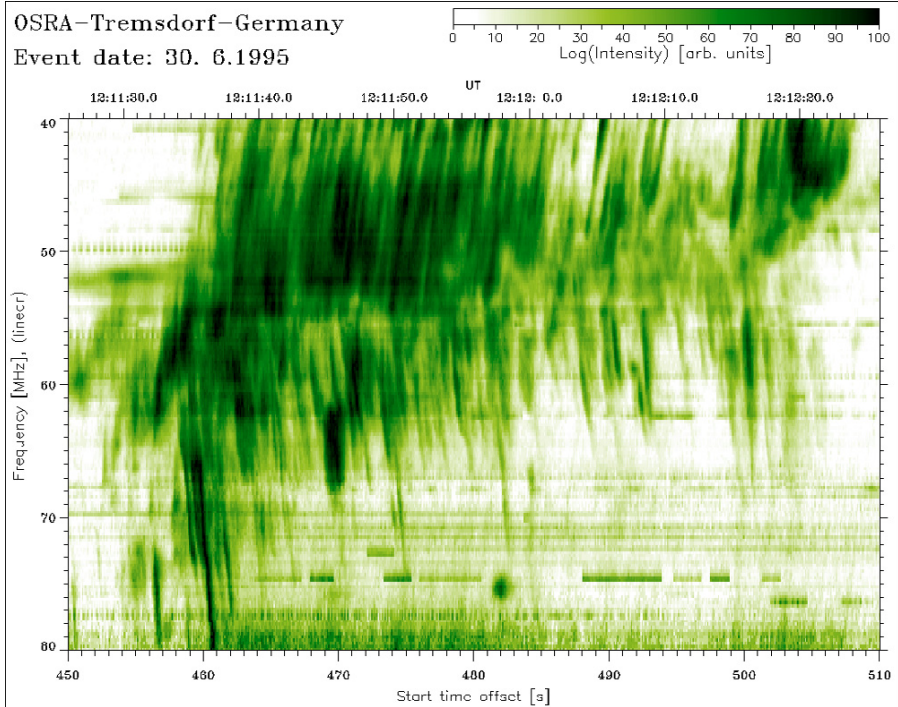


Figure 1.22: Fine structure observed in a type II radio burst known as ‘Herringbones’. Each spike is an individual beam of electrons accelerated away from the coronal shock. The presence of herringbones drifting to both low and high frequencies is indicative of electron beams traveling toward and away from the Sun.

lines) whereby ‘shock fronts propagate normal to the magnetic field and continuously eject bunches of fast electrons long the field’ (verbatim from Wild (1964)); this assertion was also illustrated in Stewart & Magun (1980). Such a mechanism could occur if the CME flank drove a shock transversely through the corona (parallel to the solar surface). An alternative theory is one where the herringbones are produced in the termination shocks of super-Alfvénic outflow jets of a reconnection region (Aurass & Mann, 2004; Aurass *et al.*, 2002). Such a process could be the result of a reconnection region in a current sheet in the wake of a CME, as described by the standard solar flare model. The rarity of herringbone observations has resulted in no consensus on how they might be produced, and their formation mechanism remains unconfirmed.

Related to particle accelerations in the corona are type III radio bursts. These are fast drifting features in dynamic spectra ($\sim 20 \text{ MHz s}^{-1}$) and are the characteristic radio signature of electrons beams traveling on open magnetic field lines in the corona (Pick & Vilmer, 2008). Type IIIIs are mainly associated with an acceleration process directly from the flaring active region e.g., acceleration directly out of the reconnection process. However, some type IIIIs are thought to be associated with the in-situ detection of shock accelerated electrons. Indeed sometimes type II shock signatures are seen to occur with type IIIIs, an indication of electron acceleration from the shock – these type IIIIs are sometimes labelled ‘shock-associated’ or SA type IIIIs (Bougeret *et al.*, 1998). In certain instances the particle acceleration as indicated by type III bursts has been related to shock feature seen the corona. This is usually in the context of coronal bright front studies.

1.3.3 Coronal Bright Fronts

As mentioned, some of the explanations as to why a type II source may appear behind the CME front was the possibility of a shock driven by the CME flanks. As well as this, certain studies of type III radio burst associated with in-situ detection of solar energetic particles have been related to some shock driver low in the corona. One possible observational signature of shock activity in the low corona is a coronal bright front (CBF), also known as an ‘EUV wave’.

CBFs were discovered in 1997-1998 (Moses *et al.*, 1997; Thompson *et al.*, 1998) by the EIT instrument on SOHO (they are sometimes called ‘EIT waves’). CBFs are are bright fronts imaged at EUV and observed to propagate from an eruptive active at typical speeds of between $200\text{-}400 \text{ km s}^{-1}$ (Thompson & Myers, 2009). Given their speed of propagation and their tendency to undergo reflection

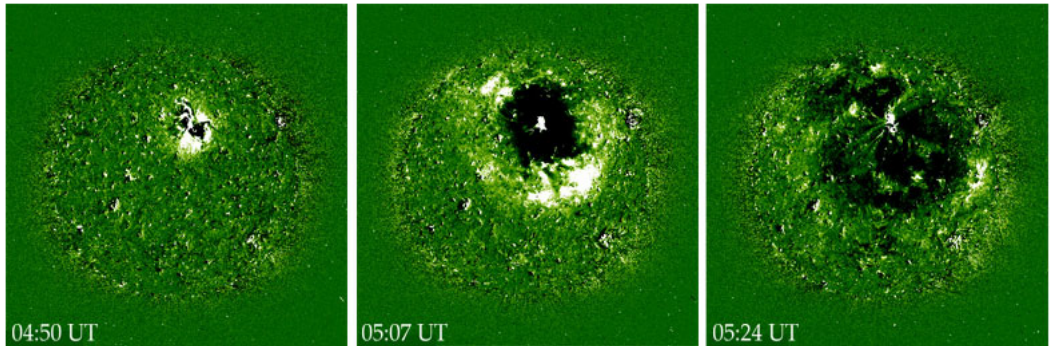


Figure 1.23: One of the first observed coronal bright fronts, reported by (Thompson *et al.*, 1998). The images are EIT Å base differenced so the bright front can be seen expanding across the solar disk. This bright front is postulated to be a magnetohydrodynamic wave propagating in response to an eruptive event in the solar corona.

(Gopalswamy *et al.*, 2009b), refraction (Wang, 2000), and pulse broadening (Long *et al.*, 2011b), there is a prevailing hypothesis that these features are fast mode magnetohydrodynamic waves propagating through corona (Veronig *et al.*, 2010). They are known to accompany CME eruption quite closely (Biesecker *et al.*, 2002), so it is thought that a CME may be their driver i.e., as the CME expands it drives a disturbance through the corona which manifests itself as bright front in EUV images. Like CME eruption, CBFs show a clear association with type II radio bursts, with up 90% of type IIs being associated with CBFs (Klassen *et al.*, 2000). The fact that this MHD wave-like phenomena shows a clear association with an MHD shock signature prompted the interpretation that they belong to the same MHD disturbance in the corona (Warmuth *et al.*, 2004), both driven by a CME. Indeed, type II kinematics can sometimes show a very closely correspondence with CBF kinematics (Grechnev *et al.*, 2011b; Vršnak *et al.*, 2005b) (Figure 1.24). Also, CBFs images at EUV may also have a counterpart images at soft X-ray (SXR) with a type II closely tied to the event e.g., the type II burst in Fig. 1.17 showed such a relationship with SXR activity (Khan & Aurass, 2002)

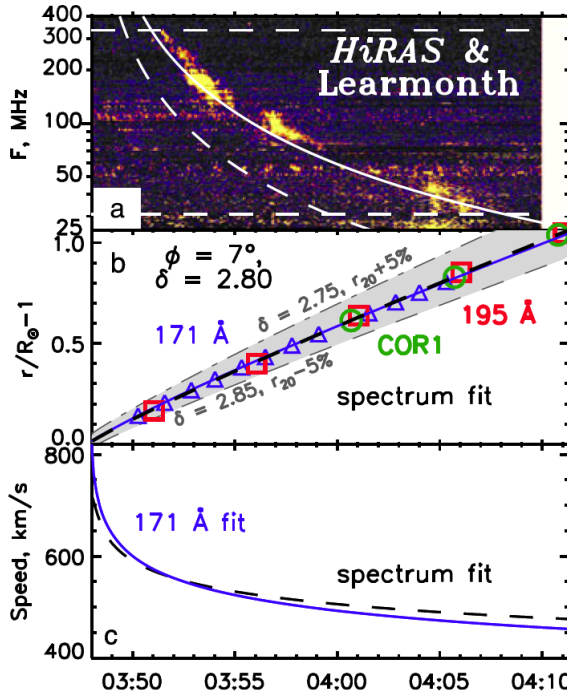


Figure 1.24: Top: Type II radio burst observed by the HiRAS spectrograph at Learmonth, Australia. Middle: Coronal bright front height time measurements from EUVI 195 Å (red squares), 171 Å (blue triangles), and COR1 (green circles). Fit to the type II burst converted to height is shown by the dashed black line. The type II burst height-time perfectly matches the eruption of the CBF as seen by EUVI and CME as seen by COR1 (Grechnev *et al.*, 2011a)

To further this hypothesis, there are a number of studies which suggest that the origin of in-situ detection of SEPs, and the type III bursts they are associated with, have their origin in the same disturbance responsible for the CBF (Klassen *et al.*, 2002; Kozarev *et al.*, 2011; Krucker *et al.*, 1999). The idea naturally leads to the following physical scenario: the CME eruption drives a pressure pulse, observable in the low corona as a propagating CBF; this scenario is modeled in Figure 1.25. Higher in the corona this same pulse forms a shock, accelerating particles and producing type II. If this shock encounters open magnetic field lines it may accelerate particles along the open field, producing type III emission and the possible subsequent detection of in-situ SEPs. Hence the unifying theme amongst the CME, CBF, radio burst, and accelerated particles is a CME driven

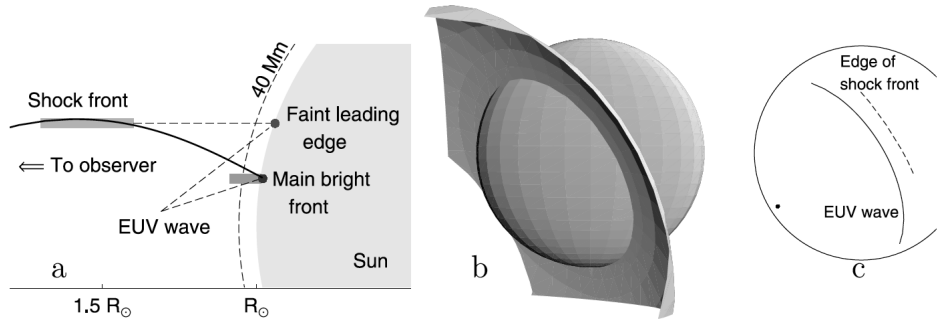


Figure 1.25: Model of a coronal disturbance resulting in a CBF in the low corona, and a steepening into a shock higher in the corona (Grechnev *et al.*, 2011a).

shock.

However, such a mechanism may be called into doubt, given that CBFs can often display kinematics that may not be explained by a wave. This has prompted a ‘pseudo-wave’ interpretation, whereby the erupting CME produces a large-scale restructuring or reconnecting of coronal magnetic field (Attrill *et al.*, 2007; Chen *et al.*, 2002). The bright front may also be due to current shell around the CME as it encounters the coronal field during eruption, this may result in a bright pulse via Joule plasma heating that is not actually a driven wave (Delannée *et al.*, 2008). In this scenario, any relationship with shock observables is indirect, and the relationship with the particle acceleration process may be brought about by magnetic reconnection, such as interchange reconnection at the flanks of a CME (Maia & Pick, 2004). Hence it is not clear how close the relationship of CBFs is to the many shock observables in the corona e.g., is the CBF a low-coronal, low-amplitude counterpart of a shock front higher in the corona? Are radio bursts and particle acceleration in any way associated with this shock front? Does the CME drive this shock front? Despite a close temporal correspondence between CMEs, radio bursts and CBFs, the shock wave link between these phenomena has not been definitively proven or discredited.

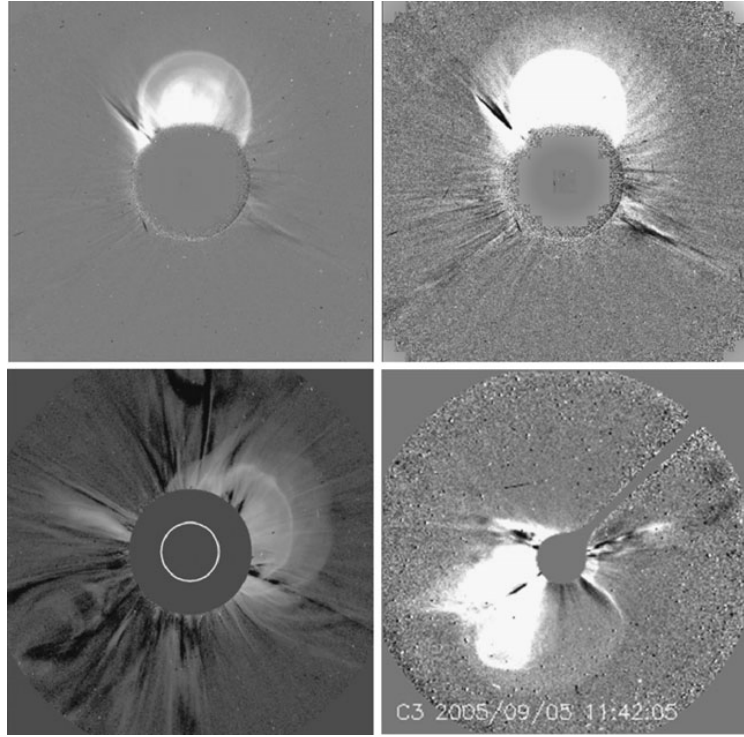


Figure 1.26: Coronal mass ejections displaying evidence of shocks. The much fainter secondary front is a candidate for a CME driven shock (Vourlidas *et al.*, 2013)

1.3.4 White-light Shocks

There is a wealth of evidence in radio and ultraviolet to suggest the transit of CME driven shocks in the corona. Some of this evidence suggests that these shocks may occur at the CME flank as well as ahead of its apex. It has been shown in some studies that these shocks may be directly imaged in white-light coronagraph images (Vourlidas & Bemporad, 2012; Vourlidas *et al.*, 2013). Under high contrast a much fainter front may be seen ahead of the main front, four such events are shown in Figure 1.26. This ‘two-front’ morphology is a common occurrence in white-light CME structure and constitutes a reliable signature of a CME front followed by a stand-off shock (Vourlidas *et al.*, 2013). In many instances they have been used as qualitative confirmation for the presence of a

1.4 Thesis Outline

CME-driven shock in the corona. Indeed, it has been used to identify shock candidates at the flank of a CME (Vourlidas *et al.*, 2003). However, some studies have inferred various quantitative shock parameters such as the compression ratio (Ontiveros & Vourlidas, 2009), or by considering the shock geometry. Stand-off shocks are a common occurrence in nature and their theoretical development in an astrophysical context has been applied to planetary magnetospheric bow shocks whereby the radius of curvature of the driver and the stand-off distance between the nose of the driver and the bow shock may allow a calculation of the Mach number (Spreiter *et al.*, 1966). This applies to shocks on all physical scales, from bullets and aircraft, to planetary magnetospheres and CMEs (Russell & Mulligan, 2002). In its application to CMEs, the theory was used to derive coronal magnetic field (Kim *et al.*, 2012), shock Mach numbers in the low corona (Gopalswamy *et al.*, 2012), as well as Mach numbers in the outer corona as far as ~ 0.5 A.U. (Maloney & Gallagher, 2011).

1.4 Thesis Outline

The work in this thesis firstly advances the understanding of CME masses, energies and forces. As outlined above, very few observational studies of CME masses exist, and CME energy studies a fewer still. Almost no observational studies of CME forces exist. The reason for this is that, to date, CME masses and dynamics observations have been severely hindered by the very large uncertainties in CME mass. This has been due to the unknown propagation direction and width of the CME, making a determination of the uncertainties on the mass impossible. Very uncertain masses combined with equally uncertain kinematics has lead to virtually no quantification of the total force acting on CMEs as they propagate. This thesis will address this issue by showing that CME mass and energies may

1.4 Thesis Outline

be quantified more reliably and with much reduced uncertainty when the dual vantage points of the STEREO spacecraft are used. Also, for the first time in the field, an observational quantification of the forces acting on CMEs will be presented.

Secondly, this thesis will outline the behavior of CMEs and radio bright shocks in the low corona. Up until now, the relationship between CME, CBFs, and radio bursts has remained unknown. It is not known whether CMEs dive shocks through the corona, the low coronal manifestation of which is a CBF. It is also undetermined if the radio bursts are generated in this same wave/shock system. This work will show that the relationship between CMEs, CBFs, and radio bursts is a plasma shock. Furthermore, it will show that this shock was driven by the expansion of the CME flank, and was responsible for bursty particle acceleration.

Chapter 2 will first discuss MHD, CME theory and related phenomena. Secondly it will discuss the plasma shock theory that is relevant to this study i.e., the MHD Rankine-Hugoniot relations, shock particle acceleration, and radio burst generation. Chapter 3 will discussed the variety of instrumentation used in this study, including the installation of the Rosse Solar Terrestrial Observatory (RSTO). Chapter 4 involves the CME masses, kinematics and dynamics work, while Chapter 5 will discuss the CME, CBF, radio bursts and plasma shock work. Chapter 6 will summarise the main findings and conclusions of this thesis and present the future direction of the study.

2

Coronal Mass Ejection and Plasma Shock Theory

This chapter introduces the theory used to study coronal mass ejections and coronal shocks. Since the corona is a plasma, the theoretical framework under which all coronal phenomena are treated is in plasma physics and a fluid description of plasmas known as magnetohydrodynamics (MHD). Coronal mass ejections are a large scale phenomena and can therefore be treated using MHD. While plasma shocks on the large scale may also be treated in an MHD continuum framework, it is necessary to consider individual particle motions when describing particle acceleration and radio emission in shocks, requiring a departure from MHD and the use of distribution functions, the Boltzmann equation, and individual particle kinematics. Therefore, both the MHD equations and the Boltzmann equation are presented in this chapter, followed by an application of this theory to CMEs and plasma shocks.

2.1 Plasma Physics and Magnetohydrodynamics

2.1.1 Maxwell's Equations

Since plasmas are an electrically conducting fluid which may interact with electromagnetic fields, Maxwell's equations are an essential starting point for all plasma theory. Maxwell's equations form a closed set of four unknowns and four equations describing relationships between the electric field \mathbf{E} , the magnetic field \mathbf{B} , the current density \mathbf{j} , and the charge density ρ_q

$$\nabla \cdot \mathbf{E} = \frac{\rho_q}{\epsilon_0} \quad (2.1)$$

$$\nabla \cdot \mathbf{B} = 0 \quad (2.2)$$

$$\nabla \times \mathbf{E} = -\frac{d\mathbf{B}}{dt} \quad (2.3)$$

$$\nabla \times \mathbf{B} = \mu_0 \mathbf{j} + \frac{1}{c^2} \frac{d\mathbf{E}}{dt} \quad (2.4)$$

μ_0 and ϵ_0 are the magnetic permeability and electric permittivity of free space, respectively, and all bold face quantities represent vector variables. At velocities typically found in a plasma equation (2.4), Ampére's law, reduces to

$$\nabla \times \mathbf{B} = \mu_0 \mathbf{j} \quad (2.5)$$

where the displacement current is no longer included. Maxwell's equations describe electromagnetic behaviour and they constitute an important part of the fluid description of plasmas. Before we define this fluid description a brief discussion of plasma kinetic theory, from which the fluid theory is derived, is provided here.

2.1.2 Plasma Kinetic Theory

The general approach to the majority of plasma phenomenon is in a collective description using particle distribution functions and the use of differential equations to describe the evolution of these distribution functions. This is known as plasma kinetic theory, and the distribution functions can be of the form of the Maxwell-Boltzmann velocity distribution, while the differential equation used to describe its evolution is the Boltzmann equation. Many non-equilibrium or unstable states of a plasma, such as those that produce radio bursts described in sections 2.3.4–2.3.5 require a kinetic theory description of plasma. A brief overview of kinetic theory is therefore given here before describing specifically its application to plasma emission and radio bursts.

As with a neutral gas, the particle distribution function $f(\mathbf{r}, \mathbf{v}, t)d\mathbf{v}d\mathbf{r}$ describes the number of particles having positions between \mathbf{r} and $\mathbf{r} + d\mathbf{r}$ and velocities between \mathbf{v} and $\mathbf{v} + d\mathbf{v}$, at time t . This distribution function can be used derive a number of useful physical properties of the plasma, such as the particle number density at position \mathbf{r} and time t

$$n(\mathbf{r}, t) = \int f(\mathbf{r}, \mathbf{v}, t)d\mathbf{v} \quad (2.6)$$

as well as the bulk velocity particle velocity, given by

$$\mathbf{v}(\mathbf{r}, t) = \frac{1}{n(\mathbf{r}, t)} \int \mathbf{v}f(\mathbf{r}, \mathbf{v}, t)d\mathbf{v} \quad (2.7)$$

The evolution of this distribution function in time and space is described by the

Boltzmann equation, given by

$$\frac{\partial f(\mathbf{r}, \mathbf{v}, t)}{\partial t} + (\mathbf{v} \cdot \nabla_r) f(\mathbf{r}, \mathbf{v}, t) + (\mathbf{a} \cdot \nabla_v) f(\mathbf{r}, \mathbf{v}, t) = \left(\frac{\partial f(\mathbf{r}, \mathbf{v}, t)}{\partial t} \right)_{coll} \quad (2.8)$$

This equation describes the changes in occupation number of particles at positions $(\mathbf{r}, \mathbf{v}, t)$ in phase space due to a configuration space flux $\mathbf{v} \cdot \nabla_r f$, a velocity space flux $\mathbf{a} \cdot \nabla_v f$, as well as collisions experienced by the particles (last term in the right). Equation 2.8 is the fundamental basis of all plasma and neutral gas kinetic theory and provides a very powerful tool for describing the time and space evolution of equilibrium and, more importantly, non-equilibrium distributions of particles. It is the most general description of the behavior of an ensemble of particles, and all other macroscopic fluid dynamical equations may be derived from it.

Assuming the plasma to be collisionless and stating the accelerations in the plasma in terms of the electric field \mathbf{E} and magnetic field \mathbf{B} , Equation 2.8 may be reduced to the Vlasov equation for a plasma interacting with electromagnetic fields.

$$\frac{\partial f}{\partial t} + (\mathbf{v} \cdot \nabla_r) f + \left(\frac{q}{m} [\mathbf{E} + \mathbf{v} \times \mathbf{B}] \cdot \nabla_v \right) f = 0 \quad (2.9)$$

where q is Coulomb charge, m is particle mass, and $f(\mathbf{r}, \mathbf{v}, t)$ is reduced to f for simplicity of notation. This form of the Vlasov equation is used in the formulation of wave-particle interactions, and wave growth in plasmas, that ultimately lead to plasma emission in solar radio bursts, this will be described in further detail sections 2.3.4–2.3.5.

In equations 2.6 and 2.7, the number density and bulk velocity of the plasma were obtained by taking appropriate weighted integrals of the distribution function. This is done to obtain information on the macroscopic properties of the

2.1 Plasma Physics and Magnetohydrodynamics

plasma when the specific details of the particle distribution are not needed. A behaviour of the plasma on a macroscopic or fluid scale may be obtained by taking the appropriate integrals of the Boltzmann equation in a procedure known as ‘taking the moments of the Boltzmann equation’. The moments of a function are given by

$$\mu_n = \int x^n f(x) dx \quad (2.10)$$

where the n describe the moments e.g., $n = 0$ is the *zeroth moment*, $n = 1$ is the *first moment* etc. Taking the moments of the Boltzmann equation lead to a set of fluid conservation equations that describe the dynamics of a plasma on a continuum scale (no individual particle motion available). The moments are as follows

$$\begin{aligned} \int [\text{Boltzmann eq.}] \times v^0 dv &\rightarrow \text{conservation of mass} \\ \int [\text{Boltzmann eq.}] \times v^1 dv &\rightarrow \text{conservation of momentum} \\ \int [\text{Boltzmann eq.}] \times \frac{v^2}{m} dv &\rightarrow \text{conservation of energy} \end{aligned}$$

In their most fundamental form, these conservation equations are used in what is known as a multi-fluid description of the plasma, where the dynamics and conservations of the various properties are treated separately for each particle species e.g., electrons and protons will have different conservation equations and described separately as an ‘electron fluid’ and ‘proton fluid’. However, combining these separate fluids into one ‘single fluid’ framework constitutes a description of plasmas known as magnetohydrodynamics¹.

¹The moments of the distribution function and the reduction of multi-fluid to single fluid conservation equations involve lengthy derivations that are not provided here but can be found in many texts (Goossens, 2003; Inan & Golkowski, 2011).

2.1.3 Magnetohydrodynamics

The conservation principles derived from moments of the Boltzmann equation are firstly the mass conservation equation

$$\frac{D\rho}{Dt} = -\rho \nabla \cdot \mathbf{v} \quad (2.11)$$

where ρ is mass density, \mathbf{v} is bulk flow velocity, t is time, and D represents a Lagrangian derivative ($D/Dt = \partial/\partial t + \mathbf{v} \cdot \nabla$). This expression simply states that the rate of change of particles into or out of a volume is controlled by the fluid flow into and out of the volume. It has units of $\text{kg m}^{-3} \text{s}^{-1}$.

Secondly, the momentum conservation equation is

$$\rho \frac{D\mathbf{v}}{Dt} = -\nabla p + \mathbf{j} \times \mathbf{B} + \mathbf{f} + \nabla \cdot \mathbf{S} \quad (2.12)$$

where p is thermal pressure, \mathbf{j} is the current density, \mathbf{B} is the magnetic field, \mathbf{f} are all body forces e.g., gravity, and \mathbf{S} is a stress tensor. This equation shows that the change in momentum of a fluid may be due to a pressure gradient, the ‘ \mathbf{j} cross \mathbf{B} ’ or Lorentz force, gravity, and any stresses in the plasma e.g., kinematic viscosity ν . Note that with $\nabla \cdot \mathbf{S} = \rho\nu\nabla^2\mathbf{v}$, and setting gravity and the Lorentz term to zero gives the Navier-Stokes equation of motion of a viscous fluid. Note that all terms in this equation have the form of a body force (force per unit volume), and integration over volume would render this equation an explicit version of Newton’s second law ($m\mathbf{a} = \mathbf{F}$).

The third conservation equation is the energy conservation equation

$$\rho \frac{De}{Dt} + p \nabla \cdot \mathbf{v} = \nabla \cdot (\kappa \cdot \nabla T) + \eta_e \mathbf{j}^2 + Q_\nu - Q_r \quad (2.13)$$

where

$$e = \frac{p}{(\gamma - 1)\rho} \quad (2.14)$$

is the internal energy per unit mass, γ is the ratio of specific heats, κ is the thermal conductivity, T is the temperature, η_e is electrical resistivity, Q_ν is heating by viscous dissipation, and Q_r is a radiative term. This equation demonstrates that any changes in the fluid internal energy are due to divergence in the flow field, conduction, ohmic and vicious dissipation, and radiative losses.

The fluid momentum equations can be used to formulate Ohm's law for a plasma which describes the behaviour of current in terms of electric and magnetic fields and the fluid flow velocity

$$\mathbf{j} = \sigma(\mathbf{E} + \mathbf{v} \times \mathbf{B}) \quad (2.15)$$

This is a reduced version of the generalised Ohm's law and does not contain terms for the Hall effect, ambipolar diffusion, and electron inertia. The set of equations (2.11 - 2.15), combined with an equation of state

$$p = nk_B T \quad (2.16)$$

results in a fully closed set of variables and equations, which can be solved for any fluid or electromagnetic property. In order to further simplify these set of equations the electric field \mathbf{E} and current \mathbf{j} are often eliminated by using Faraday's law in combinations with Ampère's and Ohm's law to produce the induction equation

$$\frac{\partial \mathbf{B}}{\partial t} = \nabla \times (\mathbf{v} \times \mathbf{B}) + \eta \nabla^2 \mathbf{B} \quad (2.17)$$

which describes the evolution of the magnetic field in terms of the plasma flow

and the magnetic diffusivity $\eta = \eta_e/\mu_0$. The mass, momentum, internal energy equation, the induction equation, and the solinoidal constraint then define a fully closed system of resistive MHD equations in terms of the variables $(\mathbf{B}, \mathbf{v}, p, \rho)$

$$\frac{D\rho}{Dt} = -\rho \nabla \cdot \mathbf{v} \quad (2.18)$$

$$\rho \frac{D\mathbf{v}}{Dt} = -\nabla p + \frac{1}{\mu_0} (\nabla \times \mathbf{B}) \times \mathbf{B} + \mathbf{f} \quad (2.19)$$

$$\frac{D\rho}{Dt} = -\gamma p \nabla \cdot \mathbf{v} + (\gamma - 1) \frac{\eta}{\mu_0^2} (\nabla \times \mathbf{B})^2 \quad (2.20)$$

$$\frac{\partial \mathbf{B}}{\partial t} = \nabla \times (\mathbf{v} \times \mathbf{B}) + \eta \nabla^2 \mathbf{B} \quad (2.21)$$

$$\nabla \cdot \mathbf{B} = 0 \quad (2.22)$$

It is also assumed here that the fluid is inviscid and not subject to any conductive or radiative energy losses or gains. Under this reduced set of equations, the ideal MHD equations are simply produced by setting $\eta = 0$ e.g., zero resistivity, which would eliminate the second terms on the right in equations 2.20 and 2.10. Under such an assumption the ideal induction equation

$$\frac{\partial \mathbf{B}}{\partial t} = \nabla \times (\mathbf{v} \times \mathbf{B}) \quad (2.23)$$

may be used to show the ‘frozen flux’ condition. This shows that when $\eta = 0$ the field is advected with the plasma or the field is ‘frozen-in’ into the plasma and follows the flow velocity i.e., there is no ‘slipping’ of the magnetic field with respect to the fluid flow. On the other hand, a finite η leads to a variety of important diffusive effects for the magnetic field. The most important of these diffusive processes is magnetic reconnection, which plays an extremely important role in solar flares and CMEs.

2.1.4 Magnetic Reconnection

If the dissipation of concentrations of magnetic flux in the solar corona are due to diffusion processes only, a timescale for this diffusion process may be estimated from the magnetic induction equation. Assuming the diffusion term dominates over advection term

$$\frac{\partial B}{\partial t} = \eta \nabla^2 \mathbf{B} \quad (2.24)$$

As an order of magnitude estimate for the derivatives we replace $\partial/\partial t \rightarrow 1/\tau_D$ and $\nabla^2 \rightarrow 1/L^2$. Equation 2.24 then gives

$$\tau_D = \frac{L^2}{\eta} \quad (2.25)$$

The typical length scales for a coronal active region are 10^7 m, and assuming a Spitzer magnetic diffusivity $\eta = 10^9 T^{-3/2} = 1 \text{ m}^2 \text{ s}^{-1}$ (Spitzer, 1962), equation 2.25 gives a diffusive timescale of 3.1 million years. Given that active regions evolve quasi-statically over weeks and evolve dynamically over timescales of seconds and minutes during a flares and CMEs, there must be an evolution process other than a large scale diffusion in the solar atmosphere. Equation 2.25 indicates that there may be two different ways in which the evolution of magnetic fields may occur over a much shorter times scale: either the typical length scale L is much shorter, or magnetic diffusivity η is much larger.

Magnetic reconnection is the dynamical process that describes the short timescale evolution of magnetic fields in the corona (and other astrophysical and laboratory systems). It involves a change in magnetic topology that converts magnetic energy in kinetic and thermal energy of the bulk plasma and accelerates particles to high speeds. Magnetic reconnection typically occurs in a boundary between two

oppositely directed magnetic field regions. At the very center of the boundary layer the magnetic field must go to zero to account for a continuous change from positive to negative magnetic field. The total pressure balance in the boundary layer and on either side is (Aschwanden, 2004)

$$B_1 + p_1 = p_{dr} = B_2 + p_2 \quad (2.26)$$

where $p_{1,2}$ and $B_{1,2}$ represent thermal and magnetic pressure on either side of the diffusion region, respectively, and p_{dr} is the pressure inside the diffusion region (no magnetic pressure).

The existence of inflows into the diffusion region at right angles to the magnetic field creates an electric field in this layer that is perpendicular to the inflow plane. This creates a current in the diffusion region, hence this layer is often called a ‘current sheet’. The diffusion of magnetic fields occurs within this current sheet. Sweet and Parker were the first to devise a mechanism by which magnetic reconnection occurs in such a current sheet Parker (1963); Sweet (1958).

The Sweet-Parker were the first to devise a model whereby the diffusive time scale of the field (equation 2.25) could be made much faster by considering a diffusion region much smaller than the size scales of active regions. The model consists of a current sheet (diffusion region) that is much longer than it is wide i.e., in the top panel of Figure 2.1 $\Delta \gg \delta$, where Δ is current sheet half-length and δ is current sheet half-thickness. Conservation of mass implies that the rate at which mass enters the sheet must equal the rate that mass exits the sheet

$$\rho\Delta v_{in} = \rho\delta v_{out} \quad (2.27)$$

where v_{in} and v_{out} are the inflow and outflow speeds respectively. Using equa-

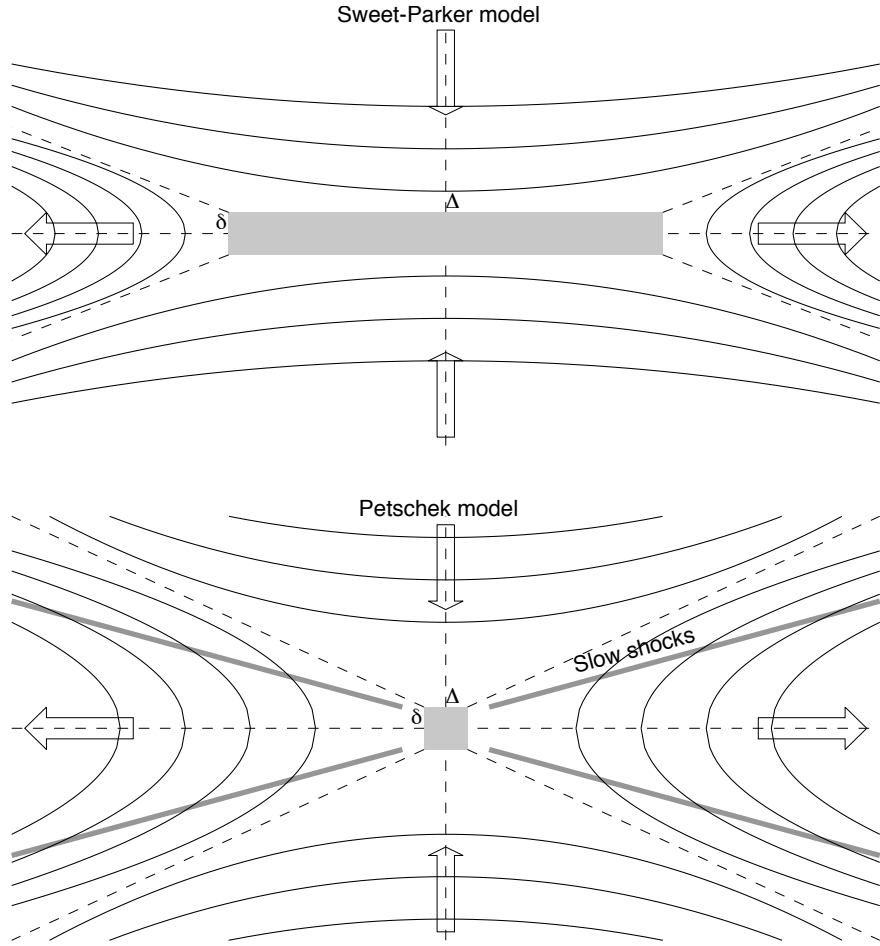


Figure 2.1: The reconnection models of Sweet-Parker (top) and Petschek (bottom). The Sweet-Parker mechanism employs a long and thin ($\Delta \gg \delta$) current sheet as the diffusion region. It produces reconnection rates that are much too slow to describe flare and CME energy dissipations rates. Petschek proposed a similar model but with a diffusion region that is much smaller, with $\Delta \approx \delta$, resulting in reconnection rates that are consistent with flare and CME timescales. The dissipation of energy in this model is partly controlled by the presence of two slow-mode shocks which separate the sub-Alfvénic inflow region and the super-Alfvénic outflow region (Aschwanden, 2004).

tions 2.25 and 2.27 the inflow speed may be written as

$$v_{in}^2 = \frac{\eta v_{out}}{L} \quad (2.28)$$

The reconnection rate depends on in the ratio of the inflow speed v_{in} to the

outflow speed v_{out} in the form of the Mach number

$$M = \frac{v_{in}}{v_{out}} = \frac{1}{\sqrt{S}} \quad (2.29)$$

where $S = v_A L / \eta$ is the Lundquist number (equivalent to the magnetic Reynold's number at the Alfvén speed). The rate of reconnection depends on the length scale and magnetic diffusivity in the current sheet. Despite the fact that the Sweet-Parker mechanism provides a rate of magnetic energy dissipation that is faster than the global process, it is much too slow to explain the process of magnetic energy release in solar flares. For example for typical Lundquist numbers of 10^{12} , the Sweet-Parker model produces a reconnection rate of 10^{-6} of the Alfvén speed.

To over come the problem, Petscheck proposed a model with a much smaller diffusion region where $L \approx \delta$ (Petschek, 1964) . With this smaller diffusion region, the boundary between inflow and outflow regions are separated by slow mode magnetoacoustic shocks. Alongside the diffusion region, these shocks also help to dissipate some of the inflowing kinetic energy into thermal energy. Again, no analytical solution to the model exists but Petscheck found that when the diffusion regions is allowed to be small, the reconnection rate is given as

$$M \approx \frac{\pi}{8 \ln(S)} \quad (2.30)$$

This gives a much faster reconnection rate of 0.01 of the Alfvén speed (hence it is known as fast reconnection), which is comparable to solar flares. When Petscheck presented the model it was thought to be a complete description of 2D magnetic reconnection, however other solutions would soon be discovered, with the Petscheck model being just one of a family of possible 2D reconnection

mechanisms. These mechanisms describe steady, uniform, 2D reconnection, the rate of which may be summarised as (Priest & Forbes, 1986)

$$\left(\frac{M_e}{M_i}\right)^2 \approx \frac{4M_e(1-b)}{\pi} \left[0.834 - \ln \tan\left(\frac{4S\sqrt{M_e M_i}}{\pi}\right)^{-1} \right] \quad (2.31)$$

This contains the Sweet-Parker, the Petscheck ($b = 0$) and Sonnerup (Sonnerup, 1970) ($b = 1$) reconnection rates.

2D reconnection, an the more complicated 3D models, play a role in many theoretical models describing the eruption of coronal mass ejections and flares. Although some CME models have no need for reconnection to occur, there is a growing consensus that it is an integral part of the solar eruptive process.

2.2 Coronal Mass Ejections

Magnetohydrodynamic models of eruptive coronal mass ejections use either ideal or resistive MHD (without and with reconnection, respectively) to bring about a loss of equilibrium of some complex magnetic structure in the corona. The magnetic structure usually takes the form of a flux rope, a helical or twisted magnetic structure embedded in the coronal magnetic field. The main goal of every model is to induce a loss of equilibrium of the structure, but the mechanism by which this is done varies greatly amongst the models. *Storage models* assume a slow build up of magnetic stress in a non-potential field that may store free energy over long time scales before some loss of equilibrium occurs and the stored magnetic energy is rapidly converted to mechanical energy and the expulsion of a magnetic structure (Antiochos *et al.*, 1999a; Forbes & Priest, 1995; Wolfson & Saran, 1998). *Dynamo models* involve a rapid generation of magnetic flux by either stressing of the field or flux-injection into the system. As the name suggests, these models

usually consider the interplay between current and magnetic field in the system that may bring about a Lorentz force which provides an expulsion of the flux rope from the low corona (Chen, 1989; Fan, 2005; Krall *et al.*, 2001; Schrijver *et al.*, 2008a). Finally there are the *thermal blast models*, which produce an expulsion of the CME into interplanetary space by an enhanced pressure gradient due to the rapid heating of a flare i.e., an explosive ejection of plasma from the corona. This model is somewhat out-dated now since CMEs are no longer thought to be the result of flares, with some CMEs preceding flare onset and some occurring without any flare (Gosling, 1993).

The main goal of every model is to induce a loss of equilibrium of the structure, but the mechanism by which this is done varies greatly amongst the models e.g., there is still some debate on whether the flux rope is formed as a result of eruption or it is a pre-existing structure. The need for reconnection is also a source of contention, with some models inducing eruption using only ideal MHD and other models employing resistive MHD (Chen, 2011). The most prominent of these models are discussed here.

2.2.1 Catastrophe Model

The catastrophe model assumes a flux-rope is formed in the corona prior to eruption and considers the balance between magnetic tension holding the flux rope in position, and magnetic pressure (from compression of field lines under the rope) that supply an outward directed force (Forbes & Isenberg, 1991; Lin & Forbes, 2000; Priest & Forbes, 2000). A loss of equilibrium is brought about by photospheric motions, either convergence or shearing of the foot points, which are well-known precursors to eruptive activity in the corona (Rust, 1972). the reduction of the distances between the foot points, 2λ , decreases and this initially

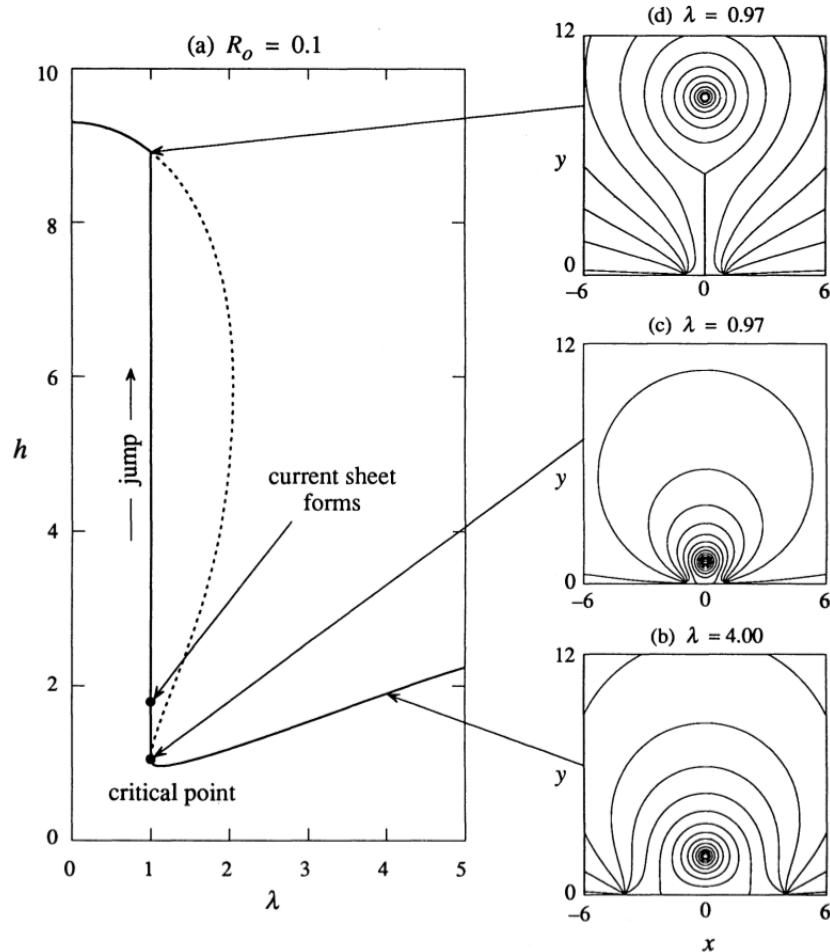


Figure 2.2: The catastrophe model of (Forbes & Priest, 1995). The model consists of a 2D pre-existing flux rope with foot points rooted in the photosphere. The fluxrope is driven toward instability by motions of the photospheric footpoints, in this case the distance between the footpoints λ decreases slowly (timescales much longer than the Alfvén crossing time $\tau = L/v_A$). As the foot points converge the fluxrope initially contracts indicated by a decreasing height in panel (a). Eventually this convergence brings the system to critical point where magnetic pressure outwards dominates inward magnetic tension. The system rises, reaches a new equilibrium position, and forms a current sheet. The evolution of the system after it reaches this new equilibrium largely depends on whether or not magnetic reconnection occurs in the sheet. the rate of reconnection may also bring about different evolutions in kinematics (Priest & Forbes, 2000).

causes an increase in the magnetic tension which makes the rope contract and reduce its height Fig. 2.2. However, continued contraction results in a magnetic compression that dominates tension, resulting in a flux rope rise. As the rope rises it forms a current sheet behind it, and its evolution after this point depends

2.2 Coronal Mass Ejections

on whether or not reconnection occurs in the current sheet. If no reconnection is present then the flux rope simply rises and finds a new equilibrium position at a greater height, in this case the net release of magnetic energy is less than 1% of the energy stored in the pre-field configuration (Forbes & Isenberg, 1991). If reconnection occurs, then the eruption proceeds uninhibited and up to 95% of the stored magnetic energy is released (Forbes & Priest, 1995).

Forbes & Priest (1995) provided expressions for the development of current in the flux rope with respect to height which was used to estimate the free magnetic energy in the system. By assuming a rapid reconnection rate, and that all of this free energy was converted to the rope's kinetic energy they were able to derive velocity-time kinematics, and under the constraint of the flux rope radius $a \rightarrow 0$ an analytical expression for the rope velocity may be derived as (Priest & Forbes, 2000)

$$v \approx \sqrt{\frac{8}{\pi}} v_{A0} \left[\ln\left(\frac{h}{\lambda_0}\right) + \frac{\pi}{2} - 2\tan^{-1}\left(\frac{h}{\lambda_0}\right) \right] + v_0 \quad (2.32)$$

where h is the fluxrope height, $2\lambda_0$ is the foot point separation at $\lambda = h$, v_0 is an initial perturbation velocity (1% of the Alfvén speed), and v_{A0} is the Alfvén speed where $\lambda = h$. Magnetic power output in the early phase of eruption is given by

$$\frac{dW}{dt} \approx -\frac{2A_0^2}{\pi\mu} \left(\frac{h}{\lambda_0} - 1 \right)^2 \frac{v}{\lambda_0} \quad (2.33)$$

where $h \sim t + t^{5/2}$ and $v \sim t^{3/2}$ i.e., the initial power output grows with time. In the later phases of propagation the power output decays with time as

$$\frac{dW}{dt} \approx \frac{4A_0^2}{\pi\mu t} \quad (2.34)$$

so the growth in power output occurs approximately 100 times quicker than the decay in power output.

A later study by Priest & Forbes (2000) analysed how reconnection in the underlying current sheet may influence the eruption of the flux rope. The kinematics of the rope after equilibrium is lost depend on the rate of reconnection in the sheet, parameterised by the Alfvén Mach number of the inflow into the reconnection site. If $M_A = 0$ then the fluxrope does not escape but oscillates around an equilibrium height like a yo-yo. If $0 < M_A < 0.005$, escape is possible but the rope may show a number of oscillations in height before escape, this behaviour has never been directly observed so reconnection must occur at a rate $M_A > 0.005$ to produce eruption. For $0.005 < M_A < 0.041$ the rope escapes but undergoes a period of deceleration between 20 and 100 Alfvén crossing times, while for $M_A > 0.041$ no deceleration occurs and the fluxrope escapes and approaches an asymptotic velocity.

The catastrophe model provides a successful way of evolving a flux system to the point of catastrophic loss of equilibrium and consequent eruption. However, a major limitation is that it is a 2D model and does not take into account that the ends of the flux rope will be anchored in the photosphere. This would produce a curvature in the rope that would increase its tension and hence change the dynamics, but it is unlikely that it would prevent eruption (Steele *et al.*, 1989)

2.2.2 Magnetic Breakout Model

The magnetic breakout model was first proposed by (Antiochos *et al.*, 1999a) and involves a quadrupolar (or more complex) magnetic flux system. A core magnetic field is flanked by two side-lobe fields, which collectively lie underneath an over-arching field that stabilizes the whole system. The overarching field and core field are almost anti-parallel, creating a magnetic null point between the two Figure 2.3. Non potentiality is injected into the core by twisting/shearing

2.2 Coronal Mass Ejections

of the foot points or by flux emergence. This non-potentiality causes the core field to grow and encounter the overarching field, distorting the null point into a current sheet and eventually allowing reconnection to occur. The reconnection removes field lines from the overarching field and adds it to the side-lobe systems, allowing further growth of the core field. The growth of the core field in turn drives further breakout reconnection resulting in a positive feedback required for explosive expulsion of the core. Finally, as the core is accelerated a current sheet forms in its wake, eventually leading to a separation of the core flux from the solar surface that forms a plasmoid structure typical of a three part CME (Lynch *et al.*, 2004); an important aspect of this is that flux rope formation happens as a consequence of eruption i.e., it is not pre-existing. The magnetic breakout model was used to circumvent the Aly-Sturrock limit (Aly, 1991; Sturrock, 1991) i.e., it allowed a flux system to erupt, without having to open the constraining field lines to infinity.

Kinematically, the CME/central field system should experience a slow rise (1 km s^{-1}) for several hours due to shearing/twisting of the foot points. Once breakout reconnection has begun the CME experiences a much larger acceleration (100 km s^{-1}). The reconnection in the current sheet in the wake of the CME is the source of energetic particles that ultimately lead to flaring (ribbons and soft x-ray loops). Therefore magnetic breakout predicts that the flaring process and SXR peak should only begin after CME acceleration (after breakout reconnection) has begun (Lynch *et al.*, 2004). However, the precedence in breakout reconnection over flaring reconnection may not always be case, with the latter sometimes driving the former (MacNeice *et al.*, 2004). The above studies have mainly been through 2.5 D simulations but a 3 D simulation of the breakout model was given in (Lynch *et al.*, 2008). This allowed a full estimate of the conversion

2.2 Coronal Mass Ejections

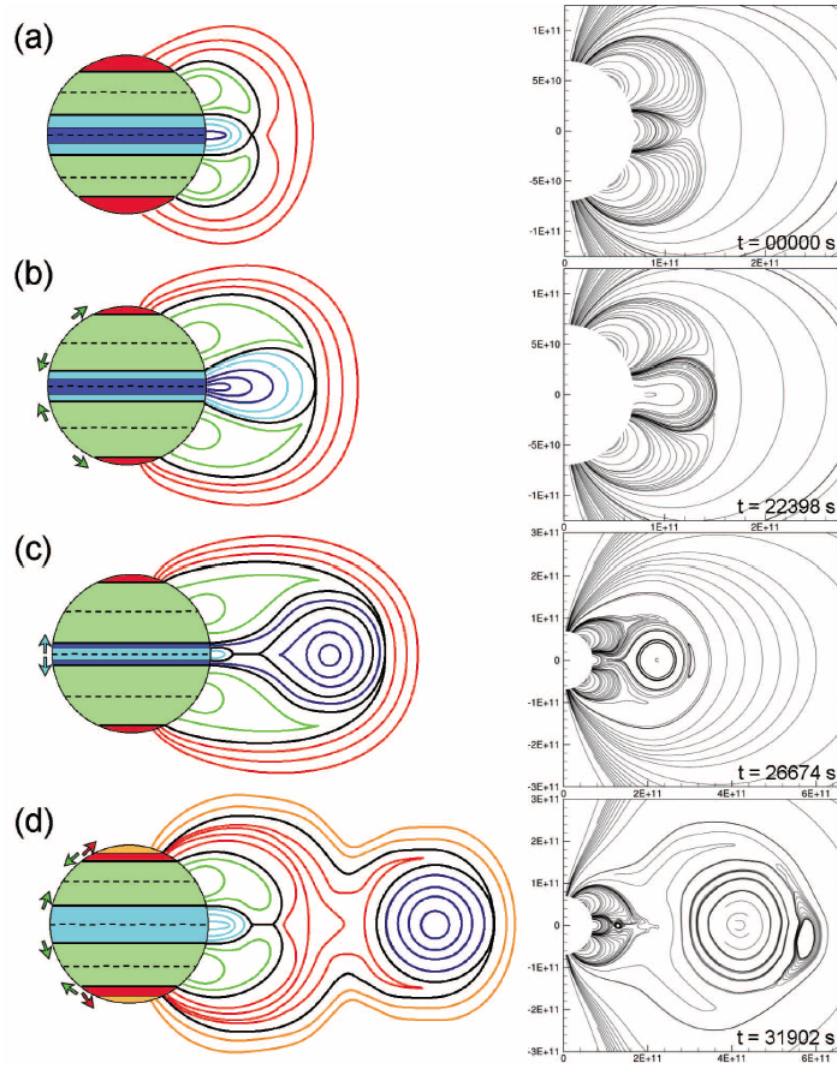


Figure 2.3: The breakout model, consisting of a quadrupolar flux system in which the central flux (blue) is flanked by two side lobe flux systems (green), with the entire system kept in stability by the tension of the overlying red field. Shearing and/or twisting on the underlying flux causes it to grow slowly. Eventually a current sheet forms at the magnetic null above the central flux, causing reconnection. This reconnection transfers overlying field to the side-lobes, effectively creating a conduit for the central flux to escape as a CME (Lynch *et al.*, 2008).

of magnetic energy into kinetic energy. It is found that during the flare impulsive phase 17.8% of the free magnetic energy (4.6×10^{31} ergs) is converted into plasma kinetic energy (8.1×10^{30} ergs). During the gradual phase the proportion of free magnetic energy converted to kinetic energy drops to 15.4%

There has been observational tests of the magnetic-breakout model, showing it to be a viable explanation of some flaring and CME events, the most notable of which is the Bastille Day event (Aulanier *et al.*, 2000). The observational signatures of the model include the presence of a null point in the corona above a complex multipolar flux system (inferred from potential field source surface extrapolations), a radio source imaged to be above the erupting structure (implying a reconnection site), and radio bursts beginning at frequencies indicative of high altitude (again indicating energy release above the erupting structure, prior to eruption) (Manoharan & Kundu, 2003). However, in some instances magnetic breakout is implied by observations of the above, but the kinematics are inconsistent with model predictions. For example the model predicts a long slow rise of the central flux system as the underlying field is increasingly sheared, after which there is a rapid acceleration once breakout reconnection is initiated. However, in the study of Bong *et al.* (2006) the breakout reconnection occurred at the end of the CME acceleration phase, prompting a two-phase acceleration scenario.

2.2.3 Toroidal Instability

The toroidal instability model incorporates a pre-existing flux rope structure that is built from a torus of magnetic flux, some of which is buried beneath the photosphere (Chen, 1989). The flux system is can be broken down into a combination of toroidal magnetic field, toroidal current , poloidal magnetic field and poloidal current Figure 2.4. This flux rope system is embedded in a surrounding coronal magnetic field \mathbf{B}_{corona} . The stability of the system depends on the nature of the $\mathbf{J} \times \mathbf{B}$ force due to the interaction toroidal and poloidal components of both the field and current. The interaction of \mathbf{J} and \mathbf{B} internal to the flux rope is usually termed the Lorentz self-force or the ‘hoop’ force. An instability may be induced

2.2 Coronal Mass Ejections

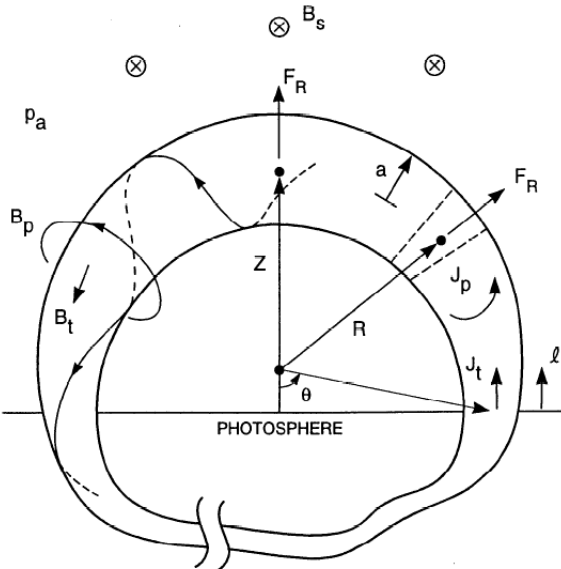


Figure 2.4: The flux rope model of Chen (1989), used to study the toroidal instability of a twisted flux system in the corona.

via twisting of the fluxrope footpoints to increases the amount of poloidal flux (effectively increasing the helicity of the system). The instability arrises when the outward hoop force deccreses more slowly within the ring radius than the opposing Lorentz force due to an external magnetic field. Once the instability is induced, the fluxrope begins a bulk motion as well as a growth in its semi-minor axis. Hence the motion of the system can be analysed by looking at the central axis or the minor axes (leading and trailing edges). The three axes display slightly different kinematics e.g., the leading edge has a faster velocity than the trailing edge (due to fluxrope expansion). This has proved a useful test of the model when comparing the observations of erupting fluxrope structures as seen in white-light coronagraphs. Krall *et al.* (2001) analysed the leading and trailing edges of erupting flux rope, as well as the rope aspect ratio, and compared the observations to model expectations. Good agreement is found between the model kinematics and aspect ratio and the observed events. The equation of motion of

2.2 Coronal Mass Ejections

the entire system is given by

$$M \frac{d^2Z}{dt^2} = \frac{I_t}{c^2 R} \times \left[\ln\left(\frac{8R}{a}\right) - 1 + \frac{\xi_i}{2} + \frac{\beta_p}{2} - \frac{B_t^2}{B_{pa}^2} - \frac{2RB_{\perp c}}{aB_{pa}} \right] - F_g - F_{drag} \quad (2.35)$$

where I_t is the toroidal current, R is the flux rope major radius, a is the rope minor radius, ξ_i is internal inductance of the flux system, B_t is the toroidal field, B_{pa} is the poloidal field at a , $B_{\perp c}$ is the perpendicular component of the ambient coronal field, F_g is the force due to gravity, F_{drag} is the drag force, M is the mass per unit length of the rope, and Z is the rope axis height above the photosphere. The equation of motion shows that an increase in the toroidal current (or poloidal flux) contributes positively to the acceleration. The terms in the square brackets are each unitless and take into account the rope geometry, self-inductance and interplay between poloidal and toroidal flux. The first three terms in the square brackets are what give rise to the hoop-force. If the rope is mass loaded with a prominence, this can contribute to the rope's stability via the gravity term. The drag term only becomes an important contributor to rope dynamics later in the propagation, when the solar wind speed begins to increase i.e., at around $10R_\odot$ (Sheeley *et al.*, 1997). The eruption is driven by flux-injection, which typically lasts for 4-8 hours, during which time the unstable system loses its equilibrium and begins to rise Krall *et al.* (2001). This model is perhaps the only one to calculate the magnitudes of the forces explicitly (Figure 2.5)

It is significant the fluxrope is already established in the corona before eruption begins i.e., the rope formation is not addressed in the model and it is not a consequence of eruption. Hence magnetic reconnection is not a necessary aspect of the model and the eruption may proceed without employing resistive MHD. The model has been tested against observations and found to provide consistent result with the acceleration and jerk profiles of destabilized filaments during eruption

2.3 Coronal Shocks and Plasma Emission

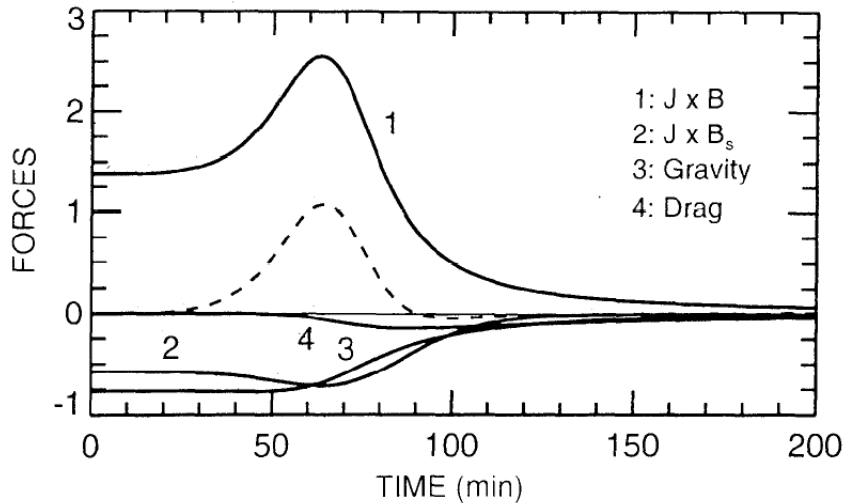


Figure 2.5: Forces acting on a flux rope from the Toroidal instability model. The y axis units are in 10^{21} dyn. The dashed curve is the new force from all contributions (Chen, 1989).

(Schrijver *et al.*, 2008a)

2.3 Coronal Shocks and Plasma Emission

2.3.1 Alfvén Speed in the Corona

The speed at which perturbations travel in a magnetized plasma is the Alfvén speed, given by

$$v_A = \frac{B_0}{\sqrt{\mu_0 \rho}} \quad (2.36)$$

where B_0 is the unperturbed (equilibrium) magnetic field, μ_0 is the magnetic permeability, and ρ_0 is the unperturbed mass density of the medium. This is a highly anisotropic wave driven by the restoring force of magnetic tension, with the inertia provided by the plasma mass density. Perturbations in the magnetic field, B_1 , are transverse to the direction of B_0 and the group velocity always has a wave \hat{k} vector parallel to the magnetic field direction. The quiet solar corona in the range of $1 - 3 R_\odot$ has typical magnetic field strengths

2.3 Coronal Shocks and Plasma Emission

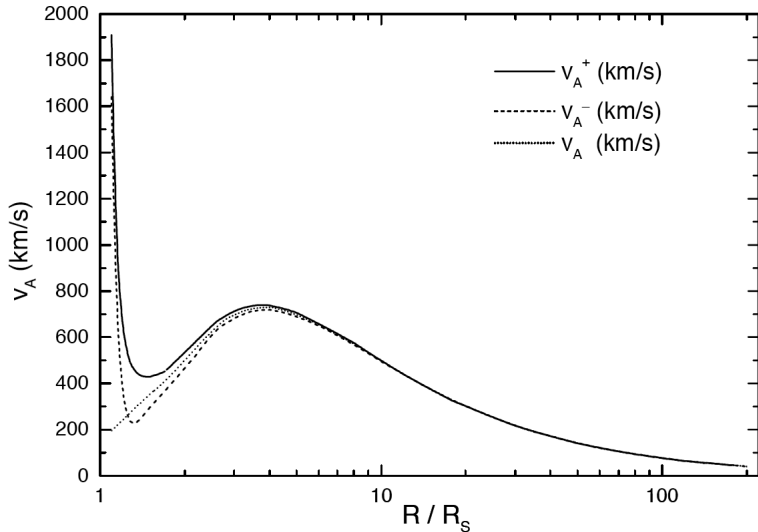


Figure 2.6: Alfvén speed of the corona as a function of heliocentric distance. The dotted line is the quite sun, with only the Sun's global dipole field. The solid line is the Alfvén speed calculated from a combination of the global dipole field and a smaller active region dipole field oriented parallel to the global dipole. The dashed line is the the speed when the active region dipole is anti-parallel to the global field. The two profiles from the active region show a distinct minimum in the coronal Alfvén speed at $\sim 1.5 R_\odot$

on the order of $1-100 \text{ G} = 10^{-2}-10^{-3} \text{ T}$, and typical electron number densities of $10^6-10^9 \text{ cm}^{-3} = 10^{12}-10^{15} \text{ m}^{-3}$, so for $B_0=5 \text{ G}$ and $n_e=10^8 \text{ cm}^{-3}$ the Alfvén speed in the corona is $\sim 1000 \text{ km}\cdot\text{s}^{-1}$. The variation in magnetic field and density in the corona, especially nearby an active region, v_A may be on the order of $10^2-10^3 \text{ km}\cdot\text{s}^{-1}$. If displacement components of the wave are perpendicular as well as parallel to the equilibrium magnetic field and non-zero perturbations in plasma thermal pressure and density occur, the result is a wave propagation known as a magnetoacoustic wave, such as the fast and slow mode MHD waves. However, given the corona is a low- β plasma, magnetic perturbations are faster than thermal pressure ones, so the Alfvén speed is a good estimate of plasma perturbation speeds in the corona. Mann et al. produced a 1D model of the variation of Alfvén speeds in the quiet and active region corona as a function of height Figure. Warmuth then improved this to a 2D model. It shows that CMEs

2.3 Coronal Shocks and Plasma Emission

are well capable of producing plasma shocks in the corona, since they may travel far in excess of the Alfvén speed. The theory of plasma shocks and the resulting effects of particle acceleration and plasma emission are discussed in the following sections.

2.3.2 MHD Shocks

For acoustic shock waves there are a number of conservation equations that quantify the strength of a shock by relating the upstream gas pressure, density, flow speed, and temperature to their downstream counterparts. Such conservation equations are known as the jump conditions and the shock is considered a surface at which the fluid properties change discontinuously. The shock thickness is usually of the order of a few mean free paths of the particles in the gas, in such a case the processes in the shock surface itself are inconsequential and the relationship between upstream and downstream parameters provide a sufficient description of the shock.

When the gas is ionized and a magnetic field is present, the jump conditions must be modified to take into account the magnetic pressure and the field orientation with respect to the flow velocity and shock normal \hat{n} (unit vector normal to the shock plane). In the general case of oblique shock waves where the magnetic field direction has some arbitrary angle with respect to shock normal we may derive a set of conservation equations for the frame of the shock wave.

The flow velocity v and magnetic field B are considered to be in the xy -plane.

2.3 Coronal Shocks and Plasma Emission

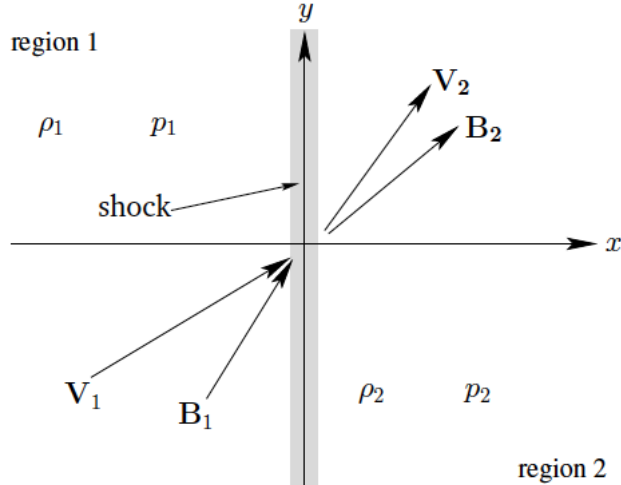


Figure 2.7: Orientation of magnetic field and velocity field with respect to shock plane, in the rest frame of the shock. Shock normal in this case would be along the $-x$ direction i.e., into upstream region 1. (Fitzpatrick, 2000)

The appropriate conservation equations are

$$[\rho v_x] = 0 \quad (2.37a)$$

$$[\rho v_x^2 + p + \frac{B_y^2}{2\mu}] = 0 \quad (2.37b)$$

$$[\rho v_x v_y - \frac{B_x B_y}{\mu}] = 0 \quad (2.37c)$$

$$[\frac{1}{2}v^2 + \frac{\gamma p}{(\gamma - 1)\rho} + \frac{B_y(v_x B_y - v_y B_x)}{\mu \rho v_x}] = 0 \quad (2.37d)$$

$$[B_x] = 0 \quad (2.37e)$$

$$[v_x B_y - v_y B_x] = 0 \quad (2.37f)$$

These are the general MHD shock jump conditions where v is the fluid velocity and B is the magnetic field (with their corresponding components ‘x’ or ‘y’), ρ is the mass density, p is the thermal pressure, and γ is the ratio of specific heats (or the polytropic index). The meaning of the square brackets is $[F] \equiv F_1 - F_2$, for any

2.3 Coronal Shocks and Plasma Emission

quantity F , and the 1 or 2 subscripts represent upstream or downstream values of each quantity F , respectively. These set of jump conditions differ only from the purely acoustic ones due the presence of the magnetic field. For example, taking (4a), (4b), and (4d) and setting $B_x = B_y = 0$ we obtain the jump conditions for a neutral gas. Each conservation equation has a specific meaning;

- (4a) is a mass conservation equation whereby the mass flux entering the shock must equal the mass flux leaving. It has units of $\text{kg m}^{-2} \text{s}^{-1}$.
- (4b) indicates that if mass flux $\rho_1 v_{x,1}$ enters the shock with momentum $(\rho_1 v_{x,1})v_{x,1}$ it leaves the shock with momentum $(\rho_1 v_{x,1})v_{x,2}$, the difference being equal to the the changing force per unit area across the shock. In this case both thermal and magnetic pressures contribute to change in momentum flux. (4c) implies the same process but relates the x and y components of the v and B vector fields. Both equations have units of momentum flux $\equiv (\text{kg m}^{-2} \text{s}^{-1})(\text{m s}^{-1}) = (\text{kg m s}^{-2} \text{m}^{-2}) = \text{N m}^{-2} \equiv \text{pressure}$.
- (4c) is an energy conservation term, accounting for the rate at which gas and magnetic pressure do work per unit area at the shock and equates this to the growth (or loss) in internal energy and kinetic energy across the shock. All components of magnetic field pressure are taken into in the last term on the left of the equation. All quantities are in units of $\text{J}\cdot\text{kg}^{-1}$.
- (4d) simply states that the x component of the magnetic field i.e., the component of the field that is (anti-)parallel to the shock normal \hat{n} is unaffected by the shock transition.
- (4f) relates the orientations of the upstream and downstream magnetic field to the flow speed tangential and perpendicular to the shock normal. Magnetic field orientation and hence the distribution of low speed amongst the

2.3 Coronal Shocks and Plasma Emission

velocity components largely depends on the whether the shock is slow-mode, intermediate, or fast mode. The equation has units of $T \cdot m \cdot s^{-1} = V \cdot m^{-1} \equiv$ electric field.

4(a-f) are the general case of the jump conditions across an MHD shock, they are usually known as the MHD Rankine-Hugoniot (RH) equations. Their generality make the solution of the six unknowns from the six equations quite complicated. However the extreme cases of parallel and perpendicular shocks provide very useful and simplified expressions. It can be shown that parallel shocks i.e., $\hat{v} \parallel \hat{B} \parallel \hat{n}$ reduces to the jump conditions of a hydrodynamic shock in a neutral gas (here parallel and anti-parallel are used synonymously). The more interesting case when considering radiating shockwaves in the low solar corona is the perpendicular (or quasi-perpendicular) MHD shock, in this case the flow speed is parallel to the shock normal, and the magnetic field is perpendicular (or at a high angle) to it i.e., $\hat{v} \parallel \hat{n}$ and $\hat{B} \perp \hat{n}$. As will be shown it is this special case of quasi-perpendicular shocks that lead to efficient shock drift particle acceleration, a necessary precursor to the generation of radio emission at a coronal shockwave.

In the case of fully \perp shocks there is no need for the decomposition of the magnetic and velocity vector fields, meaning the x and y subscripts on 4(a) and 4(b) can be dropped. 4(c) is an obsolete jump condition, likewise for 4(e) since no B_x field exists. We can also rid the $B_x B_y$ terms from the last quotient in the energy conservation 4(d) –replacing it simply with $B^2/2\mu\rho$. 4(f) reduces to a simpler form of $[Bv] = 0$. Such a reduction in the generalized jump conditions allows us to express the upstream and downstream plasma properties in terms of the shock compression ratio $\chi = \frac{\rho_2}{\rho_1}$ as well as the upstream sonic Mach number

2.3 Coronal Shocks and Plasma Emission

$$M_1 = \frac{v_1}{c_1} \quad (\text{Priest \& Forbes, 2000}) \text{ e.g.,}$$

$$\frac{v_2}{v_1} = \frac{1}{\chi} \quad (2.38a)$$

$$\frac{B_2}{B_1} = \chi \quad (2.38b)$$

$$\frac{p_2}{p_1} = \gamma M_1^2 \left(1 - \frac{1}{\chi} \right) - \frac{1 - \chi^2}{\beta_1} \quad (2.38c)$$

where $\beta_1 = 2\mu p/B_1^2$ is the upstream plasma beta parameter. The exact value of the compression ratio may be obtained by using 4(b) to eliminate p from the energy flux equation 4(d) and incorporating 4(a,c,e,f) (and a lot of algebra) a quadratic for χ may be obtained

$$2(2 - \gamma)\chi^2 + [2\beta_1 + (\gamma - 1)\beta_1 M_1^2 + 2]\gamma\chi - \gamma(\gamma + 1)\beta_1 M_1^2 = 0 \quad (2.39)$$

Equation (6) has one positive real root such that

$$1 < \chi < \frac{\gamma + 1}{\gamma - 1} \quad (2.40)$$

Using a polytropic index of $\gamma = 5/3$ (monatomic) means the shock compression can be no more than a factor of 4. Another extremely important fact arising from this is that magnetic compression can also be no greater than 4 i.e., from equation 4(b) $B_2/B_1 = \chi$. $\chi < 4$ has consequences for the shock drift acceleration mechanism and provides an upper limit to the particle energy gain.

2.3.3 Shock Particle Acceleration

The framework of shock particle acceleration for solar type II radio bursts is called the shock drift acceleration (SDA) mechanism (Holman & Pesses, 1983).

2.3 Coronal Shocks and Plasma Emission

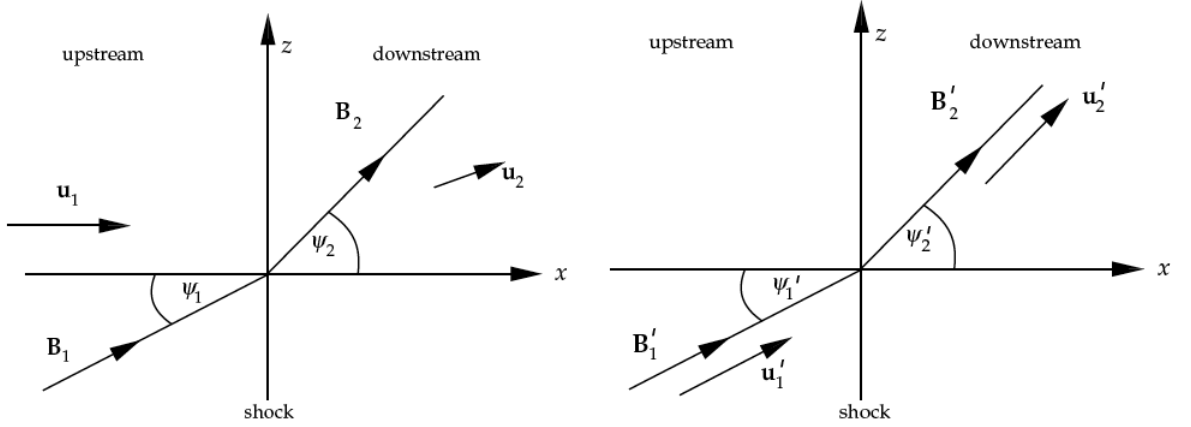


Figure 2.8: (Left) Normal incidence frame (NIF) where the shock is at rest and the upstream plasma approaches the shock head-on at velocity \mathbf{u}_1 . The magnetic field makes some arbitrary angle θ_{Bn} with the shock normal. (Right) Transformation to a de Hoffman-Teller frame ensures that the plasma velocity and magnetic field are in the same direction on both sides of the shock (Ball & Melrose, 2001).

The mechanism involves a gyrating particle encountering the magnetic gradient caused by the shock, resulting in a guide center drift and an energy gain due to the presence of a convective electric field at the shock.

There are two important frames of reference through which SDA is studied. In the rest frame of the shock, known as the ‘normal incidence frame’ (NIF), the upstream plasma has velocity \mathbf{u}_1 along the normal \hat{n} to the shock front. The upstream magnetic field \mathbf{B}_1 creates an angle θ_{Bn} with the shock normal \hat{n} , and the downstream counterparts have values \mathbf{u}_2 and \mathbf{B}_2 , Figure 2.8(left).

Due to the motion of the plasma across the magnetic field, there is a convective electric field given by $\mathbf{E} = \mathbf{v} \times \mathbf{B}$, which causes a drift of the particles with speed $\mathbf{v}_E = \mathbf{E} \times \mathbf{B}/B^2$. The kinematics of the particle in the shock drift acceleration mechanism are best treated in a frame where the convective electric field vanishes such that $\mathbf{E} = |\mathbf{v} \times \mathbf{B}| = v_x B_y - v_y B_x = 0$. The frame where this criterion is fulfilled is known as the de Hoffmann-Teller frame (dHTf) (de Hoffmann &

2.3 Coronal Shocks and Plasma Emission

Teller, 1950) and has a frame velocity with respect to the NIF frame given by.

$$v_{HT} = v_y = u_1 \tan \theta_{Bn} \quad (2.41)$$

This frame guarantees the plasma motion is in the same direction as the magnetic field on both sides of the shock. Given the absence of any electric fields in this frame, the particle motions may be treated as having a conserved magnetic moment (Ball & Melrose, 2001)

$$\mu = \frac{mv_{1\perp}^2}{B_1} = \frac{mv_{2\perp}^2}{B_2} = \text{const} \quad (2.42)$$

where the subscripts [1,2] represent pre an post-encounter shock values respectively. In the dHTf, the conservation of the magnetic moment may be used to derive the particle kinematics given either reflection or transmission though the shock. Rearrangement of equation shows that particles with a pitch angle fulfilling the relationship

$$\alpha > \alpha_c \quad \text{where} \quad \sin^2 \alpha_c = \frac{B_1}{B_2} \quad (2.43)$$

will be reflected at the shock. This pitch angle α_c defines a ‘loss-cone’ in velocity space $f(v_\perp, v_{||})$, whereby any particle within the cone (large $v_{||}$) will be lost downstream, while particles outside the loss cone will be reflected at the shock. This is known as a ‘magnetic mirroring’, a process that shocks are known to exhibit (Feldman *et al.*, 1983). Inside the dHT reference frame, the particles energy (whether reflected or transmitted) is completely conserved and there is no energy gain. Conceptually, the best way to see where the acceleration takes place is in the normal incidence frame (NIF).

2.3 Coronal Shocks and Plasma Emission

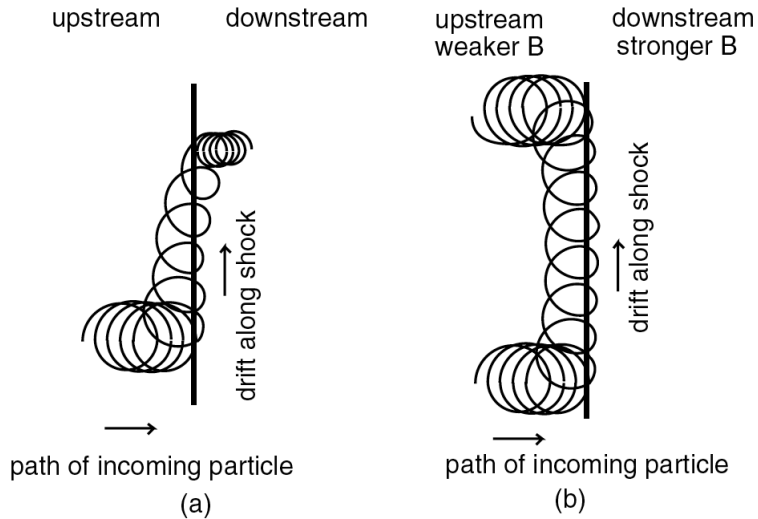


Figure 2.9: Particle drift paths due during both a transmitted (a) and reflected (b) motion. The increased magnetic field in the downstream region caused a drift along the surface. This drift occurs in the presence of a convective electric field (which will have a component parallel to the drift), allowing the field to do work on the particle and hence increase its energy (Ball & Melrose, 2001).

In the NIF, the particles gyrate about the upstream magnetic field \mathbf{B}_1 , while there is a convective electric causes a small drift of magnitude $\mathbf{v}_E = \mathbf{E} \times \mathbf{B}/B^2$ towards the shock. If the particle speed is much greater than the shock speed $v \gg u$, the particle undergoes many Larmor gyrations while in contact with the shock. The difference between the Larmor radius of the orbit ahead of and behind the shock front (due to the increased downstream magnetic field) will cause the particle to drift parallel to the shock surface (Ball & Melrose, 2001; Toptygin, 1980), Figure 2.9. This is equivalent to a ‘grad-B’ drift in an inhomogeneous magnetic field. This drift allows a charged particle to move parallel to the convective electric field, allowing the E-field to do positive work on the particle and produce an energy increase. Overall, a grad-B drift at the shock surface gives the particle a component of velocity that may interact with the convective electric field, hence the process is known as ‘drift-acceleration’.

2.3 Coronal Shocks and Plasma Emission

While the energy gain is most apparent in the NIF frame, particle reflection and transmission is best handled mathematically in the dHT frame. Hence firstly, the magnetic mirroring process is described in dHT, while the post-encounter speed and energy gain are then obtained by converting back to the rest frame of the upstream plasma (NIF). Reference has shown that the particle energy gain upon reflection from the shock is given by

$$\frac{E_r}{E_i} = \frac{1 + \sqrt{1 - B_1/B_2}}{1 - \sqrt{1 - B_1/B_2}} \quad (2.44)$$

The energy gain is limited to the magnetic field strength jump across the shock, and since this field strength is limited by equation 2.40, the energy gain is limited to a factor of 13.93 (Ball & Melrose, 2001). A similar treatment may also give the reflected velocity in terms of the incident velocity (Holman & Pesses, 1983)

$$v_{||}^r = 2u_1 \sec\theta_1 - v_{||}^i \quad (2.45)$$

shock drift acceleration has been used to explain the presence of 1 – 100 keV electron at Earth’s magnetospheric bow shock (Wu, 1984), in the context of radio bursts have used it to explain the acceleration of electrons during type II and herringbone bursts (Holman & Pesses, 1983; Mann & Klassen, 2005; Schmidt & Cairns, 2012b) More sophisticated models involve multiple reflections at the shock that increase the energy gain each time, thereby producing energies that are observed in the vicinity of shocks. This multiple reflection process plays an important role in some theoretical treatments of herringbone emission; we will return to this point in Chapter 5.

2.3.4 Wave-Particle Interaction

The growth of collective oscillations in a plasma in response to the presence of some distribution of particles $f(\mathbf{r}, \mathbf{v}, t)$ in phase space is treated most simply with ‘quasi-linear theory’ (Vedenov, 1963). This is essentially a perturbation theory using the Vlasov and Maxwell’s equations and successfully described the growth of plasma oscillations in the presence of electron beams. In order to see how a particle distribution function effects wave growth we start with an equilibrium distribution f_0 and impose a perturbation $f_1(\mathbf{r}, \mathbf{v}, t)$, so that the total distribution function is $f(\mathbf{r}, \mathbf{v}, t) = f_0 + f_1(\mathbf{r}, \mathbf{v}, t)$, with $f_1 \ll f_0$. The perturbation quantities will take the form $e^{i(\omega t + \mathbf{k} \cdot \mathbf{r})}$ i.e., perturbation quantities that are periodic in space and time with wave number \mathbf{k} and angular frequency ω .

To see how $f(\mathbf{r}, \mathbf{v}, t)$ evolves in time we insert it into the Vlasov equation and linearize, ignoring any terms higher than second order

$$\frac{\partial f_1}{\partial t} + (\mathbf{v} \cdot \nabla) f_1 + \frac{q_e}{m_e} (\mathbf{E} + \mathbf{v} \times \mathbf{B}) \cdot \nabla_v f_0 = 0 \quad (2.46)$$

Replacing the time and space derivatives with their oscillatory operators ($\partial/\partial t \rightarrow -i\omega$, $\nabla \rightarrow i\mathbf{k}$), the perturbed Vlasov equation may be rearranged to give

$$f_1 = \frac{q_e}{m_e} \frac{j}{\omega - \mathbf{k} \cdot \mathbf{v}} \mathbf{E} \cdot \nabla_v f_0 \quad (2.47)$$

This equation relates the perturbed quantity f_1 to the unperturbed distribution function and the electric field. The most important aspect of this equation is the $\omega - \mathbf{k} \cdot \mathbf{v}$ term in the denominator, implying the possibility of resonance between waves of phase speed ω/\mathbf{k} and particles of speed v . Now, integrating both sides

2.3 Coronal Shocks and Plasma Emission

of 2.47 over all velocity space and again using Maxwell-1 results in

$$1 + \frac{4\pi q_e}{m_e} \frac{1}{k^2} \mathbf{k} \cdot \int_v \frac{\nabla_v f_0}{\omega - \mathbf{k} \cdot \mathbf{v}} d^3 v = 0 \quad (2.48)$$

Any electrostatic normal mode oscillations satisfy this relationship and integrating over all velocity space will result in a dispersion relation for the oscillations of the plasma property f_1 . The equation effectively gives the oscillatory response $\omega = g(\mathbf{k})$ of the perturbation f_1 of the plasma, given a particular velocity distribution function f_0 .

The integral over velocity space in this case can be performed because the delta function guarantees that there is no velocity with the property of $v = \frac{\omega}{\mathbf{k}}$. If this were to be fulfilled, there is the possibility of resonances equation 2.48 i.e., there is a singularity in the integral, requiring a non-trivial as $v \rightarrow \frac{\omega}{\mathbf{k}}$. The solution requires integration is performed in complex space using a method called contour integration (Melrose, 1989). The use of contour integration means there will be complex solutions of the dispersion relation of the form $\omega = \omega_r + i\gamma$. The complex $i\gamma$ means that a time dependency of the periodic solutions to the perturbations f_1 will be

$$e^{j\omega t} = e^{(i[\omega_r + i\gamma])} = e^{i\omega_r t} e^{-\gamma t} \quad (2.49)$$

This solution is a damped wave with damping factor γ , meaning the solution to equation 2.48 in the region $v \sim \omega/k$ provides a wave decay term. These are the essential elements of Landau damping e.g., if the phase speed of the waves in a plasma match the speed of electrons in the distribution function then those waves will experience a damping.

Quasi-linear theory uses Equation 2.47 and Maxwell's first equation to show

2.3 Coronal Shocks and Plasma Emission

that the time evolution of the wave energy density in the electrostatic waves is

$$\frac{\partial W(k, t)}{\partial t} = -\gamma W(k, t), \quad \gamma = -\frac{\pi}{n} \frac{\omega^3}{k^2} \frac{\partial f(v, t)}{\partial v} \quad (2.50)$$

where $W(k, t)$ is the spectral energy density of the electrostatic waves and γ is the wave growth term (Vedenov, 1963). Simultaneously, the distribution function is evolves according to

$$\frac{\partial f(v, t)}{\partial t} = \frac{\partial}{\partial v} \left(D \frac{\partial f(v, t)}{\partial v} \right), \quad D = \frac{4\pi e^2}{m_e^2} \frac{W(k, t)}{v} \quad (2.51)$$

with D being a diffusion coefficient. Equations 2.50–2.51 are the closed set of quasi-linear theory equations describing the interaction of electrostatic waves with energy spectrum W and particle distribution function f (Kontar, 2001; Vedenov, 1963). The wave growth term γ has an important dependence on the velocity space gradient. From Equations 2.50, $\partial f / \partial v > 0$ will result in $\gamma < 0$ and a wave growth term that increases exponentially; this can also be seen Equation 2.49. Effectively, a group of electrons is promoted to a velocity range that closely matches the phase speed of some type of waves in a medium $v \sim \omega/k$. In such a speed range the integrand of Equation 2.48 approaches the point at which there is a singularity in the solution. Such a point necessitates a complex solution to the integral, thus providing an imaginary part to the dispersion relation that gives an $e^{-\gamma t}$ term. If the promotion of electrons to a range $v \sim \omega/k$ is combined with a positive gradient of the distribution function in this velocity range, it results in $\gamma < 0$ and $e^{-\gamma t} > 0$, leading to wave growth. This is why $v - \omega/k = 0$ is known as the resonance condition (Melrose, 1989). The exchange of energy between the wave spectral energy distribution and the particle distribution is described by 2.50–2.51.

2.3 Coronal Shocks and Plasma Emission

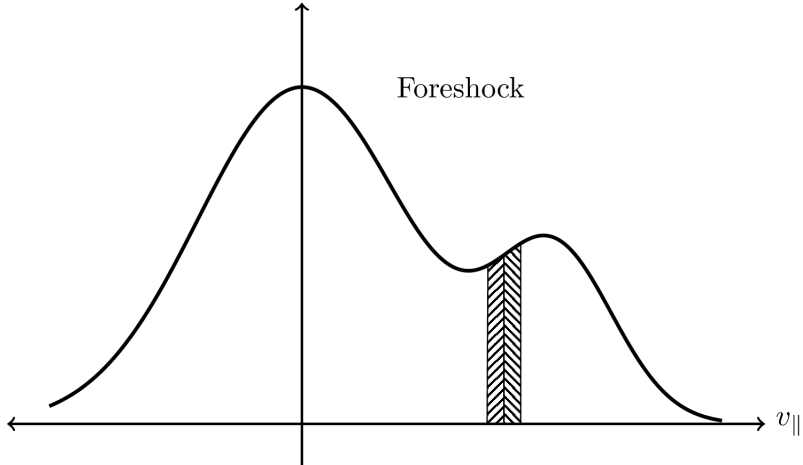


Figure 2.10: Maxwell-Boltzmann velocity distribution with a Gaussian ‘bump-on-tail’ representing the beam. The shaded region are those electrons that will produce a bump-on-tail instability due to the presence of a positive slope in the distribution function.

For type II and III radio bursts, quasi-linear theory is usually applied to the interaction of electron beams and Langmuir waves. This group of electrons in the beam is called a bump-on-tail, since it is described by a Gaussian bump on the high velocity tail of a Maxwell-Boltzmann velocity distribution function (Figure 2.10). The growth of Langmuir waves in a resonant response to this beam is called the bump-on-tail instability. Once these Langmuir waves are generated they may undergo decay or coalescence with other waves to produce electromagnetic radiation.

2.3.5 Three-Wave Interaction and Plasma Emission

Once the Langmuir waves are produced from the bump-on-tail instability a number of wave interaction processes occur in order to bring about plasma emission. This involves the interaction of various wave modes in the plasma described by a mathematical formalism called the three-wave interaction (Robinson *et al.*, 1993, 1994). In this process three wave modes in a plasma M, P, and Q are described

2.3 Coronal Shocks and Plasma Emission

by their distribution functions in a wave-number space (k -space). the distribution functions are given by $N_M(k_M)$, $N_P(k_P)$, $N_Q(k_Q)$, where the N describe the occupation number of wave quanta between k and $k + dk$ in the wave-number space. Waves in P and Q mode may interact to such that wave quanta are removed from the P and Q k-space and added to the M k-space. This is essentially an emission of an energy packet from the P and Q -space to the M k-space. The rate of change of occupation numbers in the three k-spaces are given by

$$\frac{dN_M(\mathbf{k}_M)}{dt} = - \int \frac{d^3\mathbf{k}_P}{(2\pi)^3} \int \frac{d^3\mathbf{k}_Q}{(2\pi)^3} g(\mathbf{k}_M, \mathbf{k}_P, \mathbf{k}_Q) \quad (2.52)$$

$$\frac{dN_P(\mathbf{k}_P)}{dt} = - \int \frac{d^3\mathbf{k}_M}{(2\pi)^3} \int \frac{d^3\mathbf{k}_Q}{(2\pi)^3} g(\mathbf{k}_M, \mathbf{k}_P, \mathbf{k}_Q) \quad (2.53)$$

$$\frac{dN_Q(\mathbf{k}_Q)}{dt} = - \int \frac{d^3\mathbf{k}_M}{(2\pi)^3} \int \frac{d^3\mathbf{k}_P}{(2\pi)^3} g(\mathbf{k}_M, \mathbf{k}_P, \mathbf{k}_Q) \quad (2.54)$$

where $g(\mathbf{k}_M, \mathbf{k}_P, \mathbf{k}_Q)$ is an expression that incorporates a transition probability for wave quanta into and out of energy states in the various k-spaces (Robinson *et al.*, 1994). The transition probability of waves amongst states M, P and Q is given by (Melrose, 1986)

$$u_{MPQ}(\mathbf{k}_M, \mathbf{k}_P, \mathbf{k}_Q) \propto \delta(\omega_M - \omega_P - \omega_Q) \delta^3(\mathbf{k}_M - \mathbf{k}_P - \mathbf{k}_Q) \quad (2.55)$$

where the ω are the frequency of the corresponding wave and and δ are delta functions. This is analogous to transition probabilities given by the Einstein coefficients for transferring energy packets from and atomic state to a photon state (photon emission) i.e., whereas the Einstein coefficients are used in atom-wave (atom-photon) energy exchanges, u_{MPQ} describes wave-wave energy exchanges. Given the presence of delta functions in the transition probability expression, we can see that an exchange of energy quanta amongst the wave modes can only

2.3 Coronal Shocks and Plasma Emission

occur when $\omega_M = \omega_P + \omega_Q$ and $\mathbf{k}_M = \mathbf{k}_P + \mathbf{k}_Q$.

The production of plasma emission requires a three wave interaction amongst a Langmuir wave L , ion acoustic wave S , and electromagnetic wave T . Fundamental and harmonic emission occur via

$$L \rightarrow T + S \quad (2.56)$$

$$L + L' \rightarrow T' \quad (2.57)$$

Fundamental results from the decay of a Langmuir wave to an EM wave and ion acoustic wave. Second harmonic is the product of two Langmuir waves propagating in the opposite directions. The decay and coalescence processes may only occur when

$$\omega_T = \omega_L + \omega_S \quad (2.58)$$

$$\omega_{T'} = \omega_L + \omega_{L'} \quad (2.59)$$

where L' represents a product Langmuir wave and T' represents a second harmonic EM wave. The relevant dispersion relations are

$$\omega_L = \omega_p + \frac{3v_{th}^2}{2\omega_p} k_L^2 \quad (2.60)$$

$$\omega_T = (\omega_p^2 + k_T^2 c^2)^{1/2} \quad (2.61)$$

$$\omega_S = k_s \sqrt{\frac{\gamma k_B T_e}{m_i}} \quad (2.62)$$

where

$$\omega_p = \left(\frac{n_e e^2}{m_e \epsilon_0} \right)^{\frac{1}{2}} \quad (2.63)$$

The Langmuir wave has a frequency very close to the plasma frequency, while the

2.3 Coronal Shocks and Plasma Emission

ion acoustic frequency will be much smaller than this (due to the larger ion mass in the Equation 2.62). Therefore, Equations 2.58 and 2.59 result in $\omega_T \approx \omega_p$ and $\omega_T \approx 2\omega_p$ i.e., radiobursts often occur at the plasma frequency and its harmonic. Much of the theory is confirmed by in-situ observations have provided insight into the generation of ion acoustic waves from the electrostatic decay of Langmuir waves, followed by the production of radio emissions (Thejappa & MacDowall, 1998). However, in the low corona the beam generation of Langmuir waves, ion acoustic waves, and ultimately radio emission is still a subject of research (Kontar, 2001; Ratcliffe *et al.*, 2012; Reid & Kontar, 2010)

In order to investigate the amount of energy emitted by the electromagnetic wave, elements of the three wave interaction theory need to be combined with what is known as stochastic growth theory (Robinson & Cairns, 1993)(SGT). SGT described a beam propagating in an inhomogeneous medium whereby it encounters pockets of localised density enhancement where it is unstable only intermittently, this is to prevent the beam losing all of its energy too quickly (Ginzburg & Zhelezniakov, 1958; Sturrock, 1964). As the beam propagates through this localised clump, it is unstable to the growth of Langmuir wave, giving up some of its energy to the wave, diminishing the beam slightly. Once it exits the clump it becomes stable again, allowing the beam to reform until it reaches another localised clump to give up some energy again. The Langmuir waves would then experience a growth at intermittent regions in space and time (which is actually observed (Lin *et al.*, 1986)), while the beam would be unstable for only small fractions of its lifetime. Overall, the beam energy loss is on average low enough to allow its continued propagation, but instantaneous and finite enough to allow the growth of waves. From SGT and the three-wave process, the volume emissivity

2.3 Coronal Shocks and Plasma Emission

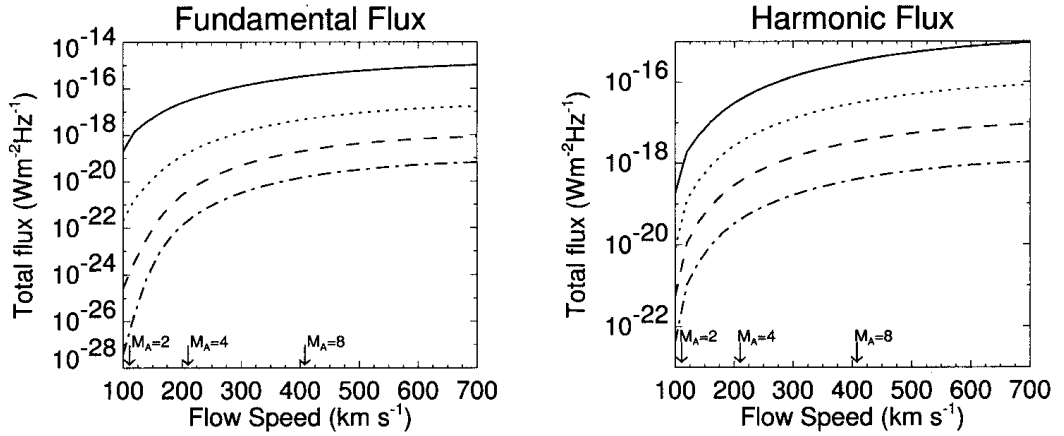


Figure 2.11: Theoretical flux of the fundamental and harmonic emission bands of a type II radio burst using three wave interaction and stochastic growth theory Cairns *et al.* (2003).

of the emission (Robinson & Cairns, 1993, 1998)

$$j_M(r) \approx \frac{\Phi_M}{\Delta\Omega_M} \frac{n_b m_e v_b^3}{3l(r)} \frac{\Delta v_b}{v_b} \quad (2.64)$$

here the M stands for either fundamental F or harmonic H emission. $\Delta\Omega_M$ is the solid angle over which the emission is spread, n_b is the electron beam number density, v_b is the beam speed, $l(r)$ is the distance from emission point to observer, Δv_b is the width of the beam in velocity space. Φ_M are known as the conversion efficiencies and are different for fundamental and harmonic emission, see Appendix A.1.

These expressions have been used to simulate radio burst flux resulting in $\sim 10^{-17} \text{ W m}^{-2} \text{ Hz}^{-1}$, which have been compared to type II and III radio bursts (Knock *et al.*, 2001; Schmidt & Cairns, 2012a). Knock *et al.* (2003) and Cairns *et al.* (2003) used the theory to predict interplanetary type II burst flux as a function of a variety of shock parameters e.g., shocks speed Fig. 2.11.

The theory outlined in section 2.3.2 – 2.3.5 was employed in a model developed by Schmidt & Cairns (2012b), completely describing the generation of radio

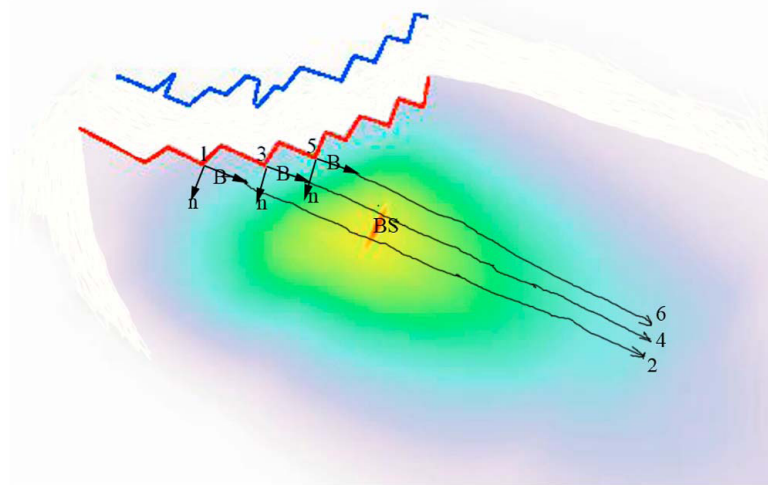


Figure 2.12: Model of the radio emission driven by electron beams on the flank of a CME. Each arrow marks the trajectory of the electron beams accelerated at the rippled shock surface. The red and blue lines outline the shock ramp. The green-red colours show radio emission intensity.

bursts from CME driven shocks. It involves the eruption of a flux rope into a background corona, the driving of a shock as described by the MHD Rankine-Hugoniot relations, the generation of electron beams via SDA, the growth of the bump-on-tail instability, and the generation of electromagnetic emission via the three-wave process and stochastic growth theory. The model finds that that radio emission is generated on the expanding flanks of a CME. The model also shows that when the shock is rippled, there will be spatially intermittent regions of electron beam generation, which could be possible explanation of herringbone emission (Figure 2.12).

2.3.6 Frequency Drift of Radio Bursts

In the previous section it was shown that when plasma emission is excited in the corona, the frequency of emission is close to the plasma oscillation frequency given by equation 2.63 As the exciter of the plasma emission moves to greater heights

2.3 Coronal Shocks and Plasma Emission

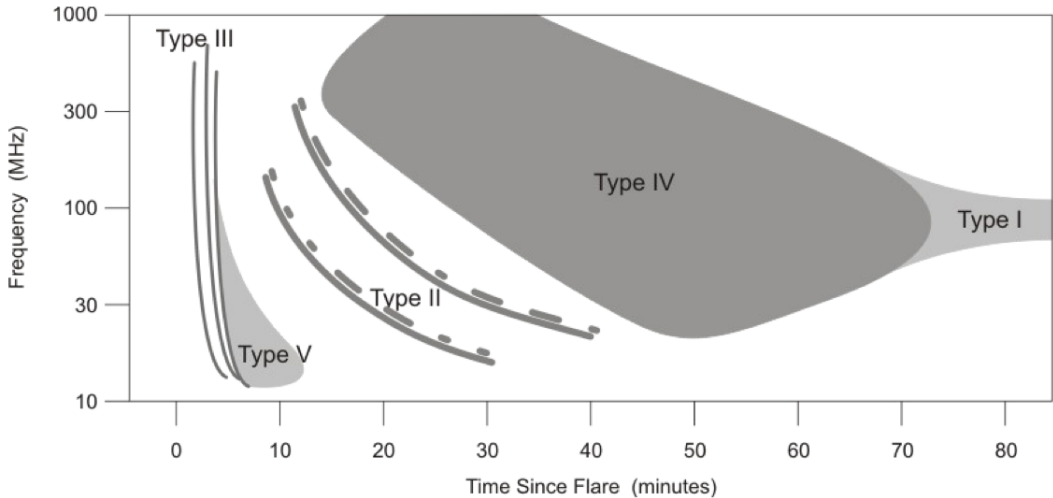


Figure 2.13: The characteristic shapes of various solar radio bursts seen in dynamic spectra. Type II radio burst are a signature of shock transit from high number density into low number density, as indicated by their drift from high to low frequency. The presence of two distinct bands is indicative of radio emission at the plasma frequency (fundamental) and its second harmonic. These two bands may also be further split themselves, a feature known as band-splitting.

in the corona it will produce plasma emission at continually decreasing frequency due to the dropping density. For example a typical signature of a coronal shock wave in dynamic spectra is two narrow emission lanes (at f_{plasma} and $2f_{plasma}$) drifting toward lower frequency as time passes. A type III radio burst is excited by a much faster source, hence its frequency drift is much faster in dynamic spectra. Generally different types of radio burst have different morphologies when viewed in dynamic spectra owing to their movement (or lack of movement) into regions of different density in the corona. A summary of the burst types is given in Figure 2.13

Generally, the frequency drift of the radio burst depends on the velocity of the exciter and the density variation in the corona. It is possible to estimate the speed of the exciter from a set of frequency time values (f_i, t_i). Such a set of values are a direct diagnostic of the number density of the environment of emission versus time e.g., using $f \approx 9000\sqrt{n_e}$, frequency versus time gives number density versus

2.3 Coronal Shocks and Plasma Emission

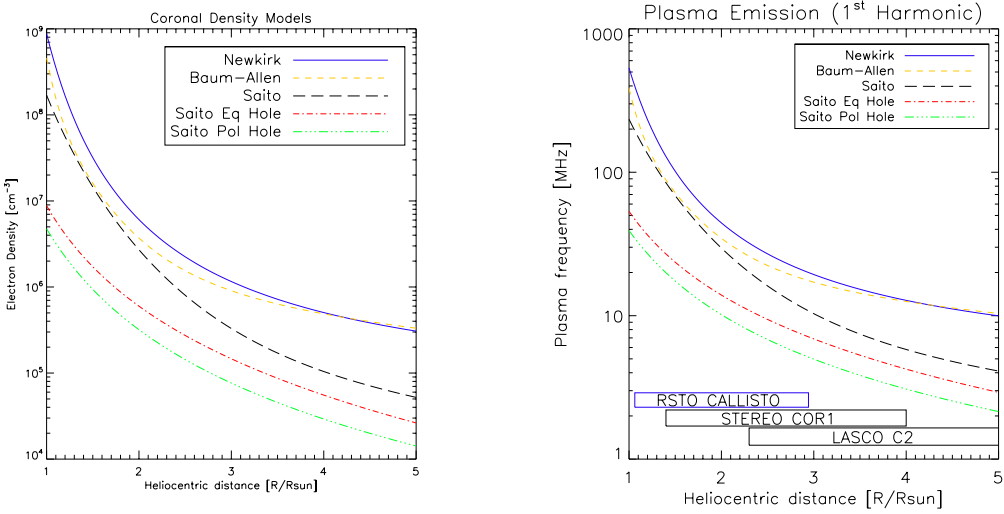


Figure 2.14: (Left) Electron number density as a function of height as defined by each of the models listed. The Newkirk, Baumbach Allen, and Saito models each describe an equatorial quiet corona electron density profile. The Saito Eq Hole and Pol Hol describe equatorial and polar hole profiles, respectively. These models are generally used to specify the height of a radio burst in the corona, and the choice of model is often arbitrary. (Right) The first harmonic of the plasma frequency as a function of height defined by the models.

time, $(f_i, t_i) \rightarrow (n_i, t_i)$. Now, in general the number density of the corona is inversely proportional to height, varying according to some exponential decrease. A very simple model is the hydrostatic case $n(r) = n_0 \exp(-r/H)$ where r is distance from sun center, and H is the scale height given by $H = kT/mg$, where k is Boltzman's constant, T is the coronal temperature, m is proton mass and g is gravity. Generally using this $n(r)$, the set of values (n_i, t_i) can be converted to as set of (r_i, t_i)

$$(f_i, t_i) \rightarrow (n_i, t_i) \rightarrow n(r) \rightarrow (r_i, t_i). \quad (2.65)$$

Hence, by some appropriate choice of coronal density model $n(r)$, a set of frequency and time values may be converted to a set of height vs time values, from which the velocity may be derived. Common practice is to use an $n(r)$ that is derived semi-empirically. For example, there exists a set of models that describe the density fall off with height of the equatorial quiet corona, coronal holes, and active

2.3 Coronal Shocks and Plasma Emission

regions Allen (1947); Newkirk (1961); Saito *et al.* (1977), shown in Figure 2.14. The choice of model affects both the resulting height of the radio emission and the derived speed. A much better diagnostic of radio bursts would be to use actual density measurements of the corona in places of these models, but this is generally not usual practice.

3

Observation and Instrumentation

In this chapter the instruments used to make observations of coronal mass ejections and the signatures of their shocks are outlined. The primary technique for observing CMEs is via white-light observations of the corona. The general corona observing techniques used by coronagraphs are firstly described, followed by specific details of coronagraphs used in this study. This is followed by a description of instrument used to observe CMEs and shocks, including extreme ultraviolet (EUV) instrumentation, and radio imaging and spectroscopy instrumentation. Part of the radio spectroscopy work includes an overview of the Rosse Solar Terrestrial Observatory (RSTO), installed at Birr Castle, Co. Offaly, Ireland in September 2011. The RSTO work was published in Zucca & Carley *et al.* *Solar Physics*, 2012.

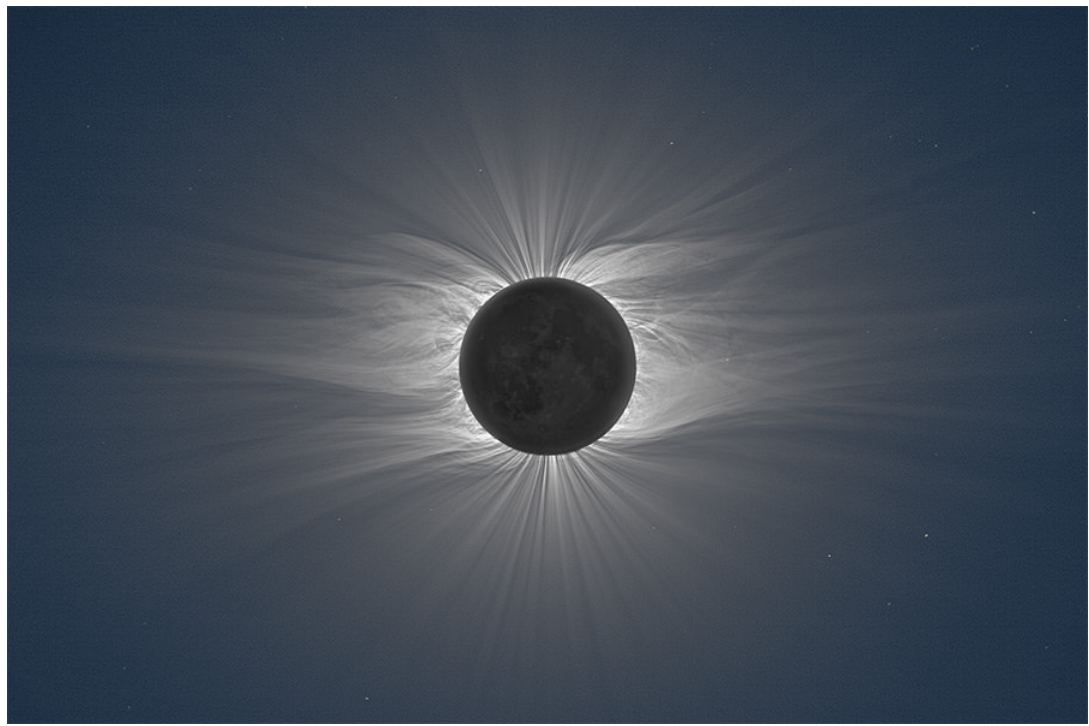


Figure 3.1: The white-light corona during a solar eclipse. Occultation of the bright solar disk by the moon reveals the faint outer atmosphere of the Sun, known as the corona. It is highly structured, showing features such as streamers and plumes. *Eclipse photograph courtesy of Miloslav Druckmüller <http://www.zam.fme.vutbr.cz>*

3.1 White-Light Observations

The first evidence for the existence of the corona was through observations during solar eclipses. The occultation of the solar disk by the moon revealed a visible outer atmosphere structured into streamers and plumes and extending far from the solar surface (Figure 3.1). This is known as the white-light corona and is due to scattering of photospheric light by coronal particles. Of particular interest here is the K-corona (as first introduced in Section 1.1.3.4); this is the corona that is visible because of Thomson scattering of photospheric light by free electrons. As described in Chapter 1, a component of the scattered white-light is the F-

3.1 White-Light Observations

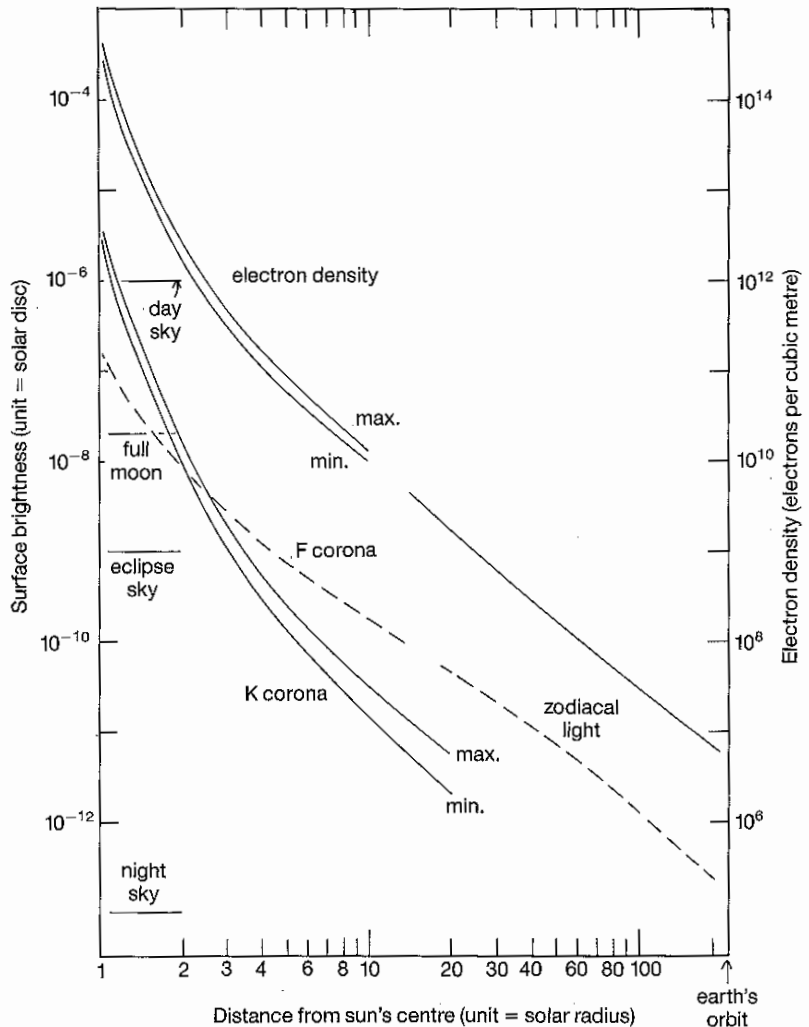


Figure 3.2: The K and F coronal brightness and the number density of electrons as a function of height. Units are in mean solar brightness ($1 \text{ MSB} = 2.01 \times 10^{10} \text{ ergs s}^{-1} \text{ cm}^{-2} \text{ sr}^{-1}$).

corona, which is formed by scattering of light off of dust grains. The F-corona is unpolarized and becomes a significant contributor to the white-light after $\sim 4R_\odot$. Figure 3.2 shows the radial variation of the K and F corona, along with coronal densities. Before the early 20th century the only way to view the corona was for a short period during a solar eclipse when the moon blocks direct photospheric light. Under normal conditions direct sunlight overwhelms the faint corona. In

3.1 White-Light Observations

1939 the French astronomer Bernard Lyot developed a telescope, known as a coronagraph, which allowed observation of the corona at any time (Lyot, 1939). A coronagraph is an optical system that provides an artificial eclipse of direct photospheric light so the much fainter corona can be imaged. a description of Lyot's original design, and the space based instruments based on this design, is given here.

3.1.1 Lyot Coronagraph

A basic schematic of the Lyot coronagraph is given in Figure 3.3. The objective lens O1 forms an image of the solar disk onto to the internal occulting disk D1 (a metal cone), where the light is reflected away from the field lens O2. Lyot's key invention was the Lyot stop (A1) and Lyot spot (D2). The field lens O2 images the aperture A0 and its diffraction pattern onto the Lyot stop. If the Lyot stop were not there, this light would reach the focal plane and contaminate the image. The Lyot spot (D2) blocks spurious light caused by multiple reflections in the field lens O2. It also blocks any light diffracted by the occulter D1. In theory, the only light that is transmitted through the system is that coming from beyond the solar disk. This light is focused onto the image plane F by O3. In practice there may be undesired and excess light that is transmitted through the system and great care is taken to reduce this as much as possible. The Lyot coronagraph is described as internally occulting due to the placement of the occulting disk behind the first objective lens. This is to distinguish it from a externally occulted system in which an extra disk is placed in front of the objective lens. The externally occulted coronagraph prevents photospheric light from entering the optical system in the first place, thus allowing much fainter objects to be imaged. However, the external occulter prevents imaging of the

3.1 White-Light Observations

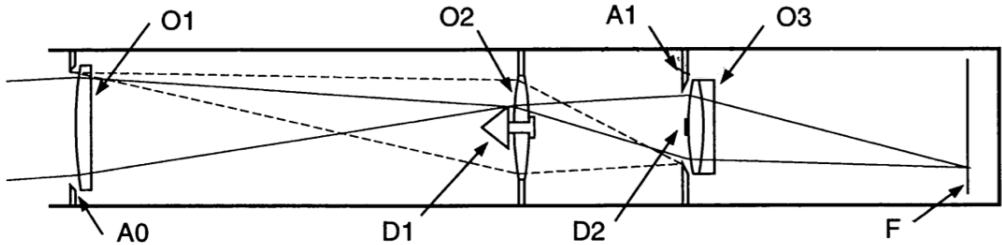


Figure 3.3: A schematic of the basic optical design of the Lyot coronagraph. Lyot's key inventions were the placement of a Lyot stop (A1) and Lyot spot (D2) at the positions where diffracted light would contaminate the image and obscure the faint corona.

very low corona. Hence there is a choice between very low contaminant light levels in the telescope or imaging of the low corona.

All coronagraphs inherit their basic design from Lyot's original, and a number of these are space based instruments providing observation of the corona over many height ranges.

3.1.1.1 SOHO LASCO

The Solar and Heliospheric Observatory (SOHO) is located at Lagrangian point 1 and carries a suite of in-situ and remote sensing instruments, including three coronagraphs collectively known as the Large Angle Spectrometric Coronagraph (LASCO) (Brueckner *et al.*, 1995). LASCO comprises three different coronagraphs, C1, C2, and C3, that were built to observe the corona over heliocentric distance range of $1.1\text{--}30 R_\odot$.

C1 is a reflector version of the internally occulted Lyot coronagraph that images the corona over a distance range of $1.1\text{--}3 R_\odot$. A tunable Fabry-Perot interferometer is placed after the Lyot stop to allow narrow passband images of the solar corona at the lines of Fe xiv, Ca xv, Na i, Fe x, and H α . C1 operates a 1024×1024 CCD with a pixel size of $5.6''$, giving a spatial resolution of $\sim 11''$. The Rayleigh diffraction limited resolution of the telescope is $3.3''$ at 530.3 nm.

3.1 White-Light Observations

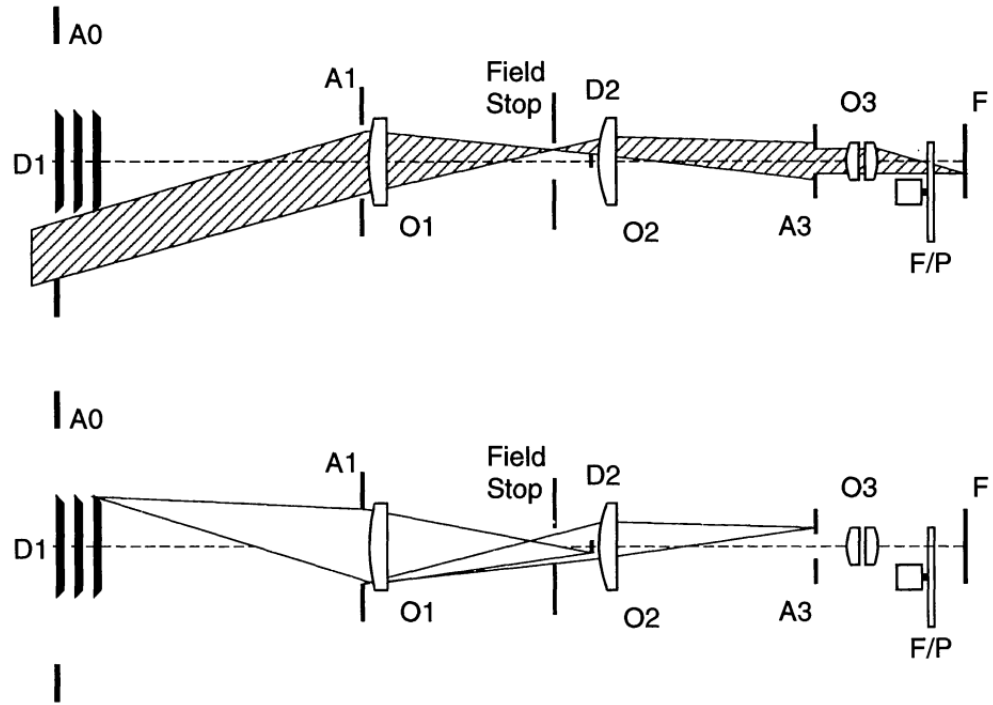


Figure 3.4: Conceptual optical layout of the LASCO C2 coronograph. The top ray-tracing diagram shows the image formation, while the bottom diagram demonstrates the stray light suppression and occultation (Brueckner *et al.*, 1995).

Unfortunately C1 failed in 1997 and is no longer in operation.

C2 is an externally occulted, broadband, refractor coronagraph that images the corona from $1.5\text{--}6 R_{\odot}$ (see footnote¹). The conceptual diagram for its optical layout is shown in Figure 3.4. The front aperture A0 is on the left of the diagram and includes the external occulter D1, consisting of three consecutive circular disks on a common spindle, these disks completely shadow the entrance aperture A1 from direct sunlight. The disks also successively intercept diffracted sunlight from the one before to minimize the total diffracted light from the solar disk falling on the object lens O1. The disks have fine threads on their edges that have been diamond machined, and have a cone opening angle that is slightly

¹The levels of stray-light just beyond the occulter mean that in practice the C2 inner field of view limit is $2.2 R_{\odot}$

3.1 White-Light Observations

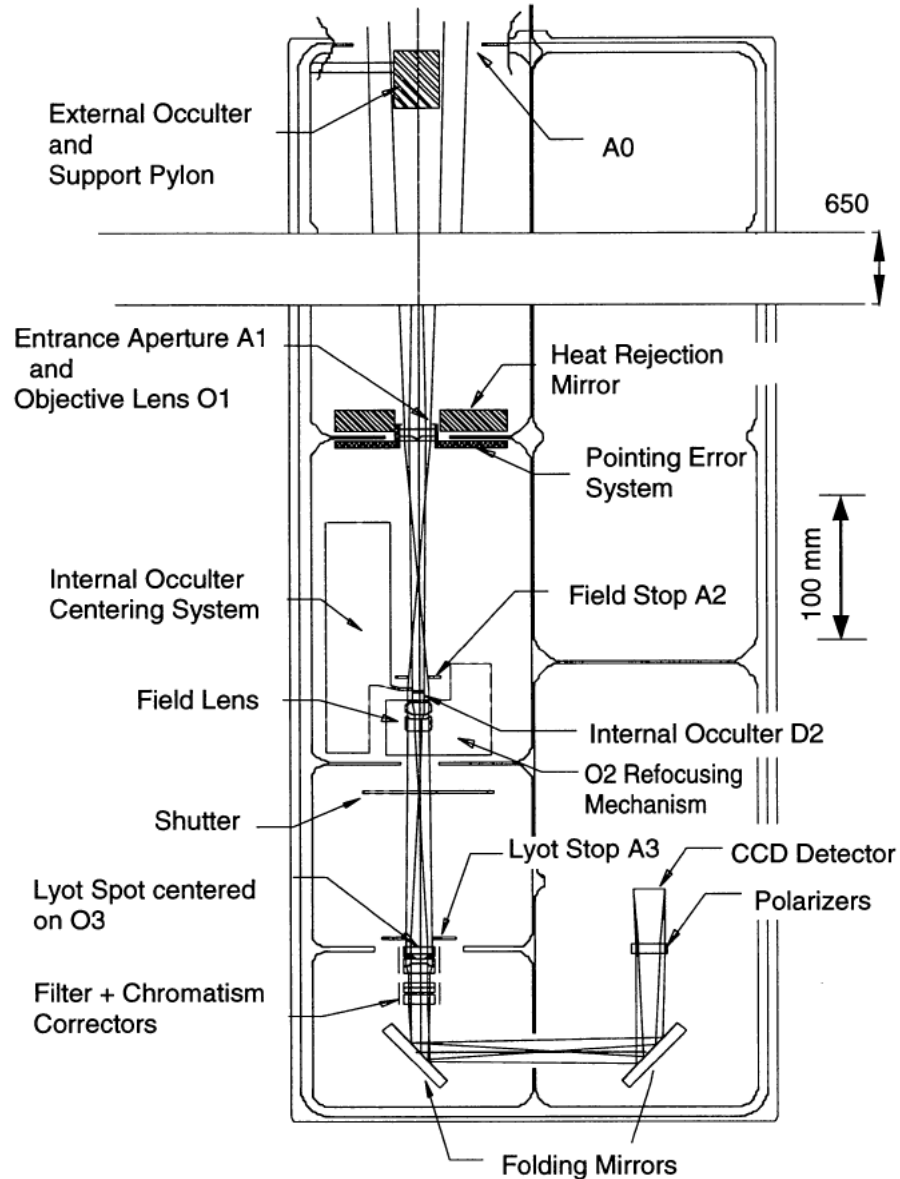


Figure 3.5: A detailed layout of the C2 coronagraph optics and mechanical construct (Brueckner *et al.*, 1995).

bigger than the solar disk at L1 ($32.31'$). This ensures a very high level of light rejection at the external occulter. The objective lens O1 images the corona at the field stop, which sets the outer limit to the field of view of the telescope ($5 R_{\odot}$ for C2). O1 also images D1 onto the D2 internal occulter, which also serves to

3.1 White-Light Observations

intercept any residual stray light diffracted at D1. The lens O2 collimates the coronal image and also images the entrance aperture A1 onto the Lyot stop A3. Finally the lens O3 images the corona onto the focal plane F. The combination of the internal and external occulters, the aperture stops, and a heat rejection mirror at the entrance aperture (Figure 3.5), mean that the the coronagraph has stray light levels that are an order of magnitude improvement over previous space based coronagraphs e.g., stray light levels are typically an order of magnitude or more lower than the coronal brightness, allowing the detection of features in the range of 2×10^{-7} – $15 \times 10^{-10} B_{\odot}$ where B_{\odot} is mean solar brightness (MSB) unit (Brueckner *et al.*, 1995).

The light focused onto the focal plane by the O3 lens first passes through a colour filter and polarizer wheel, which selects the band pass and takes three polarization images at 0° , -60° and $+60^\circ$ such that total or polarized brightness images of the corona may be taken. Mounted at the focal plane is a front-side illuminated 1024×1024 CCD, with 21μ square pixels (equivalent angular size if $11.4''$), operating in a nominal spectral range of 500 – 700 nm, at a temperature of -80° C. CCD readout takes approximately 22 seconds, after which the image may be compressed by a number of algorithms before being sent to the ground station. Among the observing nominal modes are routine flat-field exposures and dark current exposures to be used in calibration. At current operations the C2 coronagraph offers a total brightness image of the corona every 15 minutes.

Finally, C3 is an externally occulted broadband lens coronagraph that images the corona from 3.7 – $30 R_{\odot}$, with a pixel size of $5.6'$ and brightness range of 3×10^{-9} – 1×10^{-11} . It has the same optical design as C2 (Figure 3.4).

The C1, C2 and C3 coronagraph data is processed on-board using a number of steps that may compress the data before transmission to an Earth ground station.

3.1 White-Light Observations

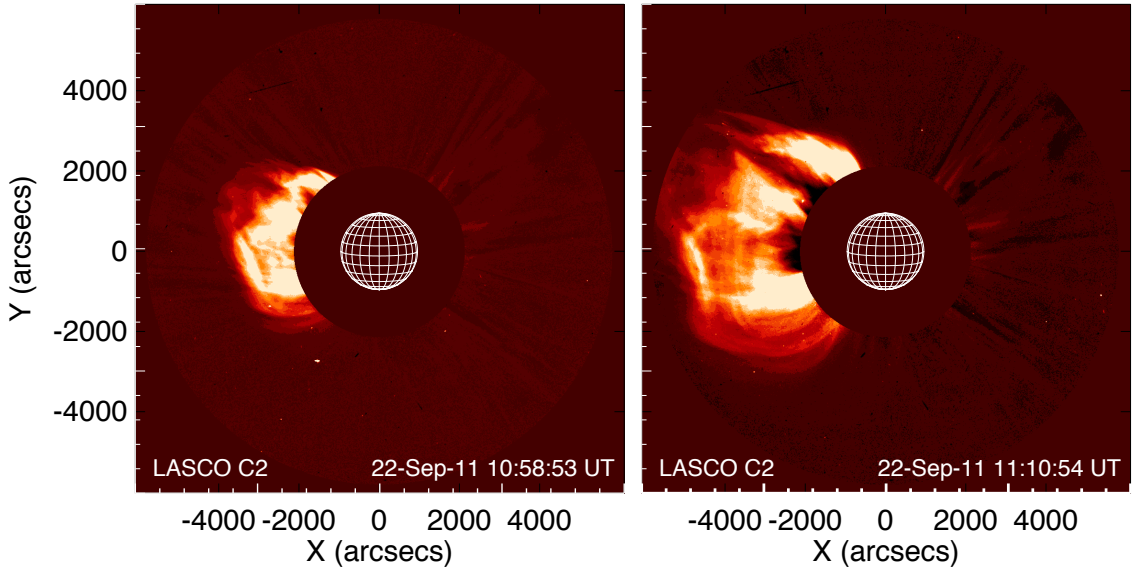


Figure 3.6: LASCO C2 Observations of a CME occurring on 22 September 2011. The central disk is from the occulter. A heliographic grid is over-layed to show the size of the sun.

Each telescope feeds its compressed data to the same telemetry buffer which can store up to 2 Mb. The LASCO telemetry rate is 4.2 kbs^{-1} and communication with the ground is via the Deep Space Network (DPS). The SOHO spacecraft is usually in contact with the DPS for approximately 2 hours per day. Data captured by the DPS is then transmitted to servers at NASA’s Goddard Space Flight Centre (GSFC) and the Naval Research Laboratory (NRL). Only the C2 coronagraph is used in this thesis, and some sample level-2 data for C2 is shown in Figure 3.6

3.1.1.2 STEREO COR1 and COR2

The *Solar Terrestrial Relations Observatory* (STEREO; Kaiser *et al.*, 2008) Ahead and Behind are two nearly identical spacecraft traveling ahead and behind Earth in its orbit. Each spacecraft is receding from Earth at a rate of $\pm 22^\circ$ per year, such that they are effectively traveling around the Sun in opposite directions.

3.1 White-Light Observations

For the spacecraft locations at three different times see Figure 3.7. They carry an identical set of instruments known as the Sun Earth Coronal Connection and Heliospheric Investigation (SECCHI) suite, including in situ detectors and a variety of imagers. On each spacecraft there are two coronagraphs, COR1 and COR2 (Howard *et al.*, 2008). The Ahead COR1 and COR2 combined with Behind COR1 and COR2 offer a stereoscopic view of the corona and any transient event taking place, such as a CME.

COR1 is an internally occulted Lyot refractive coronagraph (Figure 3.8) and derives its basic design from Figure 3.3. It images the inner corona with a field of view from $1.4\text{--}4.5 R_{\odot}$, centered on the H α line at 656 nm with a 22.5 nm wide passband. It has an internal polarizer located after the first doublet lens in the optical system (Figure 3.8) and takes three images at 0° , $\pm 60^{\circ}$, so that polarized or total brightness images of the inner corona may be produced. Stray light levels of both COR1 A and B lie between $0.1\text{--}1 \times 10^{-6} B_{\odot}$, and some defects in the field lens can cause ring shaped features with $1.4 \times 10^{-6} B_{\odot}$ (Howard *et al.*, 2008). The focal plane of the instrument has a 1024×1024 pixel CCD, with a platescale of $3.75''$ per pixel (Thompson & Reginald, 2008). To improve the signal to noise, a 2×2 pixel binning may be performed. A typical observing sequence will perform three 1 second exposures (one for each polarization state at 0° , -60° , and $+60^{\circ}$), in total taking 11 seconds. Typical CCD read-out times result in an image sequence cadence of 8 minutes (time between a three image set and the next three image set).

COR2 is an externally occulted Lyot coronagraph and derives much of its design from the LASCO C2 and C3 coronagraphs. Externally occulted coronagraphs have an extra occulting disk in front of the objective lens, see Figure 3.9 or Figure 3.4. As described, a downside to this design is that the external occul-

3.1 White-Light Observations

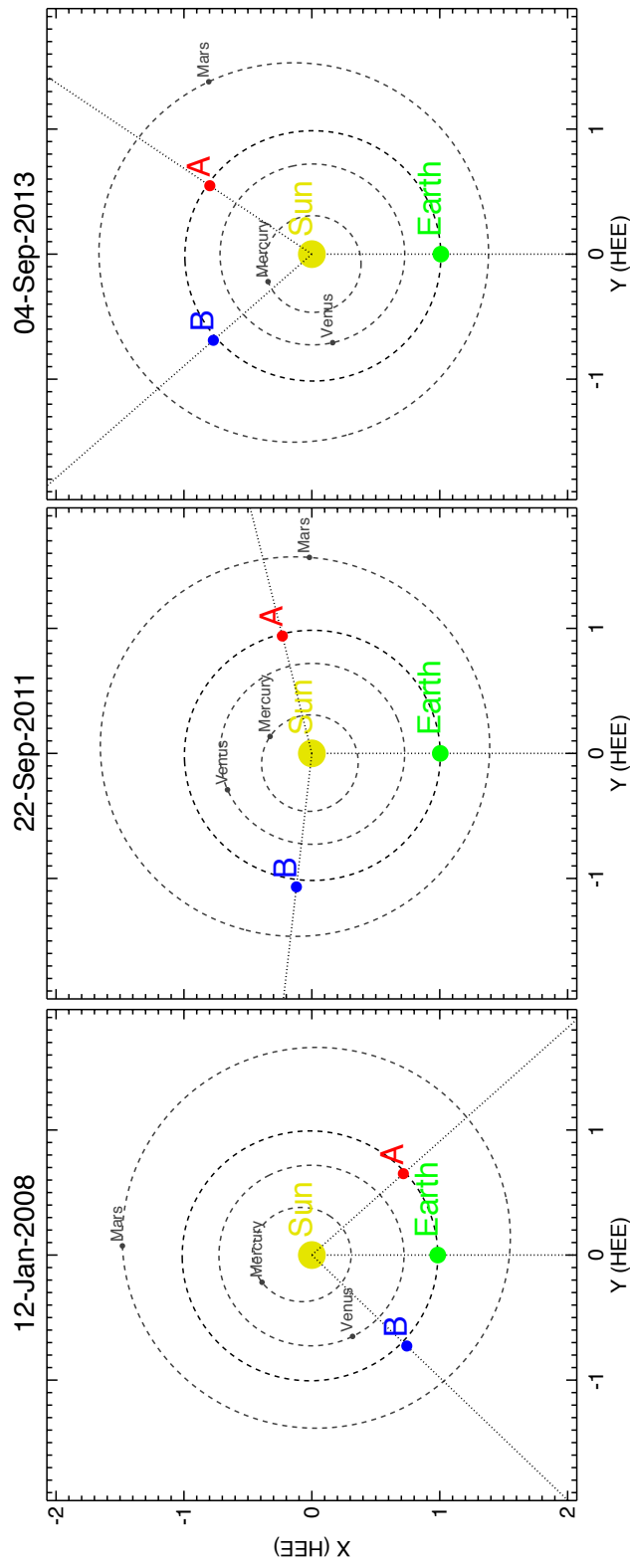


Figure 3.7: The STEREO A and B spacecraft positions with respect to Sun, Earth and inner planets on 12 January 2008, 22 September 2011 and 04 September 2013

3.1 White-Light Observations

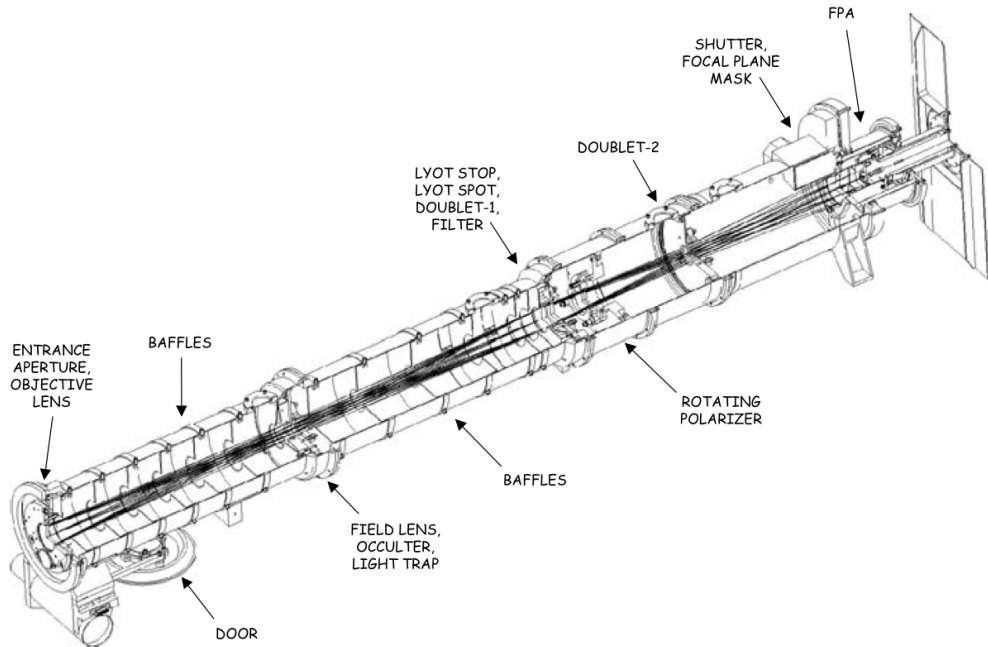


Figure 3.8: A schematic of the basic optical design of the COR1 coronagraph. There are two such identical instruments, one on the Ahead and one on the Behind spacecraft. It is the same basic design as the Lyot coronagraph with the addition of baffles to prevent scattered light and a polarizer behind the Lyot stop (Thompson & Reginald, 2008).

ter does not allow the inner corona to be imaged, hence such coronagraphs are usually used to observe the extended corona to larger heights. The COR2 inner edge field of view limit is defined by the external occulter, while the outer edge is determined by the field stop, resulting in a field of view from $2.5\text{--}15 R_{\odot}$. The filter used in the assembly has a bandpass of 650–750 nm at FWHM. The focal plane contains a back-lit CCD that nominally produces 2048×2048 images, with 14.7" per pixel. Like COR1 it has an internal polarizer producing three linearly polarized images per observing sequence (30 minutes).

These white light imagers of the corona allow for a stereoscopic view of CMEs in a total field of view covering $1.4\text{--}15 R_{\odot}$. The two viewpoint capabilities of these telescopes offer a more accurate observational estimation of both CME

3.1 White-Light Observations

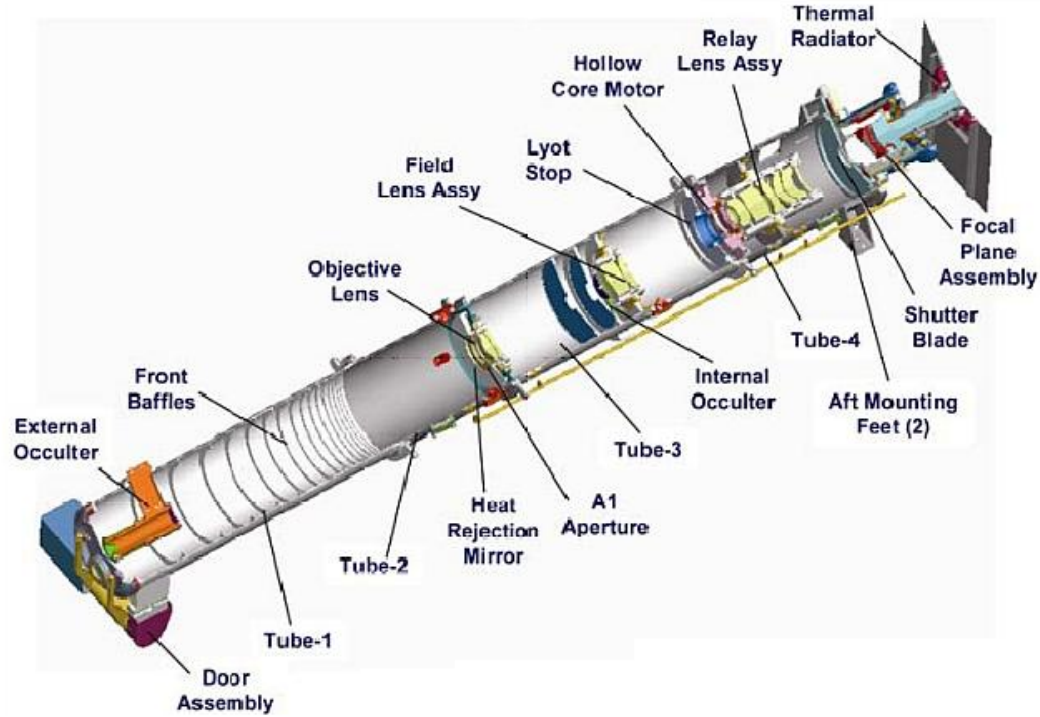


Figure 3.9: A schematic of the basic optical design of the COR2 coronagraph. This is an externally occulted coronagraph, meaning it has an extra occultation disk in front of the objective lens. This results in less internally scattered light, but also results in an obscuration of the inner corona. As with COR1, there are two such identical instruments, one on the Ahead and one on the Behind spacecraft (Howard *et al.*, 2008).

kinematics and CME mass, resulting in a better understanding of CME dynamics.

A sample observation using COR1 and COR2 from the Ahead spacecraft is shown in Figure 3.10

3.1.1.3 Whilte-light Image Data Reduction

All coronagraph images, including those produced by COR1, COR2, and the LASCO coronagraphs, have a number of basic image processing steps in common. The amount by which the data has been processed is described in terms of ‘levels’, with the most basic raw data product of the telescope being level-0. Level-0 usually comprises the compressed data that comes directly from the spacecraft

3.1 White-Light Observations

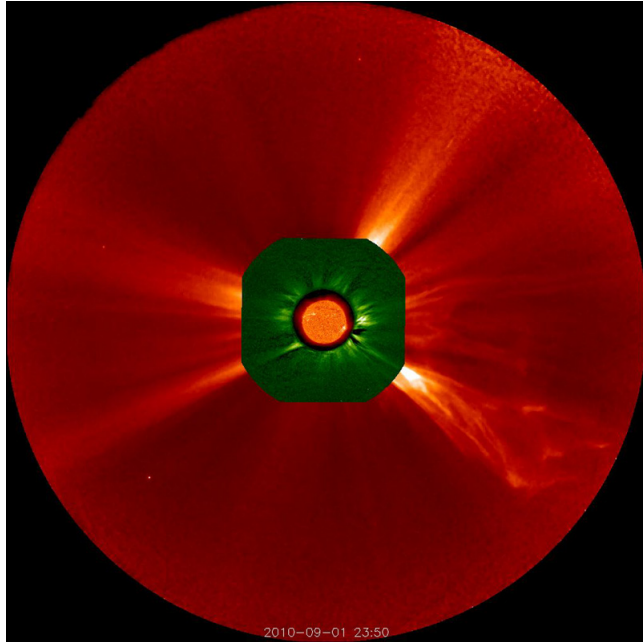


Figure 3.10: Observation of the corona from the COR1 (green), and COR2 (red) coronagraphs on board the STEREO Ahead spacecraft, 01 Sep 2009 23:50 UT. An Extreme Ultraviolet Imaging (EUVI) 304 Å image of the sun is shown at the center. A CME was observed, erupting to the south-west. *Image Courtesy of Alex Young, <http://www.thesuntoday.org/>.*

telemetry stream via the DPS. The data is processed from level-0 to level-0.5 by decompressing the spacecraft data and re-packaged into flexible image transport system (FITS) files, which is an open standard format for all astronomical images.

Calibration of the data into a scientifically usable format results in level-1 data. The steps to produce level-1 data are as follows:

- Darks current image subtraction. Each CCD will carry some level of residual voltage even when the camera shutter is closed. This residual voltage is due to the thermal energy of the electrons in each well of the CCD. The voltage (thermal energy) must be removed from the image since it is not due to light from an observed source. The ‘dark image’ is taken with the camera shutter closed and an exposure performed as normal (exposure time the same as the raw image). The dark image is simply subtracted from the raw

3.1 White-Light Observations

image

- Bias image subtraction. Similar to dark current the CCD will have some charge due systematic defects. These are usually exposed by taking an image with the shutter closed and for the shortest possible exposure times. The bias image is also subtracted from the raw image.
- Flat field correction. Every CCD will have a non-uniform response across its photon collecting area. One side of the CCD, or any arbitrary grouping of pixels, may naturally be more sensitive than the other pixels. As well as this, the optical system itself may produce some brightness variation across the focal plane. To account for this, the raw image must be divided by a ‘flat-field’ in order to normalize the spatially non-uniform response detected by the CCD. The ‘flat-field’ is an image taken of a uniformly illuminated surface. For space based telescopes this uniformly illuminated image is usually taken by closing the telescope front aperture and lighting a lamp placed near the aperture cover, or the telescope front door may contain a ‘diffuser’ that scatters sun light to provide uniform illumination. The LASCO system uses a quartz filter on the telescope cover that diffuses exterior light, allowing a uniform illumination of the CCD (Brueckner *et al.*, 1995). It is important that the dark current and bias images be subtracted from the flat-field before the raw images (which are also dark and bias image subtracted) is divided by the flat field.

Accounting for dark current, bias, and flat-fielding are the most fundamental of all CCD imaging calibration routines. They can be summarised as

$$I_{cal}(x_i, y_i) = \frac{I_{raw}(x_i, y_i) - I_{dark}(x_i, y_i) - I_{bias}(x_i, y_i)}{|I_{flat}(x_i, y_i) - I_{dark}(x_i, y_i) - I_{bias}(x_i, y_i)|} \quad (3.1)$$

3.1 White-Light Observations

where I are the images, (x_i, y_i) are pixel coordinates, and the $| |$ in the denominator mean that the dark and bias subtracted flat-field is normalized (divided by itself). Other standard techniques beyond the most basic ones include

- Vignetting. All camera imaging systems suffer from vignetting, a reduction in brightness at the edge of the field of view. In coronagraph systems this is particularly important since a vignette can occur at the inner field of view, due to the occulting disk and also due to the pylon supports of the disk. Special vignetting calibration images are performed to account for this effect; they are used to normalise the image in the same way as the flat-field is performed.
- De-warping. The image may suffer some geometric distortions due to a deformity in one of the numerous optical components of the telescope. This may result in the image being warped. Pre-flight experiments completely characterize any optical distortion so that all raw image may be ‘de-warped’
- Brightness calibration. This is the conversion from CCD data numbers per second (DN s^{-1}) to physical measures of intensity e.g., mean solar brightness (MSB) units ($1 \text{ MSB} = 2.01 \times 10^{10} \text{ ergs s}^{-1} \text{ cm}^{-2} \text{ sr}^{-1}$). The conversion factors may be calculated in a pre-flight lab, or during inflight via observations of objects with known intensities. Mercury, Venus, or Jupiter have served as calibrators for COR 1 and 2 (Thompson & Reginald, 2008).

The above steps are the most frequently taken to ensure clean and calibrated astronomical images. They apply to every telescope using a CCD imaging system and every telescope type, including ground and spaced-based systems. For the coronagraphs mentioned above, the steps are performed on each polarization image separately before summing to total or polarized brightness using the following

equations

$$B = \frac{2}{3}(I_0 + I_{+60} + I_{-60}) \quad (3.2)$$

$$pB = \frac{4}{3}\sqrt{(I_0 + I_{+60} + I_{-60})^2 - 3(I_0I_{+60} + I_0I_{-60} + I_{-60}I_{+60})} \quad (3.3)$$

adapted from Billings (1966a). I are the intensity values in each pixel and the 0° , $+60^\circ$, and -60° represent the three polarizations states e.g., the polarizations states of COR 1 and 2.

Anything beyond the above calibration steps is termed level-2 and is usually instrument specific or specific to the scientific goal. Chapter 4 will discuss the production of ‘mass images’ where the pixel values have units of grams, this may also be termed level-2 processing.

3.2 Ultraviolet Observations

Ultraviolet imaging can provide observations of the high temperature corona. Quiet coronal plasma temperatures of $\sim 1 \times 10^6$ K, up to flaring temperatures on the order of $\sim 10^7$ K, can produce a variety of ionization species of heavy elements such as Fe, O, Mg, or Si, for example. These ionization species are strong emitters in the ultraviolet and extreme ultraviolet wavelengths. Any imagers that have bandpasses centered on such wavelengths can therefore allow us to observe a variety of quiet and active coronal processes such as flares and large scale coronal bright fronts. All ultraviolet imagers of the corona are space-based, the latest of this fleet of telescopes is the Atmospheric Imaging Assembly (AIA) on board the Solar Dynamics Observatory (SDO) (Lemen *et al.*, 2012), launched in 2010.

3.2 Ultraviolet Observations

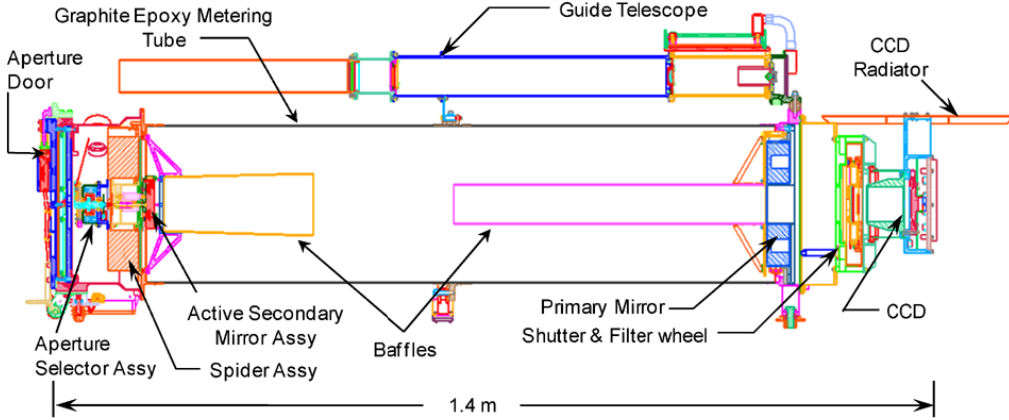


Figure 3.11: The Atmospheric Imaging Assembly (AIA) telescope design. AIA employs four Cassegrain type telescopes, with telescope 1, 2 and 4 serving as dual channel passbands, and telescope 3 permitting imaging at three separate passbands (Lemen *et al.*, 2012).

3.2.1 The Atmospheric Imaging Assembly

SDO is in a geosynchronous orbit at 102° W longitude, inclined at 28.5° . AIA consists of four Cassegrain telescopes that provide visible, ultraviolet (UV), and extreme ultraviolet (EUV) full-disk images of the transition region and corona up to $0.5 R_\odot$ above the photosphere with $0.6''$ spatial resolution and 12-second temporal resolution (Lemen *et al.*, 2012). The telescopes provide imaging in seven extreme ultraviolet passbands centered on the lines Fe XVIII (94 \AA), Fe VIII, XXI (131 \AA), Fe IX (171 \AA), Fe XII, XXIV (193 \AA), Fe XIV (211 \AA), He II (304 \AA), Fe XVI (335 \AA). One of the telescopes observes longer wavelengths at C IV (1600 \AA), the nearby continuum at (1700 \AA) and a broadband visible filter centered on (4500 \AA) giving a full temperature coverage of $5 \times 10^3 \text{ K}$ to $2 \times 10^7 \text{ K}$.

Each telescope has a field of view is $41'$ circular diameter, a 20 cm primary mirror and an active secondary mirror that is pointed in response to signals from a guide telescope. Each mirror is polished to a roughness of $< 5 \text{ \AA}$ rms in the spatial frequency range 10^{-3} – $5 \times 10^{-1} \text{ nm}^{-1}$. The telescopes are dual channel i.e.,

3.2 Ultraviolet Observations

the mirrors in each telescope have two different multi-layer coatings on either half so as to be reflective at a single desired central wavelength on one half. For example, half of mirror 2 has a peak reflectance at 195.5 Å with the other half reflects at 211.3 Å. These two-channel combinations for each mirror in all four telescopes is shown in Figure 3.12. Half of mirror 3 provides the broadband UV and visible channel, with a coating that gives the ability to reflect at 1600, 1700, and 4500 Å, while the other half of the mirror provides the primary optics for the 171 Å channel. Hence telescope 3 provides the optics for four different bandpasses. The temperature response of each telescope channel is shown in Figure 3.13

Metal entrance filters at the aperture of each telescope, combined with a filter wheel located in front of each focal plane, suppress unwanted UV, visible, and infrared radiation. The filters are either made of aluminium, used for wavelengths of 171 Å or longer, and zirconium used for the shorter 94 Å and 131 Å wavelengths. Telescope 3 has an aluminium (for 171 Å) and MgF–2 (for the UV broadband) entrance window and 3 different filters on the filter wheel that cater for observation in 171 Å (aluminium), 1600 Å (MgF–2), 1700 Å and 4500 Å (fused silica). A mechanical shutter regulates exposure time to nominal short exposure of 5 ms and nominal long exposure of 80 ms. Flight software can also select any custom exposure time. The focal plane of each telescope contains a back-illuminated 4096×4096 pixel CCD, with each square pixel having a $12\text{ }\mu\text{m}$ size. Each CCD is read out in 4 quadrants, via an amplifier, into a camera box with four interfaces (one for each quadrant). Each quadrant is read out at a rate of 2 Mpixels s^{-1} and data transmission to the on-board computer occurs at a rate of 100 Mb s^{-1} . All of the steps above described for white-light calibration are relevant for ultraviolet CCD imaging also. The AIA calibration procedure to bring the data from level-0.5 to level-1 include de-biasing, dark subtraction,

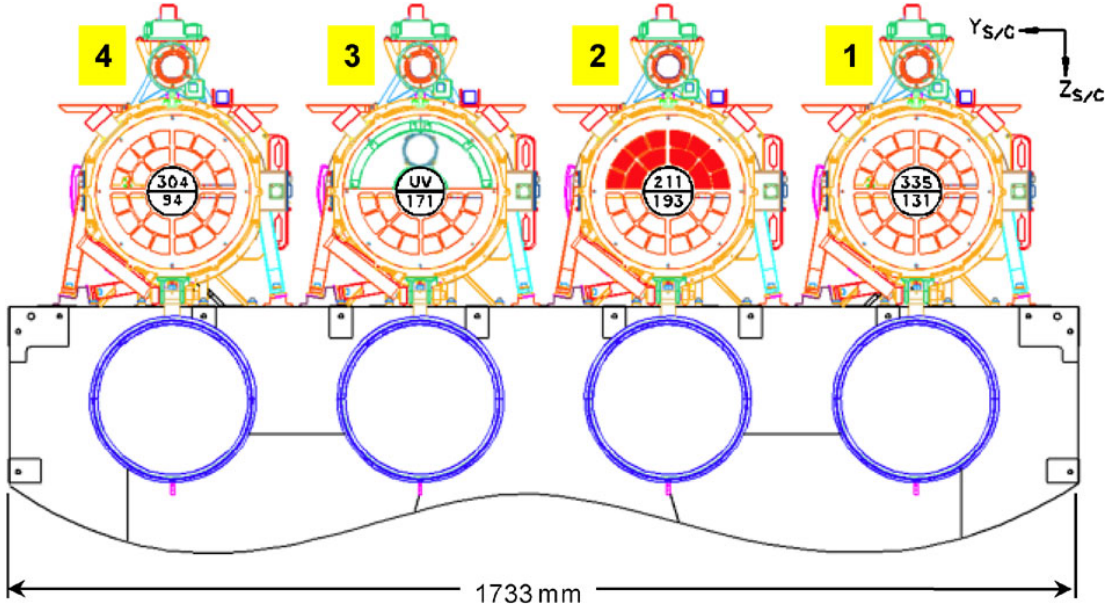


Figure 3.12: The four telescopes making up the Atmospheric Imaging Assembly (AIA) (Lemen *et al.*, 2012). Each telescope is dual channel.

flat-fielding, de-vignetting, de-warping, and brightness calibration, as described in the white-light calibration section. Some example images of AIA are shown in Figure 1.6

3.3 Radio Observations

Radio observations provide insight into the thermal process on the quiet sun as well as the high-energy non-thermal processes occurring during solar flares or coronal mass ejections. Radio emission mechanisms are varied and sometimes extremely complex, including thermal and non-thermal bremsstrahlung, cyclotron, gyrosynchrotron, and synchrotron radiation, and coherent free particle emissions such as electron-cyclotron masers and plasma emission. These emission mechanisms cover the entire radio band from microwave to low frequency. The observations in this thesis mainly include the low frequency bands cover-

3.3 Radio Observations

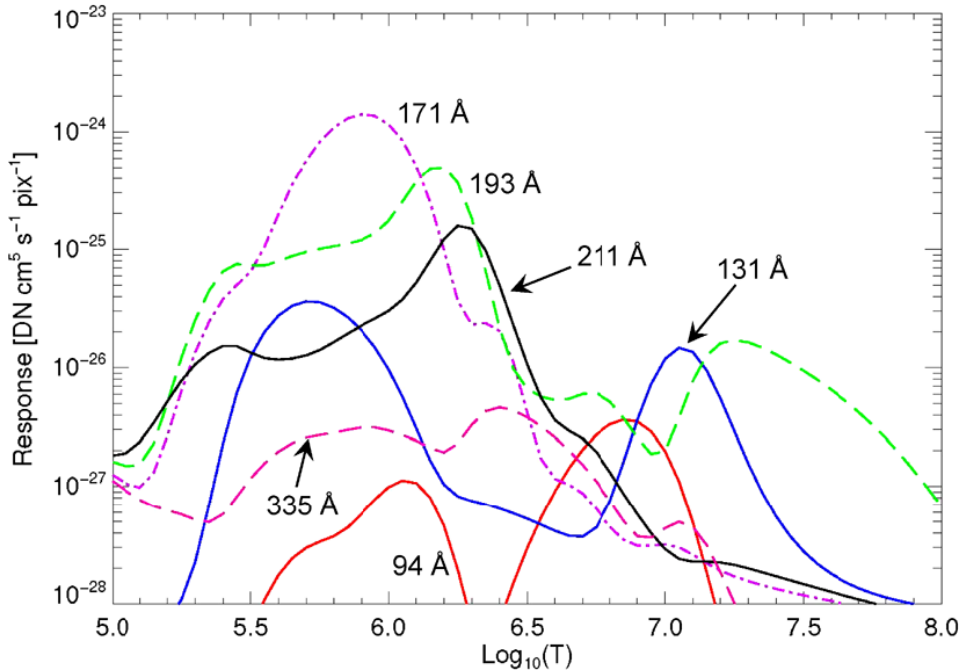


Figure 3.13: The Atmospheric Imaging Assembly temperature responses for each of its passbands. The passbands cover temperatures that include the transition region, to quiet corona, to flaring corona. The 4500 Å passband is not shown here, it's temperature coverage results in photospheric imaging. (Lemen *et al.*, 2012).

ing kHz–MHz ranges. These ranges allow observations of the quiet sun (thermal bremsstrahlung), as well as the non-thermal radio burst plasma emission outlined in Sections 2.3.4–2.3.6. Some imaging and spectroscopy instruments for these observations are outlined below.

3.3.1 Nançay Radioheliograph

The Nançay Radioheliograph is a solar-dedicated radio interferometer located at Nançay, central France (47°N 2°E), that observes at ten frequencies between 150 and 450 MHz (Kerdraon & Delouis, 1997). The array antennas are arranged in a perpendicular ‘T’ shape. The east west array consists of 19 antennas providing baselines in the range of 50 m to 3200 m. Four of these antennas have parabolic collectors with four orthogonal thick dipole feeds at the focus providing

3.3 Radio Observations

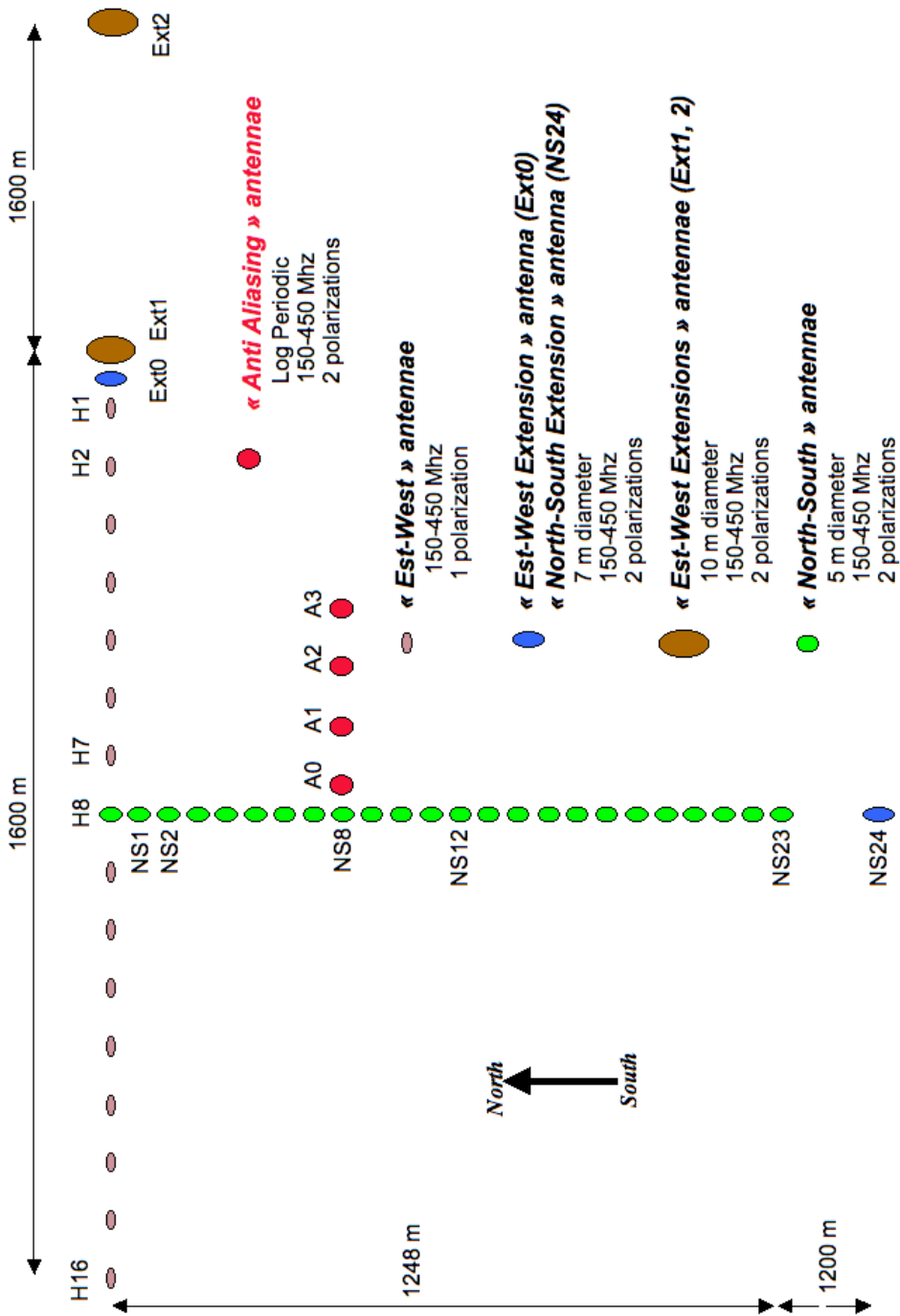


Figure 3.14: The Nançay Radioheliograph layout, showing the east-west baselines and north-south baselines. The antenna types are also shown. *Image courtesy of Alain Kerdraon.*

3.3 Radio Observations

two orthogonal polarizations in the 150-450 MHz band. The remaining 15 have no collectors (no dishes) and consist only of thick dipole antennas providing linear polarization only. The north-south array consists of 24 five meter dishes with wide band feeds, covering baselines between 54 to 1248 m. The antenna front end electronics include low noise high dynamic range (45 dB) pre-amplifiers, band filters for frequency switching and a local oscillator which mixes the signal 113 MHz before it is sent to the receiver (Avignon *et al.*, 1989). At the receiver the signal is further mixed down to 10.7 MHz and fed through a bandpass filter of 700 kHz width (final bandwidth of each observed frequency), digitized and sent to the correlator.

The original array consisted of only the east-west baselines, with the north-south being added later in the early 1980s (Bonmartin *et al.*, 1983), hence the two separate arrays operate off different correlators. The visibility outputs of each correlator are digitized by sampling every 5 ms, resulting in 4 images every 5 ms (Stokes I and V for the east-west and north south arrays), with a down sampling by integrating at least 4 successive images in order to ease storage loads (Avignon *et al.*, 1989). These images are only 1D, offering projected intensity profiles along two axes. Originally, full 2D maps were created by Earth rotation synthesis using the standard 1D observations over one entire day (The Radioheliograph Group, 1993). Such limitations were mainly due to the use of an analog correlator. However, a digital correlator installed in 1997 now provides fast 2D images using the most westerly 17 antennas of the east-west baseline (Kerdraon & Delouis, 1997), resulting in a spatial resolution that is 4 times lower than the 1D east-west images. Systematic daily observations of 2D images are usually performed at between 0.1 and 1 image per second.

All radio interferometers measure a property known as visibility, which is the

3.3 Radio Observations

Fourier transform of the observed sky brightness distribution

$$V(u, v) = \int I(l, m) \exp(i2\pi[ul + vm]) dl dm \quad (3.4)$$

where V is the visibility, (u, v) are the spatial frequency of fringes on the sky, corresponding to the angular sky coordinates (l, m) . $I(l, m)$ is the brightness distribution across the sky. The inverse of this means that the output of an interferometer may be inverse Fourier transformed to obtain the sky brightness distribution

$$I(l, m) = \int V(u, v) \exp(-i2\pi[ul + vm]) du dv \quad (3.5)$$

This equations apply to the ideal case. In reality the visibility function is initially uncalibrated $V'(u, v)$, and sampling of the visibility is discrete in (u, v) space i.e., if an interferometer has n telescopes in the array, then it will have $n(n - 1)/2$ baselines (telescope pairs). This means that there is only $n(n - 1)/2$ samples of visibility V . The sampling of the discrete points in space is represented by a sampling function $S(u, v) = \delta(u - u_k, v - v_k)$, where δ is a Dirac delta function and (u_k, v_k) are the positions in (u, v) space at which there is sampling. Equation 3.5 thus becomes

$$I(l, m) = \int S(u, v) V'(u, v) \exp(-i2\pi[ul + vm]) du dv \quad (3.6)$$

Firstly, the original visibilities must be calibrated to obtain $V(u, v)$ from $V'(u, v)$. Calibration usually involves characterising the gain G of an interferometer and any phase corrections P that need to be made. This is done by observing a strong radio point source of known flux (known ideal V) such that G and P may

3.3 Radio Observations

be characterised in the equation

$$V'(u, v) = G[P[V(u, v)]] \quad (3.7)$$

NRH instrument phase and gain calibration is performed by observing Cygnus A. Phase and gain accuracy for these measurements are 5° and 5%, respectively, with only 1 calibration per week necessary because of good system stability (Avignon *et al.*, 1989)

Calibrated visibilities are then used in Equation 3.6. If we represent the Fourier transform by $\mathfrak{F}[\cdot]$, and using the convolution theorem then Equation 3.6 becomes

$$I(l, m) = \mathfrak{F}[S(u, v)V(u, v)] = \mathfrak{F}[S(u, v)] * \mathfrak{F}[V(u, v)] \quad (3.8)$$

Given that the Fourier transform of the sampling function is the beam of the instrument $\mathfrak{F}[S(u, v)] = B(l, m)$ i.e., its point spread function, and as shown above $\mathfrak{F}[V(u, v)] = I(l, m)$, this gives

$$I_D(l, m) = \mathfrak{F}[S(u, v)] * \mathfrak{F}[V(u, v)] = B(l, m) * I(l, m) \quad (3.9)$$

Hence the result of Equation 3.6 is the sky brightness distribution convolved with the instrument beam, this image is known as the dirty map $I_D(l, m)$. The dirty map will contain the sources in the actual sky brightness distribution but they are contaminated with the side lobes of the instrument beam (Figure 3.15). In order to obtain $I(l, m)$ from $I_D(l, m)$ we must ‘deconvolve’ the beam from the dirty map. The main deconvolution algorithm used to obtain $I(l, m)$ from $I_D(l, m)$ is known as CLEAN. CLEAN works by locating the peak emission in the dirty map $I_{D,max}(l_i, m_i)$, subtracting the dirty beam $B(l, m)$ from the peak, and placing a

3.3 Radio Observations

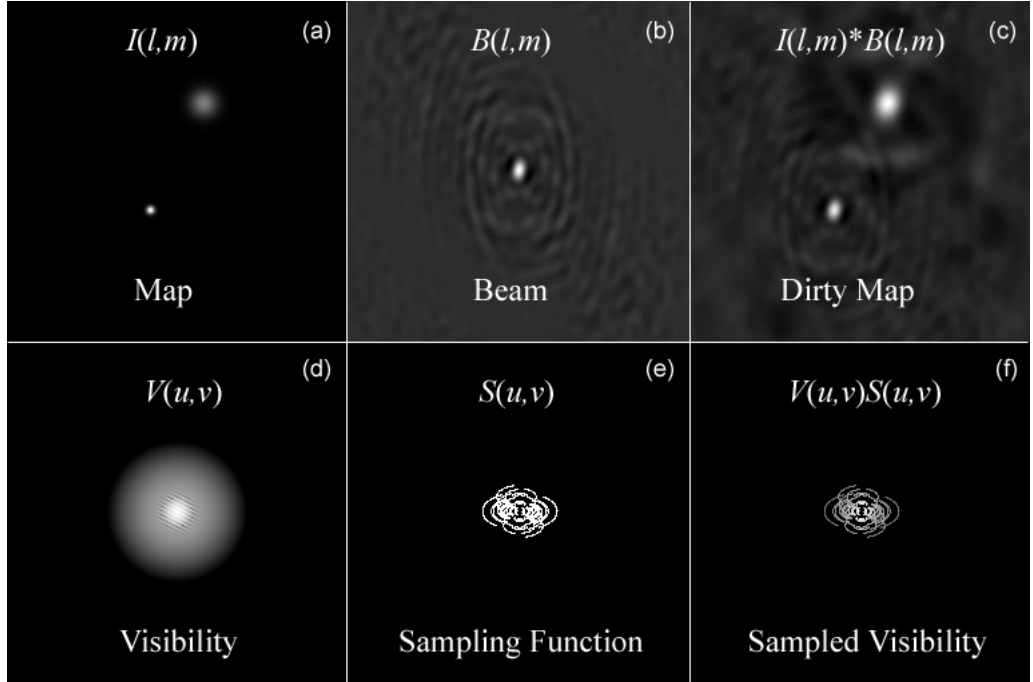


Figure 3.15: Relationship between sky brightness distribution $I(l, m)$, visibility $V(u, v)$, instrument beam $B(l, m)$, and sampling function $S(u, v)$. Panel (c) shows the dirty map, showing the original sky brightness distribution convolved with the instrument beam. *Image courtesy of Dale Gary (<http://web.njit.edu/gary/728/>).*

point source at a corresponding location (l_i, m_i) in an ‘empty’ clean image. It then finds the next peak and repeats the process. The result is a clean image of point sources at locations that correspond to the peak locations in the dirty map. The clean image is then convolved with a ‘clean beam’ i.e., a beam without sidelobes (a 2D gaussian in the simplest case). After all sources are subtracted from $I_D(l, m)$, we are left with a ‘residual’ map. This residual map is added to the clean image to take into account that the sources in the image have different intensities. The result is an image of the sky-brightness distribution without contamination from the beam sidelobes CLEAN works best when all sources in the image have the same spatial scale, however it performs poorly when sources in the image exhibit size structure on a variety of scales (Wakker & Schwarz, 1988).

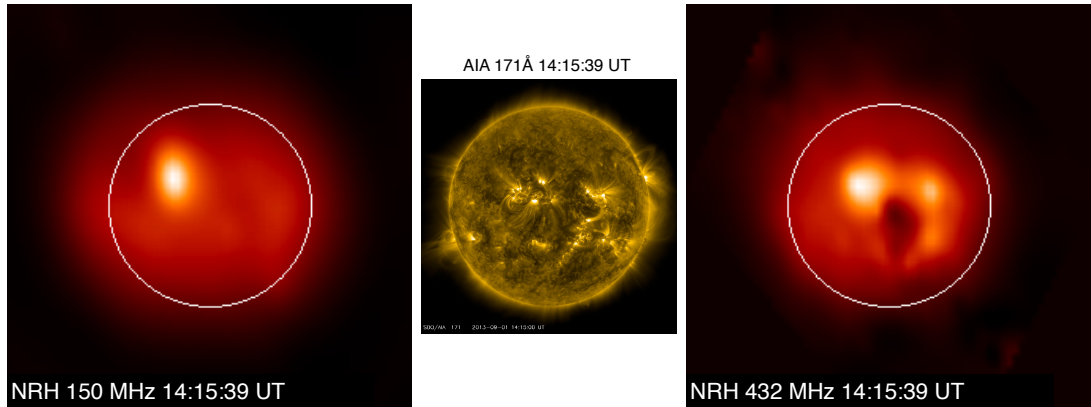


Figure 3.16: Observations from NRH at 150 MHz and 432 MHz, with AIA 171 Å for comparison. All three images were taken at the same time at 14:15 UT on 01 September 2013.

Nancay Radioheliograph Properties	
No. of Antennas	19 EW, 24 NS ('T' shape)
Time resolution	5 ms (integrated to 0.1–1 s for 2D images)
Spatial Resolution	0.3 – 6 ″, depending on freq. and direction
Dynamic range	> 45 dB
Observing frequencies	10 frequencies between 150–450 MHz
Bandwidth	700 kHz
Polarization	Stokes I and V
Observing time	7.5 hr centered around 12 UT

Table 3.1: NRH properties compiled from (Kerdraon & Delouis, 1997)

When observing the Sun there are multiple size scales on which sources occur in the image, therefore NRH uses a custom Multiscale-CLEAN algorithm that operates on the dirty map at different scales (Mercier *et al.*, 2006). Some examples of NRH images are given in Figure 3.16. The NRH instrument properties are summarised in Table 3.1

3.3.2 Nançay Decametric Array

The Nançay Decametric Array consists of 72 (6 east × 12 west) conical antennas, with each antenna consisting of a left-handed helically wound component and

3.3 Radio Observations

a right handed helical component – this makes the array contain 144 antennas in total, with 8000 m^2 effective aperture at 30 MHz (Lecacheux, 2000). Each helix antenna is made of eight copper-steel wires wound on the surface of a cone and connected to the output coaxial cable by diode switches; only six wires are used at a time to form the antenna; the other two, diametrically opposite, are left disconnected. By changing the connections through the diode switches, the antenna can be electrically rotated around the cone axis, corresponding to a phase change of the antenna by steps of 45° . The antennas are broadband (20–120 MHz), low gain (low directivity) with a half power beam width of 90° centered on the cone axis (Boischot *et al.*, 1980). The entire array is steerable by phase delays within the 90° beam width of the individual antennas resulting in a possible tracking time of ± 4 hr around the meridian, within a declination range of -20° to $+50^\circ$.

The backend of the array consists of three possible receivers: a wide-band swept-frequency analyzer which operates 400 channels between 20-90 MHz. Left and right hand circular polarization are alternately sampled every 0.5 seconds from the left and right hand helical feeds of the antennas. The nominal operations for solar radio burst monitoring use this swept frequency receiver but there are other more sophisticated receivers available such as a spectro-polarimeter with 1 ms time sampling over 1024 channels and with a 60 dB dynamic range. However, it has only a 12.5 MHz instantaneous band, which is not so useful for solar radio burst monitoring.

3.3.3 STEREO WAVES

Below ~ 10 MHz the Earth's ionosphere prevents the propagation of radio waves, hence radio emission below this frequency cannot be observed from ground-based

3.3 Radio Observations

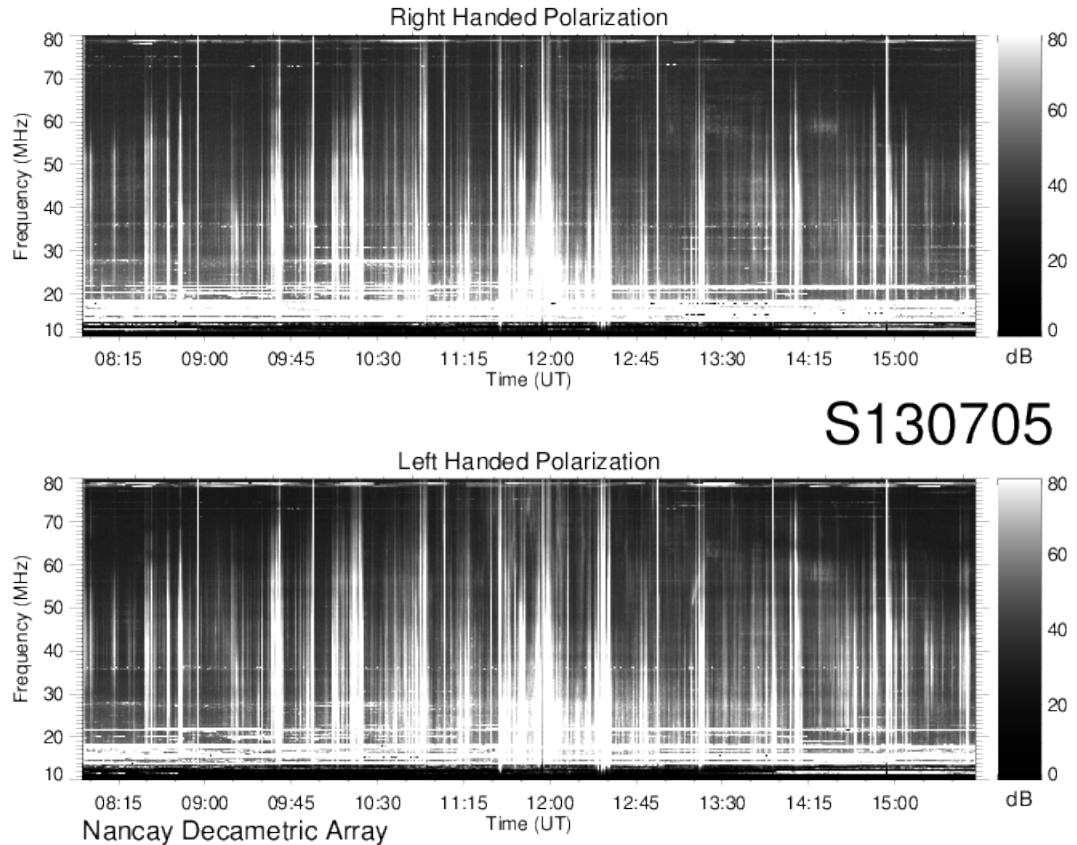


Figure 3.17: Nançay Decametric Array observations of an active period of type III radio bursts on 07 May 2013. Image courtesy of the <http://secchirh.obspm.fr/survey.php>

observatories. To overcome this problem, there are a number of space based instruments that observe frequencies in the deca and kilometric wavelength ranges; the STEREO Ahead and Behind spacecraft each carry such an instrument, known as STEREO WAVES or S/WAVES (Bougeret *et al.*, 2008). This instrument directly inherits its design from the Ulysees (Stone *et al.*, 1992), Wind (Bougeret *et al.*, 1995), and Cassini (Gurnett *et al.*, 2004) spacecraft.

The antenna system on each STEREO spacecraft consists of three mutually orthogonal 6-meter Beryllium-Copper monopole elements (Bale *et al.*, 2008), Figure 3.19. The elements' diameter at the base is 1 inch and tapers to 0.6 inches at

3.3 Radio Observations

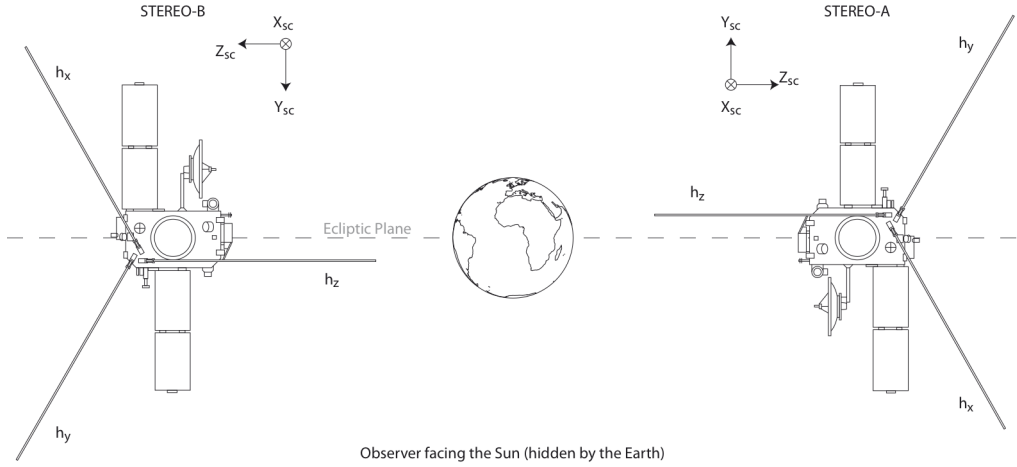


Figure 3.18: Configuration of the STEREO/WAVES antennas as seen from the Sun-Earth line, facing the Earth. Each monopole is 6 m long and feeds a number of receiving instruments.

the tip. The three monopoles are each connected to low noise and high impedance preamplifier, each feeding a number of receiving systems including the Fixed Frequency Receiver (FFR), the Time Domain Analyzer (TDS), and two frequency domain analyzers known as the Low Frequency Receiver (LFR) and High Frequency Receiver (HFR); only the LFR and HFR are described here.

The LFR is a direct conversion receiver that performs dynamic spectral analysis in the 2.5–160 kHz band. The signal feed from the antennas and pre-amp is passed through a wavelet-like transform to perform digital spectral analysis in three 2-octave bands which each have 16 logarithmically spaced frequency channels (resulting in 48 log spaced channels in the 2.5–160 kHz range). Receiver automatic gain control (AGC) ensures a high dynamic range of 120 dB. Various combinations of the three antenna elements can be made to produce pseudo-dipole or monopole configurations. The signal is then 12-bit digitized and sent to a Digital Processing Unit (DPU).

The HFR is a dual sweeping receiver operating in the frequency range 125

kHz–16.025 MHz. It uses a super-heterodyne technique to down-convert the signal frequencies to odd multiples of 25 kHz that specifically avoid lines of noise generated by the spacecraft power supply, which may produce harmonic multiples of 50 kHz. Due to the down-conversion process the HFR frequency range is covered in multiple steps of 50 kHz increments, thus the highest spectral resolution is 50 kHz. It has a dynamic range of 80 dB. Like the LFR, it can receive various combinations of the three antenna elements in dipole or monopole modes. The signal is digitized by the same DPU as the LFR.

The time domain resolution for both the LFR and HFR is determined by the DPU. Nominal time resolution of the dynamic spectra produced by both receivers is 1 minute. Sample dynamic spectra of the LFR and HFR from both Ahead and Behind spacecraft is shown in Figure 3.19

3.3.4 Rosse Solar Terrestrial Observatory

3.3.4.1 Antennas and Spectrometers

The Rosse Solar Terrestrial Observatory was established in 2010 at Birr Castle, Co. Offaly, Ireland ($53^{\circ} 05' 38.9''$, $7^{\circ} 55' 12.7''$) (Zucca *et al.*, 2012). The primary objective of the observatory is to observe low frequency radio bursts occurring in the solar atmosphere and the ionospheric and geomagnetic response following this radio activity. To date, three *Compound Astronomical Low-cost Low-frequency Instrument for Spectroscopy and Transportable Observatory* (CALLISTO; Benz *et al.*, 2005) spectrometers have been installed, with the capability of observing in the frequency range 10–870 MHz. The receivers are fed simultaneously by biconical and log-periodic antennas. Nominally, frequency spectra in the range 10–400 MHz are obtained with 4 sweeps per second over 600 channels. The instrumental set-up is described here.

3.3 Radio Observations

STEREO/WAVES Daily Summary - 22-Sep-2011 (DOY 265)

Ahead source file = swaves_ahead_2011_265_1_04.fin
Ahead PSE Angle = xxx.x

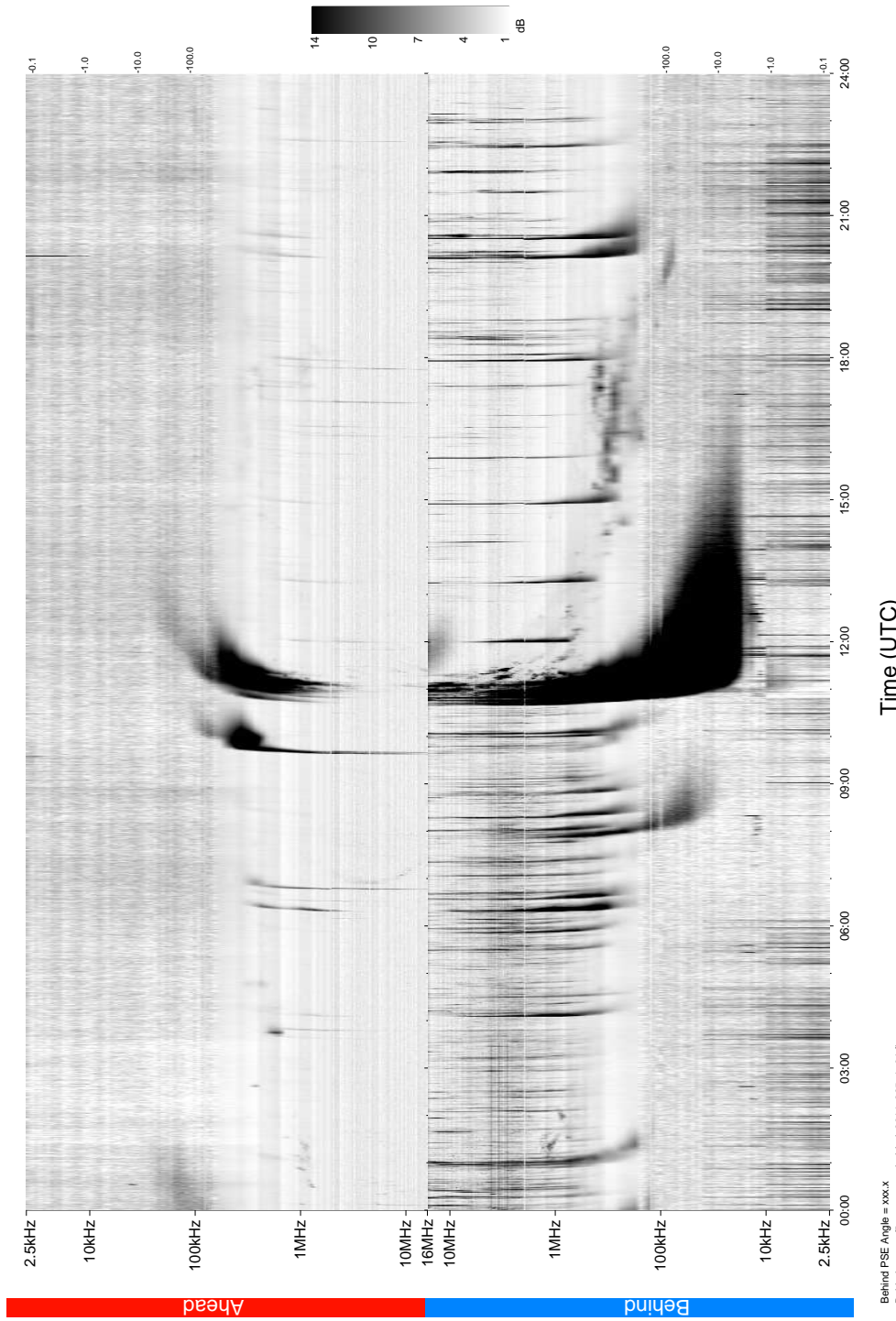


Figure 3.19: STEREO WAVES observations from the Ahead and Behind spacecraft from 22 September 2011. A strong type III and interplanetary type II burst were observed by the Behind spacecraft. *Image courtesy of the STEREO Waves team <http://swaves.gsfc.nasa.gov/>.*

3.3 Radio Observations

RSTO employs three callisto receivers that cover the ranges of 10–100, 100–200, 200–400 MHz, respectively. The 10–100 MHz receiver (Callisto-1), is fed (via frequency up-converter) by a biconical Schwarzbeck antenna, model number VHBD 9134. The antenna elements are 4 m long allowing a nominal frequency bandwidth of 20–200 MHz. Signal feed from the bicone to Callisto-1 is via 70Ω coaxial cable, ~ 20 meters in length Figure 3.20. The bicone is mounted on a Yaesu-1 motor that permits solar tracking in the azimuth direction only (the antenna beam is symmetric in elevation).

The 100–200 and 200–400 MHz (Callisto-2 and -3, repsectively) are fed by a Tennadyne T28 log-periodic antenna. The antenna has a frequency band of 50–1300 MHz with a ~ 50 degree half-power beam width (HPBW). Signal from the antenna is fed into a 10 dB pre-amplifier followed by a signal splitter which feeds Callisto-2 and Callisto-3, see Fig. 3.20. The digitized data for these two receivers is sent to the control PC via four RS422 conversion units. RS422 is used because of the high baud-rate and length of the cables (~ 30 m) i.e., there may be interrupts and losses over this path length so the signal is sent differentially. The log-periodic antenna is fixed to an Eiges Alt-Az motor with an EPS-103 control unit, allowing tracking of the Sun throughout the day.

Callisto spectrometers were designed and built in ETH Zurich to monitor solar radio bursts in a frequency range of 10–87 MHz (Benz *et al.*, 2005). The receiver is composed of standard electronic components, employing a Digital Video Broadcasting-Terrestrial (DVB-T) tuner assembled on a single printed circuit board. The number of channels per frequency sweep can vary between 1 and 400, with a maximum of 800 measurements per second. An individual channel has a 300 kHz bandwidth during a typical frequency sweep of 250 ms, and can be tuned by the control software in steps of 62.5 kHz to obtain a more detailed spectrum

3.3 Radio Observations

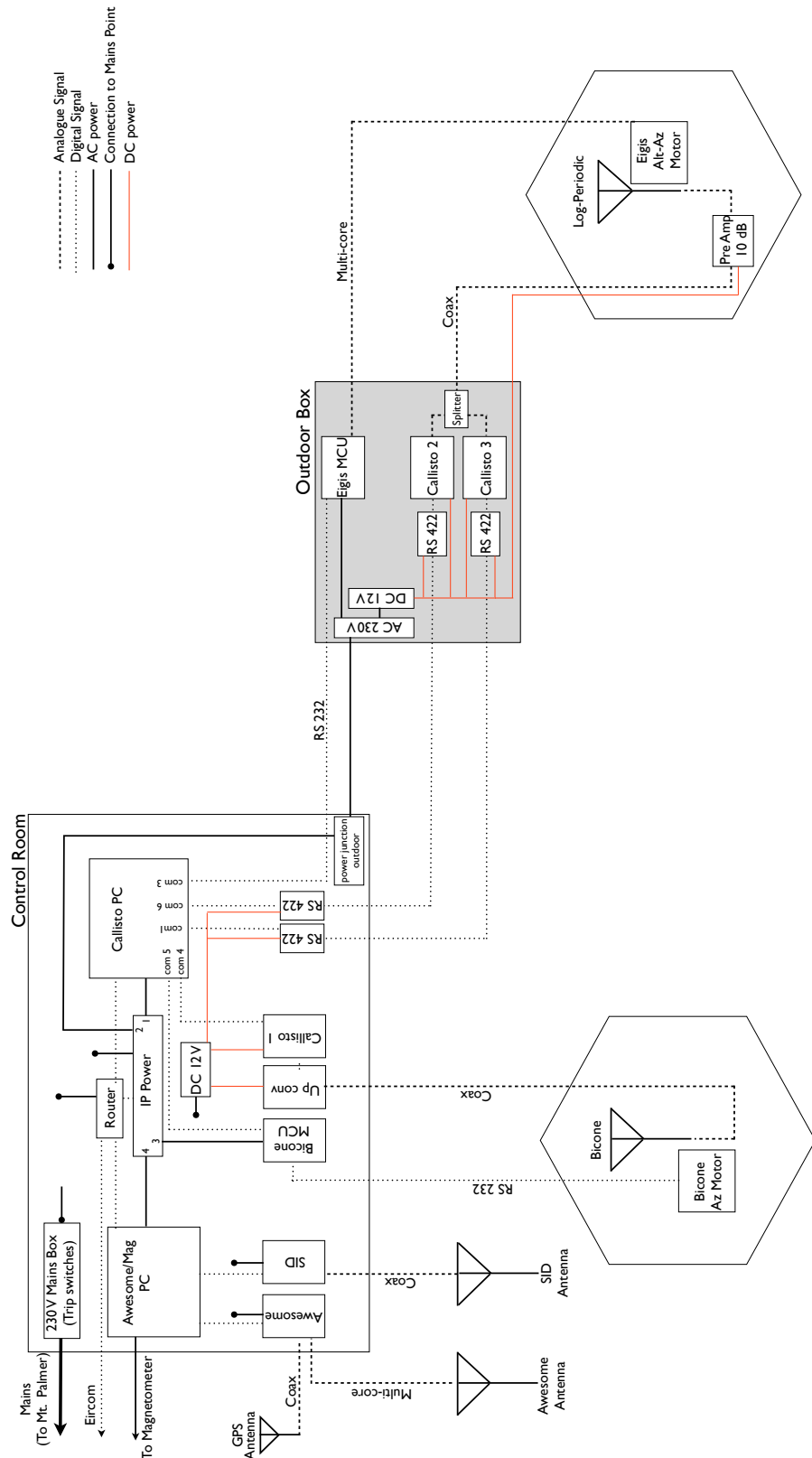


Figure 3.20: The Rosse Solar Terrestrial Observatory instrument and communications lay-out.

of the radio environment. The narrow channel width allows for the measurement of selected channels that avoid known bands of radio interference from terrestrial sources.

3.3.4.2 Nominal Operations

The system is controlled by a Dell Vostro, Intel core i5, allowing the system to be completely automated and stand alone, without the need for an on-site observer. Automatic nominal daily operations include (i) commence data recording of all three Callistos at 04:00 UT, (ii) begin antenna solar tracking at sunrise, (iii) at 10 minutes past every hour the data is processed, background subtracted, and images are produced for online display at www.rosseobservatory.ie, (iv) at mid-day a high frequency resolution (62.5 kHz) spectrum is taken, (v) stop solar tracking at sunset, (vi) archive the data products of the entire day (archive accessible online). The entire automated process is carried out by a combination of Callisto GUIs, dedicated solar tracking GUIs, DOS Shell scripts, and IDL scripts. This fully automated system is stable and requires maintenance or check up only every 6 or more months. If the system stops recording data, remote recovery can be achieved via a virtual desktop. The entire system is remotely accessible from Trinity College Dublin via a virtual desktop ‘VNC’ software. The system may be remotely configured and nominal operations changed at any time. Should the system crash, a remote power recycling facility is available using an IP power board with its own web address, accessible from any web browser. Automated steps (i)-(vi) are recovered and begin automatically upon power recycling.

3.3.4.3 Dynamic spectra from RSTO

Since the installation of RSTO in September 2010 there has been a number radio bursts detected. The burst vary in their type, duration, and level of fine structure. The observatory has been successful in picking up type I storms, type IIIs, type IIIIs, a number of herringbone observations, and type V and VI. Some samples of these are given in Figures 3.21 to 3.23, with further dynamic spectra in the Appendix.

3.3.4.4 eCallisto Network

RSTO is part of the e-Callisto network¹. The network consists of a number of spectrometers located around the globe, and designed to monitor solar radio emission in the meter and decameter bands (Benz *et al.* 2009; Figure 3.24). Each of the instruments observes automatically, and data is collected each day via the Internet and stored in a central database at Fachhochschule Nordwestschweiz (FHNW), and operated by ETH Zurich². One of the important features of RSTO is the particularly low radio frequency interference (RFI) of the site.

To compare RSTO to other radio observing sites, an survey of RFI at RSTO was performed in June 2009. The detected spectrum is shown in Figure 3.25. A commercial DVB-T antenna covering the range from 20 MHz up to 900 MHz was used for the survey, which was directly connected via a low-loss coaxial cable to a Callisto receiver with a sensitivity of 25 mV/dB. The channel resolution was 62.5 kHz, while the radiometric bandwidth was about 300 kHz. The sampling time was 1.25 ms per frequency interval, while the integration time was about 1 ms. Figure 3.25 shows the RFI radio surveys of RSTO, Bleien Observatory in

¹www.e-callisto.org

²soleil.i4ds.ch/solarradio/CALLISTOQuicklooks/

3.3 Radio Observations

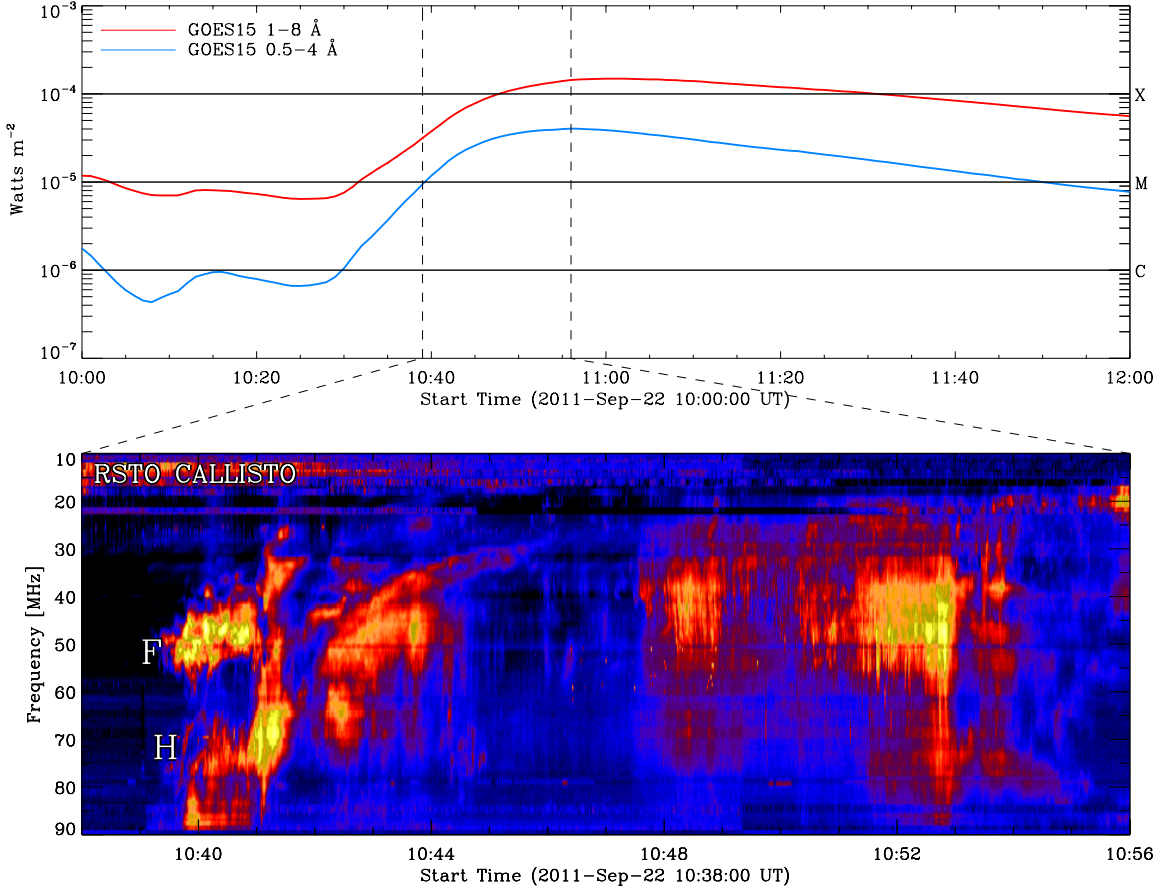


Figure 3.21: A radio burst from 22 September 2011 observed at RSTO. This radio burst was detected by the 10–100 MHz Callisto fed by the bicone antenna. The radio burst was quite complex, consisting of the fundamental and harmonic of a type II burst followed by herringbone fine structures. The top plot shows the GOES light curves for comparison, with the dashed vertical line indicating start and end times of the dynamic spectra. Adapted from (Zucca *et al.*, 2012)

Switzerland, and the Potsdam LOFAR station in Germany. There is a high level of interference at 20–200 MHz for the Bleien and Potsdam sites, while the RSTO site has a low level of RFI.

3.3 Radio Observations

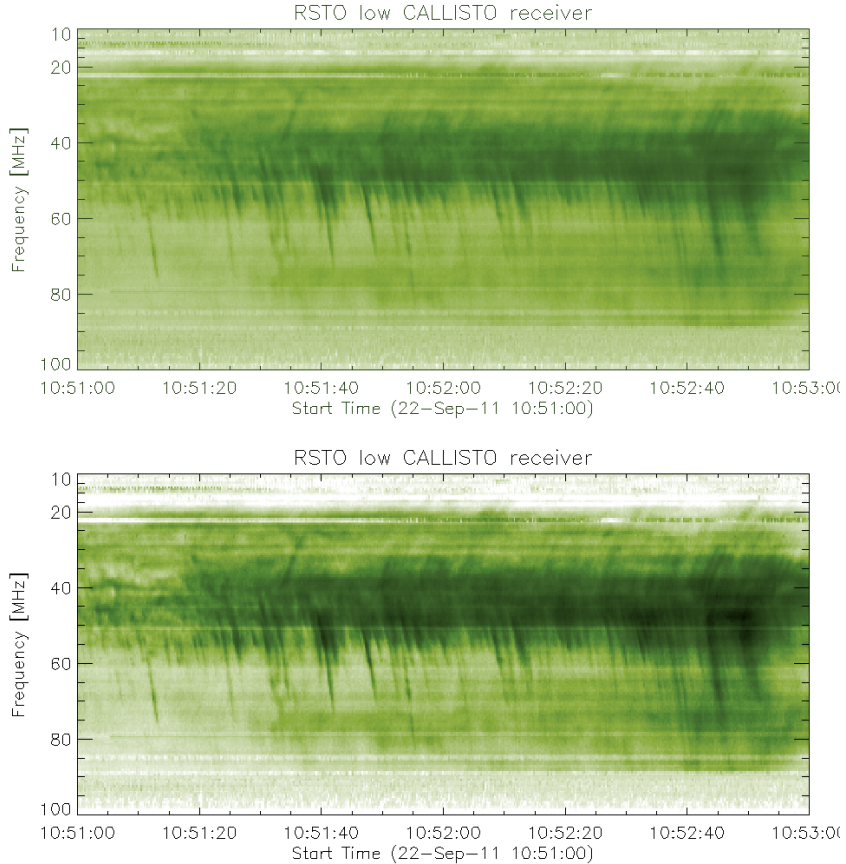


Figure 3.22: (Top) A zoom of the herringbone structure shown in Figure 3.21. The time sampling of the Callisto spectrometers (0.25 s) is fast enough to catch such herringbone features. (Bottom) Same spectrum but background subtracted, the herringbones have a much better contrast in this spectrum.

3.3.5 Dynamic Spectra Data Reduction

The Nançay Decametric Array, STEREO WAVES, and the Callisto spectrometers each have basic data reduction techniques in common. The most basic of these is background subtraction. Analogous to the dark current on a CCD, there will be some background signal detected due to the system electronics. This is due to a number of effects including the any DC bias and the noise produce by system thermal properties. This background may be subtracted by a variety of techniques, such as averaging the dynamic spectrum through time and using this

3.3 Radio Observations

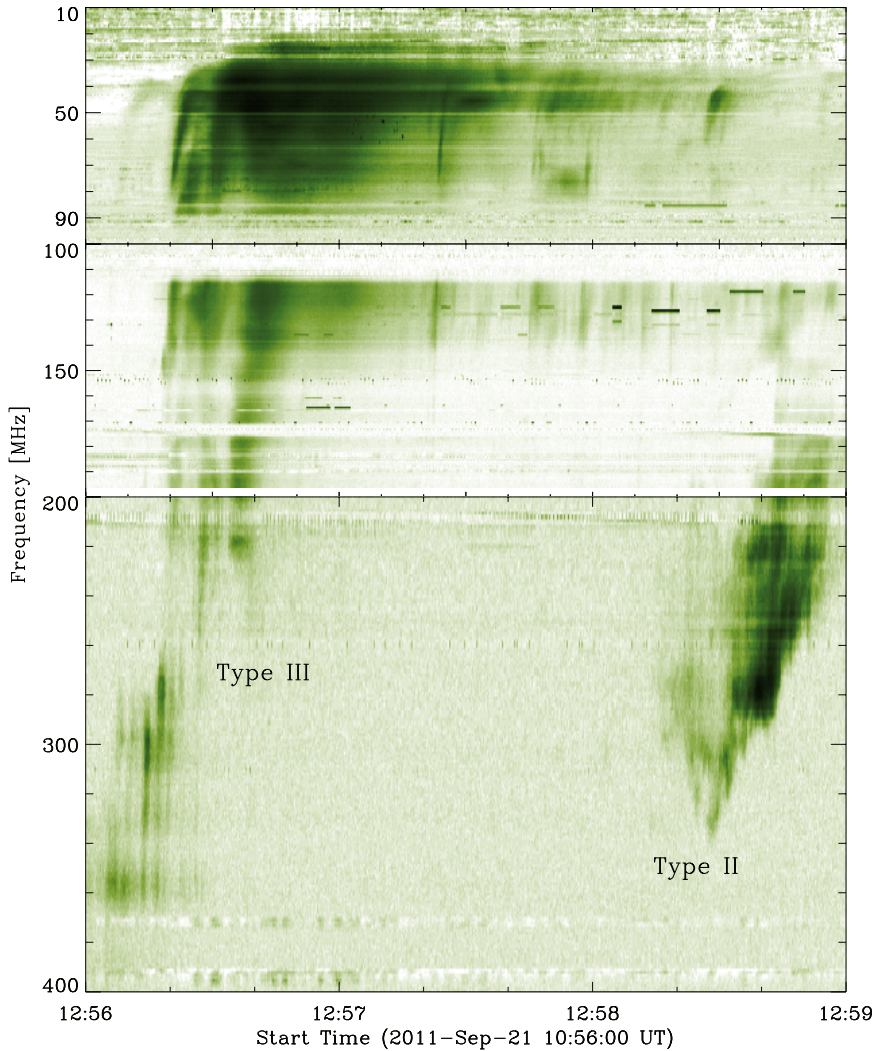


Figure 3.23: A type III and II radio burst observed on 21 September 2011. This spectra demonstrates the low levels of RFI at RSTO, especially in the 200–400 MHz range where there is almost no RFI.

as a background, subtracting a spectrum occurring just before a detected radio burst, or automatically detecting a spectra with no radio burst and using this as a background. The last type is the one implemented on the dynamic spectra used in this thesis work. The procedure is implemented in the IDL procedure *const-backsub.pro*. This function firstly computes the average of each frequency channel in time and subtracts this from the original spectrogram. It then computes the standard deviation of each time-step. The time-steps containing a radioburst

3.3 Radio Observations

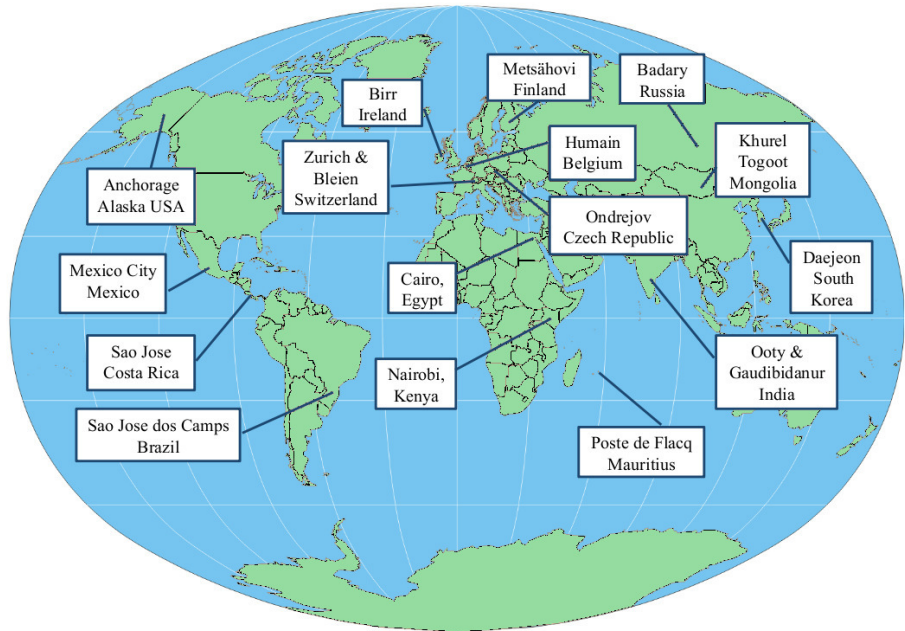


Figure 3.24: Worldwide distribution of Callisto sites, offering almost 24 coverage of solar radio activity at most latitudes.

should have the largest standard deviation, while those without a burst will have small standard deviation. By default the smallest 5% of the standard deviations is averaged and used as a background. An example of raw and background subtracted data is shown in Figure 3.22

Dynamic spectra may also be contaminated by radio frequency interference (RFI). This may be sporadic, periodic and regular, or continuous in time. RFI is generally very difficult to remove from a dynamic spectra while still maintaining the desired signal (radio burst). The techniques of RFI removal may be a simple smoothing of the data or convolution with a Gaussian to ‘average out’ the signal. Much more sophisticated RFI identification algorithms are based on multiscale filtering of the dynamic spectra image or using a kurtosis estimator (Nita & Gary, 2010; Nita *et al.*, 2007)(RFI is generally much more ‘peaked’ in either frequency or

3.3 Radio Observations

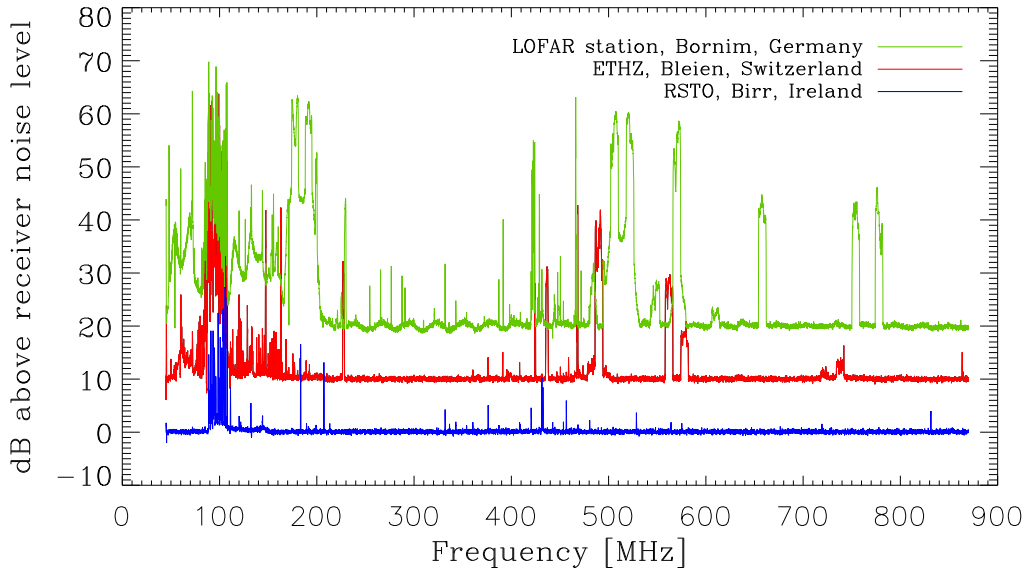


Figure 3.25: Radio frequency survey from the RSTO in Birr Castle Demesne (blue), Bleien Radio Observatory in Switzerland (red; offset by 10 dB) and Potsdam Bornim (green; offset by 20 dB). The RSTO spectrum is quiet at all frequencies that were tested, except for the FM band covering 88–108 MHz. The surveys were conducted using the same equipment.

time). Generally, frequency channels with bad contamination by RFI are avoided if possible.

4

Coronal Mass Ejection Masses, Energetics, and Forces

In the past, measurement of CME dynamics have been hindered by highly uncertain estimates of the total mass of the ejection. The primary source of uncertainty is the unknown position and geometry of the CME, leading to an erroneous treatment of the Thomson scattering equations which are used to estimate the mass. Geometrical uncertainty of the CMEs position and size has primarily been due to observations of the eruption from a single vantage point. However, with the launch of the *Solar Terrestrial Relations Observatory (STEREO)* mission, the two viewpoints can be exploited to derive the CMEs position and size, ultimately resulting in mass uncertainty that is both reliably quantified and much reduced. This then leads to better estimates of the energies and forces. In this chapter I will first outline the Thomson scattering theory used to compute CME mass, followed by a discussion of the mass uncertainties. This is followed by results showing the smallest uncertainties in the literature on CME mass, and the first estimate CME force magnitude from observations. This chapter is based on work published in Carley, McAteer, & Gallagher, *The Astrophysical Journal*, 2012.

4.1 Introduction

Despite many years of study, the origin of the forces that drive coronal mass ejections (CMEs) in the solar corona and interplanetary space are not well understood. From an observational viewpoint a complete understanding of CME kinematics, dynamics and forces requires not only a study of CME speed, acceleration and expansion but also an accurate knowledge of CME mass. The measurements of CME mass combined with acceleration measurements can be used to quantify the magnitude of the force that drives a CME. Knowledge of this force magnitude can lead to an identification of the possible origin of the CME driver.

There are numerous theoretical models that attempt to explain the triggering of CME eruption and its consequent propagation. Each describe the destabilization and propagation of a complex magnetic structure, such as a flux rope, via mechanisms that include the catastrophe model (Forbes & Isenberg, 1991; Forbes & Priest, 1995; Lin & Forbes, 2000), magnetic breakout model (Antiochos *et al.*, 1999b; Lynch *et al.*, 2008), or a toroidal instability model (Chen, 1996; Kliem & Török, 2006), as described in Chapter 2. The loss of equilibrium induced by such mechanisms results in CME propagation into interplanetary space. The predictions of these models have been investigated in observational studies whereby the CME kinematics are used to constrain what forces might be at play and hence which model best describes CME propagation. Such studies show that early phase propagation can be reasonably described by the existing models (or a combination of them) involving some form of magnetic CME driver (Chen *et al.*, 2006; Lin *et al.*, 2010; Manoharan & Kundu, 2003; Schrijver *et al.*, 2008b), and that aerodynamic drag of the solar wind may have a significant role at later stages

4.1 Introduction

of CME propagation (Byrne *et al.*, 2010; Howard *et al.*, 2007; Maloney & Gallagher, 2010). Comparisons between modeling and observational estimates of the forces that drive CMEs requires an accurate determination of CME kinematics properties as well as CME mass.

To date, the most prevalent method of determining CME mass has been through the use of white light coronagraph imagers, such as the Large Angle Spectroscopic Coronagraph (LASCO; Brueckner *et al.*, 1995) on board the *Solar and Heliospheric Observatory (SOHO)*; Domingo *et al.*, 1995 and the twin Sun Earth Connection Coronal and Heliospheric Investigation (SECCHI) COR1 and COR2 coronagraphs (Howard *et al.*, 2008) on board the *Solar Terrestrial Relations Observatory (STEREO)*; Kaiser *et al.*, 2008). The white-light emission imaged by such coronagraphs occurs via Thomson scattering of photospheric light by coronal electrons (Billings, 1966b; Minnaert, 1930a; van de Hulst, 1950), the so called K-corona. From classical Thomson scattering theory, the intensity of the light detected by an observer depends on the particle density of the scattering plasma. Hence, any density enhancement, such as a CME, over the background coronal density appears as enhanced emission in white light. The enhanced emission allows for a calculation of the total electron content and hence mass.

Some of the first measurements of CME mass using scattering theory were carried out by Munro *et al.* (1979) and Poland *et al.* (1981) using space-based white light coronagraphs on board *SkyLab* and U.S. military satellite *P78-1*. Both the early studies and later statistical investigations determined that the majority of CMEs have masses in the range of 10^{13} – 10^{16} g, (Vourlidas *et al.*, 2002, 2010). However, due to only a single viewpoint of observation, the longitudinal angle at which the CME propagates outwards was largely unknown in these studies and it is generally assumed that the CME propagates perpendicular to the observers

line-of-sight (LOS). There is also the added assumption that all CME mass lies in the two-dimensional plane-of-sky (POS). Such assumptions can lead to a mass underestimation of up to 50% or more (Vourlidas *et al.*, 2000). More recent studies have employed the two viewpoint capabilities of the *STEREO* mission to determine the mass of numerous CMEs with much less uncertainty (Colaninno & Vourlidas, 2009).

In this Chapter I will present an analysis of mass development of the 2008 December 12 CME using the *STEREO* COR1 and COR2 coronagraphs. We use a well constrained angle of propagation to determine the mass and position of the CM, and completely characterise the uncertainties on this mass. Combining the mass measurements with values for CME velocity and acceleration, the kinetic energy and the magnitude of the force influencing propagation is determined for each point in time. The first section described the observations of the event from first appearance of the front in COR1 A and B to the time when the front exits the COR2 A and B fields of view. The data analysis section describes the methods by which the masses are calculated with *a priori* knowledge of the propagation angle, as well as a discussion of the primary sources of uncertainty. Following this are the results, including masses, energies and forces on the CME. Finally, a discussion is given of the possible forces attributable to the observed accelerations and whether they are magnetic or aerodynamic in origin.

4.2 Observations

The COR1 images used in this analysis span from 2008 December 12 04:05 UT to 15:45 UT, with a cadence of 10 minutes. The three polarization states of COR1 were combined to make total brightness images in units of mean solar brightness (MSB). Base difference images were produced using the 04:05 UT image (in both

4.2 Observations

COR1 A and B) as a background to be subtracted from all subsequent images. A sample of such images for both COR1 A and B can be found in Figure 4.1. The COR2 images analyzed range from 07:22 UT to 17:52 UT, with a cadence of 30 minutes. As with the COR1 images, total brightness images were created for COR2, and a set of base difference images were then produced using the 07:22 UT image as a suitable background. A selected set of images from COR2 can be found in Figure 4.2. Note that the pixel values in Figures 4.1 and 4.2 have been converted to grams; the method by which this is done is described in the next section.

At 04:35 UT the leading edge of a CME appeared in COR1 A and B coronagraphs at a height of $\sim 1.4 R_{\odot}$, off the east and west limb respectively. In COR1B the CME first appears as a set of rising loop-like structures followed by a prominence, part of which appears to fall back to the surface at 08:00 UT while the remainder was ejected and follows the rising loop-like structures which eventually become the CME front. The rising prominence was not apparent at any stage of the propagation in COR1A and the advancing front remains the only distinguishable facet of the CME from this line-of-sight (LOS).

A noteworthy caveat of using base difference imaging is the assumption that the background corona in the pre-event image has the same brightness in all subsequent images. This may not always be true and any excess brightness in the pre-event image will produce negative pixel values in the base difference. This is apparent in the COR1 images as the CME interacts with a streamer, displacing it as the leading CME front expands laterally as well as moves outward. The streamer is visible as a dark feature that grows with time at the southward flank of the CME in the COR1B images, Figure 4.1. The black areas are indicative of negative pixel values. The COR1A images also suffer from negative pixels,

4.2 Observations

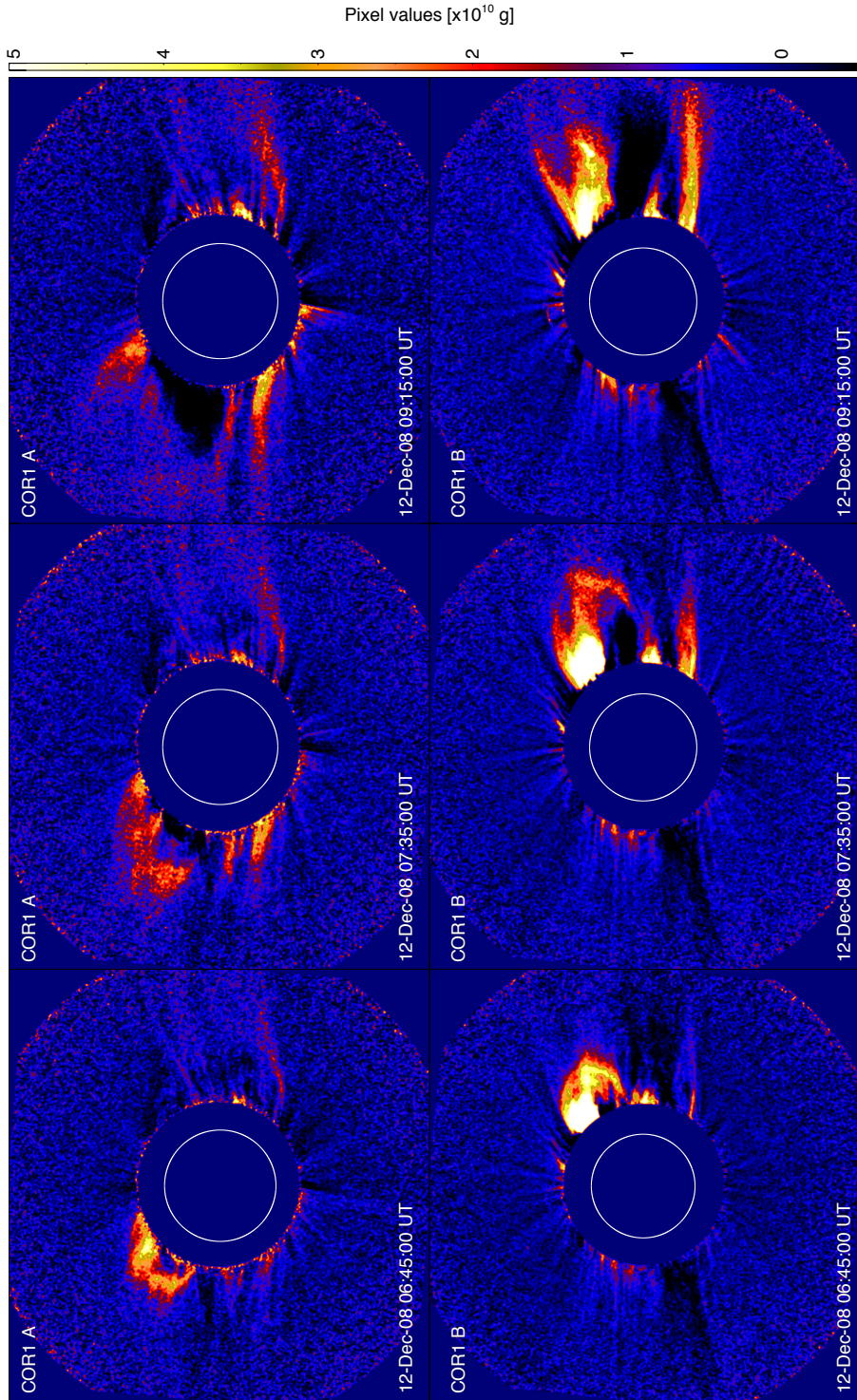


Figure 4.1: Selection of base difference images of the CME in COR1 A (top row) and COR1 B (bottom row). The CME is quite faint in the A images and appears not to have as much structure as in B. As indicated by the color bar on the right, this image has units of grams. The method by which pixel units of grams are derived is described below. Figure adapted from (Carley *et al.*, 2012).

4.2 Observations

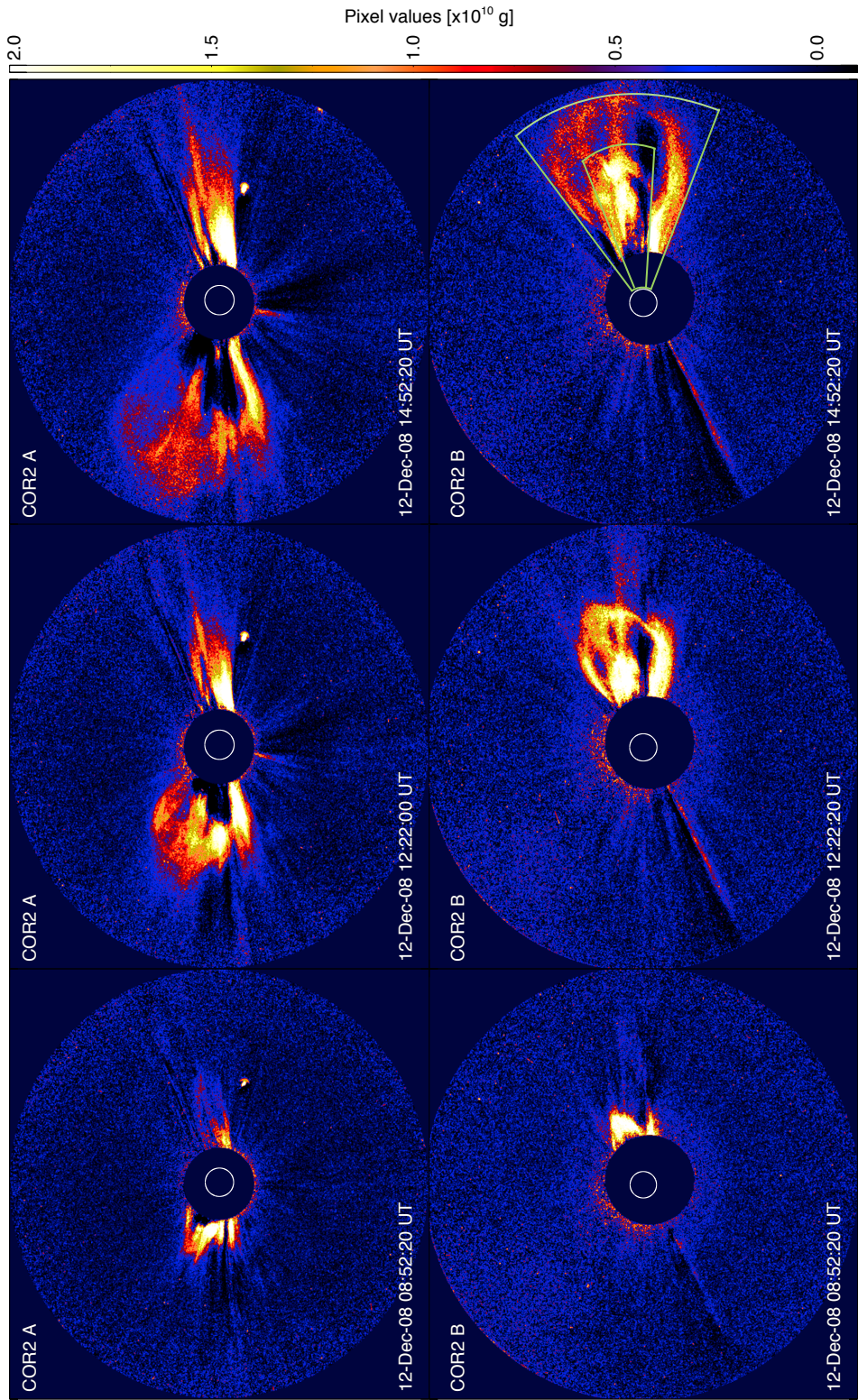


Figure 4.2: Selection of base difference images of the CME in COR2 A (top row) and COR2 B (bottom row). The CME is clearly distinguishable in both fields of view. Only the B field view shows clearly the three part structure of core, cavity and front. As with the COR1 images these images also have units of grams; the method by which grams are calculated is described below. Figure adapted from (Carley *et al.*, 2012).

4.3 Data Analysis

especially at later times, see Figure 4.1 top row, 09:15 UT image. The front of the CME starts to exit both the A and B field of view at \sim 08:35 UT.

The CME first appears in the COR2 field of view at \sim 07:52 UT with the CME apex at a height of \sim 3 R_{\odot} in both A and B images. In the B coronagraph, by 10:52 UT the three part structure of core, cavity, and bright front is clearly visible and the overall structure grows in size as the CME propagates to larger heights. The core becomes more tenuous and the mass distribution becomes homogenous after 15:52 UT when the front starts to exit the field of view. The distinction between core and front is not as clear in COR2 A and the mass distribution appears more homogenous throughout the propagation. As with the COR1 images, COR2 A is also affected by excess brightness in the pre-event image, as is apparent by a growing dark feature in its southern half. As the pre-event image for COR2 B is the cleanest of the pre-event images (it contains the least contamination by streamers), the COR2 B data are considered the best candidate for accurate CME mass measurements.

4.3 Data Analysis

As mentioned, a CME is visible through the Thomson scattering of photospheric light by all electrons in the CME. A conversion from pixel units of mean solar brightness to grams requires a knowledge of how electrons scatter photospheric light in the corona. Before discussing how CME masses are calculated, a brief overview of Thomson scattering theory is given here, along with a discussion of the uncertainties due to some unknowns about the CME position and shape.

4.3.1 Thomson Scattering in the Corona

Thomson scattering involves an incident electromagnetic wave exciting an oscillation of an electron such that the electron radiates like a small dipole. In this way some of the incident electromagnetic energy is ‘scattered’ in a variety of directions, given by the radiation pattern of the oscillating electron. The differential scattering cross section is given by

$$\frac{d\sigma}{d\Omega} = \frac{\text{Radiated Power/unit solid angle}}{\text{Incident Power/unit area}} \quad (4.1)$$

Following (Jackson, 1975), for completely unpolarized incident energy this equates to

$$\frac{d\sigma}{d\Omega} = \left(\frac{e^2}{4\pi\epsilon_0 m_e c^2} \right)^2 \frac{1}{2} (1 + \cos^2 \chi) \quad (4.2)$$

where e is electron charge, m_e is electron mass, c is the speed of light, ϵ_0 is the electric permittivity of free space, and χ is the angle between incident and scattered radiation \mathbf{k} vectors. Integrating this over all solid angles we obtain

$$\sigma_T = \frac{8\pi}{3} \left(\frac{e^2}{4\pi\epsilon_0 m_e c^2} \right)^2 = \frac{8\pi}{3} r_e^2 = 6.65 \times 10^{-29} \text{ m}^2 \quad (4.3)$$

This is the Thomson scattering cross section and the term in brackets is termed the classical electron radius r_e . Classically, any radiation falling on the area defined by r_e^2 will be scattered. An important result is that the cross-section is independent of wavelength of the incident wave; all wavelengths are scattered equally.

Solar photospheric radiation is completely unpolarized, hence the radiation incident on a coronal electron will set it into an oscillation with an amplitude that is equal in all directions. In Figure 4.3, there are two components to the incoming

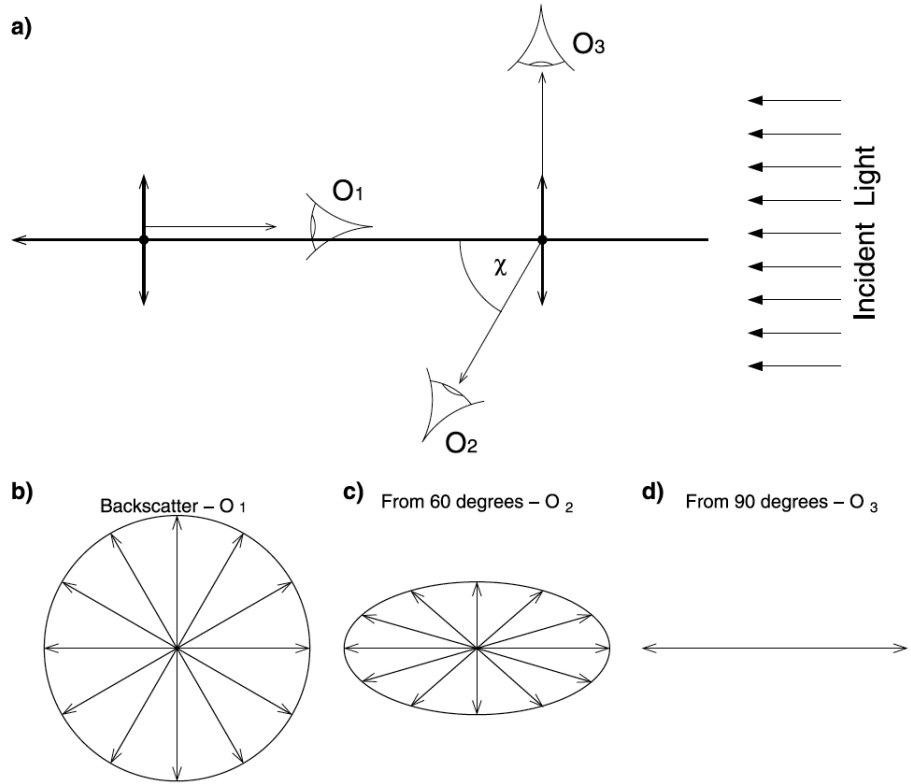


Figure 4.3: Thomson scattering schematic geometry in three dimensions. The incident light is unpolarised and sets the electron into oscillation in directions out of the plane of the page and parallel to it, (a) shows the viewing angles relative to incident radiation. O₁ shows a viewing angle at 0° or 180° and the directions of oscillations seen by the observer (b) – this is completely unpolarised radiation. (c) shows a viewing angle of χ , where the oscillation in the plane of the page is foreshortened, resulting in partially polarised light. (d) shows viewing angles of $\chi = 90^\circ$, which is linearly polarised (Howard & Tappin, 2009).

light, setting the electron into oscillation parallel to the page and perpendicular to it. No matter what the viewing angle, χ , the perpendicular oscillation will always be observed to have the same amplitude. However, the parallel component will be fore-shortened, depending on χ . In this way, the radiation may appear unpolarized (Figure 4.3(b)), partially polarized (Figure 4.3(c)), or completely linearly polarized (Figure 4.3(d)).

Schuster (1879) and Minnaert (1930b) were the first to formalise the Thomson

4.3 Data Analysis

scattering theory for an electron in the solar atmosphere. The electron is set into oscillation by an unpolarized incident intensity I_0 . The two components of radiation observed are the tangential component, I_T in the plane perpendicular to the page, and radial component, I_R in the plane of the page Figure 4.4. These two components are given by the expressions (Howard & Tappin, 2009)

$$I_T = I_0 \frac{\pi\sigma_e}{2z^2} [(1-u)C + uD] \quad (4.4)$$

$$I_P = I_0 \frac{\pi\sigma_e}{2z^2} \sin^2 \chi [(1-u)A + uB] \quad (4.5)$$

$$I_R = I_T - I_P \quad (4.6)$$

where I_0 is incident intensity, σ_e is the electron scattering cross section, z is the distance from scatterer to observer, u is a limb darkening coefficient. I_R is given via a polarization intensity I_P for ease of derivation. These equations describe theoretically the concepts outlined in Figure 4.3 e.g, both I_T and I_R are fully observed at $\chi = 0^\circ$ and $\chi = 180^\circ$, while only I_T is observed at $\chi = 90^\circ$. The main complication for Thomson scattering by a coronal electron is that the Sun is not a point source. The effects of the finite size of the Sun are incorporated into A , B , C , and D in equations (4.2)–(4.4). These are trigonometric expressions known as the van de Hulst coefficients (van de Hulst, 1950), and completely characterise the reception of light by the electron from across the entire solar disk, using only the angle Ω , the angle subtended by the solar disk from point Q shown in Figure 4.4

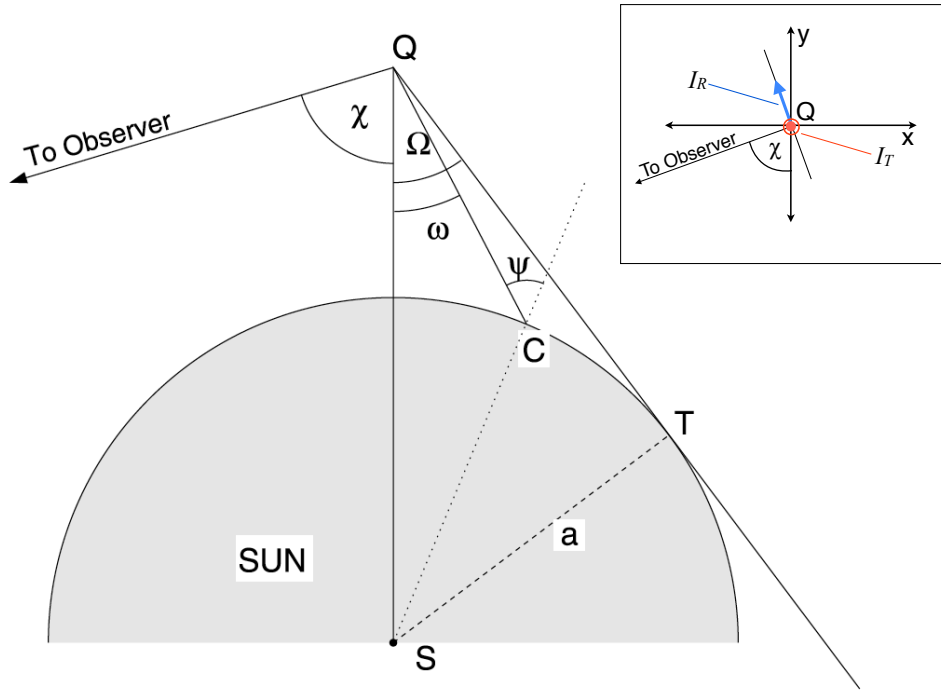


Figure 4.4: Thomson scattering geometry in the solar corona. The orientation of I_R and I_T is shown in the inset. I_R is the projection of electron oscillation in the x direction onto a plane perpendicular to the line from Q to observer. I_R is zero when $\chi = 90$. I_T is due to electron oscillation out of the plane of the page (z -direction), and is completely unaffected by viewing angle. Figure adapted from Figure 3 of Howard & Tappin (2009).

(Billings, 1966a,a; Minnaert, 1930b)

$$A = \cos \Omega \sin^2 \Omega \quad (4.7)$$

$$B = -\frac{1}{8} \left[1 - 3 \sin^2 \Omega - \frac{\cos^2 \Omega}{\sin \Omega} (1 + 3 \sin^2 \Omega) \ln \left(\frac{1 + \sin \Omega}{\cos \Omega} \right) \right] \quad (4.8)$$

$$C = \frac{4}{3} - \cos \Omega - \frac{\cos^3 \Omega}{3} \quad (4.9)$$

$$D = \frac{1}{8} \left[5 + \sin^2 \Omega - \frac{\cos^2 \Omega}{\sin \Omega} (5 - \sin^2 \Omega) \ln \left(\frac{1 + \sin \Omega}{\cos \Omega} \right) \right] \quad (4.10)$$

Each electron in a CME will scatter light according to equations (4.2)–(4.8). They described light scattered by an electron at any position in the solar atmosphere

4.3 Data Analysis

(any Ω), with the observer at viewing angle χ . The intensities given by these equations are for a single electron. If there is a number of electrons N_e at point Q in Figure 4.4, then the intensity would simply be IN_e ; the intensity of scattered light from a point Q depends linearly on the total number of scattering electrons at that point. Hence if we know the intensity of scattered light we may directly infer the total number electrons contributing to this intensity. This allows a calculation of the total electron content of a CME, resulting in a mass calculation. However, the intensity calculation is very sensitive to χ , the viewing angle, and some important aspects of CME observation arise from this.

Along any LOS through the corona, the point at which $\chi = 90^\circ$ will be the point of minimum distance from the Sun Figure 4.5. Three effects must be considered at this point; (i) scattering efficiency is a minimum, (ii) the incident intensity (I_0) received from the Sun is a maximum, and (iii) the electron density is a maximum. The latter two effects, (ii)–(iii), are a bigger contributor to the scattered light than the former, (i). As a result, scattered light is maximized at the point of $\chi = 90^\circ$ along the line of sight, despite the efficiency of scattering being a minimum at this point. Close to the Sun, the plane making an angle of $\chi = 90^\circ$ with the line of sight is known as the plane-of-sky (POS) (Figure 4.5), and is the plane of maximum scattered intensity. Any CME erupting close to the POS will be well observed. However, eruption of a CME at a large angle away from the POS will result in less scattered light from the CME electrons, making the CME appear quite faint. If the angle from the POS is unknown, there is no way of telling the amount by which the intensity is reduced. This can lead to an underestimation of its mass content by up to a factor of 2 (Vourlidas *et al.*, 2000). As described in the next section, unknown viewing angles, θ or χ , are the largest contributor to CME mass uncertainty.

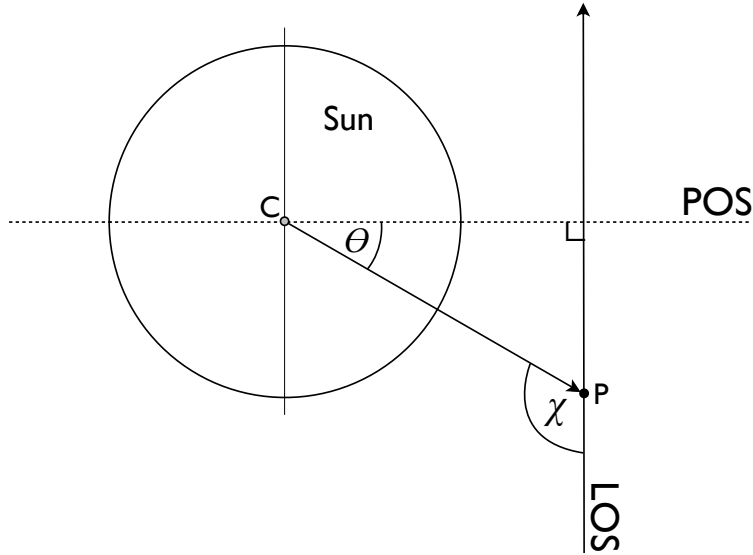


Figure 4.5: Schematic showing the relative orientation of the line-of-sight (LOS), and the plane-of-sky (POS). Electron position is at point P and C is Sun center. The vector CP may also represent CME propagation direction. Scattering efficiency is heavily dependent on the angle θ (or χ) and is least efficient when $\theta = 0^\circ$ ($\chi = 90^\circ$).

4.3.2 Mass Measurement and Geometrical Uncertainties

Calculating the total mass of a CME requires an estimate of the total amount of electrons contributing to the light scattered by the CME. Then assuming that the corona is 90% hydrogen and 10% helium (by number density), each electron will be associated with a mass of 1.97×10^{-24} g. The mass in each pixel of an image of a CME is then

$$m_{pixel} = \frac{I_{obs}}{I_e(\theta)} \times 1.97 \times 10^{-24} \text{ g} \quad (4.11)$$

where I_{obs} is the observed pixel brightness and I_e is a single electron brightness at the position that the pixel images. The brightness $I_e(\theta)$ may be derived from the Thomson scattering equations (4.2)–(4.8), provided the angle θ from the POS

4.3 Data Analysis

is known. If not, a number of assumptions must be made about the position of the electrons along the line of sight. The primary assumptions in all CME mass measurements from white-light observations are

- The CME propagates at right angles to the line-of-sight, along the plane-of-sky at $\theta = 0$.
- All CME electrons are confined to the plane θ ; the CME is a flat 2D object.

These assumption arrises because no information is available on the propagation angle of the CME with respect to the POS. To investigate the effects of the first assumption we need only consider the CME to be a group of electrons located at some P located at angle $\theta > 0^\circ$ from the POS (Figure 4.5). Since for single viewpoint observations no information on θ is available, we must assume $\theta = 0^\circ$ i.e., the electrons are located on the POS. We are assuming that each electron scatters a intensity $I_e(\theta = 0^\circ)$, when in fact it is scattering a smaller intensity of $I_e(\theta > 0^\circ)$. This means we are overestimating the contribution from each electron I_e , leading to an underestimate of the number of scattering electrons $n_e = I_{obs}/I_e$ in equation 4.11. This will give an underestimate of the mass located at point P.

To quantify this underestimation, we plot a single electron brightness at $\theta > 0^\circ$ divided by the POS electron brightness, $I(\theta = 0^\circ)$, as a function of θ (Figure 4.6). For example, an electron located at $\theta = 40^\circ$ will be ~ 0.8 times as bright as an electron on the POS. Although this is for a single electron, it describes the effects of first assumption above. The CME is simply a collection of electrons at $\theta = 40^\circ$, but we assume that the CME is at $\theta = 0^\circ$. In such a case we only observe 80% of the CMEs maximum brightness, but assume we are observing 100%. In this way, we underestimate the total mass content of the CME by 20%. This is the primary source of CME mass underestimation and it is expected that on

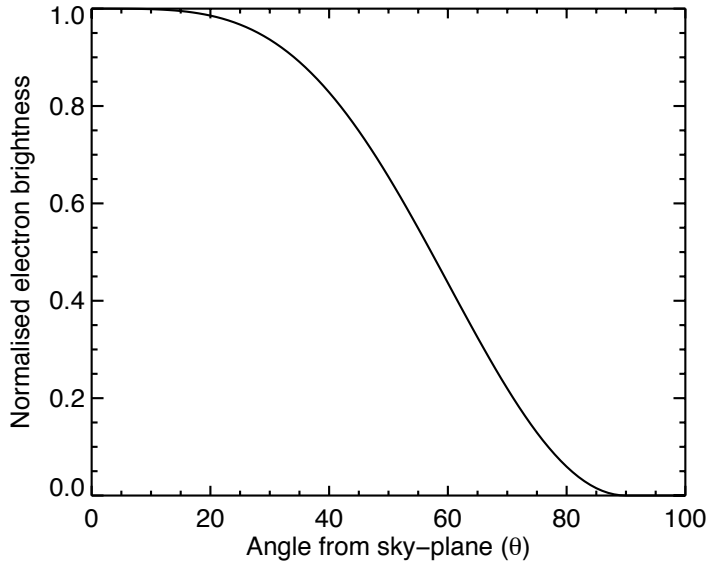


Figure 4.6: Normalized electron brightness ($I_e(\theta > 0)/I_e(\theta = 0)$) as a function of angle from POS θ .

average we underestimate total CME mass by up to a factor of 2 (Vourlidas *et al.*, 2000). For single vantage point observations there is no information about θ , and, realistically, the amount by which the mass is underestimated is completely unknown.

The second above assumption is that all CME material lies on a 2D plane. This arises from the fact that we do not know the distribution of CME material along the line of sight. Since the 3D extent of the CME is unknown it is also assumed that the CME is confined to the 2D sky plane. In order to quantify this, we follow the method of (Vourlidas *et al.*, 2000). This simulates the brightness of a CME with homogeneous density distribution and finite angular width ϕ along the LOS. We use equations the Thomson scattering equations (4.2)–(4.8) to simulated brightness of the CME and calculate a simulated observed mass by assuming that all the brightness is from electrons on the sky plane. This simulated observed mass is then compared to the actual mass as a function of CME height and width (Figure 4.7). For example, our assumption is that all

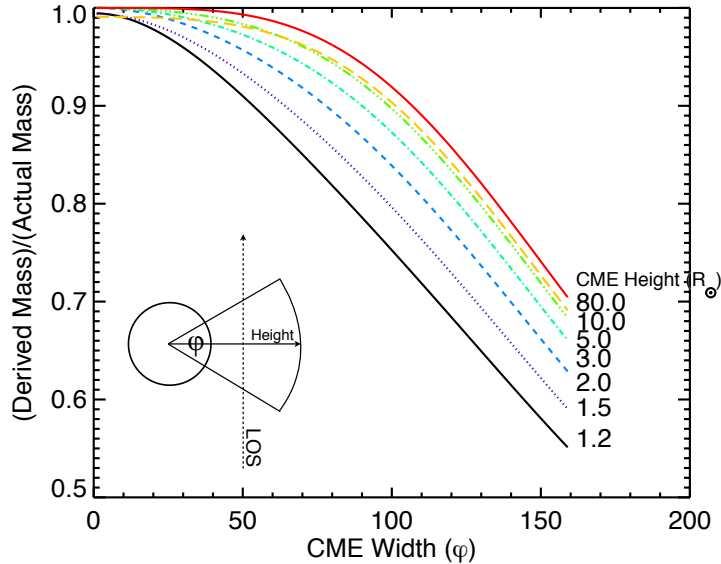


Figure 4.7: CME mass underestimation as function of angular width and height. These results are from a simulated CME with height r , and angular width ϕ . The simulated observed mass (derived mass) is calculated assuming that all electrons lie on the 2D POS, leading to a mass underestimation. This underestimate is quantified by comparing the derived mass with the actual mass.

CME material lies on the POS. However, the CME is centered on the sky-plane with angular width of 100° and a height of $10 R_\odot$. We will derive a mass of ~ 0.9 of the actual mass. The underestimation arises because all electrons are emitting their maximum brightness, when in fact some electrons are away from the sky plane and; this over-estimates the brightness contribution from those electrons, leading to an underestimate in the mass. The mass underestimation from unknown angular width is smaller than the unknown POS angle. However it can be significant for large angular widths at small heights.

Finally, we need to take into account that the CME will be propagating at some angle with respect to the POS *and* have a finite angular width. To estimate the effects of this, we use the Thomson scattering theory to simulate a CME at central position angle from POS θ and width ϕ . We derive the simulated observed mass, given the assumption that the CME is on the sky-plane, and also

4.3 Data Analysis

the assumption that the CME material is in a 2D plane at θ . This simulated observed mass is compared to actual mass to derive mass underestimation in both cases. This simulation is shown in Figure 4.8. The dashed lines are the derived mass assuming that the CME has no angular width ($\pi = 0^\circ$) and is on the sky-plane ($\theta = 0^\circ$), when in fact it has finite width ϕ and is located at some $\theta > 0$ (x-axis). The solid lines are derived mass assuming the CME lies on a 2D plane at the plane of sky angle θ , this is called a 'de-projection' of the CME from the POS to its propagation plane at θ . For example in Figure 4.8(b), if the CME is at a height of $5 R_\odot$, has a position angle of 40° , and an angular width of 120° , but we assume it has no width (2D) and is located on the sky-plane ($\theta = 0^\circ$), then its derived mass will be ~ 0.6 times the actual mass (underestimate of $\sim 40\%$). If the CME is de-projected (we account for its sky-plane angle), then the derived mass is improved to a factor of 0.8 of the actual mass. Note that de-projection still assumes the CME has no width ($\phi = 0$), hence there is still a mass underestimation after de-projection.

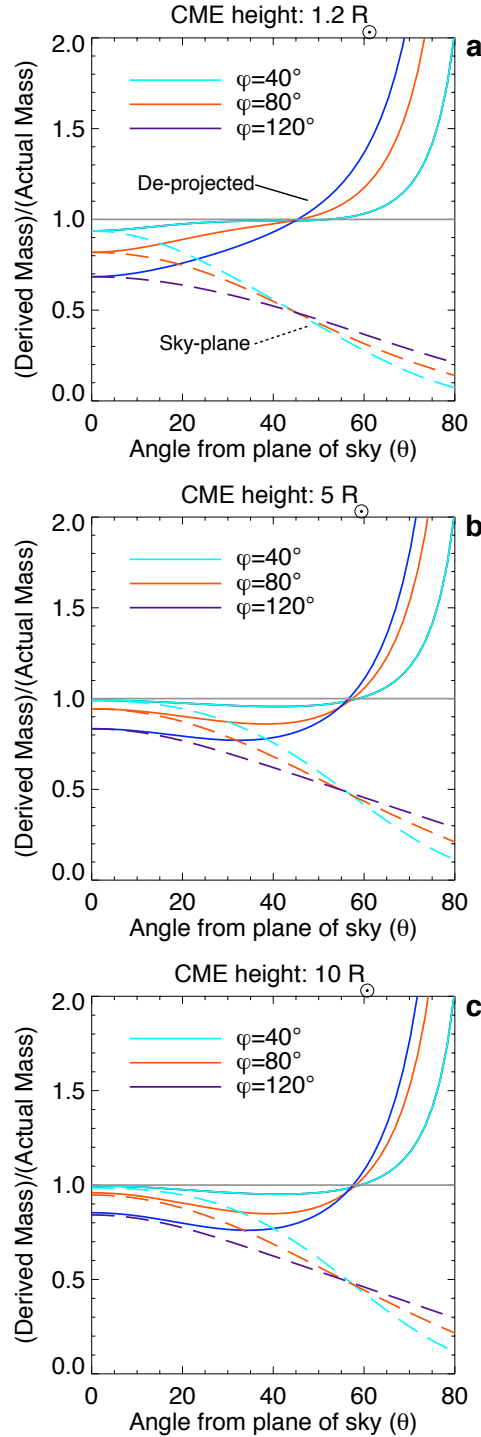


Figure 4.8: Underestimation of CME mass as a function of angle from the plane of sky. The colors correspond to a CME of angular width ϕ . Three different heights are shown. The dashed lines are mass underestimation assuming the CME has zero width ($\phi = 0$) on the POS ($\theta = 0$), when in fact it has finite width of ϕ and is located at θ from POS. The solid lines account for the plane of sky angle θ (they are deprojected). De-projection improves the mass underestimation up to $\theta = 60^\circ$, after which it severely overestimates the CME mass.

There is an interesting point at $\theta = 55^\circ$ for the $5 R_\odot$ and $10 R_\odot$ plots (and all larger heights). For all angular widths ϕ , a de-projection will derive exactly the actual CME mass. Beyond this point, de-projection starts to over-estimate the CME mass and eventually overestimates it by a severe estimate at sky-plane angle greater than 70° . As we will see, the CME in this study had a POS angle of 45° and an angular width no greater than 90° for the height range of $1.4\text{--}12 R_\odot$. Therefore, as shown in Figure 4.8, a de-projection of the CME brightness to its propagation plane underestimates the mass by a smaller factor than assuming the CME is on the POS.

4.3.3 Evaluation of uncertainties

The CME of 2008 December 12 was Earth-directed (Byrne *et al.*, 2010), making it roughly the same angular distance from both the *STEREO* A and B spacecraft, then located ± 45 degrees from Earth. This known angle of propagation was used to convert from pixel values of MSB to grams via the equation 4.11. The known angle of propagation allowed the correct value of I_e to be computed resulting in a significant reduction in the uncertainties associated with the propagation angle e.g., mass uncertainty due to the first assumption above was eradicated and the only remaining uncertainty was from the unknown finite angular width. Given that we know the de-projection angle, a measure of the angular width along the line of sight ϕ is needed to quantify the finite angular width uncertainty. It is possible derive the angular width along the line of sight, ϕ , in terms of the CME latitudinal width ψ . We assume that $\phi \leq 2\psi$. Such an upper limit is in agreement with simulations of flux-rope CMEs which give a typical aspect ratio of broadside to axial angular extents of $1.6\text{--}1.9$ (Krall & St. Cyr, 2006). Byrne *et al.* (2010) provided a measure of latitudinal width as a function heliocentric distance of

4.3 Data Analysis

the CME, $\psi(r) = 25r^{0.22}$, giving $\phi \leq 50r^{0.22}$. Given that the position from the sky-plane of each spacecraft was 45° , and the angular widths of the CME were $< 90^\circ$, there was a CME mass underestimation estimates of between 5–10% for de-projected finite angular width uncertainty. Since the angular width along the line of sight is likely to be much less than 2ψ , the 10% uncertainty is an upper limit.

Apart from the geometrical uncertainties quoted above there were a number of other minor uncertainties. The deflection of a small streamer during CME propagation produces negative pixels in the base difference images. The effect is particularly apparent in the COR1 images, Figure 4.1. It is difficult to unambiguously distinguish between streamer and CME, making it difficult to quantify the uncertainty introduced due to streamer interaction. To make an estimate of the streamer’s effects, a calculation of its mass in the pre-event image was made. A number of different samples of the area of the streamer in the COR1 B pre-event image that effects all subsequent images produced a mass estimate of $\sim 5 \times 10^{14}$ g. This mass was used as a measure of the uncertainty introduced due to streamer interaction in the COR1 B images. A similar analysis of the COR1 A pre-event images gave a streamer mass estimate of $\sim 7 \times 10^{14}$ g. COR2 images are relatively unaffected by significant changes in background coronal brightness and do not suffer from negative pixel values to as large an extent as COR1. The pre-event image of COR2 B is particularly clean and free of background streamers, hence COR2 B images are considered to provide most accurate CME mass estimation. Finally, An extra mass uncertainty of 6% was added to account for the assumption of coronal abundance of 90% hydrogen and 10% helium which can lead to slight errors while converting from pixel values of MSB to grams (Vourlidas *et al.*, 2010).

4.4 Results

4.4.1 Mass vs. Time and Height

To calculate the total CME mass a user-selected area (the extent of the CME, for example) of the base difference image was chosen and the pixel values within this area were summed to obtain total mass. Figure 4.2 COR2 B images show an example of the sector over which pixels were summed (the smaller sectors indicate a different summing region used at a later stage). In order to obtain a more complete and continuous estimate of CME mass growth, the masses determined from both COR1 and COR2 coronagraphs were summed in those cases where image times of the inner and outer coronagraphs overlapped. This was done for each point and time to produce CME mass development with height and time

The results of the calculation for CME mass development with time and height for both *STEREO* A and B coronagraphs are shown in Figure 4.9. In panel (a), the height values are those taken from a point-and-click method of tracking the CME apex; these heights are corrected for CME propagation angle of $\sim 45^\circ$. In both panels (a) and (b), the mass estimates of *STEREO* A and B follow a similar trend and have similar values at each stage in the propagation. Such good agreement between mass values is a good indicator that $\sim 45^\circ$ is the correct angle of propagation from the sky-plane. A change in the cadence of mass measurements is noticeable at $\sim 08:00$ UT (or $\gtrsim 5 R_\odot$). This is due to the use of only COR1 images (with a cadence of 10 minutes) prior to this time, and the use of the COR2 plus COR1 images after this time (the cadence of these measurements follows that of COR2 – 30 minutes). Comparing A and B below $4.5 R_\odot$, mass values show a similar trend and increase at the same rate, but at approximately $3 R_\odot$ the mass measurements in COR1B appear to increase to a much larger value than fall

4.4 Results

again. This effect is visible in the COR1A measurements, albeit diminished. It is probably due to the presence of a prominence which contains a significant mass content and therefore contributes a large amount to total measured CME mass. Also, early on in its propagation, the prominence may still be emitting H- α line radiation (656.28 nm) due to the larger fraction of neutral hydrogen at its cooler temperatures. The COR1 imaging passband is centered on H- α so any emission in the prominence from neutral hydrogen could be contributing to light received by the COR1 coronagraphs, this is apparent from the saturation region in the COR1B images in Figure 4.1. Since this is resonance line emission, and not Thomson scattered emission, it leads to an erroneous measurement in CME mass. Thus, it is assumed the larger rise and fall in CME mass is caused by the prominence entering and exiting the COR1B field of view. The effect is diminished in COR1A since the prominence does not enter the FOV to as large an extent as in COR1B. The interpretation that the ‘mass bump’ is not actual mass growth (or loss) is supported by previous measurements where CME mass increase follows a trend with height described by

$$M_{cme}(h) = M_a(1 - e^{-h/H_a}) \quad (4.12)$$

where M_a is the final mass the CME approaches asymptotically and H_a is the height at which the CME reaches $0.63M_a$ (Colaninno & Vourlidas, 2009), with no ‘bump’ in mass earlier on. The decline in mass after the peak may be explained by the ionization of neutral hydrogen such that H α emission diminishes and simply becomes Thomson scattering of free electrons, as with the rest of the CME material.

In order to produce a fit to the data, the COR2B mass results were chosen because its pre-event image was largely free of any bright streamers or other

4.4 Results

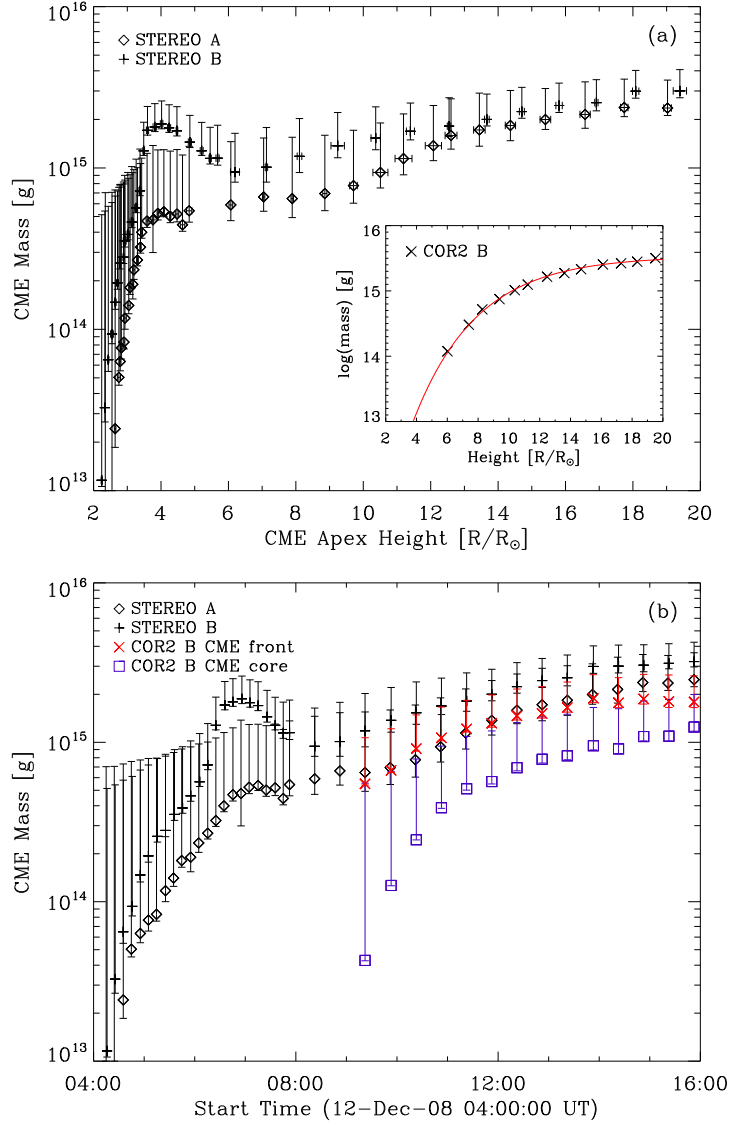


Figure 4.9: CME mass development with height (a) and time (b), for the 2008 December 12 CME. After $\sim 08:00$ UT ($\gtrsim 5 R_\odot$) the masses from the inner and outer coronagraphs are summed to show uninterrupted mass development from ~ 2 – $20 R_\odot$ over a period of 12 hours. The small bump in the CME mass at $\sim 07:00$ UT ($\sim 4 R_\odot$) is probably due to an unknown amount of H- α emission from the prominence. Mass of CME front and core are also shown, red ‘ \times ’ and blue square, for COR2 B, panel (b). After 14:52 UT they share approximately equal mass. The inset of (a) shows mass development with height for COR2 B only; the red curve represents a fit to the data whereby the mass asymptotically approaches $3.4 \pm 1.0 \times 10^{15}$ g (Carley *et al.*, 2012).

4.4 Results

features which introduce unwanted effects in the production of base difference images, as described above. A fit with the above equation resulted in a final asymptotic CME mass of $3.4 \pm 1.0 \times 10^{15}$ g, with a scale height of $h_a = 2.9 R_\odot$. This fit is plotted along with the COR2B data in the inset panel of Figure 4.9(a). Note that the mass increase is due to material coming up from below the occulting disk, and not actual mass gain of the CME. The uncertainty on the above asymptotic mass value was taken to be 30%, from the largest uncertainty due to finite width, the conversion factor uncertainty as described above, the standard error user-generated uncertainty, and uncertainty due to streamer interaction.

In each image where the CME core and front are distinguishable, their masses were measured separately. This was regions demarcating the areas of core and front, see COR2B at 12:22 UT and 14:52 UT in Figure 4.2 for an example of the separate core and front sectors over which pixel values were summed to obtain total mass. The uncertainties due to finite width of the observed object also apply to the core and front measurements, however, since the widths of these particular areas of the CME are unknown we chose the maximum uncertainty of 10% from the above analysis since neither core nor front can be any wider than the maximum width assigned to this CME. The remaining uncertainties described above were also applied. The mass development of core and front with time is shown in Figure 4.9(b). The two mass measurements are subject to an observational effect of apparent exponential mass growth, however by the time the CME is fully in the field of view at 14:45 UT the core and front share approximately equal mass.

4.4.2 Kinematics and Dynamics

In the following calculations, all measurements of force and kinetic energy use the asymptotic mass of $3.4 \pm 1.0 \times 10^{15}$ g and not the instantaneous mass values calculated from each coronagraph image i.e., the CME is considered to begin its propagation with this mass and does not acquire any mass as it propagates.

Estimates of the force and kinetic energy use the 3-D velocity and acceleration measurements produced by Byrne *et al.* (2010). Their method firstly identifies the CME front in each coronagraph image using a multiscale edge detection filter. The front edges were then used to define a quadrilateral in space into which an ellipse is fit, this method is known as elliptical tie-pointing. This was done for multiple horizontal planes through the CME so that the fit ellipses outline a curved front in 3-D space. The speed and acceleration were then deduced from the change in position of the front, with time, through the *STEREO* COR1, COR2 and HI fields of view. Since mass measurements in this study use only the COR1 and COR2 coronagraphs, HI kinematics measurements have been excluded here. The CME front position uncertainty in *STEREO A* and *B* coronagraphs was determined from the filter width in the multiscale analysis. Velocity and acceleration uncertainties were then propagated from position uncertainty. Figure 4.10(a) shows CME velocity as a function of heliocentric distance, along with acceleration in panel (b).

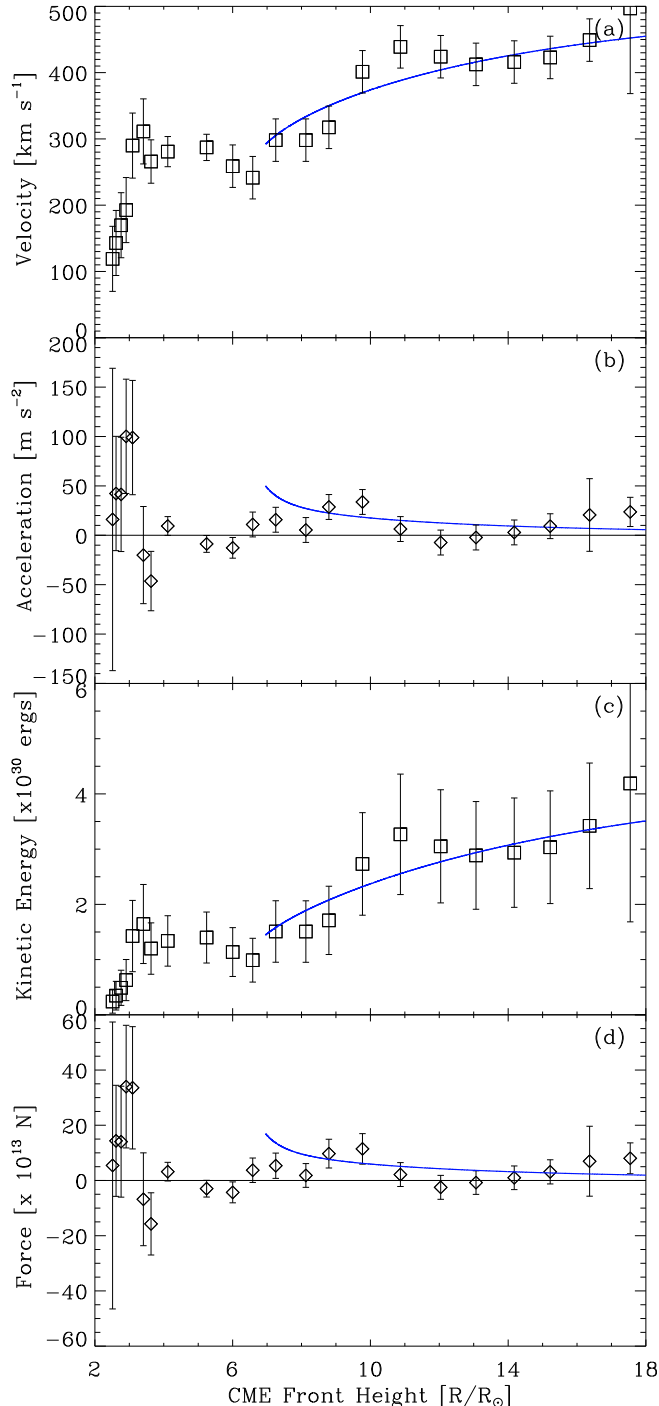


Figure 4.10: (a) CME velocity as a function of heliocentric distance, including a fit to the data produced using an aerodynamic drag model beyond $\sim 7 R_{\odot}$ (Byrne *et al.*, 2010). (b) Acceleration of CME, including fit, derived from the velocity data and fit. Panel (c) and (d) show the kinetic energy and force, respectively, both calculated using constant CME mass of $3.4 \pm 1.0 \times 10^{15} \text{ g}$ and kinematics results from (a) and (b). Also shown are the fits to energy and force produced from fits to velocity and acceleration (Carley *et al.*, 2012).

4.4 Results

The CME kinetic energy was calculated using $E_{kin} = 1/2M_{cme}v_{cme}^2$, where M_{cme} is the final asymptotic mass of $3.4 \pm 1.0 \times 10^{15}$ g and v_{cme} are the instantaneous velocity measurements, results of this calculation are shown in Figure 4.10(c). The kinetic energy shows an initial rise towards $6.3 \pm 3.7 \times 10^{29}$ ergs at $\sim 3 R_\odot$, beyond which it rises steadily to $4.2 \pm 2.5 \times 10^{30}$ ergs at $\sim 18 R_\odot$, these values are similar to those reported in Vourlidas *et al.* (2000, 2010) and Emslie *et al.* (2004).

The total force on the CME was calculated using $F_{total} = M_{cme}a_{cme}$, where M_{cme} is as above and a_{cme} is taken from the instantaneous acceleration values. As shown in panel (d) of Figure 4.10, the force initially grows significantly, reaching a maximum value of $3.4 \pm 2.2 \times 10^{14}$ N at $\sim 3 R_\odot$. The early rise and fall in acceleration (or force) is in agreement with a previous study of a CME observed to reach peak acceleration at $\sim 1.7 R_\odot$ after which it reaches a constant velocity beyond $\sim 3.4 R_\odot$ (Gallagher *et al.*, 2003). Such results are also found in a statistical study which shows that the majority of CMEs have peak acceleration in the low corona with a mean height of maximum acceleration at $1.5 R_\odot$ (Bein *et al.*, 2011). Similarly, observational studies by Zhang *et al.* (2001) and Zhang *et al.* (2004) also show early phase peak acceleration between $2\text{--}5 R_\odot$ and forces on the order of 10^{15} N and 10^{12} N, depending on whether the CME shows large initial acceleration or a slow, more gradual acceleration.

After this early peak, the force drops to an average value of $3.8 \pm 5.4 \times 10^{13}$ N at distances between $7\text{--}18 R_\odot$. It is apparent from Figure 4.10(a) that the velocity continues to increase beyond $7 R_\odot$, implying that a positive radial force must be present. To clarify this, a fit to the velocity data using a model for solar wind drag on the CME beyond $7 R_\odot$ (as outlined in Byrne *et al.* (2010)) is shown in Figure 4.10(a). Although the data suggest a non-monotonic increase in velocity,

the fit reveals that propagation is best described by a steadily increasing velocity between $7\text{--}18 R_{\odot}$. The acceleration and kinetic energy curves derived from this velocity fit are shown in Figure 4.10(b) and (c). In Figure 4.10(d), the curve for the force derived from the velocity fit initially deviates from the data at $\sim 7 R_{\odot}$, however beyond this distance there is good agreement with the data and the derived force is entirely positive. This suggests that the solar wind exerts a positive aerodynamic drag force on the CME, resulting in a velocity that approaches the asymptotic solar wind speed at large heliospheric distances.

4.4.3 Evaluation of Forces

It should be noted that Figure 4.9 shows an overall exponential increase in CME mass with height which could be interpreted as the CME rapidly gaining mass as it propagates. Care should be taken with this interpretation since this apparent exponential mass increase is almost certainly due to the CME moving into the field of view, therefore allowing us to measure more of its mass content; such an interpretation is in agreement with similar assertions made in Vourlidas *et al.* (2010). It is difficult to distinguish between actual CME mass growth and an apparent growth due to more of the CME being observed. If the initial early rise in CME mass is assumed to be an observational artifact then we can interpret the CME mass to be in the range of $(3\text{--}3.5)\times 10^{15} \text{ g}$ for most of its early propagation i.e., the CME already has such a mass before launch and does not acquire more mass (via inflows or otherwise) during propagation. Such an interpretation is in agreement with CME mass measurements calculated from dimmings in *STEREO* Extreme Ultraviolet Image(EUVI) images, which show the mass calculated from EUV images to be approximately equal to CME mass in COR2 images, $m_{\text{EUVI}}/m_{\text{COR2}} = 1.1 \pm 0.3$ (Aschwanden *et al.*, 2009). Once the CME

4.4 Results

bubble is in the field of view at $\sim 10 R_\odot$ the mass in its entirety can be measured and the increase beyond this point, if any, is slow and steady, Figure 4.9.

The early stages of CME propagation are dominated by a sharp rise to a peak force of $3.4 \pm 2.2 \times 10^{14}$ N at $\sim 3 R_\odot$ followed by a sharp decline, Figure 4.10(d). The catastrophe model (Forbes & Isenberg, 1991; Forbes & Priest, 1995; Lin & Forbes, 2000), magnetic breakout model (Antiochos *et al.*, 1999b; Lynch *et al.*, 2008), and toroidal instability model (Chen, 1996; Kliem & Török, 2006) employ a number of forces acting on the CME to produce an over all acceleration into interplanetary space. For example, the toroidal instability model used by Chen (1996) uses a Lorentz hoop force (or Lorentz self-force), solar wind drag, and gravity to provide a net force acting on the CME between $2\text{--}3 R_\odot$ that quickly rises to a peak total force of $\sim 10^{16}$ N and then falls rapidly.

If we assume that the peak force observed for the 2008 December 12 CME is the net force due to similar forces used in the above models, such as the solar wind drag, gravity, and some form of magnetic CME driver e.g., a $\mathbf{J} \times \mathbf{B}$ force, we may estimate their relative contribution. The force due to solar wind drag on the CME is given by

$$\mathbf{F}_d = -\frac{1}{2}C_d\rho_{sw}A_{cme}(\mathbf{v} - \mathbf{v}_{sw}) | \mathbf{v} - \mathbf{v}_{sw} | \quad (4.13)$$

where M_{cme} is the CME mass, \mathbf{v} is the CME velocity, C_d is the drag coefficient, ρ_{sw} is the solar wind mass density, A_{cme} is the CME area exposed to solar wind drag and \mathbf{v}_{sw} is the solar wind velocity (Maloney & Gallagher, 2010). To estimate the effects of this force we use $\rho_{sw} = n_p m_p$, where m_p is proton mass, and assume ionization fraction of $\chi = 1$ such that $n_p = n_e [cm^{-3}]$. Electron density, and hence proton density, is then given by an interplanetary density model derived from a special solution of the Parker solar wind equation (Mann *et al.*, 1999), solar wind

4.4 Results

velocity values as a function of height are also determined using this model. A_{cme} is estimated using the expression derived in Byrne *et al.* (2010) for latitudinal angular width of the CME as a function of height, $\psi(r) = 26r^{0.22}$. This is used to derive an arc length of the CME front and, as above, making the assumption $\phi = 2\psi$, the two arc lengths derived from these angles then give the surface that the solar wind acts on, thus $A_{cme} = 1352r^{2.44}$. Setting the drag coefficient $C_d = 1$, and using the Mann *et al.* (1999) model to derive a density and a solar wind velocity of $2.3 \times 10^5 \text{ cm}^{-3}$ and 70 km s^{-1} , respectively, equation [1] then gives a force of $\mathbf{F}_d = -8.0 \times 10^{12} \hat{r} \text{ N}$ for solar wind drag at $\sim 3 R_\odot$, where \hat{r} is a unit vector in the positive radial direction.

A simple estimate of force due to gravity is given by $\mathbf{F}_g = GM_\odot M_{cme}/\mathbf{r}^2$, where G is the universal gravitational constant, M_\odot is solar mass, M_{cme} is CME mass, and \mathbf{r} is a heliocentric position vector¹. Given a CME mass of $3.4 \times 10^{15} \text{ g}$ the force due to gravity at a heliocentric distance of $3 R_\odot$ is $\mathbf{F}_g = -1.0 \times 10^{14} \hat{r} \text{ N}$. From the MHD momentum conservation equation (equation 2.12), the only remaining contribution is due to some form of magnetic CME driver, F_{mag} , which is estimated using

$$\mathbf{F}_{mag} = \mathbf{F}_{total} - \mathbf{F}_d - \mathbf{F}_g \quad (4.14)$$

(the pressure gradient in the CME equation of motion is assumed to be negligible and has been omitted here). Using the above values, the total magnetic contribution to CME force is calculated to be $\mathbf{F}_{mag} \approx 4.5 \times 10^{14} \hat{r} \text{ N}$ at $3 R_\odot$, indicating that this is the largest driver of CMEs at low coronal heights. Lorentz force dominated dynamics in early phase CME propagation are reported in Bein

¹Ideally the heliocentric distance of the CME centre of mass would be used here. However an unknown amount of mass is obscured by the coronagraphs occulting disk, making the mass distribution and hence COM difficult to determine. Thus the CME front height is used in the calculation of force due to gravity

et al. (2011), in which a statistical study of a large sample of CMEs in EUVI, COR1, and COR2 indicated an early phase acceleration for the majority of CMEs that is attributable to a Lorentz force. A similar result of an observational study by Vršnak (2006) found that the Lorentz force plays a dominant role within a few solar radii. It should be noted that although we have labelled the force F_{mag} , there is no distinction on the exact form of this force e.g., whether it is magnetic pressure, magnetic tension, or a Lorentz self-force that acts as the driver. Also, any non-radial motion of the CME, such as that described in Byrne *et al.* (2010), is not taken into account here; any force estimates are purely radial in direction.

4.5 Conclusion

The *STEREO* COR1/2 coronagraphs have been used to determine the mass development of the 2008 December 12 CME. Knowledge of the longitudinal propagation angle of the CME allowed for a significant reduction in the mass uncertainty, giving a final estimate of $3.4 \pm 1.0 \times 10^{15}$ g. Using kinematics results of a previous study (Byrne *et al.*, 2010), the velocity and acceleration of the CME were combined with the mass measurements to determine the kinetic energy and total force on the CME. The early phase propagation of the CME was found to be dominated by a force of peak magnitude of $3.4 \pm 2.2 \times 10^{14}$ N at $\sim 3.0 R_\odot$, after which the magnitude declines rapidly and settles to an average of $3.8 \pm 5.4 \times 10^{13}$ N. This early rise and fall in total force (or acceleration) is in agreement with previous observations of CME kinematics (Bein *et al.*, 2011; Gallagher *et al.*, 2003). Similarly results of observational studies by Zhang *et al.* (2001) and Zhang *et al.* (2004) also show early phase peak acceleration between $2\text{--}5 R_\odot$ and forces on the order of 10^{15} N and 10^{12} N. The kinetic energy shows an initial rise steadily to $4.2 \pm 2.5 \times 10^{30}$ ergs at $\sim 18 R_\odot$, such order of magnitudes are similar to those

4.5 Conclusion

reported in Emslie *et al.* (2004); Vourlidas *et al.* (2000) and are typical of CME kinetic energies (Vourlidas *et al.*, 2010).

Such CME kinematics and dynamics property estimates cannot be carried out when unknown propagation angle hinders an accurate calculation of CME mass, hence adding unacceptable uncertainty to any subsequent calculations. This highlights the need for similar studies using the *STEREO* mission's ability to accurately determine the physical properties of CMEs, such as mass, with remarkably reduced uncertainty. Increasing the accuracy of force estimates of other well studied CMEs will allow for a more complete view of the magnitude of the forces influencing CME propagation and will allow model parameters to be more accurately constrained.

5

Coronal Mass Ejection Shocks and Particle Acceleration

CMEs often erupt at speeds in excess of the local magnetoacoustic wave speeds in the corona. Traveling in excess of Alfvén Mach 1, they often drive shocks which can have a variety of physical manifestations, such as radio bursts, coronal bright fronts (CBFs), white-light enhancements, and the in-situ detection of energetic particles. Despite such a variety of shock phenomena being observed for decades, the unifying physical mechanism between these phenomena remains unknown. This chapter will provide an analysis that uses extreme ultraviolet, radio, and white-light imaging of an eruptive event on 22 September 2011 to determine the properties of a CME-driven shock in the corona. The results show that a plasma shock with an Alfvén Mach number of $2.4_{-0.8}^{+0.7}$ was coincident with a coronal bright front and an intense metric radio burst generated by electrons with kinetic energies of 2–46 keV. This work provides new evidence to show that the relationship between CMEs, CBFs, and radio radio bursts can be a coronal shock driven by the CME flank. The chapter is based on publications by Carley et al., *Nature Physics*, 2013, and Zucca et al., *Astronomy & Astrophysics*, submitted.

5.1 Introduction

Coronal mass ejections (CMEs) are often associated with plasma shocks and the acceleration of particles to relativistic speeds (Grechnev *et al.*, 2011b; Klassen *et al.*, 2002). However, the underlying mechanism relating CMEs, shocks, and particle acceleration is still a subject of intense debate (Vršnak & Cliver, 2008). By clarifying the inherent characteristics of these phenomena we learn not only about the nature of explosive plasma events but also about how they drive shocks and accelerate particles to high energies. The understanding of such processes are important for fundamental solar physics, plasma physics, and space weather predictions.

CME-associated shocks are often observed over a variety of spectral bands. At radio frequencies, high intensity ($\sim 10^8$ Jy) emissions, known as type II and type III bursts, are associated with coronal shocks and accelerated particles in the solar corona (Mann *et al.*, 1996; Wild, 1950). Fine structure in these radio bursts can often reveal a ‘bursty’ nature to the shock particle acceleration (Mann & Klassen, 2005), which can reveal details of the internal shock structure (Guo & Giacalone, 2010; Zlobec *et al.*, 1993). At extreme ultraviolet (EUV) wavelengths, the shock or pressure pulse response of the corona to an eruption may be imaged as a bright pulse propagating across the entire solar disk at typical velocities of 200–400 km s⁻¹ (Gallagher & Long, 2011). These ‘coronal bright fronts’ (CBFs) are a regular feature of solar eruptive events and often display wave-like properties such as reflection (Gopalswamy *et al.*, 2009b), refraction (Wang, 2000) and pulse broadening (Long *et al.*, 2011b). Like CMEs, CBFs are often accompanied by type II and type III radio bursts, with EUV and radio images revealing a spatial link between the phenomena that is suggestive of a common origin (Kozarev *et al.*,

2011; Maia & Pick, 2004; Vršnak *et al.*, 2005b).

It has been proposed that the common origin for these myriad phenomena may be a CME-driven shock (Grechnev *et al.*, 2011b; Warmuth *et al.*, 2004). In this scenario, the CME eruption drives a pressure pulse, observable in the low corona as a propagating wave-like CBF. Higher in the corona this same pulse forms a shock, accelerating particles and producing type II and III emission. However, much debate surrounds the suggestion that (i) the CBF is a plasma pressure wave driven by a CME, and (ii) the radio bursts, generated by accelerated particles, result from this same wave/shock system. The contention has arisen from attempts to explain non-wave kinematics of CBFs (Zhukov *et al.*, 2009). Pseudo-wave theories are employed to describe this behavior, where the erupting CME produces a large-scale restructuring of the coronal magnetic field, which results in a propagating bright pulse (via Joule plasma heating) that is not actually a driven wave (Delannée *et al.*, 2008). In this scenario, any relationship with shock observables is indirect. Further confusion is added by the possibility that high energy particles in association with the eruption may be a consequence of magnetic reconnection in the flaring active region, and not the result of a shock (Kahler, 2007).

Collectively, CMEs, CBFs and radio bursts provide direct measures of both shock kinematics and the characteristics of the accompanying accelerated particles. However, a common theory explaining these phenomena has yet to be verified. This lack of clarity can be ascribed to an EUV imaging cadence that was unable to match the fast time sampling of radio imaging and spectroscopy. Now, using the high image cadence of the Solar Dynamics Observatory (SDO; Pesnell *et al.*, 2012), combined with fast time sampling radio images and spectra, we can reveal previously unseen characteristics of the relationship between

5.2 Coronal Bright Front and Radio Source

these phenomena, proving that a CME-driven shock is the feature unifying these observations and that this shock is responsible for bursty electron acceleration. This greatly advances our understanding of the close relationship between solar eruptions, plasma shocks and their resulting EUV, radio and particle acceleration signatures.

5.2 Coronal Bright Front and Radio Source

5.2.1 Observations

On 22 September 2011 at 10:29 UT, an X-ray flare (GOES class X1.4) began in an active region located on the east limb of the Sun (NOAA active region 11302; N13E78). Approximately 11 minutes after the flare start time, a bright wave-like front (CBF) was observed propagating away from the southern edge of the active region in SDO/Atmospheric Imaging Assembly (AIA; Lemen *et al.*, 2012) 21.1 nm passband images. The CBF then propagated along the east limb from $\sim 15^\circ$ south to $\sim 50^\circ$ south of the equator (Figure. 5.1). During the same period of the CBF propagation, a bright 150.9 MHz source formed above the CBF, imaged using the Nançay Radioheliograph (NRH; Kerdraon & Delouis, 1997) (contours Figure. 5.1). In each image the contours range from T_{peak} to $0.95T_{peak}$, where T_{peak} is the peak brightness temperature at the time of the image; the intensity of the contours is indicated by the colour bar on the right. Initially, both the erupting structure seen in the AIA image and the radio source had the same spatial extent over latitude (Figure. 5.1a), showing they belong to a common structure. After this, the most southern part of the radio source reached an extremely high brightness temperature ($\sim 10^9$ K) and closely followed the propagation of the CBF southward until it eventually diminished into the thermal background

5.2 Coronal Bright Front and Radio Source

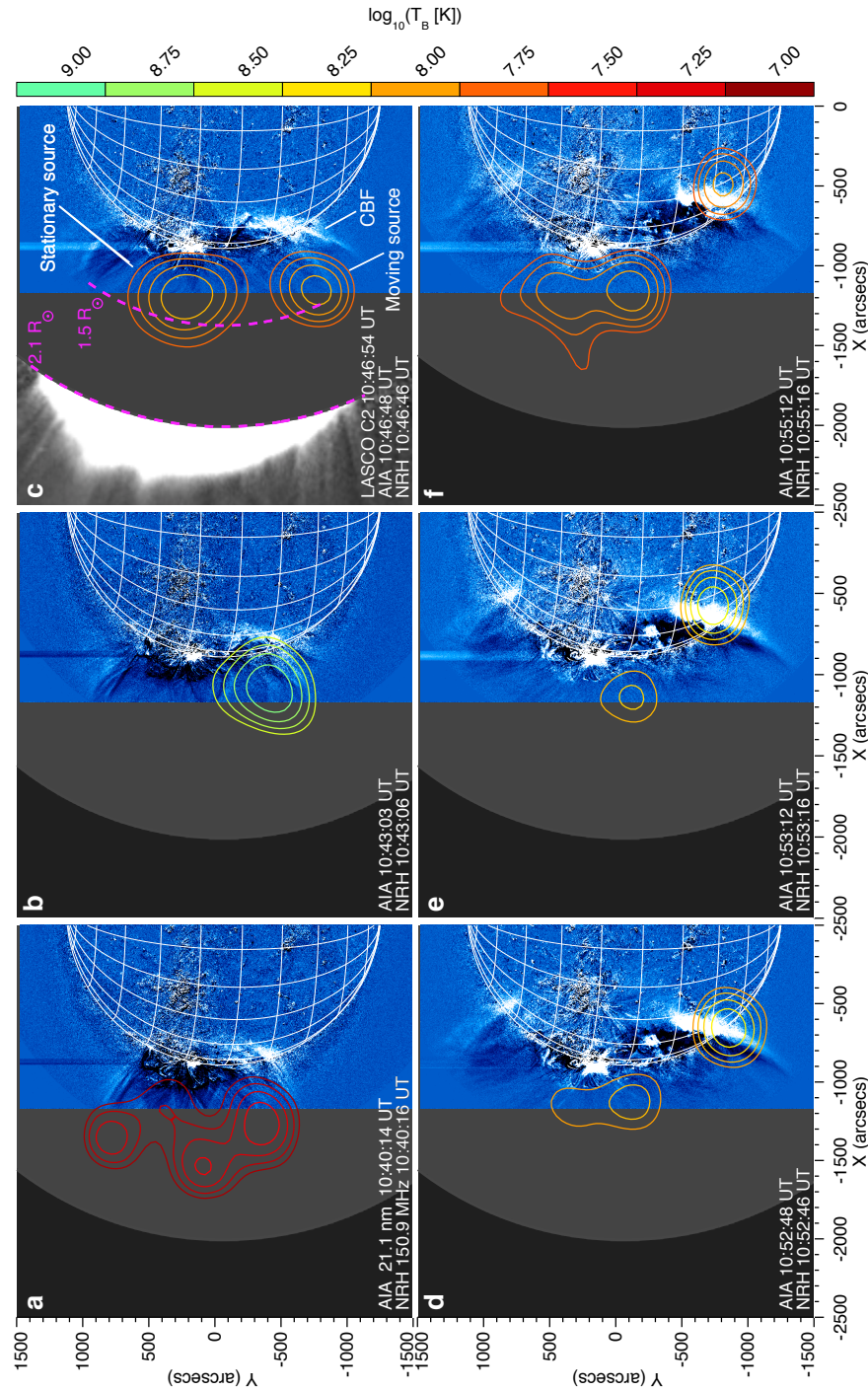


Figure 5.1: a-f show that the 150 MHz source follows closely the coronal bright front (CBF) as it propagates around the east limb, indicating they belong to a common structure. The intensity of the radio source is indicated by the colour bar on the right. c reveals the role of the CME in the event, as observed by the LASCO C2 coronagraph. The combination of the white-light coronagraph (C2) and the EUV images (AIA) reveal the full spatial extent of the CME bubble i.e., the frontal structure in white-light has clear extensions back toward the solar surface, imaged at EUV. The location of the radio source and CBF show they clearly have a relationship with the southward CME flank.

5.2 Coronal Bright Front and Radio Source

at 10:56 UT. Another emission source at 150.9 MHz was also observed at $\sim 0^\circ$ latitude on the east limb at a height of $1.1\text{--}1.3 R_\odot$ (Figure. 5.1c,d,e,f); while this source was clearly associated with the eruptive active region, any link between it and the CBF is secondary, as it shows no temporal relationship with the start and stop time of the bright front. Similar radio source motion is observed at 173, 228 and 270 MHz, however any co-propagation of these radio sources with the CBF is of much shorter duration. Figure. 5.1c reveals the role of the CME in the event, as observed by the LASCO C2 coronagraph. The combination of the white-light coronagraph (C2) and the EUV images (AIA) reveal the full spatial extent of the CME bubble i.e., the frontal structure in white-light has clear extensions back toward the solar surface, imaged at EUV. The location of the radio source and CBF show they clearly have a relationship with the southward CME flank.

5.2.2 Radio Source Height and Speed

To compare the motion of the CBF and radio source, the position angle (PA) trajectories were analyzed (Figure. 5.2). Here position angle is measured in degrees counter-clockwise from solar north. The solid lines show a fit of $\theta(t) = \theta_0 + \omega t$ to the data, where θ_0 is the starting PA, ω is the angular velocity, and t is time. The slope of each line gives ω , from which the velocity of the source may be obtained using $v = r\omega$, where r is the distance of the source from Sun center.

The 150 MHz source had an angular velocity of $6.2 \pm 0.1 \times 10^{-4} \text{ rad s}^{-1}$. In order to estimate the height of the radio source we first convert from frequency to electron number density using equation 2.63. Usually, there would be a conversion of this plasma frequency using the density models described in Section 2.3.6. However, as outlined, these models can often provide a poor description of the corona and lead to an evaluation of height for the radio burst that may be in-

5.2 Coronal Bright Front and Radio Source

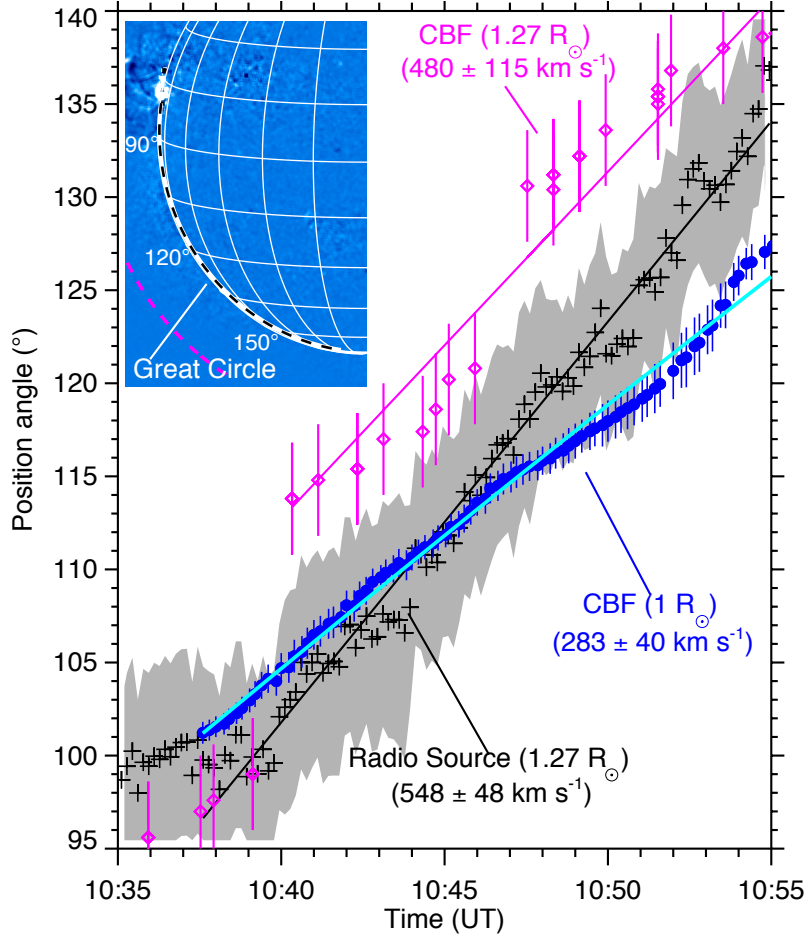


Figure 5.2: Position angle (degrees anticlockwise from solar north) versus time for the 150 MHz source, shown in plus signs, and coronal bright front (CBF) at $1 R_\odot$ (circles) and $1.27 R_\odot$ (diamonds). The great circle along which the CBF was tracked at $1 R_\odot$ is indicated by the dashed white line in the inset; the dashed pink line marks a height of $1.27 R_\odot$. Both radio burst and CBF have a consistent propagation in the same direction and have similar speeds at a height of $1.27 R_\odot$, implying they belong to a common propagating coronal structure. The uncertainty on radio source position angle is taken to be from 1σ uncertainties of the source width ($\sim 7^\circ$) plus the fluctuation of source position due to coronal and ionospheric scattering effects (3° at frequencies up to 160 MHz (Stewart & McLean, 1982)). The CBF position uncertainty is from Gaussian centroid uncertainty from a tracking and fitting algorithm of the CBF pulse (Long *et al.*, 2011a).

correct. For a more reliable calculation of radio source height we derive density models from data, rather than relying on a ‘guess’ model.

Both the LASCO C2 coronagraph and AIA were used for density diagnostics

5.2 Coronal Bright Front and Radio Source

of the corona. Firstly, six AIA passbands were used to create emission measure and density maps of the corona from $1.0\text{--}1.3 R_{\odot}$ (Zucca et al. 2013), following the method outlined in (Aschwanden *et al.*, 2013), details are provided in Appendix A.2. From $2.0\text{--}4.0 R_{\odot}$ density diagnostics were performed using the LASCO C2 coronagraph (van de Hulst, 1950). Density diagnostics via white-light studies involve the Thomson scattering theory and van de Hulst coefficients, also described in Appendix A.2. The density diagnostics of AIA and LASCO C2 are combined into a single density image. This results in density values from $1.0\text{--}4.0 R_{\odot}$, but with a gap in measurement between the two fields of view of the two telescopes ($1.3\text{--}2.5 R_{\odot}$). In order to fill this gap a hybrid of a plane parallel and a spherically symmetric hydrostatic equilibrium (HE) model were fit to the density data from AIA and C2 to form a continuous density map from $1.0\text{--}4.0 R_{\odot}$. This hybrid model has the form

$$n(r) = n_{ar}\exp\left(-\frac{r}{H}\right) + n_{qs}\exp\left[-\frac{1}{H}\left(\frac{1}{R_{\odot}} - \frac{1}{r}\right)\right] \quad (5.1)$$

where r is heliocentric distance and $H = kT/\mu m_p g_{\odot}$ is the scale height, where T is temperature, k is Boltzman's constant, m_p is a proton mass, μ is mean molecular weight, and g_{\odot} is acceleration due to gravity at $1 R_{\odot}$. Here, the plane parallel model for n_{ar} corresponds to the active region of the data derived from the EUV images, while the spherically symmetric model corresponds to the quiet corona (n_{qs}) C2 data. A spherical symmetric model is used for the coronagraph data because the range in heights given by the C2 data will be associated with decreasing gravity (as opposed to the constant gravity over the active region height range). This density model is fit for every position angle such that a 2D map of electron density values in the corona may be obtained (Figure 5.3).

These density diagnostics allowed a determination of the height from which

5.2 Coronal Bright Front and Radio Source

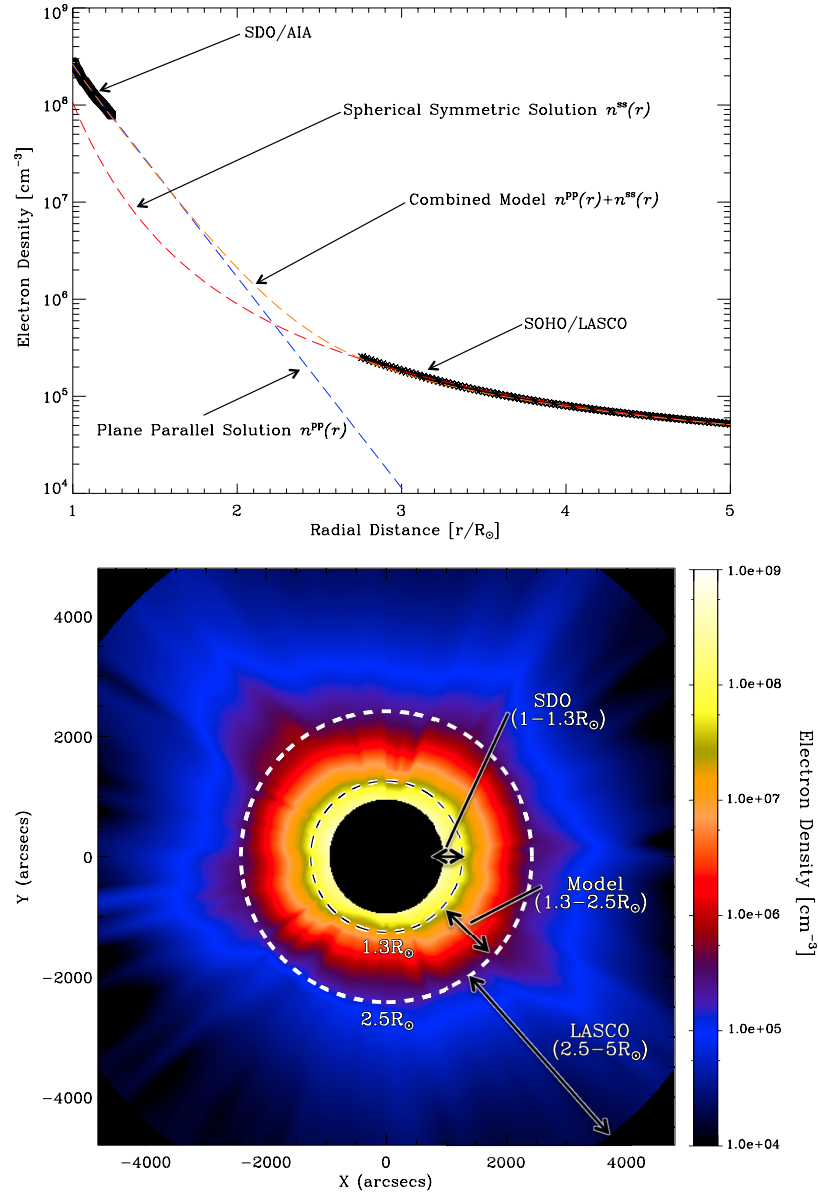


Figure 5.3: (Top) A single radial trace showing the density data derived from AIA and C2. The plane parallel model (blue dash), spherically symmetric model (red dash), and hybrid model (orange dash) are indicated. Mean molecular weight of 0.6 and temperature of 1.4×10^6 K were used in Equation 5.1 (Bottom) A 2D density map created from the hybrid model applied to density data at all position angles. Density maps such as this can provide much better estimates of radio source height, rather than using a density model which may provide a poor description of the corona.

5.2 Coronal Bright Front and Radio Source

75 MHz originated (assuming that 150 MHz observations are of harmonic plasma emission). We find that over the range of the position angles encountered by the radio source (100-140°), this frequency occurs at an average height of $1.27 R_{\odot}$, with a maximum height of $1.31 R_{\odot}$ and a minimum height of $1.21 R_{\odot}$. We must also take into account that the density measurements themselves have an uncertainty. To account for this, we add the measurement uncertainty (15%) to the density values and determine the maximum possible height of 75 MHz in the position angle range, then we subtract 15% from the density values and measure the minimum possible height. This results in a heliocentric distance of $1.27^{+0.06}_{-0.09} R_{\odot}$ for the radio source. This position, including uncertainties, combined with the value for angular velocity ($6.2 \pm 0.1 \times 10^{-4} \text{ rad s}^{-1}$) gives the tangential velocity of $548^{+34}_{-48} \text{ km s}^{-1}$ for the radio source.

5.2.3 Radio Source Alfvén Mach

To determine whether or not the radio source motion super-Alfvénic, the Alfvén speed of the environment through which it propagated was estimated. An estimate of the Alfvén speed requires a measure of density (which was derived above) and magnetic field using

$$v_A = \frac{B}{\sqrt{4\pi n_p \mu m_p}} \quad (5.2)$$

where B , μ is the mean molecular weight taken to be 0.6 for the corona, n_p is the proton number density (same as electron number density for fully ionized hydrogen plasma), and m_p is proton mass. To estimate the magnetic field strength, we used a potential field source surface (PFSS) extrapolation of the coronal magnetic field on the 22-September-2011 06:04 UT, shown in Figure 5.5. This was performed using the SolarSoft package of Schrijver & De Rosa (2003) and data from the Helioseismic and Magnetic Imager (HMI)(Scherrer *et al.*, 2012) of the

5.2 Coronal Bright Front and Radio Source

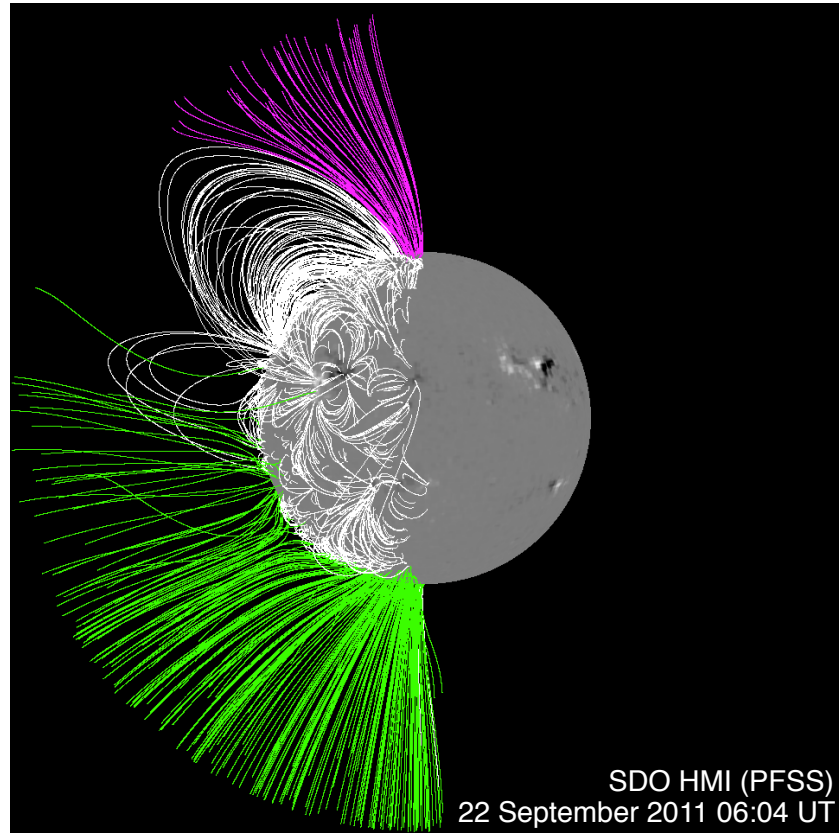


Figure 5.4: A potential field source surface (PFSS) extrapolation of the coronal magnetic field on the 22-September-2011 06:04 UT. This was performed using the SolarSoft package of Schrijver & De Rosa (2003) and data from the Helioseismic and Magnetic Imager (HMI)(Scherrer *et al.*, 2012) of the SDO spacecraft. Green and pink lines signify open field regions while white is closed field. The CBF and CME flank propagated through the south-east quadrant. Therefore a transverse propagation through these open and closed field structures suggests that the shock was likely of quasi-perpendicular orientation.

SDO spacecraft. Green and pink lines signify open field regions while white is closed field. The PFSS extrapolation provides magnetic field was combined with the density map to produce a 2D Alfvén speed map of the corona, such that the Alfvén speed position may be obtained for any position in the 2D sky-plane. This is the first time such empirical values of density and magnetic field have been produced for the 2D sky-plane. At the source heliocentric distance of $1.27 R_{\odot}$ we

5.2 Coronal Bright Front and Radio Source

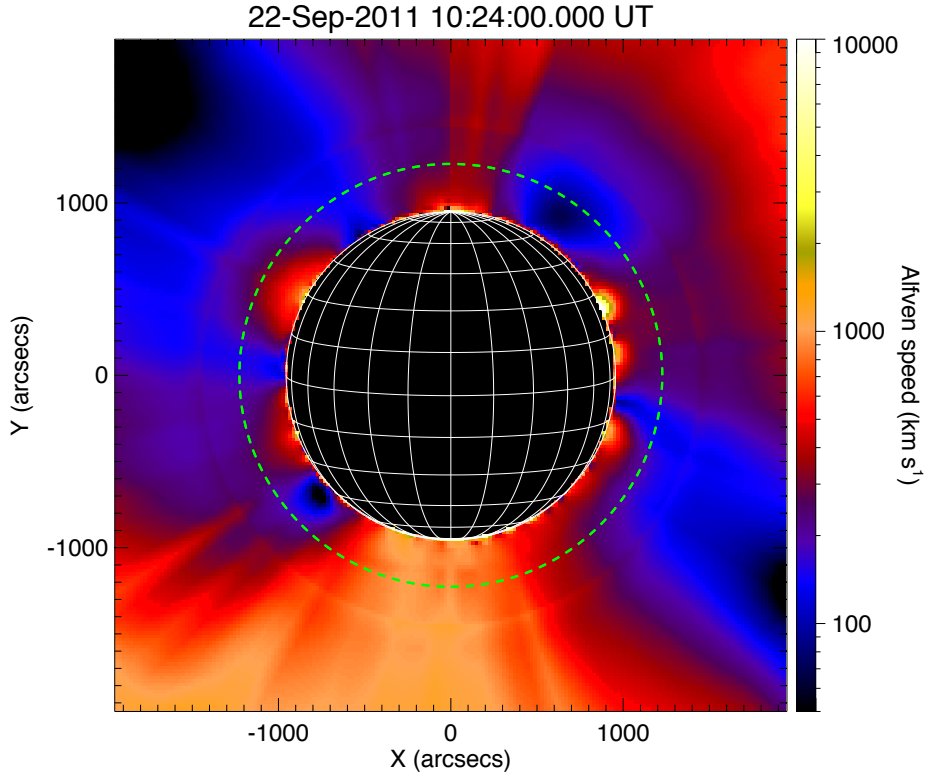


Figure 5.5: Alfvén speed map of the solar corona, derived from density values using LASCO C2, SDO/AIA, and magnetic field values from the PFSS extrapolation. These empirical observations have features which were predicted by the model Alfvén produced by Warmuth & Mann (2005) i.e., the presence of minima in Alfvén speed close to active regions. The green circle marks a height of $1.27 R_\odot$. Figure adapted from Zucca & Carley *et. al.* (submitted)

find $B = 0.67$ G. Combining this with the density at the radio source results in an Alfvén speed of 225 km s^{-1} . Taking into account that the source may be in the range from $1.18 - 1.33 R_\odot$, we find a possible range of $0.5 - 0.9$ G for the magnetic field that the source may encounter between the position angles of $100 - 135^\circ$. Again using the density at the radio source we find the possible range in Alfvén speeds that the source may encounter is $190 - 310 \text{ km s}^{-1}$. Hence we quote the Alfvén speed as $v_A = 225_{-35}^{+85} \text{ km s}^{-1}$. Using the speed of the source we then find the Alfvén Mach to be $M_A = 2.4_{-0.8}^{+0.7}$. We note that it is not possible to estimate an error on the magnetic field strength since it is an extrapolation from the sur-

5.2 Coronal Bright Front and Radio Source

face field, however, the results of super-Alfvénic Mach are tolerant to within 50% uncertainty on the PFSS B-field estimate. Also, the PFSS represents the lowest energy state of the coronal magnetic field, hence this Mach number is taken to be an upper limit.

Finally, the direction of the field is also given by the PFSS extrapolation. It shows an extended region of open and radial field structure in the south east quadrant of the corona, with a weak closed field region on disk in this quadrant. The shock propagated transversely through this region, showing there is a strong possibility of the shock encountering quasi-perpendicular orientation of the magnetic field. As was described in Section 5.5.2, quasi-perpendicular orientation is an essential aspect of the SDA process and generation of plasma emission

5.2.4 CBF Speeds

In a similar approach to the radio source motion, the CBF motion was tracked along a great circle at the solar limb to obtain its position angle trajectories with time Figure 5.2. These positions are shown as blue circles in Figure 5.2. The solid blue line shows a fit of $\theta(t) = \theta_0 + \omega t$ to the data, where θ_0 is the starting PA, ω is the angular velocity, and t is time. Again, the slope of each line gives ω , from which the velocity of the source may be obtained using $v = r\omega$, where r is the distance of the source from Sun center. For the CBF, an angular velocity of $4.1 \pm 0.4 \times 10^{-4} \text{ rad s}^{-1}$ was obtained, resulting in a velocity of $283 \pm 40 \text{ km s}^{-1}$ at $1 R_\odot$. Although the radio source and CBF show a consistent propagation southwards, the CBF does so at a slower speed, possibly because it is at a smaller height than the radio source. To compare the motion of the CBF and radio source at the same height, the CBF motion was tracked at $1.27 R_\odot$. The CBF was much fainter and more diffuse at this height, hence their are fewer data points and the

5.2 Coronal Bright Front and Radio Source

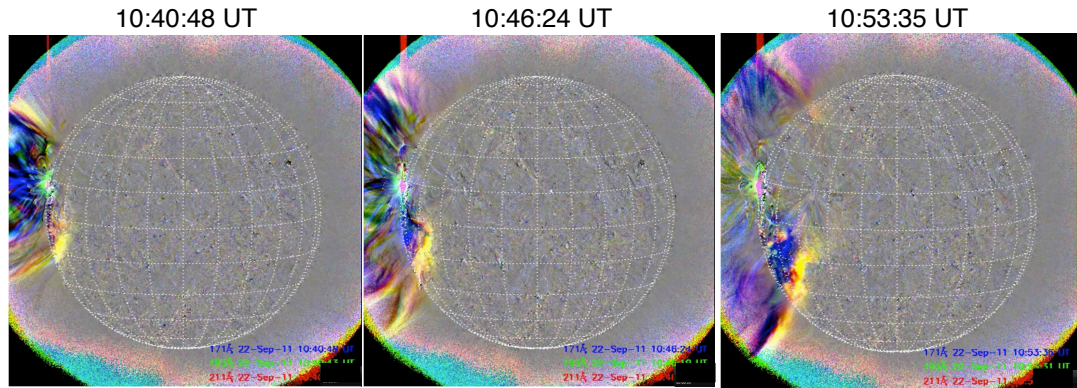


Figure 5.6: Tri-colour running ratio images of the 22-September 2011 CBF, produced from 171, 195 and 211 Å images from SDO. These images are used to discern general temperature changes of the front as it propagates, with blue color regions indicating a relative cooling, and red/yellow regions indicating a relative heating.

errors are larger than the $1 R_\odot$ data. At $1.27 R_\odot$, the CBF was found to have an angular velocity of $5.4 \pm 1.3 \times 10^{-1} \text{ rad s}^{-1}$, resulting in $v = 480 \pm 115 \text{ km s}^{-1}$. Both the CBF and radio source clearly show common kinematics at a similar height of $1.27 R_\odot$, with the two features having a consistent progression southward around the east limb.

5.2.5 CBF Thermal Properties

In order to investigate any thermal properties of the CBF we have produced tri-colour running ratio images of the CBF, shown in Figure 5.6. A ratio image is one in which the image of interest is divided by a pre-event image e.g., the one direct preceding the image of interest. Any intensity increase will show up as a brightness enhancement. A tri-colour running ratio image is one where three separate filters are used to represent running a running ratio in the three channels of a Red-Green-Blue (RGB) image. The assignment of the RGB color channels are 171 (blue), 193 (green), and 211 (red). As described in detail in Downs *et al.* (2012): “*a particular offset in the relative phases or amplitudes of*

the perturbation for each channel will be spread across the RGB color plane. By nature this representation highlights anticorrelated ratio phases as having strong color components. Correlated phases on the other hand will be confined to a mostly gray-scale range.”

Since each filter used in the images is sensitive to different temperature ranges a tri-colour movie may indicate a local temperature change due to a passing transient. For example, a positive temperature perturbation (heating) may show up as excess emission in 19.3 nm and/or 21.1 nm passbands resulting in a orange/yellow appearance. A negative temperature perturbation (cooling) will result in excess 17.1 nm channel ($6.3 \times 10^5\text{ K}$) combined with a deficiency in 19.3 nm ($1.2 \times 10^6 - 2 \times 10^7\text{ K}$) and 21.1 nm ($\times 10^6\text{ K}$) channels; this results in a blue appearance in the image. In this way, we can qualitatively identify what parts of the CBF are due to local heating and what parts are due to cooling (Cheng *et al.*, 2012; Cohen *et al.*, 2009; Downs *et al.*, 2012). The furthermost front has a yellow appearance, indicative of a positive temperature perturbation, with a secondary blue (cooler) front behind it. This is the expected behaviour of a propagating pressure pulse i.e., a traveling pressure perturbation will result in a slight heating followed by a rarefaction and cooling in its wake Downs *et al.* (2012). This is further confirmation that the CBF observed in this event is indeed a pressure pulse, making it more likely to be associated with shock activity higher in the corona.

5.3 Radio Dynamic Spectra

While the NRH imaging data reveal there was a high intensity radio source closely associated with the CBF, the radio dynamic spectroscopy reveal exactly what kind of radio activity this is. Section 2.3.6 shows that different types of physical activity in the corona, such as particle acceleration and shock activity can be

recognised by their characteristic signature in dynamic spectra.

5.3.1 Observations

The 150 MHz source observed by NRH had a brightness temperature of $\sim 10^9$ K, indicating coherent plasma emission. As described in Sections 2.3.4–2.3.5, plasma emission is generated via plasma oscillations that are due to instabilities in the presence of high velocity electron beams. The presence of electron beams was independently verified and revealed in detail using radio dynamic spectra. At $\sim 10:40$ UT the fundamental and harmonic bands of a type II burst shock signature was observed at 45 and 90 MHz (Figure 5.7b), respectively, using the Nançay Decametric Array (NDA; Boischot *et al.*, 1980). Type III bursts begin at the same time as the type II (Figure 5.7a,b), observed using NASA’s STEREO-B/WAVES instrument (Bougeret *et al.*, 2008). The speeds of these particles could be obtained from their frequency drift.

5.3.2 Particle speeds and in-situ detection

The frequency drift of these type III radio bursts provide a measure of velocity of the electrons causing the radio emission by converting frequency-time measurements to height-time via a coronal density model. From the dynamic spectra, it is possible to obtain a set of frequency time measurements (f_i, t_i) , in this case along the left edge of the type III. Using the expression for plasma oscillation (Equation 2.63), the set (f_i, t_i) may be converted into a set of density time values (n_i, t_i) . In order to convert these into a height-time set (r_i, t_i) , a density model of the solar corona is used. The density model in this case is derived from a solution to the Parker solar wind equation which is used specifically to analyze low frequency (interplanetary) type IIIIs (Mann *et al.*, 1999). Once this

5.3 Radio Dynamic Spectra

(r_i, t_i) height-time set was found, we took into account that the electron beams are traveling along open magnetic field lines which follow the Parker spiral. In cylindrical coordinates, the radius r and azimuthal angle ϕ share the relationship $r - r_0 = -\frac{v_{sw}}{\Omega_\odot}(\phi - \phi_0)$ i.e., an Archimedean spiral with parameters v_{sw} , the solar wind velocity, and Ω_\odot , the angular velocity at solar equator. The arch-length along any arm of this spiral (along an open magnetic field line) is given by

$$s(\phi) = \frac{v_{sw}}{2\Omega_\odot} (\phi\sqrt{1 + \phi^2} + \operatorname{arcsinh}(\phi)) \quad (5.3)$$

where $\operatorname{arcsinh}$ is the inverse hyperbolic sine function. Using a solar wind velocity value of 450 km s^{-1} (observed in-situ using the STEREO-B PLASTIC)

5.3 Radio Dynamic Spectra

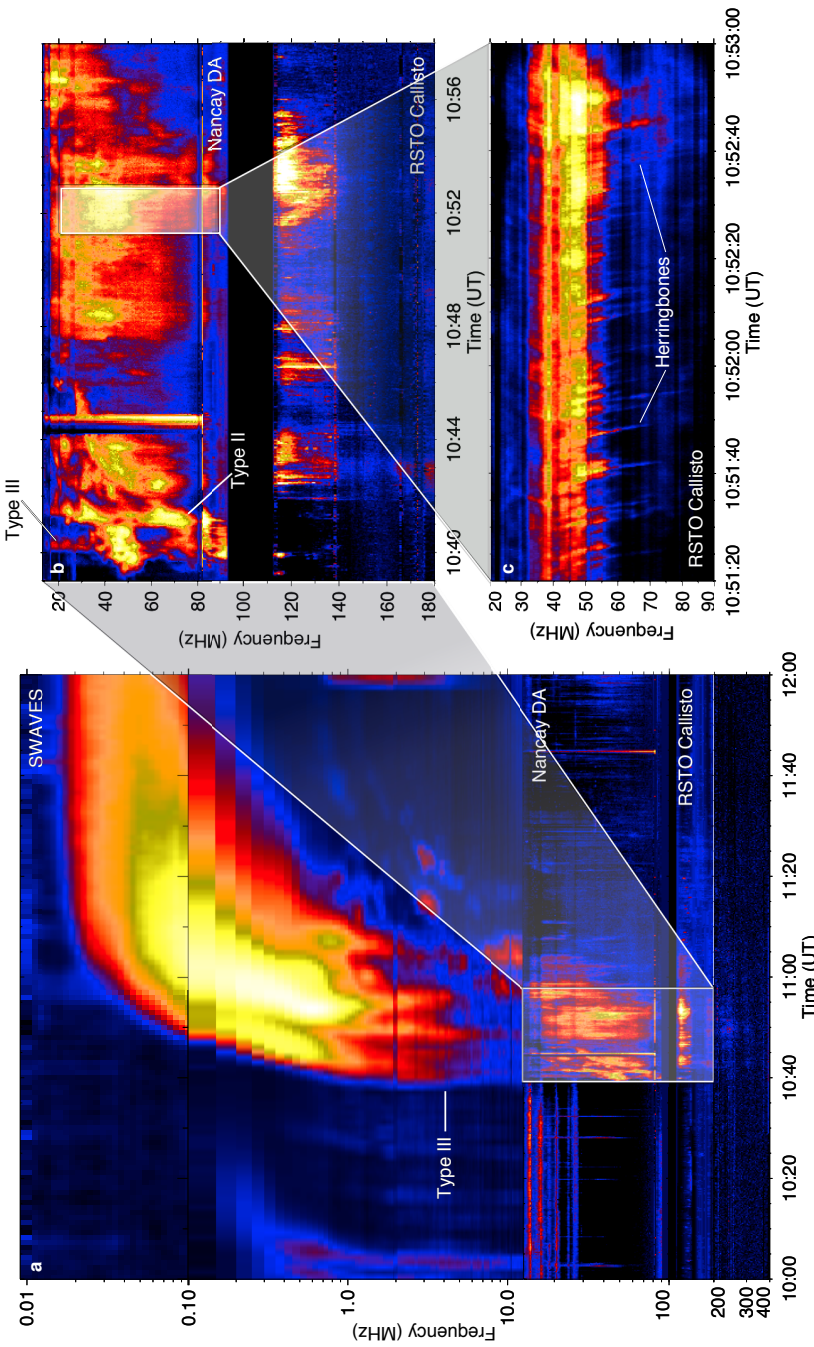


Figure 5.7: Radio dynamic spectra from STEREO-B/WAVES (0.01–16 MHz), Nançay DA (20–90 MHz), and RSTO eCallisto (10–400 MHz). The type II radio burst is indicated in **b**, with both fundamental and harmonic emission observable. This shock signature is characterized by two emission bands drifting slowly ($\sim 0.2 \text{ MHz s}^{-1}$) toward lower frequency over time. The type III bursts are indicated in **a,b**, while herringbones are shown in **c**. Each herringbone or is indicative of an electron beam traveling away from the shock. Note that all of the radio activity from **a–c** is indicative of either particle acceleration or a plasma shock in the corona. The start and stop times of this radio activity in these dynamic spectra show good temporal correspondence with the start/stop times of the activity in Figure 5.1. This is especially apparent for the features between 100–200 MHz.

5.3 Radio Dynamic Spectra

and $\phi = \frac{\Omega_\odot}{v_{sw}} r = -6.5 \times 10^{-12} \text{ rad m}^{-1} \times r$, the set (r_i, t_i) were converted to a set of distances along the Parker spiral vs time (s_i, t_i) . A linear fit to this data then gives the speed of electrons producing the type III as $0.4 c$ (Figure 5.8). Note that since the (f_i, t_i) points are taken along the left edge of the type III burst, this speed is representative of the fastest electrons contributing to the radio burst.

It is difficult to estimate an error on this speed, due to a lack of interplanetary density measurements from which this speed is derived, we may confirm the presence of particles with such energy from in-situ data. Figure ?? shows a plot of electron flux versus time from the Solar Electron Proton Telescope (SEPT)(Müller-Mellin *et al.*, 2008) onboard STEREO-B. It shows an increase in electron flux in the range of 45 - 325 keV. The vertical black line is the expected time of arrival of the electrons causing the type III burst, calculated from their speed and distance travelled on the Parker spiral. The expected time of arrival of the type III electrons match quite well the first peak in flux of the in-situ detected electrons, showing that the speeds derived from frequency drift are a reliable estimate.

More striking evidence for shock-accelerated electrons is in the form of ‘herringbone’ emission, observed using the eCallisto spectrometers (Benz *et al.*, 2009) at the Rosse Solar Terrestrial Observatory (RSTO; Zucca *et al.*, 2012) (Fig. 5.7c). The herringbones result from individual beams of shock-accelerated electrons (Mann & Klassen, 2005), traveling towards and away from the Sun i.e., to higher and lower frequencies. Similar features occur between 100–200 MHz (Fig. 5.7b), showing the same characteristics as herringbones (a bursty nature and decreasing intensity with respect to time). In a similar manner to the type III bursts, the beam velocity of herringbone electrons was estimated to be $0.15 c$, again showing the presence of near-relativistic electron acceleration in association with the

5.3 Radio Dynamic Spectra

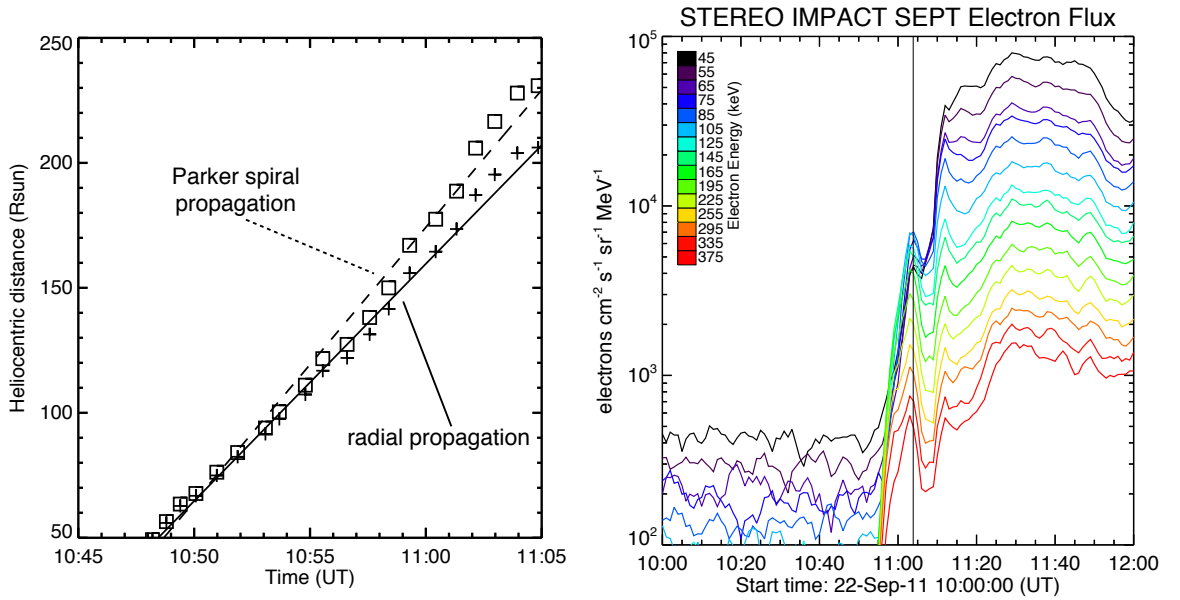


Figure 5.8: (Left) Distance-time for points chosen along the right edge of the type III radio burst observed by S/WAVES. Both radial and Parker-spiral corrected points are shown. (Right) Detection of electrons in-situ by SEPT on STEREO-B. The electrons arrive at $\sim 11:05$ UT, approximately 35 minutes after the flare start time. The black vertical line indicates the expected time of arrival (ETA) of the type III electrons. This ETA was calculated from the electron speed (derived from the frequency drift and a density model), and the distance travelled along the Parker spiral (given a solar wind speed of 450 km s^{-1}). Note that the type III electrons, calculated to have an energy of 46 keV, have an ETA that is centered on the first peak in electron fluxes as detected by the SEPT low energy channels at 45 keV. This good agreement between predicted ETA and observed time of arrival, showing the type III electron energies are a sound estimate.

presence of a shock.

While their structure in frequency reveal how fast these beams travel, their behavior in time can reveal detailed temporal characteristics of the shock acceleration process. A wavelet analysis using a derivative of a Gaussian wavelet performed on a time series at 54 MHz reveals periodicity at 2–11 seconds (see Supplementary Figure 1). Previous authors have attributed this bursty nature to rippling and inhomogeneity along the shock front, possibly revealing some level of instability or shock turbulence in the acceleration region (Burgess, 2006; Guo & Giacalone, 2010); we discuss this in the last section. We note that the features

5.3 Radio Dynamic Spectra

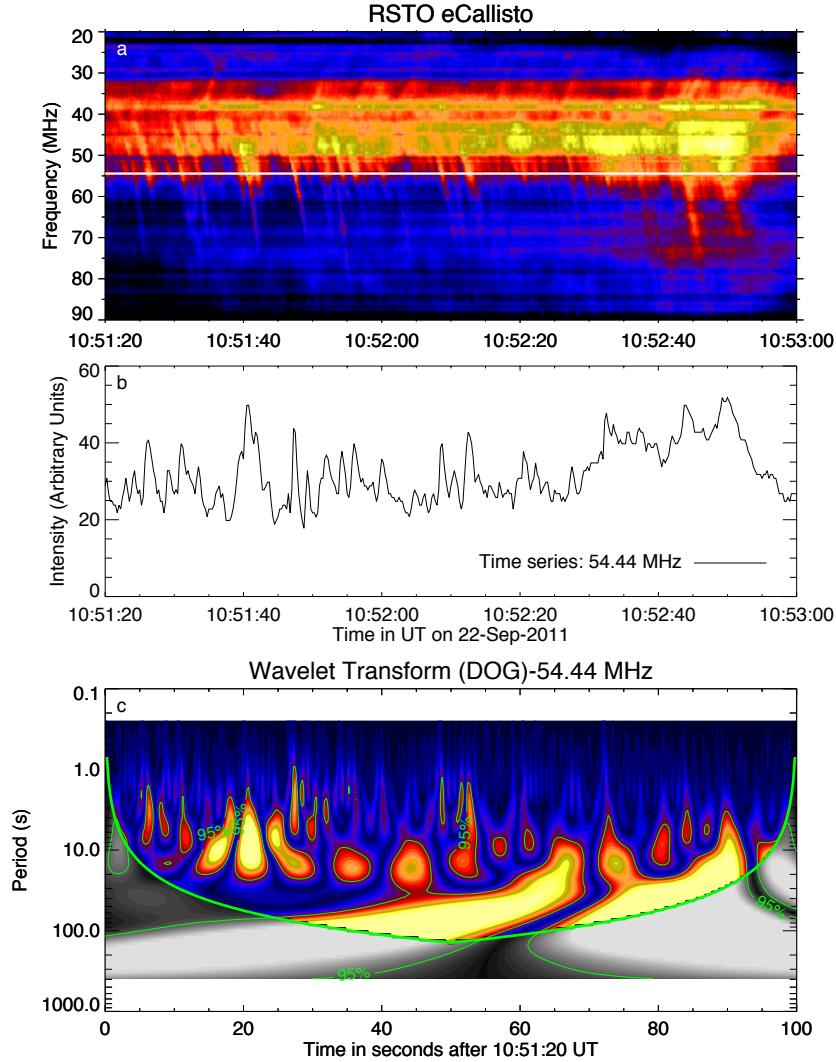


Figure 5.9: Wavelet analysis of herringbone radio bursts. Panel **a** shows the herringbones, the white line is the frequency from which a time-series has been extracted (54.44 MHz). Panel **b** shows the time series. Panel **c** shows a wavelet analysis of the time series using a derivative of a Gaussian (DOG) wavelet. The shaded grey area is the region outside the cone of influence and the green contours mark the 95% confidence level. The wavelet transform shows power in the regions of 2–11 seconds, revealing strong levels of periodicity throughout the time series.

at 100–200 MHz appear to be the extension of the herringbones into higher frequencies. These features in particular show good temporal correspondence with the radio source i.e., they have a start-stop time comparable to the radio source.

This is particularly apparent for the group of bursts at 10:52–10:56 UT.

The radio emission in the dynamic spectra have all the hallmarks of shock generation with particle acceleration closely tied to the process. The association of shock radio activity with the imaged 150 MHz source suggests that the two observables have a common origin in a plasma shock. Overall, the position of the radio source at the southern flank of the CME, the transverse motion of the source (propagation parallel to the surface) and the zero frequency-drift of the herringbones is suggestive of a shock driven parallel to the surface by the flank expansion, similar to the assertion by Stewart & Magun (1980) and Schmidt & Cairns (2012a). Indeed the association of the CBF with this radio activity is corroborative evidence of the wave/shock system at the flank. Further evidence of a shock having occurred in the corona was obtained through white-light observations, allowing us to study the position of this shock relative to the CME.

5.4 White-light CME and Shock

A CME associated with this event was observed by the Large Angle Spectroscopic Coronagraph (LASCO; Brueckner *et al.*, 1995), first appearing at 10:46 UT, with an apex heliocentric distance of $\sim 2.6 R_{\odot}$ (Fig. 5.1c). The next available image shows the bright CME front with a fainter, secondary front at the southern flank (Fig. 1.26b). This ‘two-front’ morphology is a common occurrence in white-light CME structure and constitutes a reliable signature of a CME front associated with a stand-off shock (Vourlidas & Bemporad, 2012). In order to distinguish between the CME front and shock front, we performed a 3D reconstruction of the CME using the elliptical tie-pointing method described in Byrne *et al.* (2010) (Fig. 1.26d).

This reconstruction reveals that the bright front outlined in the C2 corona-

5.4 White-light CME and Shock

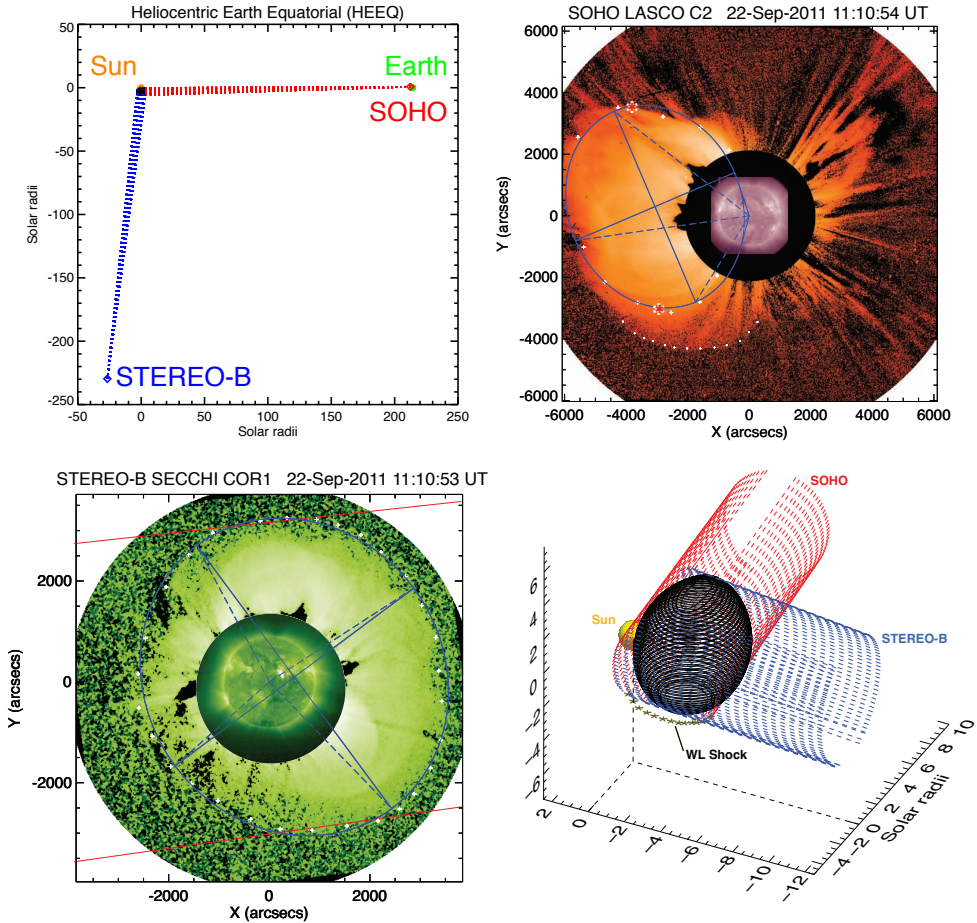


Figure 5.10: White-light CME observations and 3D reconstruction of the CME front. **a** Top-down view of the Heliocentric Earth Equatorial (HEEQ) system, showing the separations and locations of STEREO-B and SOHO spacecraft with respect to the Sun. **b** LASCO/C2 base-differenced image of the CME (logged intensity scale), with AIA 21.1 nm image inset. White crosses indicate a point-and-click along the CME front with a corresponding ellipse fit in blue, where the solid lines indicate the major and minor axes, while dashed lines indicate the apex points back toward the Sun centre. The white circles indicate the white-light shock. The red asterisk points indicate the northern and southern flanks of the CME. **c**, Base difference image of the CME from the COR1-B coronagraph, with a corresponding ellipse fit and EUVI 19.5 nm image inset. The red lines are the red asterisk points in **b** projected as lines-of-sight across the COR1 field of view. **d** 3D reconstruction of the CME with the white light shock indicated on the plane of sky (only 2D information is available for this feature). The red dotted lines are the projected points from the ellipse on the C2 image, and the blue dotted lines are the projected points from the ellipse on the COR1 image. The black ellipses are those inscribed in the resulting quadrilateral slices via the elliptical tie-pointing method for 3D CME reconstruction, as described in (Byrne *et al.*, 2010).

graph (ellipse in Fig. 1.26b) corresponds to the faint front outlined as a halo in STEREO-B COR1 (ellipse in Fig. 1.26c). Furthermore, the observations reveal that the secondary and extremely faint front at the southern edge of the CME (as imaged in LASCO/C2, Fig. 1.26b) cannot be considered as part of the CME structure, but is actually an associated shock front. We note that white-light shocks have been reported in the past, occurring both in the low corona as well as out to ~ 0.5 A.U. (Maloney & Gallagher, 2011; Vourlidas & Bemporad, 2012). Here, we have employed a 3D reconstruction from multi-viewpoint observations to qualitatively confirm the presence of a shock at the southern flank of the CME, in the same region as the CBF and radio burst. Finally, a height time analysis of this CME showed that there was no acceleration in the C2 and C3 fields of view, with the CME having a constant velocity of ~ 1300 km s $^{-1}$.

5.5 Discussion

5.5.1 Relationship Between CME, CBF, and Radio bursts

There has been much debate surrounding the assertion that CBFs are a wave phenomenon (Gallagher & Long, 2011), with numerous authors suggesting a pseudo-wave theory (Delannée *et al.*, 2008). In the past, the association of CBFs with type II and type III bursts has been used as evidence against this pseudo-wave interpretation and more in favor of the MHD wave paradigm (Grechnev *et al.*, 2011b; Warmuth *et al.*, 2004). This study reveals that the CBF in this event was indeed closely associated with shock radio activity positioned on the flanks of an expanding CME. This kind of behavior has been suggested before, but never directly imaged (Feng *et al.*, 2012, 2013; Kozarev *et al.*, 2011). It shows how a combination of radio and EUV imaging can reveal the evolution of plasmoid

driven shocks in the solar atmosphere (Bain *et al.*, 2012).

The scenario shown to be the case here, is that the expansion of the CME flanks drove a plasma pressure front through the corona. The low coronal manifestation of this pressure front was a CBF. Higher in the corona this same pressure front steepened into a shock; this shock was responsible for the acceleration of particles. These particles produced radio emission which was observed as a propagating radio source and in dynamic spectra in the form of herringbones. Such a scenario is agreement with a variety of studies that have suggested such a physical mechanism e.g., the schematic of (Grechnev *et al.*, 2011a) shown in Figure 1.25, Figure 7 of Warmuth *et al.* (2004), and Figure 3 of (Stewart & Magun, 1980). Our own schematic shows a similar scenario in Figure 5.11.

5.5.2 Bursty Particle Acceleration

Of further interest in this study is the likelihood of a quasi-perpendicular orientation of the shock, as revealed by the PFSS extrapolation. A schematic of the CME, CBF and shock orientation with respect to the coronal magnetic field and particle acceleration is shown in Figure 5.11 Quasi-perpendicularity is an essential aspect of the shock drift acceleration (SDA) mechanism (Ball & Melrose, 2001), a process believed to be responsible for particle acceleration in planetary magnetospheres (Wu, 1984) and solar radio bursts (Holman & Pesses, 1983). This mechanism involves an adiabatic reflection of particles from the shock, with the energy gain sourced in the $\mathbf{V} \times \mathbf{B}$ electric field, where \mathbf{V} and \mathbf{B} are the upstream flow speed and magnetic field, respectively. A single reflection from the shock has limited energy gain, however multiple reflections may produce relativistic energies, which is particularly important for low Mach number shocks such as that reported here ($M_A = 2.4^{+0.7}_{-0.8}$) and in (Guo & Giacalone, 2012). This multiple

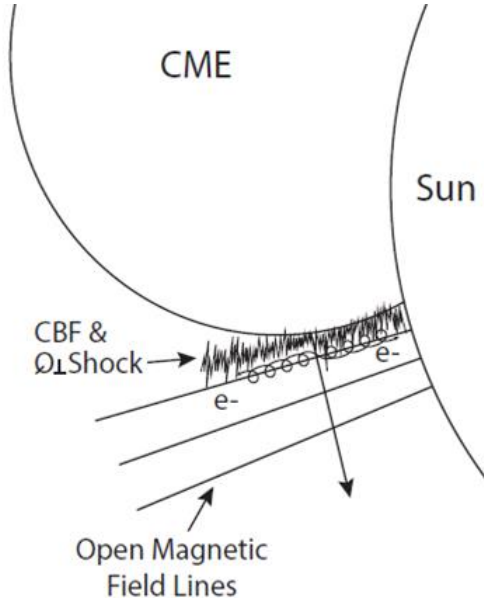


Figure 5.11: Relationship between the CME, CBF, shock and particle acceleration on the open magnetic field of the ambient corona.

reflection process may be explained by inhomogeneity in the shock front, a characteristic usually known as ‘rippling’ (Vandas & Karlický, 2011; Zlobec *et al.*, 1993). 2D hybrid simulations show that rippling is brought about by an instability (Burgess, 2006) and resembles a standing-wave mode of the shock surface (Lowe & Burgess, 2003). The presence of ripples can lead to a quasi-sinusoidal variation in shock-normal orientation with respect to the upstream magnetic field. Since the efficiency of SDA requires quasi-perpendicularity, there will be sites on the shock front that provide efficient acceleration and sites that do not – a structure that may lead to magnetic trapping and multiple reflections (Zlobec *et al.*, 1993), hence producing higher energy particle acceleration.

The presence of ripples can produce quasi-periodic herringbones in three ways. Firstly, it makes SDA more efficient and capable of producing the observed herringbone energies, especially when particle scattering is considered (Burgess, 2006). Secondly, the periodic spatial variation in the acceleration efficiency of

5.5 Discussion

the shock could explain the bursty and quasi-periodic nature of the herringbones. Guo & Giacalone (2010) suggest that shock front inhomogeneity brought about by MHD turbulence is a possible explanation of bursty herringbones. Schmidt & Cairns (2012a) produced a detailed model of SDA from a rippled shock, specifically on the flanks of an expanding CME. Their results suggest that herringbones could be produced by accelerated electrons at spatially intermittent regions of quasi-perpendicularity on a rippled shock surface (Figure 2.12). Thirdly, (Burgess, 2006) also predicts that, if rippling is present, the upstream and downstream electron beams should have similar energies, which is not predicted for a uniform or ‘smooth’ shock. A sample of the oppositely drifting herringbones in Fig. 5.7c shows that positive and negative frequency drifts are both $\sim 5 \text{ MHz s}^{-1}$, revealing that the upstream and downstream populations have similar energies (although we note the possibility that both positive and negative drifting herringbone features may be accelerated upstream, as suggested by the schematic of (Zlobec *et al.*, 1993)). There is also the possibility that the herringbones may be associated with a termination shock of a reconnection outflow occurring behind the CME (Aurass & Mann, 2004). In such a scenario, this shock would have a more indirect relationship with the CME propagation. However, the imaged radio source shows a good temporal correspondence with the shock activity in the dynamic spectra, especially between 10:52–10:56 UT, suggesting the particle acceleration indicated in the spectra shares a close relationship with the propagating source.

Our observations reveal the need for a more detailed modeling of herringbone solar radio bursts. The quasi-periodic behavior of herringbones provides a possible direct measure of shock inhomogeneity and the spatial scales over which the magnetic field varies in the shock and ambient corona; it may also provide

5.5 Discussion

a measure of the turbulence in these plasma flows (Guo & Giacalone, 2010). In the future, high cadence EUV imaging from SDO, combined with sensitive radio imaging-spectroscopy observations from instruments such as the Low Frequency Array (LOFAR; van Haarlem *et al.*, 2013), will reveal unprecedented detail of plasma shocks and their role in particle acceleration. This may reveal the fundamental nature of a plasma shock process that is universal, but currently impossible to directly observe in any other area of astrophysics.

6

Conclusions and Future Work

The first goal of this thesis was to derive CME masses from observation with an uncertainty that is the smallest and most reliable to date. This information was then used to calculate a better estimate of CME energies and the first observational quantification of the Lorentz force acting on a CME. The second goal of this thesis was to increase the understanding of the relationship between CMEs, CBFs and radio bursts. This was achieved through observational evidence for a CME-driven shock that resulted in a CBF, the acceleration of particles and production of herringbone radio emission. In this chapter, I will summarise and conclude this research and outline the future of this study

6.1 CME Masses and Energies

6.1.1 Principle results

The goal of this thesis was firstly to derive CME masses from observation that have the smallest and most reliable uncertainty to date. This was achieved using the two vantage points of the *STEREO* Ahead and Behind spacecraft, allowing CME geometry, and the associated mass underestimations, to be fully characterized. This then allowed a better estimate of CME energies and the first observational quantification of the Lorentz force acting on a CME. The principle results are as follows:

- The first assumption of nearly all CME investigations is that the CME is confined to the 2D sky-plane. This leads to two sources of mass underestimation which primarily arise from the geometrical sensitivity of the Thomson scattering equations for an electron in the solar atmosphere. Firstly, if the CME propagates at some angle away from the sky-plane, but we do not take this angle into account, we will underestimate the mass. Knowledge of the propagation angle from *STEREO* A and B observations allows us to eradicate this uncertainty. The second assumption is that all CME material is confined to a 2D plane at some angle θ . This underestimation cannot be eradicated but we can characterise its effects by simulating a CME with angular width ψ and homogenous density distribution. This allows an estimate of the simulated observed mass and a comparison of this to the actual mass. For any CME width ψ at a sky-plane angle θ we may calculate the CME mass underestimation when we deproject the CME mass onto its plane θ . A surprising result from this is that for all angular widths

6.1 CME Masses and Energies

ψ , deprojection estimates exactly the CME mass when propagation is at an angle $\theta = 60^\circ$.

- In the past CME mass uncertainties from the geometrical unknowns described above were either extremely, large at more than 50% (Vourlidas *et al.*, 2000), or entirely unquantifiable. Adding to this all the other sources of uncertainty (coronal composition and interactions with streamers) results in CME mass estimates that are entirely unusable in a scientific analysis. In this study, using the capabilities of the STEREO spacecraft, the geometrical mass uncertainties of the CME occurring on 12 December 2008 were reduced to 10%, a dramatic improvement over previous results. The biggest source of uncertainty was the interaction of this CME with a streamer, adding a further 15%. Taking everything else into account the final mass uncertainty came to 30%, which is both smaller and more reliable than any uncertainty given previously. The final total mass of the CME came to $3.4 \pm 1.0 \times 10^{15}$ g, perhaps the only quotation of mass with an uncertainty in the literature. In an ideal case of a CME that has no background streamer interactions the uncertainty could be reduced even further.
- This research included the first quantification of the Lorentz force acting on the CME during its early phase propagation. Given $F_{Lorentz} = 3.4 \pm 2.2 \times 10^{14}$ N, it was shown that this is the most dominant force on a CME at $3 R_\odot$, being greater than gravity and drag due to the solar wind. This is the first direct evidence for Lorentz force dominated dynamics, which has been only indirectly shown in previous studies (Bein *et al.*, 2011). The quantification of this force is also important for constraining parameters of MHD models of CMEs. There are a variety of models of CMEs which successfully describe the formation of a flux rope and its eruption into in-

6.1 CME Masses and Energies

terplanetary space (Sections 2.2.1–2.2.3). These models employ a number of forces, given by the MHD momentum conservation equation, to propel the CME out of the low corona. The most important of these forces for doing work against the Sun’s gravitational potential is the Lorentz ($\mathbf{j} \times \mathbf{B}$) force. While all models include a Lorentz force treated explicitly through currents and magnetic fields, or implicitly only through magnetic fields, the sizes of the force in the models is entirely unconstrained. MHD models of CMEs have the freedom to choose any size Lorentz force because no work had been done on the actual size of this force. For example, (Chen, 1996) predicts a Lorentz force of $\sim 1.5 \times 10^{16}$ N during early phase propagation. This seems to be orders of magnitude too high, and further observational investigations of the forces on CME may show this.

6.1.2 Future Work

6.1.2.1 CME Mass and Forces Catalogue

There are a variety of catalogues that list CME kinematical properties for all events detected by space based coronagraphs up to the present time, including the Coordinated Data Analysis Workshop (CDAW) Data Center (Gopalswamy *et al.*, 2009a), Computer Aided CME Tracking catalog (CACTus) (Robbrecht & Berghmans, 2004), Solar Eruptive Event Detection System (SEEDS) (Olmedo *et al.*, 2008), and Automatic Recognition of Transient Events and Marseille Inventory from Synoptic maps (ARTEMIS) (Boursier *et al.*, 2009). All of these catalogues provide the speed and acceleration of each CME, however none of them include any estimate of CME mass. The inclusion of CME masses into an entire kinematics catalogue could yield very useful statistical information on CME energies and forces. Such an effort has never been made before, hence there

6.1 CME Masses and Energies

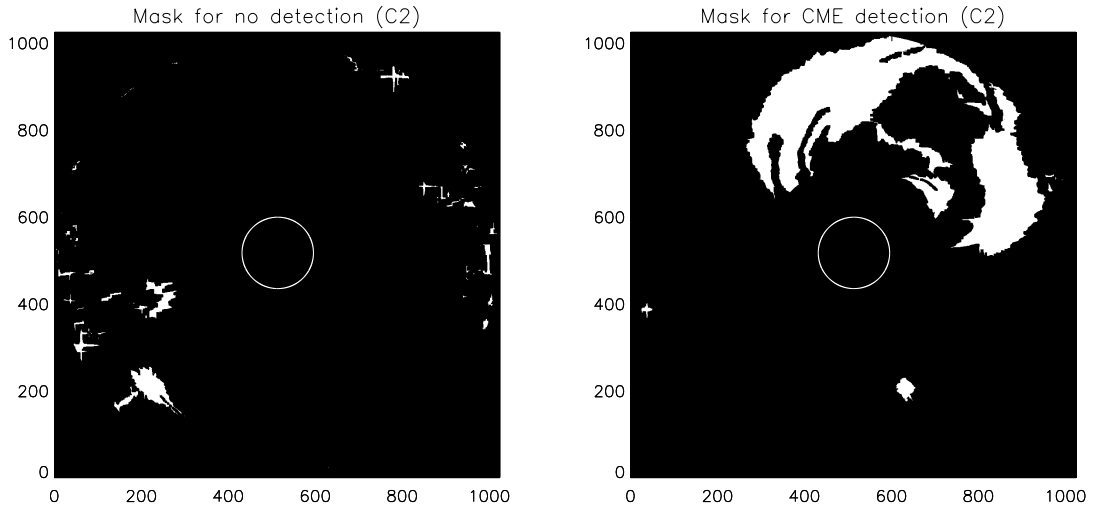


Figure 6.1: Sample C2 masks for no-detection (left) and CME-detection (right). Black arrays have a values of 0 and white areas have a value of 1. The no-detection masks has some spurious blobs, possibly due to small ejections of plasma in the solar wind, or cosmic rays on the CCD.

is a need to investigate the feasibility of a kinematics and dynamics catalogue.

The cataloguing of CME masses is currently being investigated with an automatic tracking tool known as coronal image processing (CORIMP) CME detection (Byrne *et al.*, 2012). The CORIMP detection tool is ideal since it uses sophisticated multi-scale analysis techniques to detect only the CME area in the image; isolating the CME area provides the possibility of calculating only the CME mass, without contamination from any other bright features in the image. The product of a CME detection with CORIMP is a mask containing only the area of the image containing the CME. An example of two such masks are shown in Figure 6.1, with no detection and a CME detection. A conversion of a CME image to pixel values of grams (as described in Chapter 4), application of the detection mask, and summation of all pixels would yield the total mass of the CME. This method was tested on a particularly active period of CME eruptions

6.1 CME Masses and Energies

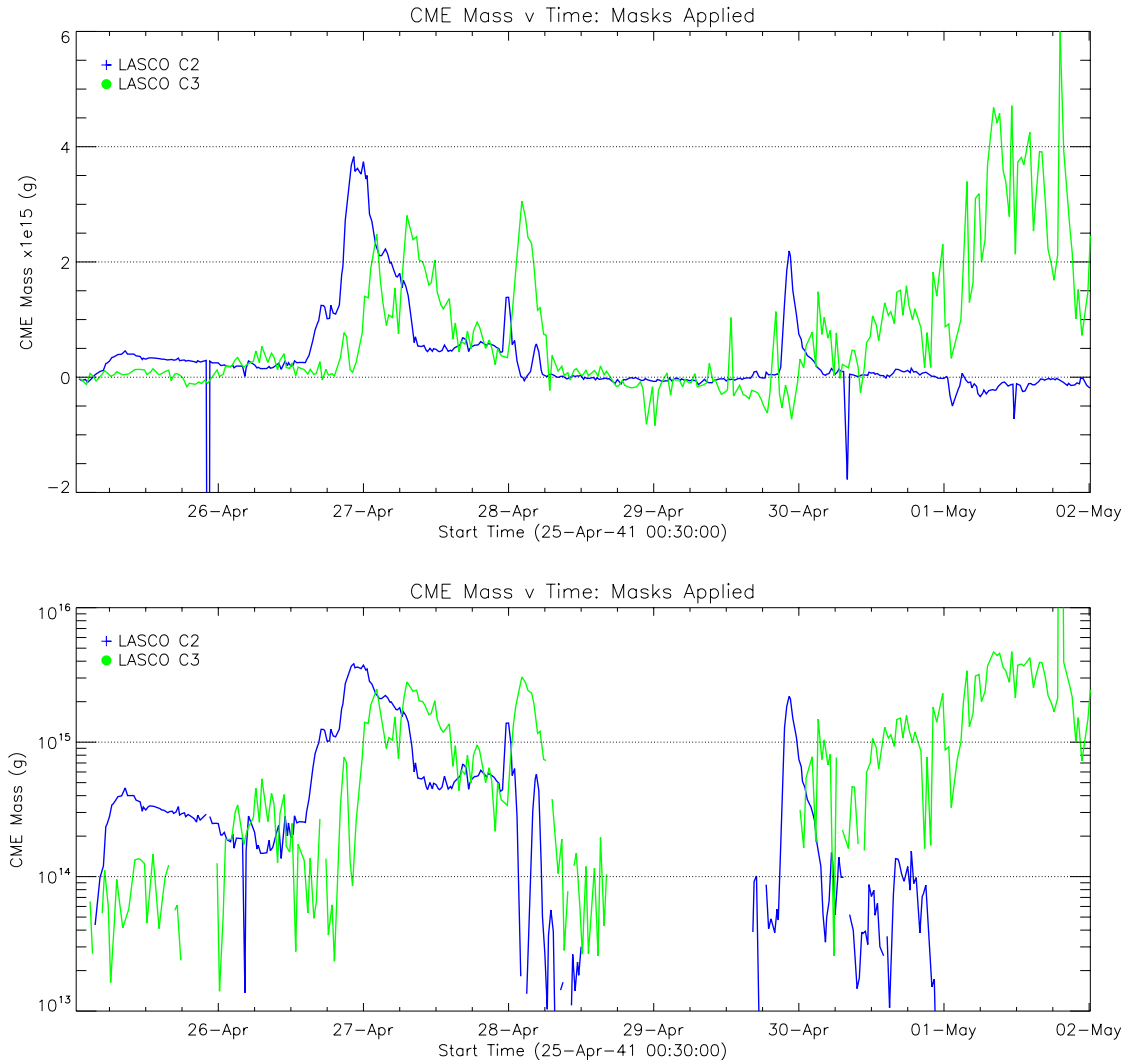


Figure 6.2: (Top) Mass estimates calculated using LASCO C2 and C3, and the detection masks of CORIMP. All images in the seven day observation sequence have been base-differenced, with the first image in the sequence used as a pre-event image. Representing mass on a linear scale shows clearly that the method results in reasonable estimates of CME mass. All CMEs are assumed to be propagating on the plane of sky (POS). (Bottom) Masses represented on log scale. The CME detection masks tend to capture spurious blobs (mass ejections, but not quite big enough to be regarded as CMEs). These blobs seem to occur in a lot of frames, making the background level sit at $\sim 10^{14}$ g or higher. This is a problem if we are to detect small CMEs.

from 25 April 2010 to 2 May 2010, observed by LASCO C2 and C3.

The detection mask was applied to each image in the sequence between the start and end date. In the majority of images there are no detections (Fig-

6.1 CME Masses and Energies

ure 6.1(left)) and if a CME is in the image it will be exposed in a mask similar to Figure 6.1(right). Each image is base-differenced and converted to pixel values of grams using the sky-plane assumption. The pixels are summed such that one image represents one mass value for each image in the sequence i.e., the image sequence allows us to calculate a mass time-series, shown in Figure 6.2. The top panel shows a mass time series on a linear scale; the CME detections of a standard $\sim 10^{15}$ g can be seen in the time series of both C2 and C3. The method is quite successful in calculating a reasonable mass value for moderate to large CMEs ($\sim 10^{15} - 10^{16}$ g).

Realistically, all of the mass plots should display mass on a log scale, given that CME masses tend to span approximately two orders of magnitude ($10^{14} - 10^{16}$ g). As shown in Figure 6.2 (lower), the log scale reveals a detection of a large background mass even during a quiet period of no CME detection. The background values amount to $\sim 10^{14}$ g or slightly higher. This is a problem since small CMEs of $\sim 10^{14}$ g will be completely swamped by the background detections, and furthermore, background values may also be misconstrued as legitimate detections. The background values result from an imperfect masking during quiet times. Even though there is no CME, the mask may still detect small clumps and blobs of solar wind that show up as positive areas in the mask Figure 6.1(left). A current line of investigation to eliminate this is by only accepting detections greater than a certain angular width. Since CMEs tend to be $> 40^\circ$, anything below this should be rejected and nulled in the mask.

Other than the spurious detections outlined above, there are a number of tests which need to be performed in order to check that (i) the background subtraction is appropriate (ii) the mask has detected the right quantity of CME mass. To

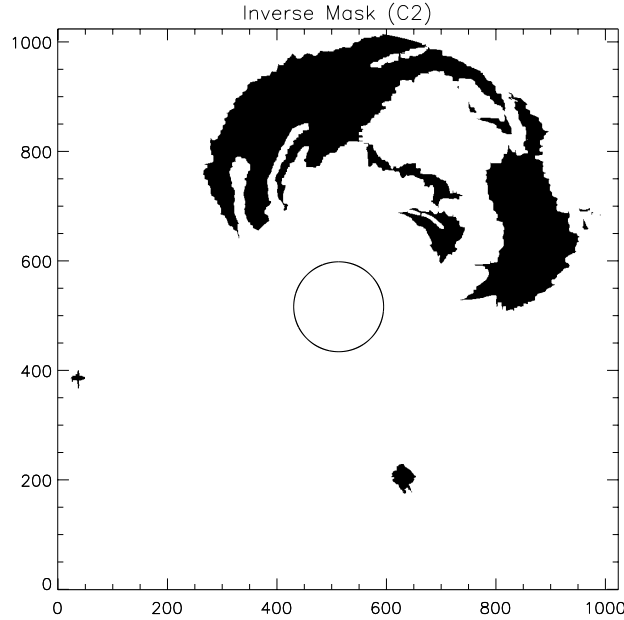


Figure 6.3: The inverse mask, with black indicating pixel values of 0 and white indicating values of 1. This allows everything *but* the CME to be summed. Black circle is solar limb.

check these two criteria we employ the fact that the following must be true

$$M_{mask} = M_{no_mask} - M_{inverse_mask} \quad (6.1)$$

where M_{mass} is mass calculated with the mask applied as normal, M_{no_mask} is just the total image array summed, and $M_{inverse_mask}$ is the CME masked with the remainder summed. The inverse mask is in Figure 6.3.

We perform the time series again to calculate M_{no_mask} and $M_{inverse_mask}$, shown in Figure 6.4. They behave as expected, with the inverse-mask being essentially the same as the no-mask, but smaller by a roughly constant amount; this roughly constant amount should equal the CME mass. The effect of a single pre-event image used in the base-difference for the whole sequence is very appar-

6.1 CME Masses and Energies

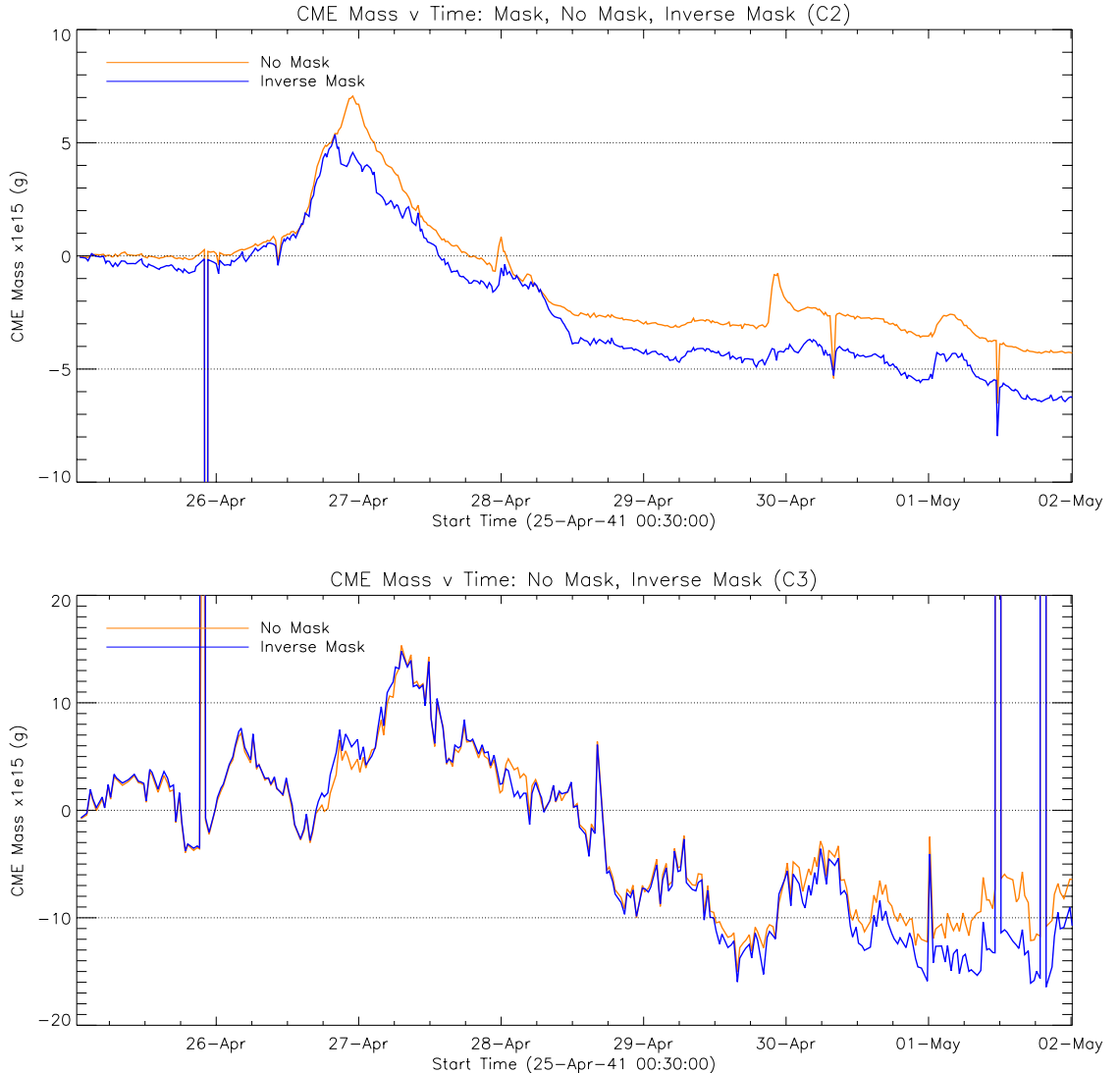


Figure 6.4: Time series of the mass obtained from using no mask and using the inverse mask. The data behave as expected, with the inverse mask being essentially the same as the no-mask but smaller by the CME mass. The drift towards negative values is symptomatic of a pre-event image (for base-difference) that is too bright. The discontinuous values are due to badly prepped images in the NRL archive.

ent. In both C2 and C3 the masses grow toward increasingly negative values. This happens because the pre-event image is too bright and is a bad representation of the background corona over the observation sequences. In the intervening hours between start and end time a number of CMEs erupt. This will result in a dimming of the background corona over time as the corona becomes depleted

6.1 CME Masses and Energies

or evacuated. This method has determined that condition (i) is not fulfilled, and is a good error check to see if an appropriate background has been chosen. An algorithm needs to be employed to recognize a period of inactivity prior to eruption, and use an image (or an average of images) from this quiet period in the subsequent base difference.

To test condition (ii) we compare the difference of the blue and orange time series in Figure 6.4 with the time series calculated using the normal mask (Figure 6.2), the results are shown in Figure 6.5. The trends in both time series match, however they diverge as time increases. The over-bright pre-event image used in the base difference is drawing the background values in no-mask and invert-mask into negative values. The blue line in Figure 6.4 (upper panel) should sit at zero, while the orange line should only show positive values when a CME is in the frame. The fact that they both drift into the negative means they will result in a positive excess when subtracting the two. Algebraically, the procedure resulting in the red line in Figure 6.5 is as follows:

$$y = \sum(I_{img} - I_{pre}) - \sum[(I_{img} - I_{pre}) \times (1 - I_{mask})] \quad (6.2)$$

where I_{img} is the current image and I_{pre} is pre-event image; $I_{img} - I_{pre}$ represents a base difference. $(1 - I_{mask})$ is the inverted mask. Ideally, Equation 6.2 would result in

$$y = M_{cme} - 0 \quad (6.3)$$

However due to excess brightness in the pre-event image we end up with a negative mass value M_{neg} combined with the CME mass M_{cme}

$$y = (M_{neg} + M_{cme}) - M_{neg} \quad (6.4)$$

6.1 CME Masses and Energies

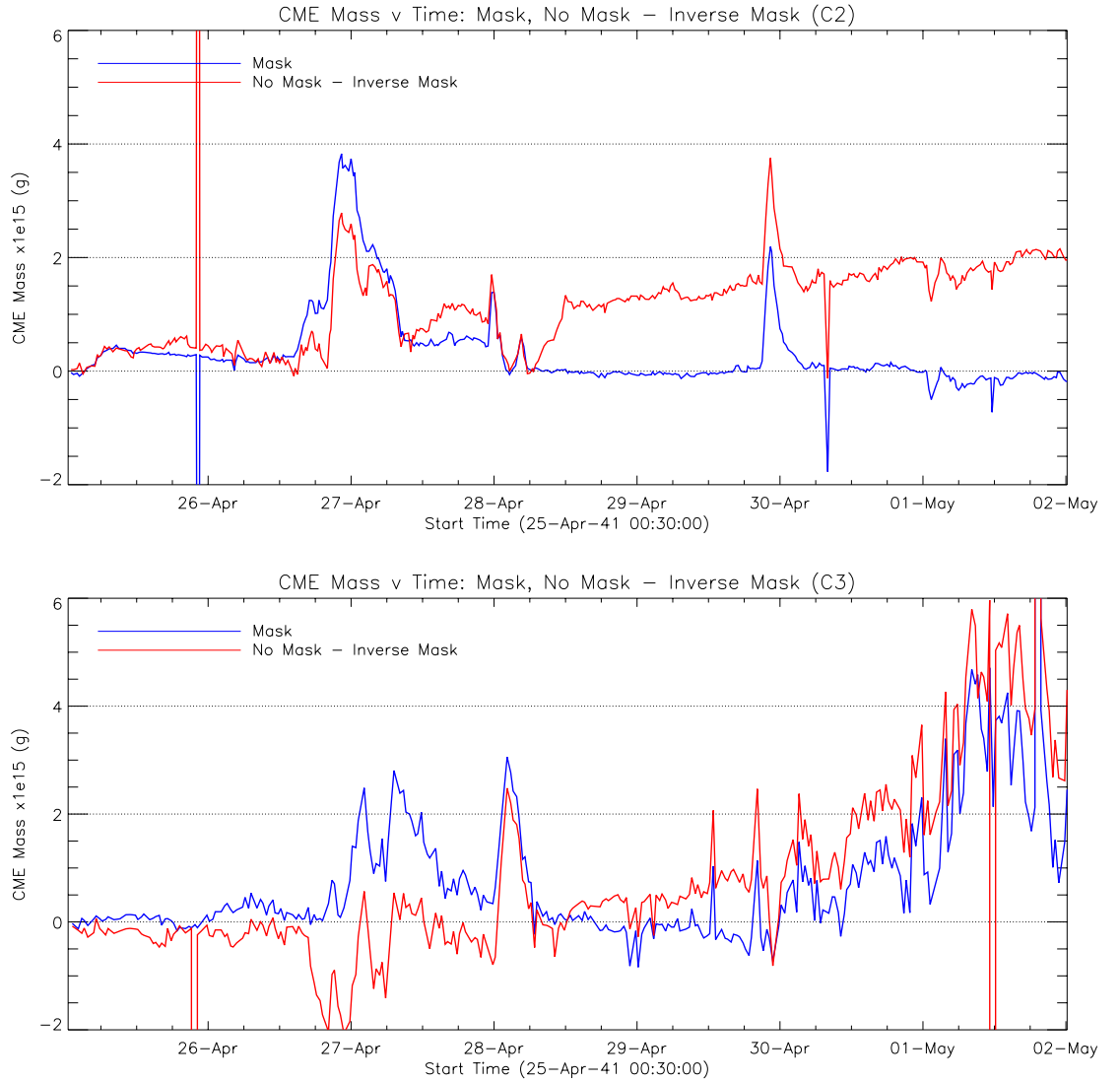


Figure 6.5: Comparison of the mass from masked images (blue) the no_mask - inverse_mask images (red) for C2 (upper) and C3 (lower). For both C2 and C3 the blue and red lines are a good match. The most obvious difference is the positive drift of the red line in C2, due to an excess background brightness subtracted in the base-differencing.

Since $M_{neg} < (M_{neg} + M_{cme}) < 0$, we end up with y value that is positive and larger than M_{cme} . Of course, if the pre-event image were chosen appropriately we would just have Equation 6.3, no problem. It's interesting to note that the difference between the blue and red line in Figure 6.5 is a measure of how much

6.1 CME Masses and Energies

the background corona changed over time; it is also a measure of how well chosen the background image is for the base-difference. If the lines diverge consistently, too much background brightness has been extracted from the images. The effect is not as pronounced in C3 for the observation sequence, probably because the CME does not perturb the background corona at this height range as much as it does at lower heights (in C2 FOV). Hence the analysis resulting in Figure 6.5 are a way of confirming that criteria (i) and (ii) are fulfilled.

There are a number of questions and issues that need to be addressed if the automatic mass detection is to produce reliable results:

- Removal of the spurious blobs in the quiet-time masks. Background values need to be brought to a maximum of 10^{13} g, this will ensure detection of even small CMEs with masses of $\sim 10^{14}$ g.
- An algorithm to choose an appropriate prevent image needs to be implemented. An average of a set of quiet images before CME detection is a possibility.
- What mass value should be taken as being representative of the CME mass? Is it appropriate to take the maximum mass value detected during the time interval when the CME is present? If so, should the maximum mass be taken from C2 or C3?

The last item here will require a number of tests to be performed on which telescope can provide the most reliable mass estimate. Primarily, C3 would seem like the most appropriate, since the large field-of-view (FOV) can contain all CME material i.e., there will be some material hidden by the occulter, as can happen in the C2 FOV. However, C3 is more susceptible to POS errors e.g., if the CME is not actually on the POS, the uncertainties introduced by assuming it *is* on

6.1 CME Masses and Energies

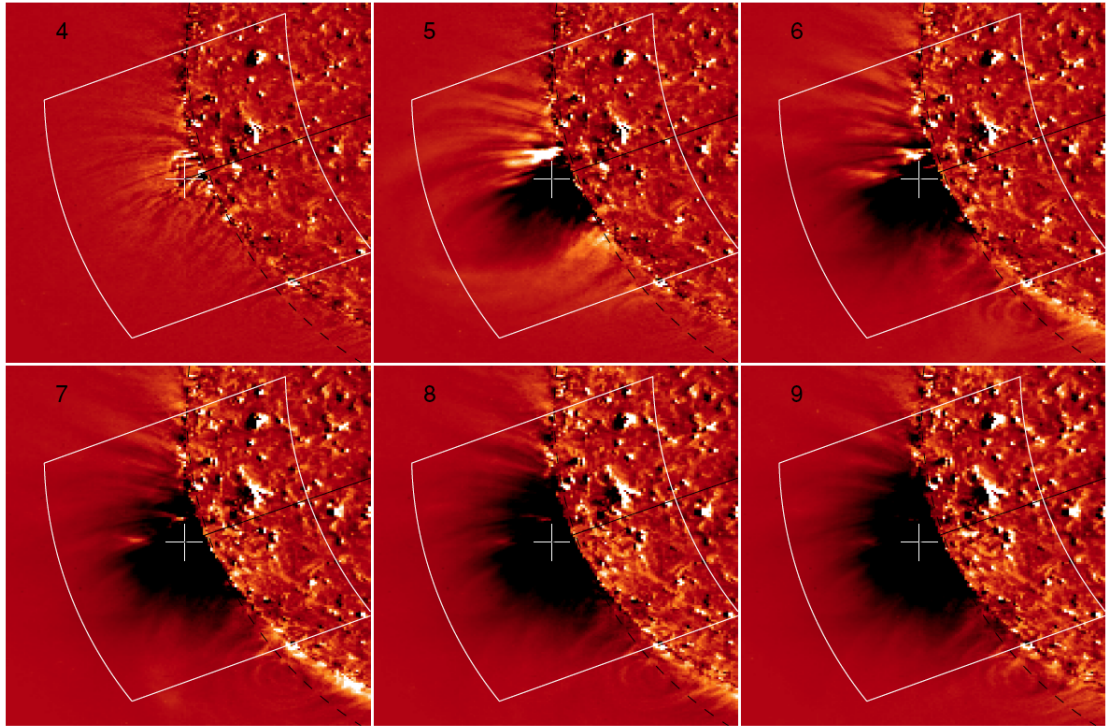


Figure 6.6: EUV dimming region observed by EUVI 195 Å channel on 31 December 2007. The dimming is due to evacuation of plasma from the region such that the emission measure drops (Aschwanden *et al.*, 2009)

the POS are worse for C3. These may be addressed by a study of the Thomson scattering geometry of the light received by each telescope.

6.1.2.2 Mass Estimates with AIA

There are a number of studies that have determined the mass of CMEs with varying degrees of accuracy from white-light observations. However very few studies, if any, have investigated where exactly the CME mass comes from. The origin of the mass is difficult to determine since the very early stages of CME development are obscured by the occulting disk of a coronagraph. This means that EUV imagers of the low corona are currently the only viable method of observing the birth of a CME. An analysis of the mass development during such an early phase of

6.1 CME Masses and Energies

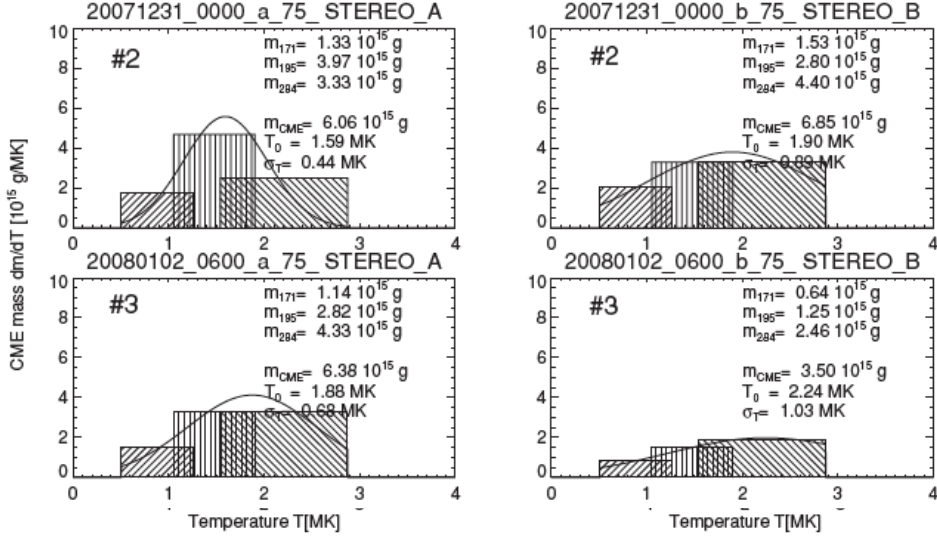


Figure 6.7: Mass-temperature distribution from EUVI/A and B for five different events. The three channels if EUVI, 171 Å, 195 Å, and 284 Å, are used to calculated the mass of the material contributing to emission in each of these channels. A construction of a Gaussian using these three measurements allows integration over temperature to find the total CME mass in the temperature range of 0.5–3.0 MK. Adapted from (Aschwanden *et al.*, 2009)

eruption may be able to reveal both the origin of the mass and what ultimately forms the CME. Currently, these are two major unknowns in CME physics.

The eruption of a CME in EUV observations is usually conspicuous by a lack of emission in the erupted active region i.e., as the CME erupts it evacuates the corona, leaving behind an emission deficit. This emission deficit is known as an EUV ‘dimming’ region and has been used to calculate the amount of evacuated mass (Aschwanden *et al.*, 2009). Dimming regions are also a regular feature of soft X-ray images (Sterling & Hudson, 1997).

The method of Aschwanden *et al.* (2009) exploits the fact that there are multiple filters in EUV imagers that can be used to measure the amount of evacuated mass in dimming regions. In one filter, the evacuated mass, m_d , may

6.1 CME Masses and Energies

be calculated from

$$m_d(t, T) = m_p n_d(t) V_D = m_p n_A \sqrt{\frac{I_d(t)}{I_A}} \frac{\pi}{4} w_d^2 \lambda_T \quad (6.5)$$

where m_p is proton mass, n_d is dimming number density, V_D is dimming volume, n_A is active region density (pre eruption), I_d is dimming region intensity, I_A is active region intensity (pre-eruption), w_d is the radius of the circular footprint of the dimming region, and λ_T is the temperature scale height. Since m_d may be measured in each of the temperature filters of the EUV imager the total mass may be constructed from a differential emission measure-type mass distribution

$$m_{cme}(t) = \int_{T_1}^{T_2} \left(\frac{dm_d(t, T)}{dT} \right) dT = \int_{T_1}^{T_2} \frac{\Delta m_D}{\Delta T_F} \exp\left(-\frac{(T - T_0)^2}{2\sigma_T^2}\right) dT \quad (6.6)$$

This analysis has been performed for EUVI on STEREO A and B. This imager only has three different passbands at 171 Å, 195 Å, and 284 Å, representing only three data points to which a gaussian is fit to the mass temperature distribution in Equation 6.6, these fits are shown in Figure 6.7. Since this may be done over time for each EUV image in the observation sequence, Aschwanden *et al.* (2009) constructed a mass evacuation curve over time (Figure 6.8). The curves correspond to different flares. This kind of analysis has the ability to give information on the eruption rate of the CME and possibly the forces acting on the ejection. However, not much work has been done in this area and the field is relatively under-explored. A number of interesting questions need to be investigated for mass evacuation rates:

- Does mass evacuation rate depend on flare size?
- Does evacuation rate depend on flare rise-time?

6.1 CME Masses and Energies

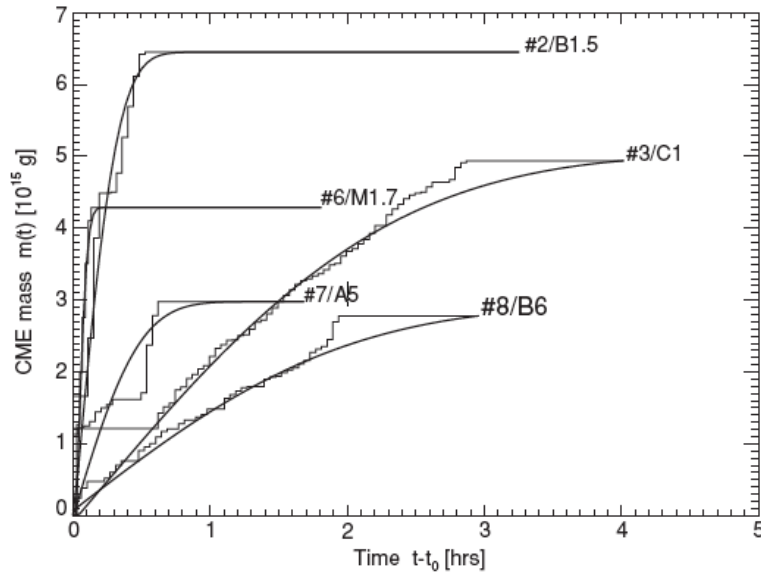


Figure 6.8: Mass evacuation from the dimming region with respect for five selected events. The biggest flare has the fastest mass loss rate but not the biggest final mass. (Aschwanden *et al.*, 2009)

- Is there any correlation with CME kinematical profiles?
- Are the mass evacuation rate and final mass correlated?
- Are mass evacuations different for events that have no associated flare?
- Ultimately, why are some evacuation rates faster than others?

These questions need to be investigated if there is to be an advance in understanding the origins of CMEs. However, EUVI observations are limited in this regard. Since there is only three data points to which the Gaussian is fit to this mass-temperature distribution, the results are quite unconstrained and sometimes unreliable. For example, panels #3 *STEREO* B of Figure 6.7 is a bad representation of a Gaussian. This may be due to the CME plasma temperature lying outside the response of the three EUVI channels. Also, the cadence of EUVI may be too slow to capture the very early stages of mass evacuation, which would be needed if a comparison was to be made with an impulsive flare.

6.1 CME Masses and Energies

The possibility for advancing this kind of study with AIA is very promising. There are at least three main areas in which AIA can advance such research

- AIA has a possible six passbands that may be used in the mass distribution curve. This will enable a better constraint on the Gaussian in Equation 6.6, producing a more reliable total mass estimate than the three passbands of EUVI. Another result that may stem from this is investigating the temperature distribution of CME material, leading to a development in an understanding of CME thermal energies, which are often overlooked.
- The above results could be advanced with the inclusion of UVCS spectroscopy data, which can give CME thermal characteristics from O VI, V and C III lines out to a height of $4 R_{\odot}$. A comparison of early and intermediate phase CME temperatures could determine if the CME expands adiabatically, which is another unknown. This is important for investigating how isolated the CME is from the solar wind plasma.
- AIA has a 12 second cadence (EUVI has 10 minutes), enabling a calculation of a mass evacuation curve in the very early stages of CME eruption. As mentioned, this will be particularly important for a comparison with very impulsive flares.

There are a wealth of physical properties in the early phase of CME eruption that could be answered with AIA. Up until current time, such an analysis has gone relatively unexplored.

6.2 Coronal Shocks and Radio Bursts

6.2.1 Principle results

The second goal of this thesis was to increase the understanding of CME-driven shocks and investigate the relationship amongst the various shock observables. A combination of white-light, EUV, and radio imaging showed CBFs and radio bursts have a common origin in a shock, and that this shock was driven by the CME flank. The principle results of this investigation were

- CBFs are closely associated to particle acceleration radio activity. The temporal correlation between CBFs and radio bursts such as type IIs and type IIIIs has been highlighted in the past (Klassen *et al.*, 2000; Maia & Pick, 2004). However, there are very few, if any, direct observations of an association between radio sources and CBFs. Vršnak *et al.* (2005a) showed a radio source which propagated around the limb in association with a CBF, however any direct comparison between the two features was hampered by the low cadence of EUV imaging. To date, the Carley *et al.* (2013) observation of a 150 MHz source closely following a CBF is the most comprehensive presentation of the clear relationship between the two features (Figure 5.1). It has confirmed that CBFs are inherently associated with radio activity. This radio activity is plasma emission generated by an instability in the presence of electron beams.
- The kinematics of the radio source was analysed giving a measure of the speed of this source. In order to estimate its Alfvén Mach number, we performed density and magnetic field diagnostics of the corona. Density diagnostics were taken from six AIA passbands and LASCO C2, while the

6.2 Coronal Shocks and Radio Bursts

magnetic field measurements were performed using a PFSS extrapolation. The combined density and magnetic field maps allowed us to produce an Alfvén speed map of the corona (Zucca et al. (in prep)). To our knowledge, this was the first time such a map was produced from observations. It provided a reliable means of comparing the source speed to the Alfvén speed of the corona in order to estimate the source Alfvén Mach number.

- The density map was also used in the analysis of the radio bursts in the dynamic spectra of S/WAVES, Nançay DA, and RSTO eCallisto. Usually, density models are employed to derive particle kinematics from drift rates in dynamic spectra. However, this can lead to erroneous positions and speeds of the particles producing the radio emission because the density models may be an unreliable description of coronal density profiles. Use of the density diagnostics from observation allowed us to derive much more reliable coronal heights for the radio activity observed in the dynamic spectra
- Analysis of the dynamic spectra activity showed there was particle acceleration of up to $0.4 c$, which manifests in the spectra as type III radio bursts. The speed of these bursts along the Parker spiral were used to estimate an ETA of the electrons at the STEREO -B spacecraft. It was found the ETA matched the observed time of arrival quite accurately. Furthermore, the observations of herringbones were the most striking evidence for particle acceleration in this study. The observations of herringbone fine structure were made possible by the installation of RSTO eCallisto spectrometers, as described in Chapter 3. The dynamic spectra from RSTO produced some of the clearest spectra of these herringbone bursts during the 22 September 2011 event, compared to other dynamic spectra observations. An analysis of these bursts showed that they are produced by electrons at a speed of

6.2 Coronal Shocks and Radio Bursts

$0.15 c$ and occur with a quasiperiodicity of 2-11 seconds.

- Both the radio source imaged by NRH and CBF had a close association with the southern flank of the CME. Since the a thermal analysis of the CBF showed that it was most likely a pressure wave, and the radio source was associated with spectral shock activity, we conclude that a shock driven by the CME flank expansion was the likely driver of CBF and radio activity. Evidence for a shock at the CME flank also came in the form of white-light observations. These observations were used to reconstruct the CME in 3D dimensions and show that the faint feature observed to the south of the CME in LASCO C2 was not part of the CME structure, and therefore must be shock.

Overall, this work has shown how a combination of radio, EUV and white-light imaging can reveal the evolution of plasmoid driven shocks in the solar atmosphere. It has shown that CBFs and radio bursts can share a common origin in a shock driven by the expansion of a CME flank.

6.2.2 Future Work

6.2.2.1 Hough Transform and Herringbone Statistics

As mentioned in Chapter 5, the frequency drift of herringbones can give information on the particle speeds, whereas there behaviour over time may depend on the shock acceleration characteristics. Also, the emissivity of plasma emission depends on the velocity of the particles inducing the emission (Equation A.4). However, it is still unknown as to what causes the herringbone bursts. Since there are many bursts in one herringbone sequence, there is an opportunity to statistically investigate the drift rates and intensities of these bursts, which can reveal

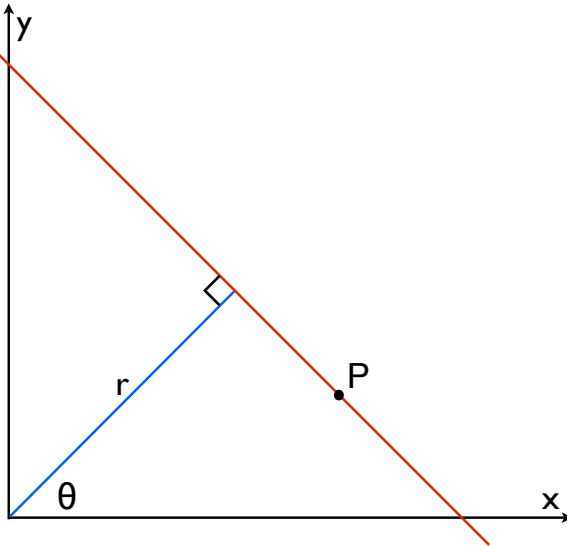


Figure 6.9: Line in the image space (x, y) and its polar coordinates (r, θ) . These two sets of coordinates are used to form a relationship by the image space and an (r, θ) Hough parameter space. For any orientation of the line through P (red line) the vector r (blue line) must intersect it at right angles. Rotating the red line about P will give a range of (r, θ) values that represent all red line orientations passing through P . These (r, θ) values will form a sinusoid when plotted in an (r, θ) space.

details of the particle acceleration process, and the plasma emission process.

To perform this statistical analysis we use the Hough transform (Hough, 1961), a feature recognition algorithm that is used to identify straight lines in images (Duda & Hart, 1972). In the Hough transform any line in an image may be represented in polar coordinates as $r = x\cos\theta + y\sin\theta$ (Figure 6.9). Any point P in the images space at (x_0, y_0) will have many lines, described by (r, θ) , that pass through it. In fact, all the values of (r, θ) which represent lines passing through (x_0, y_0) will form a sinusoid in an (r, θ) parameter space known as Hough space. The relationship between the images space and Hough space is shown in Figure 6.10. The sinusoid in Hough space is unique to the point (x_0, y_0) . Now, a second point in the image space, (x_1, y_1) , will also have its own unique sinusoid in Hough space. The point (r_i, θ_i) at which these sinusoids intersect represents a

6.2 Coronal Shocks and Radio Bursts

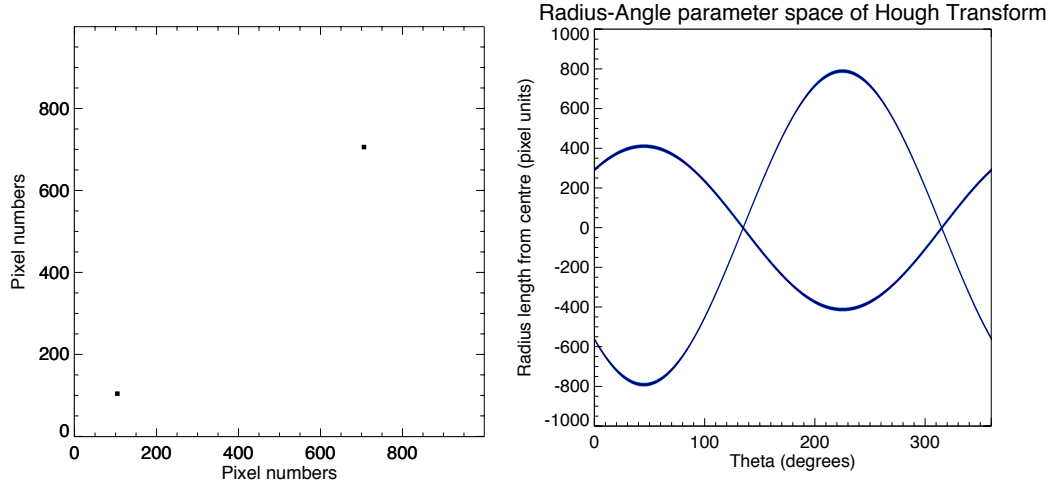


Figure 6.10: Relationship between image space and Hough space. The point in the image space have a range of (r, θ) points which represent all lines passing through the point. The (r, θ) values are sinusoids for each point, their point of intersection in Hough space will give the (r_i, θ_i) of the line passing through the points int he image space.

line that passes through both points in the image space, given by

$$y = \left(-\frac{\cos_i \theta}{\sin \theta_i} \right) x + \left(\frac{r_i}{\sin \theta_i} \right) \quad (6.7)$$

If a number of points in an image lie along a straight line, each of these points will have its own sinusoid in the Hough space and the point at which these sinusoids intersect represents the line that passes through all of the image points. A ‘back-projection’ of this Hough space to image space then returns the original image. Two examples if this are given in Figure 6.11. The top row shows an image of a number of lines of varying orientation and a square. The middle panel shows the 360° Hough space. Note that the sinusoids intersect at 90° (horizontal line), 180° (vertical line), and 135° diagonal line. The square represents a whole variety of sinusoids in the hough space that intersect at all angles, this is because there are a range of lines that represent this filled square. Back-projection of the

6.2 Coronal Shocks and Radio Bursts

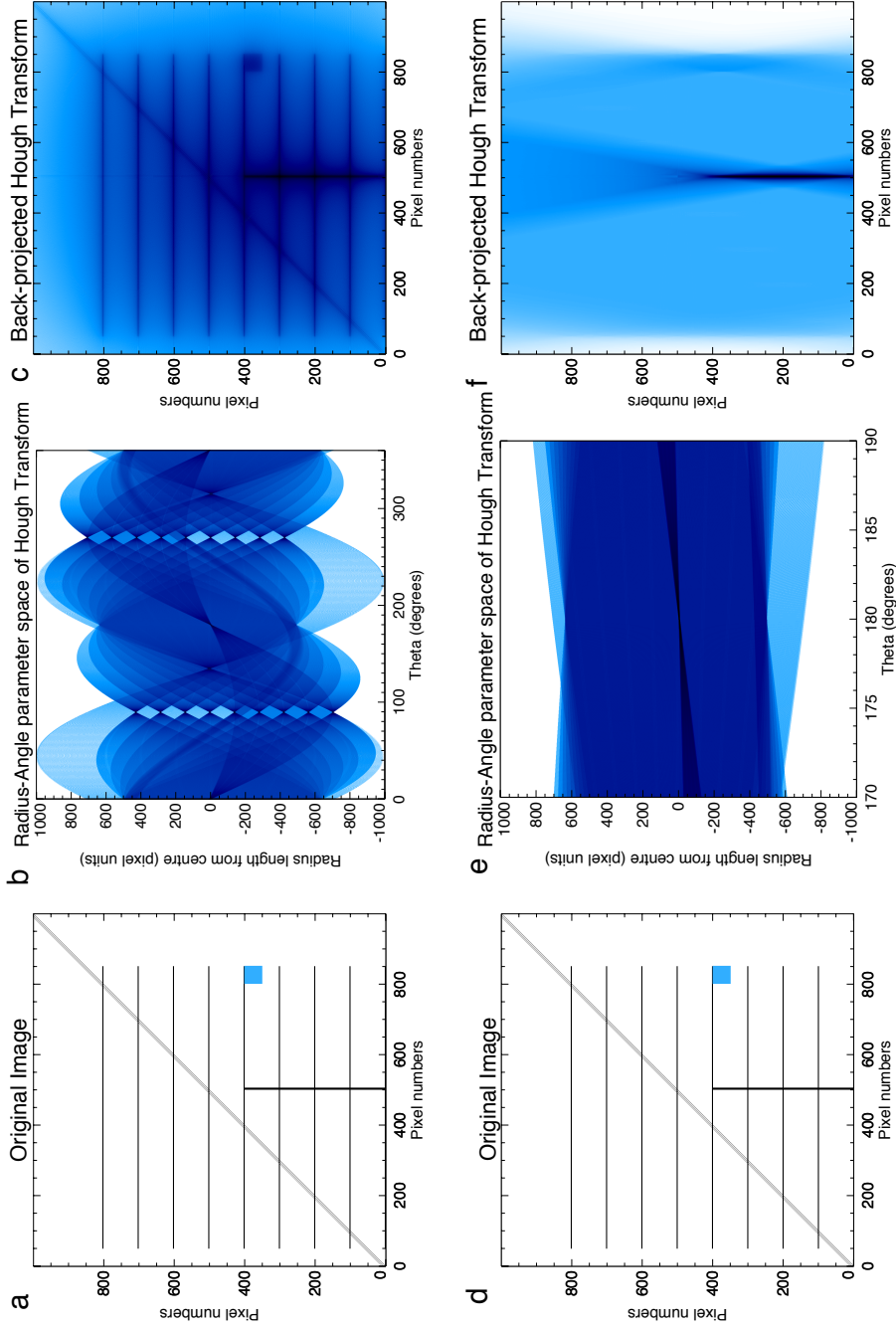


Figure 6.11: (a) An image with a number of lines of varying orientation and intensity. (b) The Hough transform of the image in (r, θ) space. The multiple intersection points at 90° and a variety of radii correspond to the multiple horizontal lines in the original image. There are also intersection points at 135° (diagonal line in original image) and 180° (vertical line). (c) The back projected Hough transform, recovering all features in the original image. The bottom row (d)-(f) show the same as the top row, expect that the back-projection is chosen over a region in hough space that only contains the vertical line. In this way only the vertical line is recovered and the remaining features are not recovered.

6.2 Coronal Shocks and Radio Bursts

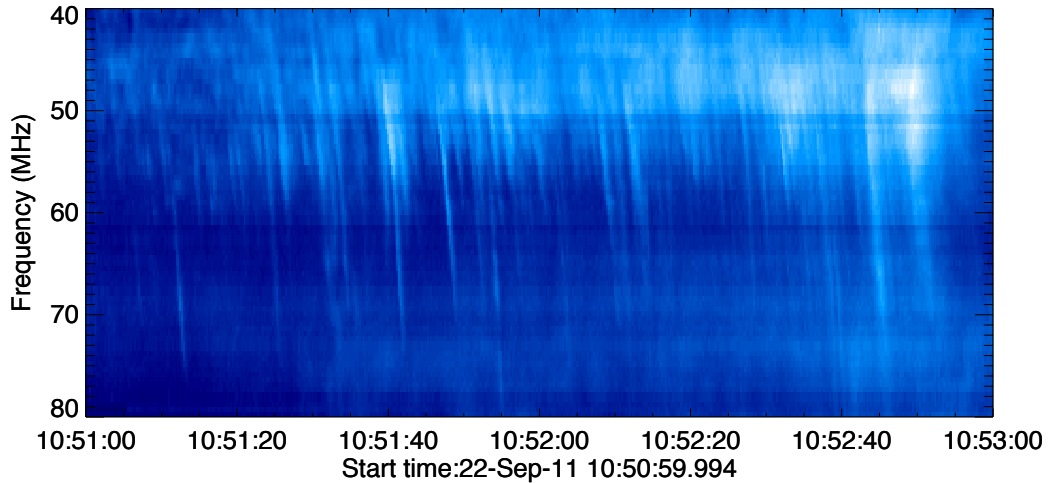


Figure 6.12: The herringbone observations from RSTO eCallisto on 22 September 2011. Given the polar coordinates defined in Figure 6.9. The herringbone orientations have an angle of $\sim 180\text{--}190^\circ$.

whole 360° space returns all lines in the original image. However, we may only back-project the Hough space in a particular angular range to extract lines of a desired orientation. This is shown in the bottom row of Figure 6.11. For the same original image we may isolate the vertical line, by only back-projecting the range $170^\circ - 190^\circ$. Note the sinusoid intersection at 180° (vertical line) in the ‘zoomed’ Hough space (panel e). The back-projection shown in Figure 6.11f contains the vertical line, and the vertical sections of the square.

Since the herringbones represent a large number of straight lines in a dynamic spectrum, a number of tests were performed with the Hough transform to investigate its use as a feature detection algorithm for these bursts. The Hough transform was performed on an RSTO eCallisto dynamic spectrum of herringbone radio bursts shown in Figure 6.12. The 360° parameter space of the Hough transform is shown in Figure 6.13. The overwhelming majority of detections are at an angle of 90° corresponding to horizontal lines. This is most likely caused by RFI in the dynamic spectrum. Interpolation amongst frequency channels in

6.2 Coronal Shocks and Radio Bursts

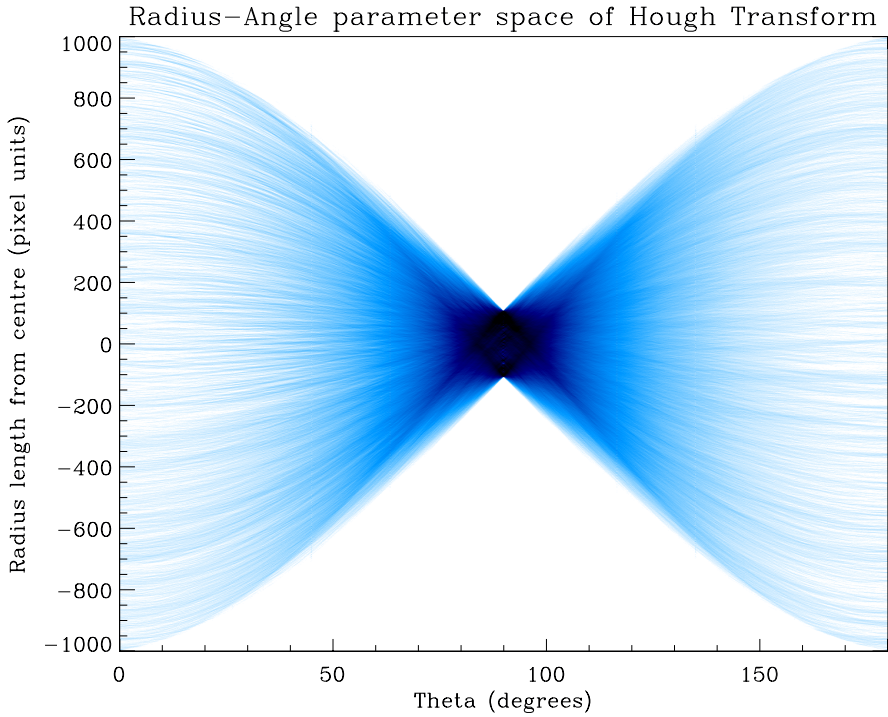


Figure 6.13: The radius-angle parameter space of the hough transform for the herringbones. The overwhelming majority of detections are at an angle of 90° corresponding to horizontal lines, most likely caused by RFI and interpolation between frequency channels.

the spectrum can also cause broad horizontal lines, this is particularly apparent in Figure 6.12.

Despite the fact there are strong detections for horizontal lines, the multiple threads in the parameter space cross each other at all angles, which means lines of every orientation are detected. An *a priori* choice of angles in the parameter space that the herringbones belong to will allow them to be detected effectively. A range of angles of $180^\circ - 190^\circ$ was chosen for the back-projection, the results of which are shown in Figure 6.14. The transform was successful in picking out many of the herringbones, but missed the particularly weak ones. Although the transform is successful in picking out straight lines, it contains no information on the start and end point of the line. This is the reason why some bursts have a

6.2 Coronal Shocks and Radio Bursts

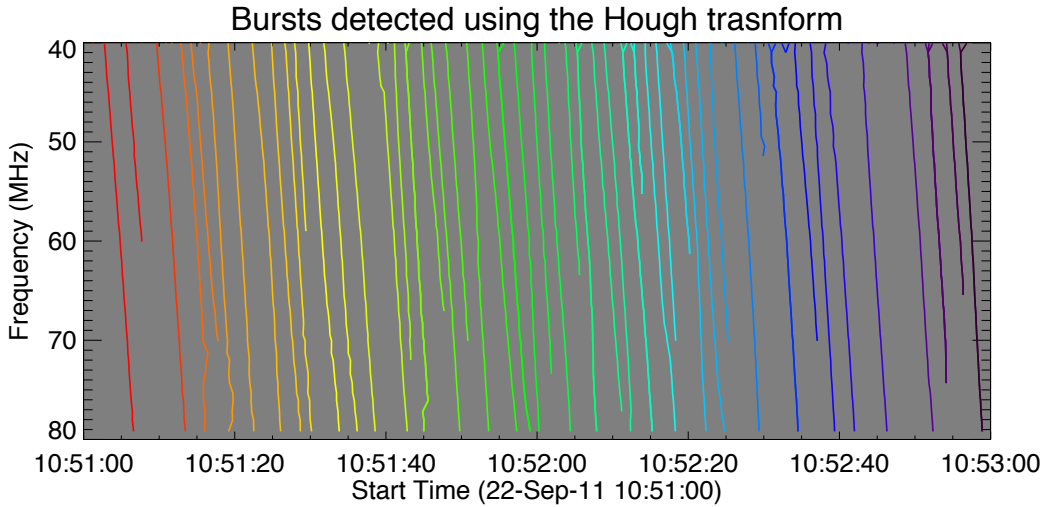


Figure 6.14: Herringbone bursts detected using the Hough transform. The Hough transform was successful in detecting most of the herringbones but failed to detect the weaker ones. The colours correspond to the statistical results shown below.

long length in the Hough transform detections, but a short length in the original dynamic spectrum. This mismatch of burst lengths is not a concern since the start and stop frequencies are not under investigation here. The identification of points that the bursts belong to allowed a number of parameters to be analysed and compared for each burst.

Figure 6.15a and b shows the intensity as a function of frequency for all bursts for both raw data and background subtracted data (colours correspond to the individual bursts in Figure 6.14). Overall the intensity increases for bursts later in the sequence (increase in intensity from red to purple), which is a general feature of the bursts in the original spectra. The background subtracted data also reveals a peak at ~ 45 MHz, which may be interpreted as the start frequency of these features. Figure 6.15b and c shows the frequency with respect to time for all bursts, with each showing a linear trend and range from $\sim 5\text{--}13\text{ MHz s}^{-1}$. The intensity with respect to time is shown in Figure 6.16a and b, revealing much of the same characteristics as Figure 6.15a and b. An interesting correlation is

6.2 Coronal Shocks and Radio Bursts

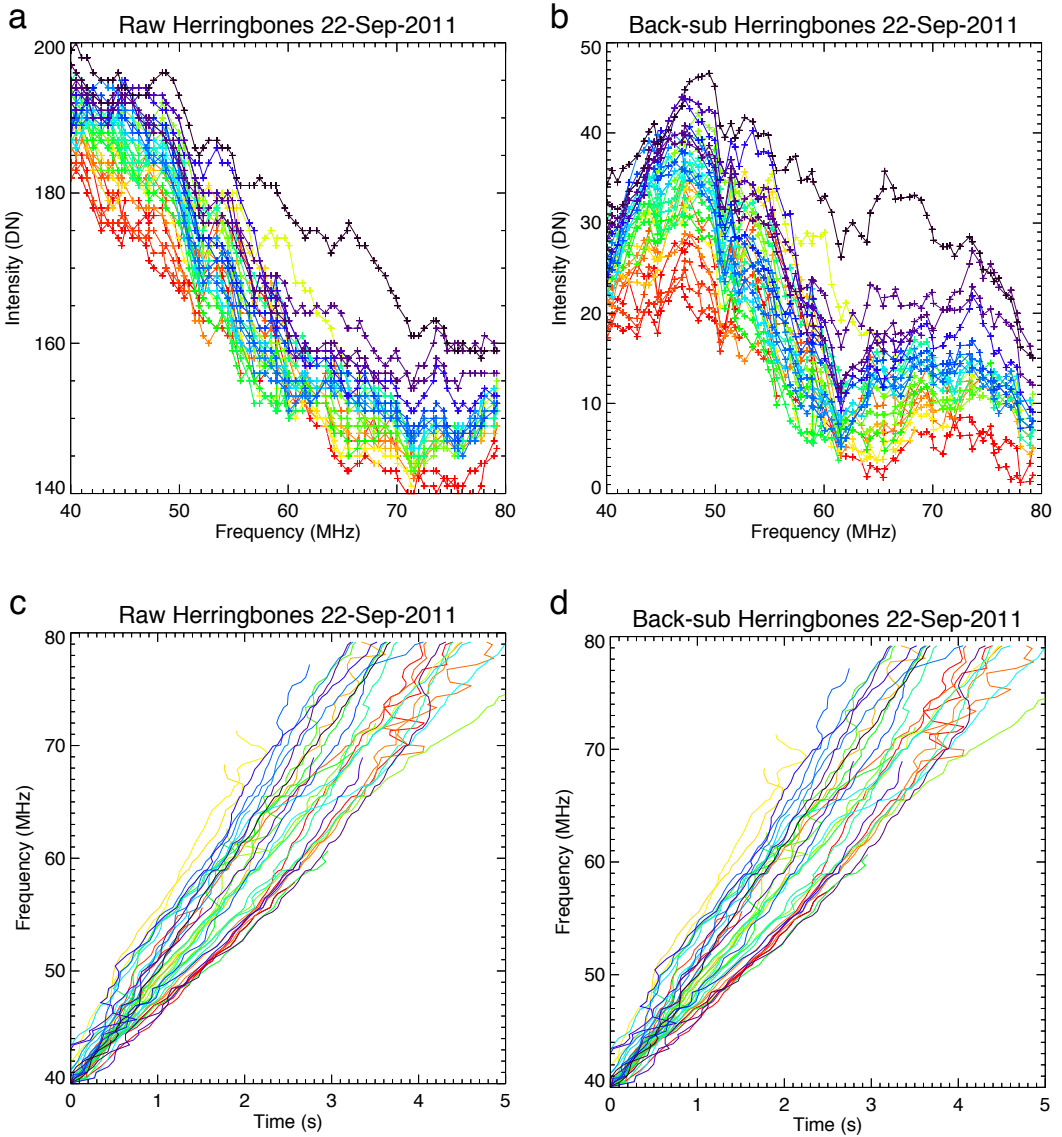


Figure 6.15: Herringbone bursts detected using the Hough transform. The transform performs well when the bursts are intense, but performs poorly when they are weak and close to background values.

shown in Figure 6.16b and c. The drift rate shows a negative correlation with the rate of change of intensity of the bursts. This may be interpreted as the faster the electron beams travel, the quicker they lose their energy and induce radiation for a shorter amount of time. This would agree with Equation A.4, which highlights the relationship between plasma emission emissivity and beam velocity. Despite the fact that there seems to be a correlation between the two parameters, there are a

6.2 Coronal Shocks and Radio Bursts

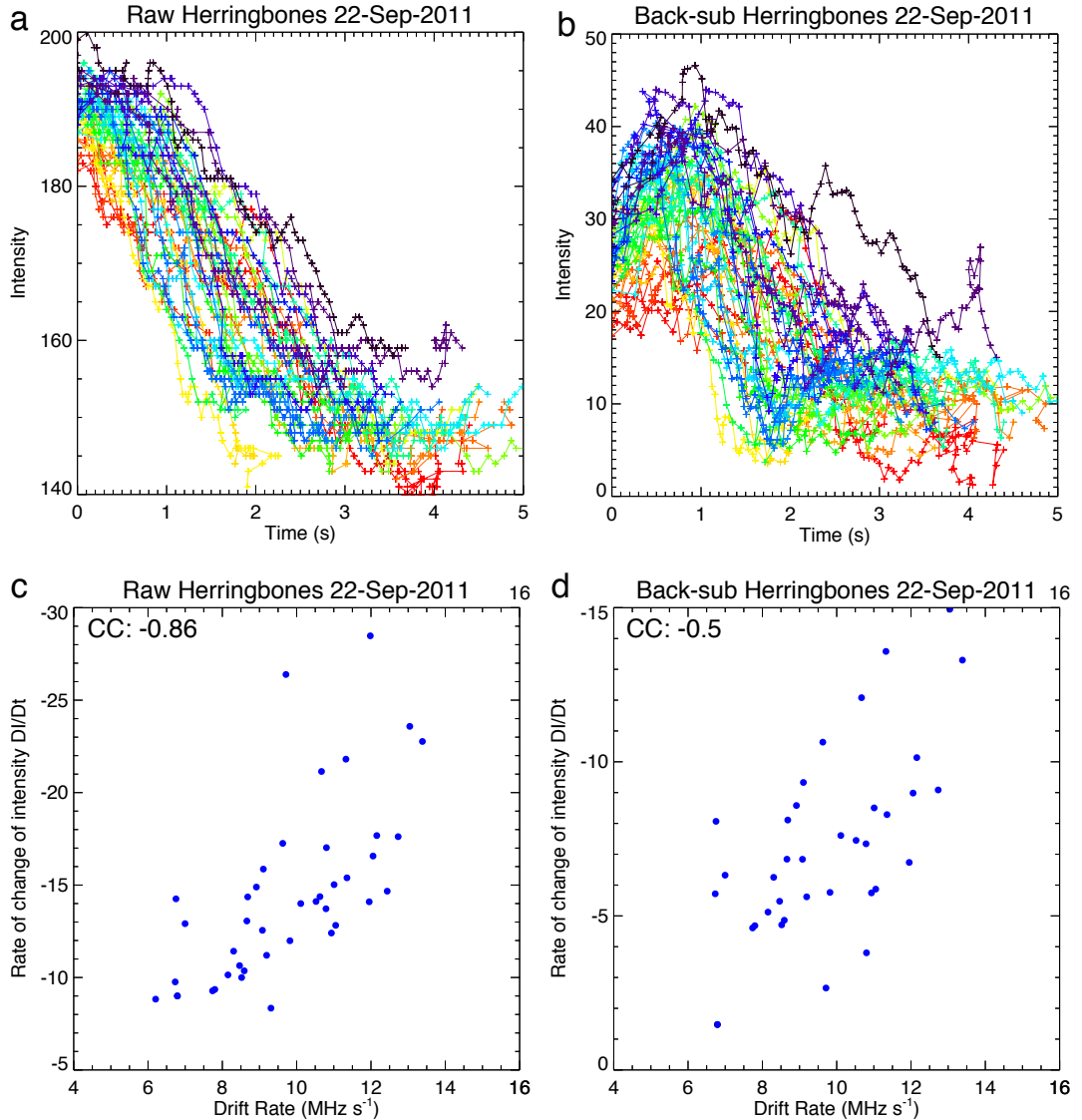


Figure 6.16: (a) Intensity versus time for raw data; (b) intensity versus time for background subtracted data. (c) and (d) show scatter plots of drift rate versus rate of change of intensity along the burst for raw and background subtracted data, respectively. The two show a good correlation which might suggest that the faster the beam, the faster it loses its energy

low number of data points and more bursts need to be included into the statistics if anything meaningful can be extracted from these results. Surprisingly, the maximum intensity and the drift rate do not show any correlation (Figure 6.17), which would be expected from Equation A.4. Again, this might be a symptom

6.2 Coronal Shocks and Radio Bursts

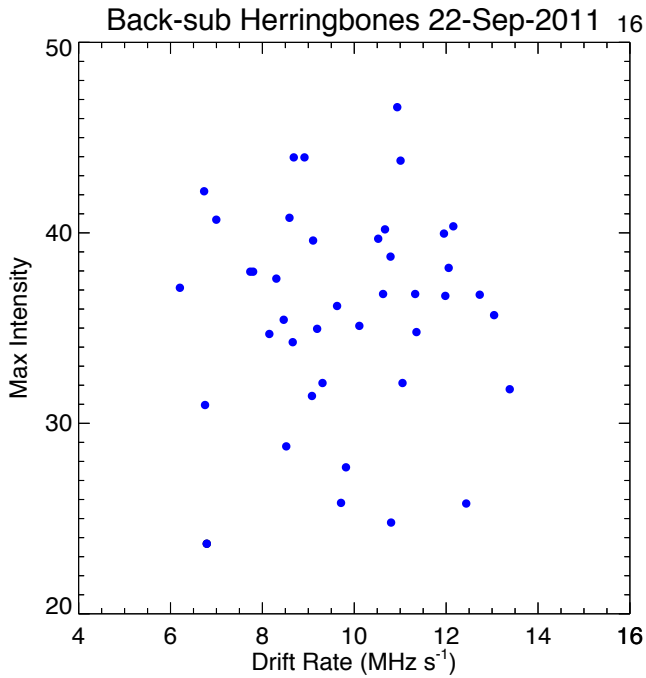


Figure 6.17: Scatter plot of drift rate and maximum intensity of the burst. They show no correlation despite the fact Equation A.4 would imply that they should. A larger data set needs to be explored in order to investigate this.

of low number statistics and needs to be further investigated.

As can be seen in Figure 6.14, the Hough transform is not perfect, and may miss some of the weaker or more patchy bursts. A greater effort needs to be made to ensure transform picks up the burst on the finest scales. One approach could be to use gradients to highlight edges in the image before using the Hough transform. A more sophisticated technique could be through multi-scale filtering using wavelets, this could highlight only the bursts, allowing the Hough transform to detect the smaller and fainter bursts more easily.

A statistical study of herringbone features has been lacking in recent times and a modern approach would compliment the herringbone statistical analysis of (Cairns & Robinson, 1987; Mann & Classen, 1995). It is still an unknown as to why some type IIs exhibit herringbones and why some do not. Future studies employing multi wavelength analysis, such as Carley *et al.* (2013), combined

6.2 Coronal Shocks and Radio Bursts

with a statistical analysis like the one presented in this section, can reveal both what caused the herringbones and what is the nature of the particle acceleration. Further analysis comparing emissivities and particle drift rates may reveal some details of the plasma emission mechanism.

A

Appendix

A.1 Radio Burst Emissivity

The full equations for emissivity of EM waves from the stochastic growth theory are

$$j_M(r) \approx \frac{\Phi_M}{\Delta\Omega_M} \frac{n_b m_e v_b^3}{3l(r)} \frac{\Delta v_b}{v_b} \quad (\text{A.1})$$

$$\Phi_F \approx 72\sqrt{3} \frac{\gamma_{L'}}{\gamma_S} \frac{v_e^3}{c^3} \frac{v_b}{\Delta v_b} \frac{e^{-u_c^2}}{u_c \sqrt{\pi}} \zeta_F \quad (\text{A.2})$$

A.2 EUV and pB Density Measurements

$$\Phi_H \approx \frac{18\sqrt{3}}{5\gamma_t} \sqrt{\frac{m_i}{\gamma_t m_e}} \frac{v_e^3 v_b^3}{c^5} \frac{v_b}{\Delta v_b} \zeta_H \quad (\text{A.3})$$

the expression involving u_c represent an ‘escape factor’ for the fundamental taking into account absorption and scattering of the radiation. $\frac{\gamma_L'}{\gamma_S}$ is the ratio of the damping rates of the product waves out of processes in equations ?? and ??. The ζ terms are the fractions of Langmuir waves that are kinematically able to contribute to the fundamental or harmonic emission, given by

$$\zeta_F \approx \exp \left[-\frac{4\gamma_t m_e}{45m_i} \left(\frac{v_b}{\Delta v_b} \right)^2 \left(\frac{3}{2} \sqrt{\frac{m_i}{\gamma_t m_e}} - \frac{v_b}{v_e} \right)^2 \right] \quad (\text{A.4})$$

$$\zeta_H \approx \frac{c}{2v_b} \sqrt{\frac{\pi}{6}} \frac{\beta \Delta v_b}{v_b} \left[\operatorname{erf} \left(\frac{\frac{v_e \sqrt{3}}{c} + \frac{2}{3} \sqrt{\frac{\gamma_t m_e}{m_i}}}{\frac{v_e \beta \Delta v_b}{v_b} \sqrt{2}} \right) + \operatorname{erf} \left(\frac{\frac{v_e \sqrt{3}}{c} - \frac{2}{3} \sqrt{\frac{\gamma_t m_e}{m_i}}}{\frac{v_e \beta \Delta v_b}{v_b} \sqrt{2}} \right) \right] \quad (\text{A.5})$$

where erf is the error function (Robinson & Cairns, 1993, 1998).

A.2 EUV and pB Density Measurements

Electron densities were calculated from emission measure maps derived using the SDO/AIAs six coronal filters and the method of (Aschwanden *et al.*, 2013). The method starts by reconstructing the differential emission measure $dEM/dT(DEM)$, using the intensity of the six SDO/AIA filters for each pixel. The DEM is a measure of the amount of plasma along the line-of-sight (LOS) that contributes to the emitted radiation in the temperature range T to $T + dT$ (Craig & Brown, 1976). Once the EM was obtained, the plasma electron density can be calculated estimating an effective length of the LOS of the emitting plasma. The 2D $EM(r, \phi)$ map, which is a function of heliocentric distance r and latitude, can

A.2 EUV and pB Density Measurements

then be written as

$$EM(r, \phi) = \int \left(\frac{dEM(r, \phi)}{dT} \right) dT \quad (\text{A.6})$$

$$= \int < N_e^2 > ds \quad (\text{A.7})$$

Knowing the line-of-sight length, s , the density of the emitting plasma can be obtained from the EM,

$$N_e(r, \phi) = \sqrt{\frac{EM(r, \phi)}{s(r)}} \quad (\text{A.8})$$

The LOS length was calculated using a geometrical method used widely in stellar atmospheres (Menzel, 1936). The LOS length s changes at different distance r and contributes to the intensity of the emitting plasma measured by the observer. This gives the LOS using an asymptotic series expansion in the form

$$S \approx \sqrt{H\pi r} \quad (\text{A.9})$$

where H is the scale height. Using a typical coronal temperature of 2 MK the scale height H is of the order of 9×10^9 cm and the LOS is in the order of 4×10^{10} cm. The LOS length does not change significantly in the $1-1.3 R_\odot$ range.

As for the polarized brightness measurements, the density diagnostic is through the use of coronagraph images and the Thomson scattering theory outlines in Chaoter. The method involves using the coronagraph data to extract polarized brightness measurements as a function of height i.e., along a radial trace in the coronagraph images. A polynomial is then fit to this data

$$I_t - I_r = \sum_s k_s x^{-s} \quad (\text{A.10})$$

A.2 EUV and pB Density Measurements

where $I_t - I_r$ is the polarized brightness, and x is the radial position in the corona, r , projected onto the plane of sky. van de Hulst (1950) showed that by use of the van de Hulst coefficients the electron density along the same radial trace can be expressed as

$$N(r) = \frac{1}{C\{A(r) - B(r)\}} \sum_s \frac{k_s}{a_{s+1}} r^{-s} \quad \text{where } a_n = \frac{\pi}{2^{n+1}} \frac{n!}{(1/2n!)^2} \quad (\text{A.11})$$

here C is constant equal to $\frac{3}{4} \times 1R_\odot \times \sigma_T$; σ_T is the Thomson scattering cross section and $A(r)$ and $B(r)$ are the van de Hulst coefficients (see Chapter 4). Here, the same k_s produced from the polarized brightness fit are used to calculate $N(r)$.

References

- ALLEN, C.W. (1947). Solar Radio-Noise of 200 Mc. /s. and its relation to Solar Observations. *Monthly Notices of the Royal Astronomical Society*, **107**, 386. (Cited on pages 38 and 97.)
- ALY, J.J. (1991). How much energy can be stored in a three-dimensional force-free magnetic field? *Astrophysical Journal Letters*, **375**, L61–L64. (Cited on page 70.)
- ANTIOCHOS, S.K., DEVORE, C.R. & KLIMCHUK, J.A. (1999a). A Model for Solar Coronal Mass Ejections. *Astrophysical Journal*, **510**, 485–493. (Cited on pages 65 and 69.)
- ANTIOCHOS, S.K., DEVORE, C.R. & KLIMCHUK, J.A. (1999b). A Model for Solar Coronal Mass Ejections. *Astrophysical Journal*, **510**, 485–493. (Cited on pages 140 and 168.)
- ASCHWANDEN, M.J. (2004). *Physics of the Solar Corona. An Introduction*. Praxis Publishing Ltd. (Cited on pages 62 and 63.)
- ASCHWANDEN, M.J., NITTA, N.V., WUELTER, J.P., LEMEN, J.R., SANDMAN, A., VOURLIDAS, A. & COLANINNO, R.C. (2009). First Measurements of the Mass of Coronal Mass Ejections from the EUV Dimming Observed with STEREO EUVI A+B Spacecraft. *Astrophysical Journal*, **706**, 376–392. (Cited on pages 30, 167, 212, 213, 214 and 215.)
- ASCHWANDEN, M.J., BOERNER, P., SCHRIJVER, C.J. & MALANUSHENKO, A. (2013). Automated Temperature and Emission Measure Analysis of Coronal Loops and Active Regions Observed with the Atmospheric Imaging Assembly on the Solar Dynamics Observatory (SDO/AIA). *Solar Physics*, **283**, 5–30. (Cited on pages 179 and 232.)

REFERENCES

- ATTRILL, G.D.R., HARRA, L.K., VAN DRIEL-GESZTELYI, L. & DÉMOULIN, P. (2007). Coronal “Wave”: Magnetic Footprint of a Coronal Mass Ejection? *Astrophysical Journal Letters*, **656**, L101–L104. (Cited on page 49.)
- AULANIER, G., DELUCA, E.E., ANTIOCHOS, S.K., McMULLEN, R.A. & GOLUB, L. (2000). The Topology and Evolution of the Bastille Day Flare. *Astrophysical Journal*, **540**, 1126–1142. (Cited on page 72.)
- AURASS, H. & MANN, G. (2004). Radio Observation of Electron Acceleration at Solar Flare Reconnection Outflow Termination Shocks. *Astrophysical Journal*, **615**, 526–530. (Cited on pages 45 and 198.)
- AURASS, H., VRŠNAK, B. & MANN, G. (2002). Shock-excited radio burst from reconnection outflow jet? *Astronomy & Astrophysics*, **384**, 273–281. (Cited on page 45.)
- AVIGNON, Y., BONMARTIN, J., BOUTEILLE, A., CLAVERIER, B. & HULOT, E. (1989). The mark IV Nancay Radioheliograph. *Solar Physics*, **120**, 193–204. (Cited on pages 120 and 122.)
- BABCOCK, H.W. (1961). The Topology of the Sun’s Magnetic Field and the 22-YEAR Cycle. *Astrophysical Journal*, **133**, 572. (Cited on page 9.)
- BAIN, H.M., KRUCKER, S., GLESENER, L. & LIN, R.P. (2012). Radio Imaging of Shock-accelerated Electrons Associated with an Erupting Plasmoid on 2010 November 3. *Astrophysical Journal*, **750**, 44. (Cited on pages 41 and 196.)
- BALE, S.D., ULLRICH, R., GOETZ, K., ALSTER, N., CECCONI, B., DEKKALI, M., LINGNER, N.R., MACHER, W., MANNING, R.E., McCUALEY, J., MONSON, S.J., OSWALD, T.H. & PULUPA, M. (2008). The Electric Antennas for the STEREO/WAVES Experiment. *Space Science Reviews*, **136**, 529–547. (Cited on page 126.)
- BALFOUR, S. (1861). On the Great Magnetic Disturbance Which Extended from August 28 to September 7, 1859, as Recorded by Photography at the Kew Observatory. *Philosophical Transactions of the Royal Society of London*, **151**, 423. (Cited on page 21.)
- BALL, L. & MELROSE, D.B. (2001). Shock Drift Acceleration of Electrons. *Publications of the Astronomical Society of Australia*, **18**, 361–373. (Cited on pages 82, 83, 84, 85 and 196.)

REFERENCES

- BEIN, B.M., BERKEBILE-STOISER, S., VERONIG, A.M., TEMMER, M., MUHR, N., KIENREICH, I., UTZ, D. & VRŠNAK, B. (2011). Impulsive Acceleration of Coronal Mass Ejections. I. Statistics and Coronal Mass Ejection Source Region Characteristics. *Astrophysical Journal*, **738**, 191. (Cited on pages 34, 166, 169, 170 and 202.)
- BENZ, A.O., MONSTEIN, C. & MEYER, H. (2005). Callisto A New Concept for Solar Radio Spectrometers. *Solar Physics*, **226**, 143–151. (Cited on pages 128 and 130.)
- BENZ, A.O., MONSTEIN, C., MEYER, H., MANOHARAN, P.K., RAMESH, R., ALTYNTSEV, A., LARA, A., PAEZ, J. & CHO, K.S. (2009). A World-Wide Net of Solar Radio Spectrometers: e-CALLISTO. *Earth Moon and Planets*, **104**, 277–285. (Cited on pages 133 and 190.)
- BIESECKER, D.A., MYERS, D.C., THOMPSON, B.J., HAMMER, D.M. & VOURLIDAS, A. (2002). Solar Phenomena Associated with “EIT Waves”. *Astrophysical Journal*, **569**, 1009–1015. (Cited on page 47.)
- BILLINGS, D.E. (1966a). *A guide to the solar corona*. (Cited on pages 114 and 150.)
- BILLINGS, D.E. (1966b). *A guide to the solar corona*. (Cited on page 141.)
- BOISCHOT, A., ROSOLEN, C., AUBIER, M.G., DAIGNE, G., GENOVA, F., LEBLANC, Y., LECACHEUX, A., DE LA NOE, J. & MOLLER-PEDERSEN, B. (1980). A new high-gain, broadband, steerable array to study Jovian decametric emission. *ICARUS*, **43**, 399–407. (Cited on pages 125 and 187.)
- BONG, S.C., MOON, Y.J., CHO, K.S., KIM, Y.H., PARK, Y.D. & CHOE, G.S. (2006). Direct Observation of Low Coronal Breakout: Does Breakout Precede or Follow Solar Eruption? *Astrophysical Journal Letters*, **636**, L169–L172. (Cited on page 72.)
- BONMARTIN, J., BOUTEILLE, A., CLAELIER, B., ISSARTEL, M.P., KERDRAON, A., LANTOS, M.F., LANTOS, P., MERCIER, C., PICK, M. & RAOULT, A. (1983). The Mark III Nancay Radioheliograph. *Solar Physics*, **88**, 383–390. (Cited on page 120.)
- BOUGERET, J.L., KAISER, M.L., KELLOGG, P.J., MANNING, R., GOETZ, K., MONSON, S.J., MONGE, N., FRIEL, L., MEETRE, C.A., PERCHE, C., SITRUK, L. & HOANG, S.

REFERENCES

- (1995). Waves: The Radio and Plasma Wave Investigation on the Wind Spacecraft. *Space Science Reviews*, **71**, 231–263. (Cited on page 126.)
- BOUGERET, J.L., ZARKA, P., CAROUBALOS, C., KARLICKÝ, M., LEBLANC, Y., MAROULIS, D., HILLARIS, A., MOUSSAS, X., ALISSANDRAKIS, C.E., DUMAS, G. & PERCHE, C. (1998). A shock associated (SA) radio event and related phenomena observed from the base of the solar corona to 1 AU. *Geophysical Research Letters*, **25**, 2513–2516. (Cited on page 46.)
- BOUGERET, J.L., GOETZ, K., KAISER, M.L., BALE, S.D., KELLOGG, P.J., MAKSIMOVIC, M., MONGE, N., MONSON, S.J., ASTIER, P.L., DAVY, S., DEKKALI, M., HINZE, J.J., MANNING, R.E., AGUILAR-RODRIGUEZ, E., BONNIN, X., BRIAND, C., CAIRNS, I.H., CATTELL, C.A., CECCONI, B., EASTWOOD, J., ERGUN, R.E., FAINBERG, J., HOANG, S., HUTTUNEN, K.E.J., KRUCKER, S., LECACHEUX, A., MACDOWALL, R.J., MACHER, W., MANGENEY, A., MEETRE, C.A., MOUSSAS, X., NGUYEN, Q.N., OSWALD, T.H., PULUPA, M., REINER, M.J., ROBINSON, P.A., RUCKER, H., SALEM, C., SANTOLIK, O., SILVIS, J.M., ULLRICH, R., ZARKA, P. & ZOUGANELIS, I. (2008). S/WAVES: The Radio and Plasma Wave Investigation on the STEREO Mission. *Space Science Reviews*, **136**, 487–528. (Cited on pages 126 and 187.)
- BOURSIER, Y., LAMY, P., LLEBARIA, A., GOUDAIL, F. & ROBELUS, S. (2009). The ARTEMIS Catalog of LASCO Coronal Mass Ejections. Automatic Recognition of Transient Events and Marseille Inventory from Synoptic maps. *Solar Physics*, **257**, 125–147. (Cited on page 203.)
- BOUVIER, A. & WADHWA, M. (2010). The age of the Solar System redefined by the oldest Pb-Pb age of a meteoritic inclusion. *Nature Geoscience*, **3**, 637–641. (Cited on page 2.)
- BRUECKNER, G.E., HOWARD, R.A., KOOMEN, M.J., KORENDYKE, C.M., MICHELS, D.J., MOSES, J.D., SOCKER, D.G., DERE, K.P., LAMY, P.L., LLEBARIA, A., BOUT, M.V., SCHWENN, R., SIMNETT, G.M., BEDFORD, D.K. & EYLES, C.J. (1995). The Large Angle Spectroscopic Coronagraph (LASCO). *Solar Physics*, **162**, 357–402. (Cited on pages 102, 103, 104, 105, 112, 141 and 193.)

REFERENCES

- BURGESS, D. (2006). Simulations of Electron Acceleration at Collisionless Shocks: The Effects of Surface Fluctuations. *Astrophysical Journal*, **653**, 316–324. (Cited on pages 191, 197 and 198.)
- BURKEPILE, J.T., HUNDHAUSEN, A.J., STANGER, A.L., ST. CYR, O.C. & SEIDEN, J.A. (2004). Role of projection effects on solar coronal mass ejection properties: 1. A study of CMEs associated with limb activity. *Journal of Geophysical Research (Space Physics)*, **109**, 3103. (Cited on pages 22, 23 and 24.)
- BYRNE, J.P., MALONEY, S.A., MCATEER, R.T.J., REFOJO, J.M. & GALLAGHER, P.T. (2010). Propagation of an Earth-directed coronal mass ejection in three dimensions. *Nature Communications*, **1**. (Cited on pages 24, 141, 158, 164, 165, 166, 169, 170, 193 and 194.)
- BYRNE, J.P., MORGAN, H., HABBAL, S.R. & GALLAGHER, P.T. (2012). Automatic Detection and Tracking of Coronal Mass Ejections. II. Multiscale Filtering of Coronagraph Images. *Astrophysical Journal*, **752**, 145. (Cited on page 204.)
- CAIRNS, I.H. & ROBINSON, R.D. (1987). Herringbone bursts associated with type II solar radio emission. *Solar Physics*, **111**, 365–383. (Cited on pages 44 and 228.)
- CAIRNS, I.H., KNOCK, S.A., ROBINSON, P.A. & KUNCIC, Z. (2003). Type II Solar Radio Bursts: Theory and Space Weather Implications. *Space Science Reviews*, **107**, 27–34. (Cited on page 93.)
- CANE, H.V. & ERICKSON, W.C. (2005). Solar Type II Radio Bursts and IP Type II Events. *Astrophysical Journal*, **623**, 1180–1194. (Cited on page 42.)
- CANE, H.V. & WHITE, S.M. (1989). On the source conditions for herringbone structure in type II solar radio bursts. *Solar Physics*, **120**, 137–144. (Cited on page 44.)
- CARGILL, P.J. (2004). On the Aerodynamic Drag Force Acting on Interplanetary Coronal Mass Ejections. *Solar Physics*, **221**, 135–149. (Cited on page 34.)
- CARLEY, E.P., MCATEER, R.T.J. & GALLAGHER, P.T. (2012). Coronal Mass Ejection Mass, Energy, and Force Estimates Using STEREO. *Astrophysical Journal*, **752**, 36. (Cited on pages 144, 145, 162 and 165.)

REFERENCES

- CARLSSON, M. & STEIN, R.F. (1997). Formation of Solar Calcium H and K Bright Grains. *Astrophysical Journal*, **481**, 500. (Cited on page 14.)
- CARRINGTON, R.C. (1859). Description of a Singular Appearance seen in the Sun on September 1, 1859. *Monthly Notices of the Royal Astronomical Society*, **20**, 13–15. (Cited on page 20.)
- CHAPMAN, S. & FERRARO, V.C.A. (1930). A New Theory of Magnetic Storms. *Nature*, **126**, 129–130. (Cited on page 21.)
- CHARBONNEAU, P. (2010). Dynamo Models of the Solar Cycle. *Living Reviews in Solar Physics*, **7**, 3. (Cited on page 9.)
- CHEN, J. (1989). Effects of toroidal forces in current loops embedded in a background plasma. *Astrophysical Journal*, **338**, 453–470. (Cited on pages 66, 72, 73 and 75.)
- CHEN, J. (1996). Theory of prominence eruption and propagation: Interplanetary consequences. *Journal of Geophysical Research*, **1012**, 27499–27520. (Cited on pages 140, 168 and 203.)
- CHEN, J., MARQUÉ, C., VOURLIDAS, A., KRALL, J. & SCHUCK, P.W. (2006). The Flux-Rope Scaling of the Acceleration of Coronal Mass Ejections and Eruptive Prominences. *Astrophysical Journal*, **649**, 452–463. (Cited on page 140.)
- CHEN, P.F. (2011). Coronal Mass Ejections: Models and Their Observational Basis. *Living Reviews in Solar Physics*, **8**, 1. (Cited on page 66.)
- CHEN, P.F., WU, S.T., SHIBATA, K. & FANG, C. (2002). Evidence of EIT and Moreton Waves in Numerical Simulations. *Astrophysical Journal Letters*, **572**, L99–L102. (Cited on page 49.)
- CHENG, X., ZHANG, J., OLMEDO, O., VOURLIDAS, A., DING, M.D. & LIU, Y. (2012). Investigation of the Formation and Separation of an Extreme-ultraviolet Wave from the Expansion of a Coronal Mass Ejection. *Astrophysical Journal Letters*, **745**, L5. (Cited on page 186.)
- CHO, K.S., LEE, J., MOON, Y.J., DRYER, M., BONG, S.C., KIM, Y.H. & PARK, Y.D. (2007). A study of CME and type II shock kinematics based on coronal density measurement. *Astronomy & Astrophysics*, **461**, 1121–1125. (Cited on page 41.)

REFERENCES

- CHO, K.S., BONG, S.C., MOON, Y.J., SHANMUGARAJU, A., KWON, R.Y. & PARK, Y.D. (2011). Relationship between multiple type II solar radio bursts and CME observed by STEREO/SECCHI. *Astronomy & Astrophysics*, **530**, A16. (Cited on page 41.)
- CLASSEN, H.T. & AURASS, H. (2002). On the association between type II radio bursts and CMEs. *Astronomy & Astrophysics*, **384**, 1098–1106. (Cited on page 40.)
- COHEN, O., ATTRILL, G.D.R., MANCHESTER, W.B., IV & WILLS-DAVEY, M.J. (2009). Numerical Simulation of an EUV Coronal Wave Based on the 2009 February 13 CME Event Observed by STEREO. *Astrophysical Journal*, **705**, 587–602. (Cited on page 186.)
- COLANINNO, R.C. & VOURLIDAS, A. (2009). First Determination of the True Mass of Coronal Mass Ejections: A Novel Approach to Using the Two STEREO Viewpoints. *Astrophysical Journal*, **698**, 852–858. (Cited on pages 29, 142 and 161.)
- CRAIG, I.J.D. & BROWN, J.C. (1976). Fundamental limitations of X-ray spectra as diagnostics of plasma temperature structure. *Astronomy & Astrophysics*, **49**, 239–250. (Cited on page 232.)
- DAVIS, R., HARMER, D.S. & HOFFMAN, K.C. (1968). Search for Neutrinos from the Sun. *Physical Review Letters*, **20**, 1205–1209. (Cited on page 4.)
- DE HOFFMANN, F. & TELLER, E. (1950). Magneto-Hydrodynamic Shocks. *Physical Review*, **80**, 692–703. (Cited on page 82.)
- DE KONING, C.A., PIZZO, V.J. & BIESECKER, D.A. (2009). Geometric Localization of CMEs in 3D Space Using STEREO Beacon Data: First Results. *Solar Physics*, **256**, 167–181. (Cited on page 24.)
- DELANNÉE, C., TÖRÖK, T., AULANIER, G. & HOCHEDÉZ, J.F. (2008). A New Model for Propagating Parts of EIT Waves: A Current Shell in a CME. *Solar Physics*, **247**, 123–150. (Cited on pages 49, 174 and 195.)
- DOMINGO, V., FLECK, B. & POLAND, A.I. (1995). The SOHO Mission: an Overview. *Solar Physics*, **162**, 1–37. (Cited on pages 22 and 141.)

REFERENCES

- DOWNS, C., ROUSSEV, I.I., VAN DER HOLST, B., LUGAZ, N. & SOKOLOV, I.V. (2012). Understanding SDO/AIA Observations of the 2010 June 13 EUV Wave Event: Direct Insight from a Global Thermodynamic MHD Simulation. *Astrophysical Journal*, **750**, 134. (Cited on pages 185 and 186.)
- DUDA, R.O. & HART, P.E. (1972). Use of the hough transformation to detect lines and curves in pictures. *Commun. ACM*, **15**, 11–15. (Cited on page 220.)
- EMSLIE, A.G., KUCHAREK, H., DENNIS, B.R., GOPALSWAMY, N., HOLMAN, G.D., SHARE, G.H., VOURLIDAS, A., FORBES, T.G., GALLAGHER, P.T., MASON, G.M., METCALF, T.R., MEWALDT, R.A., MURPHY, R.J., SCHWARTZ, R.A. & ZURBUCHEN, T.H. (2004). Energy partition in two solar flare/CME events. *Journal of Geophysical Research (Space Physics)*, **109**, A10104. (Cited on pages 36, 166 and 171.)
- EMSLIE, A.G., DENNIS, B.R., SHIH, A.Y., CHAMBERLIN, P.C., MEWALDT, R.A., MOORE, C.S., SHARE, G.H., VOURLIDAS, A. & WELSCH, B.T. (2012). Global Energetics of Thirty-eight Large Solar Eruptive Events. *Astrophysical Journal*, **759**, 71. (Cited on pages xiii and 36.)
- FAN, Y. (2005). Coronal Mass Ejections as Loss of Confinement of Kinked Magnetic Flux Ropes. *Astrophysical Journal*, **630**, 543–551. (Cited on page 66.)
- FAN, Y. (2009). Magnetic Fields in the Solar Convection Zone. *Living Reviews in Solar Physics*, **6**, 4. (Cited on page 10.)
- FELDMAN, W.C., ANDERSON, R.C., BAME, S.J., GARY, S.P., GOSLING, J.T., MCCOMAS, D.J., THOMSEN, M.F., PASCHMANN, G. & HOPPE, M.M. (1983). Electron velocity distributions near the earth's bow shock. *Journal of Geophysical Research*, **88**, 96–110. (Cited on page 83.)
- FENG, S.W., CHEN, Y., KONG, X.L., LI, G., SONG, H.Q., FENG, X.S. & LIU, Y. (2012). Radio Signatures of Coronal-mass-ejection-Streamer Interaction and Source Diagnostics of Type II Radio Burst. *Astrophysical Journal*, **753**, 21. (Cited on page 195.)

REFERENCES

- FENG, S.W., CHEN, Y., KONG, X.L., LI, G., SONG, H.Q., FENG, X.S. & GUO, F. (2013). Diagnostics on the Source Properties of a Type II Radio Burst with Spectral Bumps. *Astrophysical Journal*, **767**, 29. (Cited on page 195.)
- FITZPATRICK, R. (2000). *The Physics of Plasmas*. (Cited on page 78.)
- FONTENLA, J., REICHMANN, E.J. & TANDBERG-HANSSEN, E. (1988). The Lyman-alpha line in various solar features. I - Observations. *Astrophysical Journal*, **329**, 464–481. (Cited on pages 13, 14 and 15.)
- FORBES, T.G. & ISENBERG, P.A. (1991). A catastrophe mechanism for coronal mass ejections. *Astrophysical Journal*, **373**, 294–307. (Cited on pages 66, 68, 140 and 168.)
- FORBES, T.G. & PRIEST, E.R. (1995). Photospheric Magnetic Field Evolution and Eruptive Flares. *Astrophysical Journal*, **446**, 377. (Cited on pages 65, 67, 68, 140 and 168.)
- FORBUSH, S.E. (1946). Three Unusual Cosmic-Ray Increases Possibly Due to Charged Particles from the Sun. *Physical Review*, **70**, 771–772. (Cited on page 21.)
- FOUKAL, P.V. (2004). *Solar Astrophysics, 2nd, Revised Edition*. Wiley-VCH. (Cited on pages 2 and 5.)
- GABRIEL, A.H. (1976). A magnetic model of the solar transition region. *Royal Society of London Philosophical Transactions Series A*, **281**, 339–352. (Cited on pages 13, 14 and 15.)
- GALLAGHER, P.T. & LONG, D.M. (2011). Large-scale Bright Fronts in the Solar Corona: A Review of "EIT waves". *Space Science Reviews*, **158**, 365–396. (Cited on pages 173 and 195.)
- GALLAGHER, P.T., LAWRENCE, G.R. & DENNIS, B.R. (2003). Rapid Acceleration of a Coronal Mass Ejection in the Low Corona and Implications for Propagation. *Astrophysical Journal Letters*, **588**, L53–L56. (Cited on pages 26, 166 and 170.)
- GINZBURG, V.L. & ZHELEZNIAKOV, V.V. (1958). On the Possible Mechanisms of Sporadic Solar Radio Emission (Radiation in an Isotropic Plasma). *Soviet Astronomy*, **2**, 653. (Cited on page 92.)
- GOLD, T. (1962). Magnetic Storms. *Space Science Reviews*, **1**, 100–114. (Cited on page 21.)

REFERENCES

- GOOSSENS, M., ed. (2003). *An introduction to plasma astrophysics and magnetohydrodynamics*, vol. 294 of *Astrophysics and Space Science Library*. (Cited on page 57.)
- GOPALSWAMY, N. & KUNDU, M.R. (1992). Estimation of the mass of a coronal mass ejection from radio observations. *Astrophysical Journal Letters*, **390**, L37–L39. (Cited on page 30.)
- GOPALSWAMY, N. & THOMPSON, B.J. (2000). Early life of coronal mass ejections. *Journal of Atmospheric and Solar-Terrestrial Physics*, **62**, 1457–1469. (Cited on pages 20, 24 and 25.)
- GOPALSWAMY, N., YASHIRO, S., MICHALEK, G., STENBORG, G., VOURLIDAS, A., FREELAND, S. & HOWARD, R. (2009a). The SOHO/LASCO CME Catalog. *Earth Moon and Planets*, **104**, 295–313. (Cited on page 203.)
- GOPALSWAMY, N., YASHIRO, S., TEMMER, M., DAVILA, J., THOMPSON, W.T., JONES, S., MCATEER, R.T.J., WUELTER, J.P., FREELAND, S. & HOWARD, R.A. (2009b). EUV Wave Reflection from a Coronal Hole. *Astrophysical Journal Letters*, **691**, L123–L127. (Cited on pages 47 and 173.)
- GOPALSWAMY, N., NITTA, N., AKIYAMA, S., MÄKELÄ, P. & YASHIRO, S. (2012). Coronal Magnetic Field Measurement from EUV Images Made by the Solar Dynamics Observatory. *Astrophysical Journal*, **744**, 72. (Cited on page 51.)
- GOSLING, J.T. (1993). The solar flare myth. *Journal of Geophysical Research*, **98**, 18937–18950. (Cited on page 66.)
- GOSLING, J.T., HILDNER, E., MACQUEEN, R.M., MUNRO, R.H., POLAND, A.I. & ROSS, C.L. (1976). The speeds of coronal mass ejection events. *Solar Physics*, **48**, 389–397. (Cited on page 40.)
- GRECHNEV, V.V., AFANASYEV, A.N., URALOV, A.M., CHERTOK, I.M., ESELEVICH, M.V., ESELEVICH, V.G., RUDENKO, G.V. & KUBO, Y. (2011a). Coronal Shock Waves, EUV Waves, and Their Relation to CMEs. III. Shock-Associated CME/EUV Wave in an Event with a Two-Component EUV Transient. *Solar Physics*, **273**, 461–477. (Cited on pages 48, 49 and 196.)
- GRECHNEV, V.V., URALOV, A.M., CHERTOK, I.M., KUZMENKO, I.V., AFANASYEV, A.N., MESHALKINA, N.S., KALASHNIKOV, S.S. & KUBO, Y. (2011b). Coronal Shock Waves,

REFERENCES

- EUV Waves, and Their Relation to CMEs. I. Reconciliation of "EIT Waves", Type II Radio Bursts, and Leading Edges of CMEs. *Solar Physics*, **273**, 433–460. (Cited on pages 47, 173, 174 and 195.)
- GUO, F. & GIACALONE, J. (2010). The Effect of Large-scale Magnetic Turbulence on the Acceleration of Electrons by Perpendicular Collisionless Shocks. *Astrophysical Journal*, **715**, 406–411. (Cited on pages 44, 173, 191, 198 and 199.)
- GUO, F. & GIACALONE, J. (2012). Particle Acceleration at a Flare Termination Shock: Effect of Large-scale Magnetic Turbulence. *Astrophysical Journal*, **753**, 28. (Cited on page 196.)
- GURNETT, D.A., KURTH, W.S., KIRCHNER, D.L., HOSPODARSKY, G.B., AVERKAMP, T.F., ZARKA, P., LECACHEUX, A., MANNING, R., ROUX, A., CANU, P., CORNILLEAU-WEHRLIN, N., GALOPEAU, P., MEYER, A., BOSTRÖM, R., GUSTAFSSON, G., WAHLUND, J.E., ÅHLEN, L., RUCKER, H.O., LADREITER, H.P., MACHER, W., WOOLLISCROFT, L.J.C., ALLEYNE, H., KAISER, M.L., DESCH, M.D., FARRELL, W.M., HARVEY, C.C., LOUARN, P., KELLOGG, P.J., GOETZ, K. & PEDERSEN, A. (2004). The Cassini Radio and Plasma Wave Investigation. *Space Science Reviews*, **114**, 395–463. (Cited on page 126.)
- HEY, J.S. (1946). Solar Radiations in the 4-6 Metre Radio Wave-Length Band. *Nature*, **157**, 47–48. (Cited on page 38.)
- HOLMAN, G.D. & PESSES, M.E. (1983). Solar type II radio emission and the shock drift acceleration of electrons. *Astrophysical Journal*, **267**, 837–843. (Cited on pages 81, 85 and 196.)
- HOUGH, P.V.C. (1961). A Method for Faster Analysis of Bubble Chamber Photographs (Hough and Powell). In *Instrumentation for High-Energy Physics*, 242. (Cited on page 220.)
- HOWARD, R.A., MOSES, J.D., VOURLIDAS, A., NEWMARK, J.S., SOCKER, D.G., PLUNKETT, S.P., KORENDYKE, C.M., COOK, J.W., HURLEY, A., DAVILA, J.M., THOMPSON, W.T., ST CYR, O.C., MENTZELL, E., MEHALICK, K., LEMEN, J.R., WUELTER, J.P., DUNCAN, D.W., TARBELL, T.D., WOLFSON, C.J., MOORE, A., HARRISON, R.A., WALTHAM, N.R., LANG, J., DAVIS, C.J., EYLES, C.J., MAPSON-MENARD, H., SIMNETT, G.M., HALAIN, J.P., DEFISE, J.M., MAZY, E., ROCHUS, P., MERCIER, R.,

REFERENCES

- RAVET, M.F., DELMOTTE, F., AUCHERE, F., DELABOUDINIÈRE, J.P., BOTHMER, V., DEUTSCH, W., WANG, D., RICH, N., COOPER, S., STEPHENS, V., MAAHS, G., BAUGH, R., McMULLIN, D. & CARTER, T. (2008). Sun Earth Connection Coronal and Heliospheric Investigation (SECCHI). *Space Science Reviews*, **136**, 67–115. (Cited on pages 107, 110 and 141.)
- HOWARD, T.A. & TAPPIN, S.J. (2009). Interplanetary Coronal Mass Ejections Observed in the Heliosphere: 1. Review of Theory. *Space Science Reviews*, **147**, 31–54. (Cited on pages 148, 149 and 150.)
- HOWARD, T.A., FRY, C.D., JOHNSTON, J.C. & WEBB, D.F. (2007). On the Evolution of Coronal Mass Ejections in the Interplanetary Medium. *Astrophysical Journal*, **667**, 610–625. (Cited on page 141.)
- HUNDHAUSEN, A. (1999). Coronal Mass Ejections. In K.T. Strong, J.L.R. Saba, B.M. Haisch & J.T. Schmelz, eds., *The many faces of the sun: a summary of the results from NASA's Solar Maximum Mission.*, 143. (Cited on page 22.)
- HUNDHAUSEN, A.J. (1972). Coronal Expansion and Solar Wind. *Physics and Chemistry in Space*, **5**. (Cited on page 39.)
- ILLING, R.M.E. & HUNDHAUSEN, A.J. (1985). Observation of a coronal transient from 1.2 to 6 solar radii. *Journal of Geophysical Research*, **90**, 275–282. (Cited on page 22.)
- INAN, U. & GOLKOWSKI, M. (2011). *Principles of Plasma Physics for Engineers and Scientists*. (Cited on page 57.)
- JACKSON, J.D. (1975). *Classical electrodynamics*. (Cited on page 147.)
- KABIN, K. (2001). A note on the compression ratio in MHD shocks. *Journal of Plasma Physics*, **66**, 259–274. (Not cited.)
- KAHLER, S.W. (2007). Solar Sources of Heliospheric Energetic Electron Events - Shocks or Flares? *Space Science Reviews*, **129**, 359–390. (Cited on page 174.)
- KAISER, M.L., KUCERA, T.A., DAVILA, J.M., ST. CYR, O.C., GUHATHAKURTA, M. & CHRISTIAN, E. (2008). The STEREO Mission: An Introduction. *Space Science Reviews*, **136**, 5–16. (Cited on pages 22, 106 and 141.)

REFERENCES

- KERDRAON, A. & DELOUIS, J.M. (1997). The Nançay Radioheliograph. In G. Trottet, ed., *Coronal Physics from Radio and Space Observations*, vol. 483 of *Lecture Notes in Physics*, Berlin Springer Verlag, 192. (Cited on pages 118, 120, 124 and 175.)
- KHAN, J.I. & AURASS, H. (2002). X-ray observations of a large-scale solar coronal shock wave. *Astronomy & Astrophysics*, **383**, 1018–1031. (Cited on pages 38 and 47.)
- KIM, R.S., GOPALSWAMY, N., MOON, Y.J., CHO, K.S. & YASHIRO, S. (2012). Magnetic Field Strength in the Upper Solar Corona Using White-light Shock Structures Surrounding Coronal Mass Ejections. *Astrophysical Journal*, **746**, 118. (Cited on page 51.)
- KLASSEN, A., AURASS, H., MANN, G. & THOMPSON, B.J. (2000). Catalogue of the 1997 SOHO-EIT coronal transient waves and associated type II radio burst spectra. *Astronomy & Astrophysics Supplemental*, **141**, 357–369. (Cited on pages 47 and 217.)
- KLASSEN, A., BOTHMER, V., MANN, G., REINER, M.J., KRUCKER, S., VOURLIDAS, A. & KUNOW, H. (2002). Solar energetic electron events and coronal shocks. *Astronomy & Astrophysics*, **385**, 1078–1088. (Cited on pages 48 and 173.)
- KLEIN, K.L., KHAN, J.I., VILMER, N., DELOUIS, J.M. & AURASS, H. (1999). X-ray and radio evidence on the origin of a coronal shock wave. *Astronomy & Astrophysics*, **346**, L53–L56. (Cited on page 41.)
- KLIEM, B. & TÖRÖK, T. (2006). Torus Instability. *Physical Review Letters*, **96**, 255002–+. (Cited on pages 140 and 168.)
- KNOCK, S.A., CAIRNS, I.H., ROBINSON, P.A. & KUNCIC, Z. (2001). Theory of type II radio emission from the foreshock of an interplanetary shock. *Journal of Geophysical Research*, **106**, 25041–25052. (Cited on page 93.)
- KNOCK, S.A., CAIRNS, I.H., ROBINSON, P.A. & KUNCIC, Z. (2003). Theoretically predicted properties of type II radio emission from an interplanetary foreshock. *Journal of Geophysical Research (Space Physics)*, **108**, 1126. (Cited on page 93.)
- KONTAR, E.P. (2001). Dynamics of electron beams in the inhomogeneous solar corona plasma. *Solar Physics*, **202**, 131–149. (Cited on pages 88 and 92.)

REFERENCES

- KOSUGI, T. (1976). Type II-IV radio bursts and compact and diffuse white-light clouds in the outer corona of December 14, 1971. *Solar Physics*, **48**, 339–356. (Cited on page 39.)
- KOZAREV, K.A., KORRECK, K.E., LOBZIN, V.V., WEBER, M.A. & SCHWADRON, N.A. (2011). Off-limb Solar Coronal Wavefronts from SDO/AIA Extreme-ultraviolet Observations - Implications for Particle Production. *Astrophysical Journal Letters*, **733**, L25. (Cited on pages 48, 173 and 195.)
- KRALL, J. & ST. CYR, O.C. (2006). Flux-Rope Coronal Mass Ejection Geometry and Its Relation to Observed Morphology. *Astrophysical Journal*, **652**, 1740–1746. (Cited on page 158.)
- KRALL, J., CHEN, J., DUFFIN, R.T., HOWARD, R.A. & THOMPSON, B.J. (2001). Erupting Solar Magnetic Flux Ropes: Theory and Observation. *Astrophysical Journal*, **562**, 1045–1057. (Cited on pages 66, 73 and 74.)
- KRUCKER, S., LARSON, D.E., LIN, R.P. & THOMPSON, B.J. (1999). On the Origin of Impulsive Electron Events Observed at 1 AU. *Astrophysical Journal*, **519**, 864–875. (Cited on page 48.)
- LANTOS, P. (1999). Low Frequency Observations of the Quiet Sun: a Review. In T.S. Bastian, N. Gopalswamy & K. Shibasaki, eds., *Proceedings of the Nobeyama Symposium*, 11–24. (Cited on page 18.)
- LECACHEUX, A. (2000). The Nançay Decameter Array: A Useful Step Towards Giant, New Generation Radio Telescopes for Long Wavelength Radio Astronomy. *Washington DC American Geophysical Union Geophysical Monograph Series*, **119**, 321. (Cited on page 125.)
- LEMEN, J.R., TITLE, A.M., AKIN, D.J., BOERNER, P.F., CHOU, C., DRAKE, J.F., DUNCAN, D.W., EDWARDS, C.G., FRIEDLAENDER, F.M., HEYMAN, G.F., HURLBURT, N.E., KATZ, N.L., KUSHNER, G.D., LEVAY, M., LINDGREN, R.W., MATHUR, D.P., McFEATERS, E.L., MITCHELL, S., REHSE, R.A., SCHRIJVER, C.J., SPRINGER, L.A., STERN, R.A., TARBELL, T.D., WUELTER, J.P., WOLFSON, C.J., YANARI, C., BOOKBINDER, J.A., CHEIMETS, P.N., CALDWELL, D., DELUCA, E.E., GATES, R., GOLUB, L., PARK, S., PODGORSKI, W.A., BUSH, R.I., SCHERRER, P.H., GUMMIN, M.A., SMITH, P., AUKER, G., JERRAM, P., POOL, P., SOUFLI, R., WINDT, D.L., BEARDSLEY, S., CLAPP,

REFERENCES

- M., LANG, J. & WALTHAM, N. (2012). The Atmospheric Imaging Assembly (AIA) on the Solar Dynamics Observatory (SDO). *Solar Physics*, **275**, 17–40. (Cited on pages 114, 115, 117, 118 and 175.)
- LEWIS, D.J. & SIMNETT, G.M. (2002). Bulk flow velocities in the solar corona at solar maximum. *Monthly Notices of the Royal Astronomical Society*, **333**, 969–976. (Cited on page 33.)
- LIN, C.H., GALLAGHER, P.T. & Raftery, C.L. (2010). Investigating the driving mechanisms of coronal mass ejections. *Astronomy & Astrophysics*, **516**, A44. (Cited on page 140.)
- LIN, J. & FORBES, T.G. (2000). Effects of reconnection on the coronal mass ejection process. *Journal of Geophysical Research*, **105**, 2375–2392. (Cited on pages 66, 140 and 168.)
- LIN, R.P., LEVEDAHL, W.K., LOTKO, W., GURNETT, D.A. & SCARF, F.L. (1986). Evidence for nonlinear wave-wave interactions in solar type III radio bursts. *Astrophysical Journal*, **308**, 954–965. (Cited on page 92.)
- LINDEMANN, F. (1919). Note on the Theory of Magnetic Storms. *Philosophical Magazine Series 6*, **38**, 669. (Cited on page 21.)
- LONG, D.M., DELUCA, E.E. & GALLAGHER, P.T. (2011a). The Wave Properties of Coronal Bright Fronts Observed Using SDO/AIA. *Astrophysical Journal Letters*, **741**, L21. (Cited on page 178.)
- LONG, D.M., GALLAGHER, P.T., MCATEER, R.T.J. & BLOOMFIELD, D.S. (2011b). Deceleration and dispersion of large-scale coronal bright fronts. *Astronomy & Astrophysics*, **531**, A42. (Cited on pages 47 and 173.)
- LOWE, R.E. & BURGESS, D. (2003). The properties and causes of rippling in quasi-perpendicular collisionless shock fronts. *Annales Geophysicae*, **21**, 671–679. (Cited on page 197.)
- LYNCH, B.J., ANTIOCHOS, S.K., MACNEICE, P.J., ZURBUCHEN, T.H. & FISK, L.A. (2004). Observable Properties of the Breakout Model for Coronal Mass Ejections. *Astrophysical Journal*, **617**, 589–599. (Cited on page 70.)

REFERENCES

- LYNCH, B.J., ANTIOCHOS, S.K., DEVORE, C.R., LUHMANN, J.G. & ZURBUCHEN, T.H. (2008). Topological Evolution of a Fast Magnetic Breakout CME in Three Dimensions. *Astrophysical Journal*, **683**, 1192–1206. (Cited on pages 70, 71, 140 and 168.)
- LYOT, B. (1939). The study of the solar corona and prominences without eclipses (George Darwin Lecture, 1939). *Monthly Notices of the Royal Astronomical Society*, **99**, 580. (Cited on page 101.)
- MACNEICE, P., ANTIOCHOS, S.K., PHILLIPS, A., SPICER, D.S., DEVORE, C.R. & OLSON, K. (2004). A Numerical Study of the Breakout Model for Coronal Mass Ejection Initiation. *Astrophysical Journal*, **614**, 1028–1041. (Cited on page 70.)
- MACQUEEN, R.M., CSOEKE-POECKH, A., HILDNER, E., HOUSE, L., REYNOLDS, R., STANGER, A., TEPOEL, H. & WAGNER, W. (1980). The High Altitude Observatory Coronagraph/Polarimeter on the Solar Maximum Mission. *Solar Physics*, **65**, 91–107. (Cited on page 21.)
- MAGDALENIĆ, J., MARQUÉ, C., ZHUKOV, A.N., VRŠNAK, B. & VERONIG, A. (2012). Flare-generated Type II Burst without Associated Coronal Mass Ejection. *Astrophysical Journal*, **746**, 152. (Cited on page 42.)
- MAIA, D., PICK, M., VOURLIDAS, A. & HOWARD, R. (2000). Development of Coronal Mass Ejections: Radio Shock Signatures. *Astrophysical Journal Letters*, **528**, L49–L51. (Cited on page 40.)
- MAIA, D.J.F. & PICK, M. (2004). Revisiting the Origin of Impulsive Electron Events: Coronal Magnetic Restructuring. *Astrophysical Journal*, **609**, 1082–1097. (Cited on pages 49, 174 and 217.)
- MALONEY, S.A. & GALLAGHER, P.T. (2010). Solar Wind Drag and the Kinematics of Interplanetary Coronal Mass Ejections. *Astrophysical Journal Letters*, **724**, L127–L132. (Cited on pages 34, 141 and 168.)
- MALONEY, S.A. & GALLAGHER, P.T. (2011). STEREO Direct Imaging of a Coronal Mass Ejection-driven Shock to 0.5 AU. *Astrophysical Journal Letters*, **736**, L5. (Cited on pages 51 and 195.)

REFERENCES

- MANCUSO, S. (2011). Combined Analysis of Ultraviolet and Radio Observations of the 7 May 2004 CME/Shock Event. *Solar Physics*, **273**, 511–523. (Cited on page 41.)
- MANCUSO, S. & RAYMOND, J.C. (2004). Coronal transients and metric type II radio bursts. I. Effects of geometry. *Astronomy & Astrophysics*, **413**, 363–371. (Cited on pages 41 and 42.)
- MANN, G. & CLASSEN, H.T. (1995). Electron acceleration to high energies at quasi-parallel shock waves in the solar corona. *Astronomy & Astrophysics*, **304**, 576. (Cited on pages 44 and 228.)
- MANN, G. & KLASSEN, A. (2005). Electron beams generated by shock waves in the solar corona. *Astronomy & Astrophysics*, **441**, 319–326. (Cited on pages 44, 85, 173 and 190.)
- MANN, G., CLASSEN, T. & AURASS, H. (1995). Characteristics of coronal shock waves and solar type II radio bursts. *Astronomy & Astrophysics*, **295**, 775. (Cited on page 37.)
- MANN, G., KLASSEN, A., CLASSEN, H.T., AURASS, H., SCHOLZ, D., MACDOWALL, R.J. & STONE, R.G. (1996). Catalogue of solar type II radio bursts observed from September 1990 to December 1993 and their statistical analysis. *Astronomy & Astrophysics Supplemental*, **119**, 489–498. (Cited on pages 37 and 173.)
- MANN, G., JANSEN, F., MACDOWALL, R.J., KAISER, M.L. & STONE, R.G. (1999). A heliospheric density model and type III radio bursts. *Astronomy & Astrophysics*, **348**, 614–620. (Cited on pages 168, 169 and 187.)
- MANOHARAN, P.K. & KUNDU, M.R. (2003). Coronal Structure of a Flaring Region and Associated Coronal Mass Ejection. *Astrophysical Journal*, **592**, 597–606. (Cited on pages 72 and 140.)
- MAXWELL, A. & THOMPSON, A.R. (1962). Spectral Observations of Solar Radio Bursts. II. Slow-Drift Bursts and Coronal Streamers. *Astrophysical Journal*, **135**, 138. (Cited on page 39.)
- MELROSE, D.B. (1986). *Instabilities in Space and Laboratory Plasmas*. Cambridge University Press. (Cited on page 90.)

REFERENCES

- MELROSE, D.B. (1989). *Instabilities in Space and Laboratory Plasmas*. (Cited on pages 87 and 88.)
- MENZEL, D.H. (1936). The Structure of the Atmosphere of ζ Aurigae. *Harvard College Observatory Circular*, **417**, 1–9. (Cited on page 233.)
- MERCIER, C., SUBRAMANIAN, P., KERDRAON, A., PICK, M., ANANTHAKRISHNAN, S. & JANARDHAN, P. (2006). Combining visibilities from the giant meterwave radio telescope and the Nancay radio heliograph. High dynamic range snapshot images of the solar corona at 327 MHz. *Astronomy & Astrophysics*, **447**, 1189–1201. (Cited on page 124.)
- MIERLA, M., INHESTER, B., MARQUÉ, C., RODRIGUEZ, L., GISSOT, S., ZHUKOV, A.N., BERGHMANS, D. & DAVILA, J. (2009). On 3D Reconstruction of Coronal Mass Ejections: I. Method Description and Application to SECCHI-COR Data. *Solar Physics*, **259**, 123–141. (Cited on page 24.)
- MINNAERT, M. (1930a). On the continuous spectrum of the corona and its polarisation. With 3 figures. (Received July 30, 1930). *Zeitschrift fur Astrophysik*, **1**, 209–+. (Cited on page 141.)
- MINNAERT, M. (1930b). On the continuous spectrum of the corona and its polarisation. With 3 figures. (Received July 30, 1930). *Zeitschrift fur Astrophysik*, **1**, 209. (Cited on pages 148 and 150.)
- MITALAS, R. & SILLS, K.R. (1992). On the photon diffusion time scale for the sun. *Astrophysical Journal*, **401**, 759. (Cited on page 5.)
- MITEVA, R. & MANN, G. (2007). The electron acceleration at shock waves in the solar corona. *Astronomy & Astrophysics*, **474**, 617–625. (Cited on page 44.)
- MONTMERLE, T., AUGEREAU, J.C., CHAUSSIDON, M., GOUNELLE, M., MARTY, B. & MORBIDELLI, A. (2006). From Suns to Life: A Chronological Approach to the History of Life on Earth 3. Solar System Formation and Early Evolution: the First 100 Million Years. *Earth Moon and Planets*, **98**, 39–95. (Cited on page 2.)
- MOON, Y.J., CHOE, G.S., WANG, H., PARK, Y.D., GOPALSWAMY, N., YANG, G. & YASHIRO, S. (2002). A Statistical Study of Two Classes of Coronal Mass Ejections. *Astrophysical Journal*, **581**, 694–702. (Cited on page 25.)

REFERENCES

- MORAN, T.G. & DAVILA, J.M. (2004). Three-Dimensional Polarimetric Imaging of Coronal Mass Ejections. *Science*, **305**, 66–71. (Cited on page 24.)
- MOSES, D., CLETTE, F., DELABOUDINIÈRE, J.P., ARTZNER, G.E., BOUGNET, M., BRUNAUD, J., CARABETIAN, C., GABRIEL, A.H., HOCHEDEZ, J.F., MILLIER, F., SONG, X.Y., AU, B., DERE, K.P., HOWARD, R.A., KREPLIN, R., MICHELS, D.J., DEFISE, J.M., JAMAR, C., ROCHUS, P., CHAUVINEAU, J.P., MARIOGE, J.P., CATURA, R.C., LEMEN, J.R., SHING, L., STERN, R.A., GURMAN, J.B., NEUPERT, W.M., NEWMARK, J., THOMPSON, B., MAUCHERAT, A., PORTIER-FOZZANI, F., BERGHMANS, D., CUGNON, P., VAN DESSEL, E.L. & GABRYL, J.R. (1997). EIT Observations of the Extreme Ultraviolet Sun. *Solar Physics*, **175**, 571–599. (Cited on page 46.)
- MÜLLER-MELLIN, R., BÖTTCHER, S., FALENSKI, J., RODE, E., DUVET, L., SANDERSON, T., BUTLER, B., JOHLANDER, B. & SMIT, H. (2008). The Solar Electron and Proton Telescope for the STEREO Mission. *Space Science Reviews*, **136**, 363–389. (Cited on page 190.)
- MUNRO, R.H., GOSLING, J.T., HILDNER, E., MACQUEEN, R.M., POLAND, A.I. & ROSS, C.L. (1979). The association of coronal mass ejection transients with other forms of solar activity. *Solar Physics*, **61**, 201–215. (Cited on pages 29 and 141.)
- NELSON, G.J. & MELROSE, D.B. (1985). *Type II bursts*, 333–359. (Cited on page 37.)
- NEWKIRK, G., JR. (1961). The Solar Corona in Active Regions and the Thermal Origin of the Slowly Varying Component of Solar Radio Radiation. *Astrophysical Journal*, **133**, 983. (Cited on page 97.)
- NITA, G.M. & GARY, D.E. (2010). The generalized spectral kurtosis estimator. *Monthly Notices of the Royal Astronomical Society*, **406**, L60–L64. (Cited on page 137.)
- NITA, G.M., GARY, D.E., LIU, Z., HURFORD, G.J. & WHITE, S.M. (2007). Radio Frequency Interference Excision Using Spectral-Domain Statistics. *Publications of the Astronomical Society of the Pacific*, **119**, 805–827. (Cited on page 137.)
- OLMEDO, O., ZHANG, J., WECHSLER, H., POLAND, A. & BORNE, K. (2008). Automatic Detection and Tracking of Coronal Mass Ejections in Coronagraph Time Series. *Solar Physics*, **248**, 485–499. (Cited on page 203.)

REFERENCES

- ONTIVEROS, V. & VOURLIDAS, A. (2009). Quantitative Measurements of Coronal Mass Ejection-Driven Shocks from LASCO Observations. *Astrophysical Journal*, **693**, 267–275. (Cited on page 51.)
- PARKER, E.N. (1963). The Solar-Flare Phenomenon and the Theory of Reconnection and Annihilation of Magnetic Fields. *Astrophysical Journal Supplemental Series*, **8**, 177. (Cited on page 62.)
- PAYNE-SCOTT, R., YABSLEY, D.E. & BOLTON, J.G. (1947). Relative Times of Arrival of Bursts of Solar Noise on Different Radio Frequencies. *Nature*, **160**, 256–257. (Cited on page 38.)
- PESNELL, W.D., THOMPSON, B.J. & CHAMBERLIN, P.C. (2012). The Solar Dynamics Observatory (SDO). *Solar Physics*, **275**, 3–15. (Cited on page 174.)
- PETSCHEK, H.E. (1964). Magnetic Field Annihilation. *NASA Special Publication*, **50**, 425. (Cited on page 64.)
- PHILLIPS, K.J.H., FELDMAN, U. & LANDI, E. (2008). *Ultraviolet and X-ray Spectroscopy of the Solar Atmosphere*. Cambridge University Press. (Cited on page 14.)
- PICK, M. & VILMER, N. (2008). Sixty-five years of solar radioastronomy: flares, coronal mass ejections and Sun Earth connection. *Astronomy & Astrophysics Review*, **16**, 1–153. (Cited on page 46.)
- PICK, M., FORBES, T.G., MANN, G., CANE, H.V., CHEN, J., CIARAVELLA, A., CREMADES, H., HOWARD, R.A., HUDSON, H.S., KLASSEN, A., KLEIN, K.L., LEE, M.A., LINKER, J.A., MAIA, D., MIKIC, Z., RAYMOND, J.C., REINER, M.J., SIMNETT, G.M., SRIVASTAVA, N., TRIPATHI, D., VAINIO, R., VOURLIDAS, A., ZHANG, J., ZURBUCHEN, T.H., SHEELEY, N.R. & MARQUÉ, C. (2006). Multi-Wavelength Observations of CMEs and Associated Phenomena. Report of Working Group F. *Space Science Reviews*, **123**, 341–382. (Cited on page 22.)
- POLAND, A.I., HOWARD, R.A., KOOMEN, M.J., MICHELS, D.J. & SHEELEY, N.R., JR. (1981). Coronal transients near sunspot maximum. *Solar Physics*, **69**, 169–175. (Cited on pages 29 and 141.)

REFERENCES

- PRIEST, E. & FORBES, T. (2000). *Magnetic Reconnection*. (Cited on pages 66, 67, 68, 69 and 81.)
- PRIEST, E.R. & FORBES, T.G. (1986). New models for fast steady state magnetic reconnection. *Journal of Geophysical Research*, **91**, 5579–5588. (Cited on page 65.)
- RATCLIFFE, H., BIAN, N.H. & KONTAR, E.P. (2012). Density Fluctuations and the Acceleration of Electrons by Beam-generated Langmuir Waves in the Solar Corona. *Astrophysical Journal*, **761**, 176. (Cited on page 92.)
- REID, H.A.S. & KONTAR, E.P. (2010). Solar Wind Density Turbulence and Solar Flare Electron Transport from the Sun to the Earth. *Astrophysical Journal*, **721**, 864–874. (Cited on page 92.)
- REINER, M.J., KAISER, M.L., GOPALSWAMY, N., AURASS, H., MANN, G., VOURLIDAS, A. & MAKSIMOVIC, M. (2001). Statistical analysis of coronal shock dynamics implied by radio and white-light observations. *Journal of Geophysical Research*, **106**, 25279–25290. (Cited on pages 41 and 42.)
- ROBBRECHT, E. & BERGHMANS, D. (2004). Automated recognition of coronal mass ejections (CMEs) in near-real-time data. *Astronomy & Astrophysics*, **425**, 1097–1106. (Cited on page 203.)
- ROBBRECHT, E., BERGHMANS, D. & VAN DER LINDEN, R.A.M. (2009). Automated LASCO CME Catalog for Solar Cycle 23: Are CMEs Scale Invariant? *Astrophysical Journal*, **691**, 1222–1234. (Not cited.)
- ROBINSON, P.A. & CAIRNS, I.H. (1993). Stochastic Growth Theory of Type III Solar Radio Emission. *Astrophysical Journal*, **418**, 506. (Cited on pages 92, 93 and 232.)
- ROBINSON, P.A. & CAIRNS, I.H. (1998). Fundamental and Harmonic Emission in Type III Solar Radio Bursts - II. Dominant Modes and Dynamic Spectra. *Solar Physics*, **181**, 395–428. (Cited on pages 93 and 232.)
- ROBINSON, P.A., WILLES, A.J. & CAIRNS, I.H. (1993). Dynamics of Langmuir and ion-sound waves in type III solar radio sources. *Astrophysical Journal*, **408**, 720–734. (Cited on page 89.)

REFERENCES

- ROBINSON, P.A., CAIRNS, I.H. & WILLES, A.J. (1994). Dynamics and efficiency of type III solar radio emission. *Astrophysical Journal*, **422**, 870–882. (Cited on pages 89 and 90.)
- ROBINSON, R.D. & STEWART, R.T. (1985). A positional comparison between coronal mass ejection events and solar type II bursts. *Solar Physics*, **97**, 145–157. (Cited on page 40.)
- RUSSELL, C.T. & MULLIGAN, T. (2002). On the magnetosheath thicknesses of interplanetary coronal mass ejections. *Planet. Space Sci.*, **50**, 527–534. (Cited on page 51.)
- RUST, D.M. (1972). Flares and Changing Magnetic Fields. *Solar Physics*, **25**, 141–157. (Cited on page 66.)
- SACKMANN, I.J., BOOTHROYD, A.I. & KRAEMER, K.E. (1993). Our Sun. III. Present and Future. *Astrophysical Journal*, **418**, 457. (Cited on pages 2 and 3.)
- SAITO, K., POLAND, A.I. & MUNRO, R.H. (1977). A study of the background corona near solar minimum. *Solar Physics*, **55**, 121–134. (Cited on page 97.)
- SCHERRER, P.H., SCHOU, J., BUSH, R.I., KOSOVICHEV, A.G., BOGART, R.S., HOEKSEMA, J.T., LIU, Y., DUVALL, T.L., ZHAO, J., TITLE, A.M., SCHRIJVER, C.J., TARBELL, T.D. & TOMCZYK, S. (2012). The Helioseismic and Magnetic Imager (HMI) Investigation for the Solar Dynamics Observatory (SDO). *Solar Physics*, **275**, 207–227. (Cited on pages 181 and 182.)
- SCHMIDT, J.M. & CAIRNS, I.H. (2012a). Type II radio bursts: 1. New entirely analytic formalism for the electron beams, Langmuir waves, and radio emission. *Journal of Geophysical Research (Space Physics)*, **117**, 4106. (Cited on pages 93, 193 and 198.)
- SCHMIDT, J.M. & CAIRNS, I.H. (2012b). Type II radio bursts: 2. Application of the new analytic formalism. *Journal of Geophysical Research (Space Physics)*, **117**, 11104. (Cited on pages 85 and 93.)
- SCHRIJVER, C.J. & DE ROSA, M.L. (2003). Photospheric and heliospheric magnetic fields. *Solar Physics*, **212**, 165–200. (Cited on pages 181 and 182.)
- SCHRIJVER, C.J. & ZWAAN, C. (2008). *Solar and Stellar Magnetic Activity*. (Cited on page 12.)

REFERENCES

- SCHRIJVER, C.J., ELMORE, C., KLIEM, B., TÖRÖK, T. & TITLE, A.M. (2008a). Observations and Modeling of the Early Acceleration Phase of Erupting Filaments Involved in Coronal Mass Ejections. *Astrophysical Journal*, **674**, 586–595. (Cited on pages 66 and 75.)
- SCHRIJVER, C.J., ELMORE, C., KLIEM, B., TÖRÖK, T. & TITLE, A.M. (2008b). Observations and Modeling of the Early Acceleration Phase of Erupting Filaments Involved in Coronal Mass Ejections. *Astrophysical Journal*, **674**, 586–595. (Cited on page 140.)
- SCHUSTER, A. (1879). on the polarisation of the Solar Corona. *Monthly Notices of the Royal Astronomical Society*, **40**, 35. (Cited on page 148.)
- SHEELEY, N.R., WALTERS, J.H., WANG, Y.M. & HOWARD, R.A. (1999). Continuous tracking of coronal outflows: Two kinds of coronal mass ejections. *Journal of Geophysical Research*, **104**, 24739–24768. (Cited on page 25.)
- SHEELEY, N.R., JR., MICHELS, D.J., HOWARD, R.A. & KOOMEN, M.J. (1980). Initial observations with the SOLWIND coronagraph. *Astrophysical Journal Letters*, **237**, L99–L101. (Cited on page 21.)
- SHEELEY, N.R., JR., WANG, Y.M., HAWLEY, S.H., BRUECKNER, G.E., DERE, K.P., HOWARD, R.A., KOOMEN, M.J., KORENDYKE, C.M., MICHELS, D.J., PASWATERS, S.E., SOCKER, D.G., ST. CYR, O.C., WANG, D., LAMY, P.L., LLEBARIA, A., SCHWENN, R., SIMNETT, G.M., PLUNKETT, S. & BIESECKER, D.A. (1997). Measurements of Flow Speeds in the Corona between 2 and 30 R_{sun}. *Astrophysical Journal*, **484**, 472. (Cited on pages 34 and 74.)
- SHIPLEY, B.C. (2001). 'Had Lord Kelvin a right?': John Perry, natural selection and the age of the Earth, 1894–1895. *Geological Society of London Special Publications*, **190**, 91–105. (Not cited.)
- SONNERUP, B.U.Ö. (1970). Magnetic-field re-connexion in a highly conducting incompressible fluid. *Journal of Plasma Physics*, **4**, 161. (Cited on page 65.)
- SPITZER, L. (1962). *Physics of Fully Ionized Gases*. (Cited on page 61.)
- SPREITER, J.R., SUMMERS, A.L. & ALKSNE, A.Y. (1966). Hydromagnetic flow around the magnetosphere. *Planet. Space Sci.*, **14**, 223. (Cited on page 51.)

REFERENCES

- STEELE, C.D.C., HOOD, A.W., PRIEST, E.R. & AMARI, T. (1989). Non-equilibrium of a cylindrical magnetic arcade. *Solar Physics*, **123**, 127–141. (Cited on page 69.)
- STERLING, A.C. & HUDSON, H.S. (1997). YOHKOH SXT Observations of X-Ray "Dimming" Associated with a Halo Coronal Mass Ejection. *Astrophysical Journal Letters*, **491**, L55. (Cited on page 213.)
- STEWART, R.T. & MAGUN, A. (1980). Radio evidence for electron acceleration by transverse shock waves in herringbone Type II solar bursts. *Proceedings of the Astronomical Society of Australia*, **4**, 53–55. (Cited on pages 45, 193 and 196.)
- STEWART, R.T. & MCLEAN, D.J. (1982). Correcting low-frequency solar radio source positions for ionospheric refraction. *Proceedings of the Astronomical Society of Australia*, **4**, 386–389. (Cited on page 178.)
- STEWART, R.T., MCCABE, M.K., KOOMEN, M.J., HANSEN, R.T. & DULK, G.A. (1974). Observations of Coronal Disturbances from 1 to 9 R_{sun} . I: First Event of 1973, January 11. *Solar Physics*, **36**, 203–217. (Cited on page 39.)
- STONE, R.G., BOUGERET, J.L., CALDWELL, J., CANU, P., DE CONCHY, Y., CORNILLEAU-WEHRLIN, N., DESCH, M.D., FAINBERG, J., GOETZ, K. & GOLDSTEIN, M.L. (1992). The Unified Radio and Plasma wave investigation. *Astronomy & Astrophysics Supplemental*, **92**, 291–316. (Cited on page 126.)
- STURROCK, P.A. (1964). Type III Solar Radio Bursts. *NASA Special Publication*, **50**, 357. (Cited on page 92.)
- STURROCK, P.A. (1991). Maximum energy of semi-infinite magnetic field configurations. *Astrophysical Journal*, **380**, 655–659. (Cited on page 70.)
- SUBRAMANIAN, P. & VOURLIDAS, A. (2007). Energetics of solar coronal mass ejections. *Astronomy & Astrophysics*, **467**, 685–693. (Cited on page 33.)
- SWEET, P.A. (1958). The Neutral Point Theory of Solar Flares. In B. Lehnert, ed., *Electromagnetic Phenomena in Cosmical Physics*, vol. 6 of *IAU Symposium*, 123. (Cited on page 62.)

REFERENCES

- TEMMER, M., VERONIG, A.M., KONTAR, E.P., KRUCKER, S. & VRŠNAK, B. (2010). Combined STEREO/RHESSI Study of Coronal Mass Ejection Acceleration and Particle Acceleration in Solar Flares. *Astrophysical Journal*, **712**, 1410–1420. (Cited on page 27.)
- THE RADIOHELIOGRAPH GROUP (1993). The Nançay multifrequency radioheliograph: New developments and data acquisition for the solar physics community. *Advances in Space Research*, **13**, 411–414. (Cited on page 120.)
- THEJAPPA, G. & MACDOWALL, R.J. (1998). Evidence for Strong and Weak Turbulence Processes in the Source Region of a Local Type III Radio Burst. *Astrophysical Journal*, **498**, 465. (Cited on page 92.)
- THERNISIEN, A.F.R., HOWARD, R.A. & VOURLIDAS, A. (2006). Modeling of Flux Rope Coronal Mass Ejections. *Astrophysical Journal*, **652**, 763–773. (Cited on page 24.)
- THOMPSON, B.J. & MYERS, D.C. (2009). A Catalog of Coronal "EIT Wave" Transients. *Astrophysical Journal Supplemental Series*, **183**, 225–243. (Cited on page 46.)
- THOMPSON, B.J., PLUNKETT, S.P., GURMAN, J.B., NEWMARK, J.S., ST. CYR, O.C. & MICHELS, D.J. (1998). SOHO/EIT observations of an Earth-directed coronal mass ejection on May 12, 1997. *Geophysical Research Letters*, **25**, 2465–2468. (Cited on pages 46 and 47.)
- THOMPSON, M.J., CHRISTENSEN-DALSGAARD, J., MIESCH, M.S. & TOOMRE, J. (2003). The Internal Rotation of the Sun. *Annual Review of Astronomy & Astrophysics*, **41**, 599–643. (Cited on pages 6 and 8.)
- THOMPSON, W.T. & REGINALD, N.L. (2008). The Radiometric and Pointing Calibration of SECCHI COR1 on STEREO. *Solar Physics*, **250**, 443–454. (Cited on pages 107, 109 and 113.)
- TOPTYGIN, I.N. (1980). Acceleration of particles by shocks in a cosmic plasma. *Space Science Reviews*, **26**, 157–213. (Cited on page 84.)
- TOUSEY, R. (1973). The solar corona. In M. J. Rycroft & S. K. Runcorn, ed., *Space Research XIII*, Vol. 2, p. 713 - 730, 713–730. (Cited on page 21.)

REFERENCES

- TURCK-CHIÈZE, S. & COUVIDAT, S. (2011). Solar neutrinos, helioseismology and the solar internal dynamics. *Reports on Progress in Physics*, **74**, 086901. (Cited on pages 4, 5 and 6.)
- UCHIDA, Y. (1960). On the Exciters of Type II and Type III Solar Radio Bursts. *Publications of the Astronomical Society of Japan*, **12**, 376. (Cited on page 38.)
- UCHIDA, Y. (1974). Behavior of the flare produced coronal MHD wavefront and the occurrence of type II radio bursts. *Solar Physics*, **39**, 431–449. (Cited on page 39.)
- VAN DE HULST, H.C. (1950). The electron density of the solar corona. *Bulletin of the Astronomical Institutes of the Netherlands*, **11**, 135. (Cited on pages 141, 149, 179 and 233.)
- VAN HAARLEM, M.P., WISE, M.W., GUNST, A.W., HEALD, G., MCKEAN, J.P., HESSELS, J.W.T., DE BRUYN, A.G., NIJBOER, R., SWINBANK, J., FALLOWS, R., BRENTJENS, M., NELLES, A., BECK, R., FALCKE, H., FENDER, R., HÖRANDEL, J., KOOPMANS, L.V.E., MANN, G., MILEY, G., RÖTTGERING, H., STAPPERS, B.W., WIJERS, R.A.M.J., ZAROUBI, S., VAN DEN AKKER, M., ALEXOV, A., ANDERSON, J., ANDERSON, K., VAN ARDENNE, A., ARTS, M., ASGEKAR, A., AVRUCH, I.M., BATEJAT, F., BÄHREN, L., BELL, M.E., BELL, M.R., VAN BEMMEL, I., BENNEMA, P., BENTUM, M.J., BERNARDI, G., BEST, P., BÎRZAN, L., BONAFEDE, A., BOONSTRA, A.J., BRAUN, R., BREGMAN, J., BREITLING, F., VAN DE BRINK, R.H., BRODERICK, J., BROEKEMA, P.C., BROUW, W.N., BRÜGGEN, M., BUTCHER, H.R., VAN CAPPELLEN, W., CIARDI, B., COENEN, T., CONWAY, J., COOLEN, A., CORSTANJE, A., DAMSTRA, S., DAVIES, O., DELLER, A.T., DETTMAR, R.J., VAN DIEPEN, G., DIJKSTRA, K., DONKER, P., DOORDUIN, A., DROMER, J., DROST, M., VAN DUIN, A., EISLÖFFEL, J., VAN ENST, J., FERRARI, C., FRIESWIJK, W., GANKEMA, H., GARRETT, M.A., DE GASPARIN, F., GERBERS, M., DE GEUS, E., GRIESSMEIER, J.M., GRIT, T., GRUPPEN, P., HAMAKER, J.P., HASSALL, T., HOEFT, M., HOLTIES, H.A., HORNEFFER, A., VAN DER HORST, A., VAN HOUWELINGEN, A., HUIGEN, A., IACOBELLI, M., INTEMA, H., JACKSON, N., JELIC, V., DE JONG, A., KANT, D., KARASTERGIOU, A., KOERS, A., KOLLEN, H., KONDRAKIEV, V.I., KOOISTRA, E., KOOPMAN, Y., KOSTER, A., KUNIYOSHI, M., KRAMER, M., KUPER, G., LAMBROPOULOS, P., LAW, C., VAN LEEUWEN, J., LEMAITRE, J., LOOSE, M., MAAT, P., MACARIO, G., MARKOFF, S., MASTERS, J., MCFADDEN, R.A., MCKAY-BUKOWSKI, D., MEIJERING, H., MEULMAN, H., MEVIUS, M., MILLENAAR, R., MILLER-JONES, J.C.A.,

REFERENCES

- MOHAN, R.N., MOL, J.D., MORAWIETZ, J., MORGANTI, R., MULCAHY, D.D., MULDER, E., MUNK, H., NIEUWENHUIS, L., VAN NIEUWPOORT, R., NOORDAM, J.E., NORDEN, M., NOUTSOS, A., OFFRINGA, A.R., OLOFSSON, H., OMAR, A., ORRÚ, E., OVEREEM, R., PAAS, H., PANDEY-POMMIER, M., PANDEY, V.N., PIZZO, R., POLATIDIS, A., RAFFERTY, D., RAWLINGS, S., REICH, W., DE REIJER, J.P., REITSMA, J., RENTING, G.A., RIEMERS, P., ROL, E., ROMEIN, J.W., ROOSJEN, J., RUITER, M., SCAIFE, A., VAN DER SCHAAF, K., SCHEERS, B., SCHELLART, P., SCHOENMAKERS, A., SCHOONDERBEEK, G., SERYLAK, M., SHULEVSKI, A., SLUMAN, J., SMIRNOV, O., SOBEY, C., SPREEUW, H., STEINMETZ, M., STERKS, C.G.M., STIEPEL, H.J., STUURWOLD, K., TAGGER, M., TANG, Y., TASSE, C., THOMAS, I., THOUDAM, S., TORIBIO, M.C., VAN DER TOL, B., USOV, O., VAN VEELEN, M., VAN DER VEEN, A.J., TER VEEN, S., VERBIEST, J.P.W., VERMEULEN, R., VERMAAS, N., VOCKS, C., VOGT, C., DE VOS, M., VAN DER WAL, E., VAN WEEREN, R., WEGGEMANS, H., WELTEVREDE, P., WHITE, S., WIJNHOLDS, S.J., WILHELMSSON, T., WUCKNITZ, O., YATAWATTA, S., ZARKA, P., ZENSUS, A. & VAN ZWieten, J. (2013). LOFAR: The LOw-Frequency ARray. *Astronomy & Astrophysics*, **556**, A2. (Cited on page 199.)
- VANDAS, M. & KARLICKÝ, M. (2011). Electron acceleration in a wavy shock front. *Astronomy & Astrophysics*, **531**, A55. (Cited on pages 44 and 197.)
- VEDENOV, A.A. (1963). Quasi-Linear Equations for Quantized Plasma. *Soviet Physics Doklady*, **7**, 1008. (Cited on pages 86 and 88.)
- VERNAZZA, J.E., AVRETT, E.H. & LOESER, R. (1981). Structure of the solar chromosphere. III - Models of the EUV brightness components of the quiet-sun. *Astrophysical Journal Supplemental Series*, **45**, 635–725. (Cited on pages 13, 14 and 15.)
- VERONIG, A.M., MUHR, N., KIENREICH, I.W., TEMMER, M. & VRŠNAK, B. (2010). First Observations of a Dome-shaped Large-scale Coronal Extreme-ultraviolet Wave. *Astrophysical Journal Letters*, **716**, L57–L62. (Cited on page 47.)
- VOURLIDAS, A. & BEMPORAD, A. (2012). A decade of coronagraphic and spectroscopic studies of CME-driven shocks. In J. Heerikhuisen, G. Li, N. Pogorelov & G. Zank, eds., *American Institute of Physics Conference Series*, vol. 1436 of *American Institute of Physics Conference Series*, 279–284. (Cited on pages 50, 193 and 195.)

REFERENCES

- VOURLIDAS, A., SUBRAMANIAN, P., DERE, K.P. & HOWARD, R.A. (2000). Large-Angle Spectrometric Coronagraph Measurements of the Energetics of Coronal Mass Ejections. *Astrophysical Journal*, **534**, 456–467. (Cited on pages 29, 31, 142, 151, 154, 166, 171 and 202.)
- VOURLIDAS, A., BUZASI, D., HOWARD, R.A. & ESFANDIARI, E. (2002). Mass and energy properties of LASCO CMEs. In A. Wilson, ed., *Solar Variability: From Core to Outer Frontiers*, vol. 506 of *ESA Special Publication*, 91–94. (Cited on pages 29 and 141.)
- VOURLIDAS, A., WU, S.T., WANG, A.H., SUBRAMANIAN, P. & HOWARD, R.A. (2003). Direct Detection of a Coronal Mass Ejection-Associated Shock in Large Angle and Spectrometric Coronagraph Experiment White-Light Images. *Astrophysical Journal*, **598**, 1392–1402. (Cited on page 51.)
- VOURLIDAS, A., HOWARD, R.A., ESFANDIARI, E., PATSOURAKOS, S., YASHIRO, S. & MICHALEK, G. (2010). Comprehensive Analysis of Coronal Mass Ejection Mass and Energy Properties Over a Full Solar Cycle. *Astrophysical Journal*, **722**, 1522–1538. (Cited on pages 20, 29, 32, 141, 159, 166, 167 and 171.)
- VOURLIDAS, A., LYNCH, B.J., HOWARD, R.A. & LI, Y. (2013). How Many CMEs Have Flux Ropes? Deciphering the Signatures of Shocks, Flux Ropes, and Prominences in Coronagraph Observations of CMEs. *Solar Physics*, **284**, 179–201. (Cited on page 50.)
- VRŠNAK, B. (2006). Forces governing coronal mass ejections. *Advances in Space Research*, **38**, 431–440. (Cited on pages 33, 34, 35 and 170.)
- VRŠNAK, B. & CLIVER, E.W. (2008). Origin of Coronal Shock Waves. Invited Review. *Solar Physics*, **253**, 215–235. (Cited on pages 42 and 173.)
- VRŠNAK, B. & GOPALSWAMY, N. (2002). Influence of the aerodynamic drag on the motion of interplanetary ejecta. *Journal of Geophysical Research (Space Physics)*, **107**, 1019. (Not cited.)
- VRŠNAK, B. & LULIĆ, S. (2000a). Formation Of Coronal Mhd Shock Waves - I. The Basic Mechanism. *Solar Physics*, **196**, 157–180. (Cited on page 42.)
- VRŠNAK, B. & LULIĆ, S. (2000b). Formation of coronal MHD shock waves - II. The Pressure Pulse Mechanism. *Solar Physics*, **196**, 181–197. (Cited on page 42.)

REFERENCES

- VRŠNAK, B., MAGDALENIĆ, J. & AURASS, H. (2001). Comparative Analysis of Type ii Bursts and of Thermal and non-Thermal Flare Signatures. *Solar Physics*, **202**, 319–335. (Cited on page 42.)
- VRŠNAK, B., MAGDALENIĆ, J. & ZLOBEC, P. (2004). Band-splitting of coronal and interplanetary type II bursts. III. Physical conditions in the upper corona and interplanetary space. *Astronomy and Astrophysics*, **413**, 753–763. (Not cited.)
- VRŠNAK, B., MAGDALENIĆ, J., TEMMER, M., VERONIG, A., WARMUTH, A., MANN, G., AURASS, H. & OTRUBA, W. (2005a). Broadband Metric-Range Radio Emission Associated with a Moreton/EIT Wave. *Astrophysical Journal Letters*, **625**, L67–L70. (Cited on page 217.)
- VRŠNAK, B., SUDAR, D. & RUŽDJAK, D. (2005b). The CME-flare relationship: Are there really two types of CMEs? *Astronomy & Astrophysics*, **435**, 1149–1157. (Cited on pages 25, 47 and 174.)
- VRŠNAK, B., MARIČIĆ, D., STANGER, A.L., VERONIG, A.M., TEMMER, M. & ROŠA, D. (2007). Acceleration Phase of Coronal Mass Ejections: I. Temporal and Spatial Scales. *Solar Physics*, **241**, 85–98. (Cited on page 27.)
- WAKKER, B.P. & SCHWARZ, U.J. (1988). The Multi-Resolution CLEAN and its application to the short-spacing problem in interferometry. *Astronomy & Astrophysics*, **200**, 312–322. (Cited on page 123.)
- WANG, Y.M. (2000). EIT Waves and Fast-Mode Propagation in the Solar Corona. *Astrophysical Journal Letters*, **543**, L89–L93. (Cited on pages 47 and 173.)
- WARMUTH, A. & MANN, G. (2005). A model of the Alfvén speed in the solar corona. *Astronomy & Astrophysics*, **435**, 1123–1135. (Cited on page 183.)
- WARMUTH, A., VRŠNAK, B., MAGDALENIĆ, J., HANSLMEIER, A. & OTRUBA, W. (2004). A multiwavelength study of solar flare waves. II. Perturbation characteristics and physical interpretation. *Astronomy & Astrophysics*, **418**, 1117–1129. (Cited on pages 47, 174, 195 and 196.)

REFERENCES

- WEBB, D.F. & HOWARD, T.A. (2012). Coronal Mass Ejections: Observations. *Living Reviews in Solar Physics*, **9**, 3. (Cited on page 24.)
- WEBB, D.F. & HUNDAUSEN, A.J. (1987). Activity associated with the solar origin of coronal mass ejections. *Solar Physics*, **108**, 383–401. (Cited on page 22.)
- WILD, J.P. (1950). Observations of the Spectrum of High-Intensity Solar Radiation at Metre Wavelengths. III. Isolated Bursts. *Australian Journal of Scientific Research A Physical Sciences*, **3**, 541. (Cited on page 173.)
- WILD, J.P. (1964). Radio Observations of Solar Flares. *NASA Special Publication*, **50**, 161. (Cited on page 45.)
- WILD, J.P., MURRAY, J.D. & ROWE, W.C. (1954). Harmonics in the Spectra of Solar Radio Disturbances. *Australian Journal of Physics*, **7**, 439. (Cited on page 38.)
- WILD, J.P., SHERIDAN, K.V. & TRENT, G.H. (1959). The transverse motions of the sources of solar radio bursts. In R.N. Bracewell, ed., *URSI Symp. 1: Paris Symposium on Radio Astronomy*, vol. 9 of *IAU Symposium*, 176. (Cited on page 21.)
- WILD, J.P., SMERD, S.F. & WEISS, A.A. (1963). Solar Bursts. *Annual Review of Astronomy & Astrophysics*, **1**, 291. (Cited on page 21.)
- WOLFSON, R. & SARAN, S. (1998). Energetics of Coronal Mass Ejections: Role of the Streamer Cavity. *Astrophysical Journal*, **499**, 496. (Cited on page 65.)
- WU, C.S. (1984). A fast Fermi process - Energetic electrons accelerated by a nearly perpendicular bow shock. *Journal of Geophysical Research*, **89**, 8857–8862. (Cited on pages 85 and 196.)
- YASHIRO, S., GOPALSWAMY, N., MICHALEK, G., ST. CYR, O.C., PLUNKETT, S.P., RICH, N.B. & HOWARD, R.A. (2004). A catalog of white light coronal mass ejections observed by the SOHO spacecraft. *Journal of Geophysical Research (Space Physics)*, **109**, 7105. (Cited on pages 23 and 24.)
- YURCHYSHYN, V., YASHIRO, S., ABRAMENKO, V., WANG, H. & GOPALSWAMY, N. (2005). Statistical Distributions of Speeds of Coronal Mass Ejections. *Astrophysical Journal*, **619**, 599–603. (Cited on pages 24 and 25.)

REFERENCES

- ZHANG, J. & DERE, K.P. (2006). A Statistical Study of Main and Residual Accelerations of Coronal Mass Ejections. *Astrophysical Journal*, **649**, 1100–1109. (Cited on pages 26, 27 and 35.)
- ZHANG, J., DERE, K.P., HOWARD, R.A., KUNDU, M.R. & WHITE, S.M. (2001). On the Temporal Relationship between Coronal Mass Ejections and Flares. *Astrophysical Journal*, **559**, 452–462. (Cited on pages 28, 166 and 170.)
- ZHANG, J., DERE, K.P., HOWARD, R.A. & VOURLIDAS, A. (2004). A Study of the Kinematic Evolution of Coronal Mass Ejections. *Astrophysical Journal*, **604**, 420–432. (Cited on pages 28, 166 and 170.)
- ZHUKOV, A.N., RODRIGUEZ, L. & DE PATOUL, J. (2009). STEREO/SECCHI Observations on 8 December 2007: Evidence Against the Wave Hypothesis of the EIT Wave Origin. *Solar Physics*, **259**, 73–85. (Cited on page 174.)
- ZLOBEC, P., MESSEROTTI, M., KARLICKY, M. & URBARZ, H. (1993). Fine structures in time profiles of type II bursts at frequencies above 200 MHz. *Solar Physics*, **144**, 373–384. (Cited on pages 44, 173, 197 and 198.)
- ZUCCA, P., CARLEY, E.P., MCCUALEY, J., GALLAGHER, P.T., MONSTEIN, C. & MCA-TEER, R.T.J. (2012). Observations of Low Frequency Solar Radio Bursts from the Rosse Solar-Terrestrial Observatory. *Solar Physics*, **280**, 591–602. (Cited on pages 128, 134 and 190.)